Thomas S. E. Eriksson

Cardiovascular Mechanics

Monographic Series TU Graz

Computation in Engineering and Science

Series Editors

Monographic Series TU Graz

Computation in Engineering and Science **Volume 17**

Thomas S. E. Eriksson

Cardiovascular Mechanics

The Biomechanics of Arteries and the Human Heart

This work is based on the dissertation *"Cardiovascular Mechanics: The Biomechanics of Arteries and the Human Heart"*, presented by Thomas S. E.: Eriksson at Graz University of Technology, Institute of Biomechanics in July 2012.
Supervisor: G. A. Holzapfel (Graz University of Technology)
Co-supervisor: G. Plank (Medical University of Graz)

Bibliographic information published by Die Deutsche Bibliothek.
Die Deutsche Bibliothek lists this publication in the Deutsche Nationalbibliografie; detailed bibliographic data are available at http://dnb.ddb.de.

Cover photo	Vier-Spezies-Rechenmaschine by courtesy of the Gottfried Wilhelm Leibniz Bibliothek – Niedersächsische Landesbibliothek Hannover
Layout	Wolfgang Karl, TU Graz / Universitätsbibliothek Christina Fraueneder, TU Graz / Büro des Rektorates
Printed	by TU Graz / Büroservice

Verlag der Technischen Universität Graz

www.ub.tugraz.at/Verlag

ISBN: 978-3-85125-277-4 (print)
ISBN: 978-3-85125-278-1 (e-book)

DOI: 10.3217/978-3-85125-277-4

ABSTRACT

Modeling in biomechanics plays an important role in simulating biological functions and has great potential to aid medical clinicians in determining the cause of a disease, the type of treatment or by aiding in the training of a surgical procedure. Cardiovascular diseases (CVDs) are the leading cause of mortality today. This work therefore aims at developing a framework for modeling CVDs, such as cerebral aneurysms or heart diseases with increased myofiber dispersion as seen in, e.g., hypertrophic cardiomyopathy.

To this end, a three-dimensional growth model of a human saccular cerebral aneurysm is presented that includes the anisotropy of the medial layer. It is shown that including fibers in the media reduces the maximum principal stress, thickness increase and shear stress in the aneurysm wall. It is also shown that the axial pre-stretch has a large impact on the stress levels and thickness increase in the aneurysm wall.

In addition, the constituents needed for the numerical implementation of a structurally based constitutive law describing the behavior of passive myocardium is shown. A comparison is made between this invariant based model and a commonly used Green-Lagrange strain component based model and it is shown that using material parameters retrieved when both models is fitted using a simple shear mode experiment, the invariant based model is better suited to predict the stress in the myocardium for other modes of deformation. The passive cardiac model is coupled together with an evolution equation responsible for generating the active stress. A model of the left ventricle (LV) is presented where pressure is calculated as a response to the change in the ventricular volume in order to ensure physiologically realistic pressure-volume loops. The influence of myocardial fiber and sheet distribution is investigated by using two different setups, a generic setup and one based on experiments. The results implies that spatial heterogeneity may play a critical role in mechanical contraction of the LV and that geometrical descriptions of deformation are needed when evaluating the accuracy of a ventricular model.

Further, a novel approach to model the dispersion of both the fiber and sheet orientations evident in, especially diseased, myocardium is presented. Analytical and numerical simulations show that the dispersion parameter has great effect on myocardial deformation and stress development. The results also show that the dispersion has a significant impact on pressure-volume loops of an LV, and in future simulations the presented dispersion model for myocardium may advantageously be used together with models of, e.g., growth and remodeling of various cardiac diseases. In cases where fiber-reinforced models are extended to include the effect of distributed fiber orientations, neither the mathematical nor physical motivation for tension-compression fiber switching is clear, and in fact several choices exist for the material modeler. Therefore, methods to study such switching mechanisms is explored by analyzing six potential switching cases. Two different permeations of the dispersed fiber-reinforced model is proposed, depending on whether one can assume that the fibers are (nearly) uncoupled or strongly coupled to the isotropic ground matrix.

CONTENTS

1. INTRODUCTION AND MOTIVATION

1.1. Biomechanical Modeling

The world health organization (WHO) has stated that cardiovascular disease (CVD) is the leading cause of death in world. In Europe, for example, CVD comprises nearly half of all deaths (48 %) while in the United States nearly one of every third death (32.8 %) is attributed to CVD. Also in China, over one third of every death (35.8 %) is caused by some form of CVD [1–3]. The health care costs of CVD is estimated to be € 110 billion in the European Union alone, which is about 10 % of the total health care cost. Adding to that is another € 83 billion in indirect costs that includes production losses and informal care [1]. To put these staggering costs in perspective, NASA estimates that the cost to launch a space shuttle is about € 340 million (US$ 450 million) [4]. Thus, the total costs for CVD in the European Union alone is equivalent to nearly 570 space shuttle launches per year. The need for improvements in identification, understanding and treatment of CVD's is, therefore, of utmost importance. To this goal, biological mechanisms that underly CVD needs to be studied, e.g., chemical, electrical and mechanical mechanisms. In this thesis, we have developed a framework that includes electrophysiology and that can easily be extended to incorporate ionic cellular models. The focus, however, lies on the mechanical mechanisms in biomaterials. It is known that the mechanics of biological systems has been studied since the antiquity with Aristotle's book 'On the Motion of Animals' approximately 350 B.C., but it is with Fung's early works in the 1960's and 70's that modern day biomechanical modeling and the phrase biomechanics is born [5]. Today, modeling in biomechanics plays an important role in simulating biological functions and has great potential to aid medical clinicians in determining the cause of a disease, the type of treatment or by aiding in the training of a surgical procedure. Furthermore, through mechanobiology we know that mechanical stimulus on cells and tissue may affect biological processes. Thus, by modeling the progression of biological and mechanical processes, biomaterials can be better understood and phenomenon such as growth and remodeling as well as the development of various diseased states may be studied.

The most widely used framework for modeling soft tissue biomechanics is continuum mechanics, in which the discrete particles of a biological material, e.g., atoms and molecules on a micro scale or sometimes even cells and fibers on an intermediate scale, is considered to be a continuum and the material behavior of each particle is translated to the overall behavior of the continuum. Continuum mechanical models can, therefore, be used on a range of spatial scales, from individual cells to entire organs. Therefore, Section 1.2 offers

a brief overview of the necessary continuum mechanical framework that is used throughout this thesis. To model any type of biological tissue, it is also essential to understand the responses and underlying structure of the material. The following two Sections 1.3 and 1.4, therefore, describe the constituents and material behavior of two fascinating materials that are studied in this thesis, namely cerebral aneurysms and ventricular myocardium. However, as the focus of this thesis is dedicated to myocardial mechanics, this will be mirrored in the introduction.

1.2. Continuum Mechanical Framework

The basic relations in kinematics, stress, constitutive equations, incompressibility, invariant formulations and strong and weak forms of a boundary-value problem, needed for the completeness of this thesis, are covered in this section. For a more complete background on nonlinear continuum mechanics see the book by Holzapfel [6] and references therein.

1.2.1. Kinematics

A continuum body $\mathcal{B} = \{P_k\}$, where the mass and volume of the body is at least piecewise continuous, consists of a set of discrete points P_k. At a given time t, the body occupies a region $\Omega(t)$ set in a reference frame, $\varphi(O, \mathbf{e}_i)$, with origin O and orthonormal basis vectors $\mathbf{e}_i$, $i = \{1,2,3\}$, in a three-dimensional Euclidean space, as seen in Fig. 1.1. At some reference time t_0, a point P set in a reference region Ω_0 can be described by the position vector $\mathbf{X}(P,t_0)$. Here, $t_0 = 0$ is denoted as the initial time and the region $\Omega_0(t_0)$ as the initial (undeformed) configuration. At any time $t > t_0$ the body $\mathcal{B}$ may have transformed to occupy the current (deformed) configuration $\Omega(t)$. The position of the point P in the current configuration can be described by the position vector $\mathbf{x}(P,t) = \chi(\mathbf{X},t)$, where χ denote the motion of body $\mathcal{B}$. Thus, the deformation gradient

$$\mathbf{F}(\mathbf{X},t) = \frac{\partial \chi(\mathbf{X},t)}{\partial \mathbf{X}} \tag{1.1}$$

is used to described the deformation of the body $\mathcal{B}$. Using infinitesimal volume elements $\mathrm{d}V$ and $\mathrm{d}v$ in the reference and current configurations, respectively, the volume change of a body may be described by $J = \mathrm{d}v/\mathrm{d}V$. The volume change can also be retrieved using the determinant of the deformation gradient, i.e. $J = \det\mathbf{F}(\mathbf{X},t) > 0$, where J is the Jacobian determinant.

The deformation gradient is also used to transform a vector (e.g., a fiber) $\mathbf{a}_0$ with length $|\mathbf{a}_0| = 1$ in the reference configuration to its deformed counterpart $\mathbf{a}$ in the current configuration by $\mathbf{a} = \mathbf{F}\mathbf{a}_0$. The length of the deformed fiber is now $|\mathbf{a}| = \lambda$ which is called the stretch ratio or just the stretch. Through the deformation, the deformation gradient has rotated and stretched the undeformed vector to its deformed counterpart which is the motivation behind the polar decomposition of $\mathbf{F}$ into

$$\mathbf{F} = \mathbf{R}\mathbf{U} = \mathbf{v}\mathbf{R}, \tag{1.2}$$

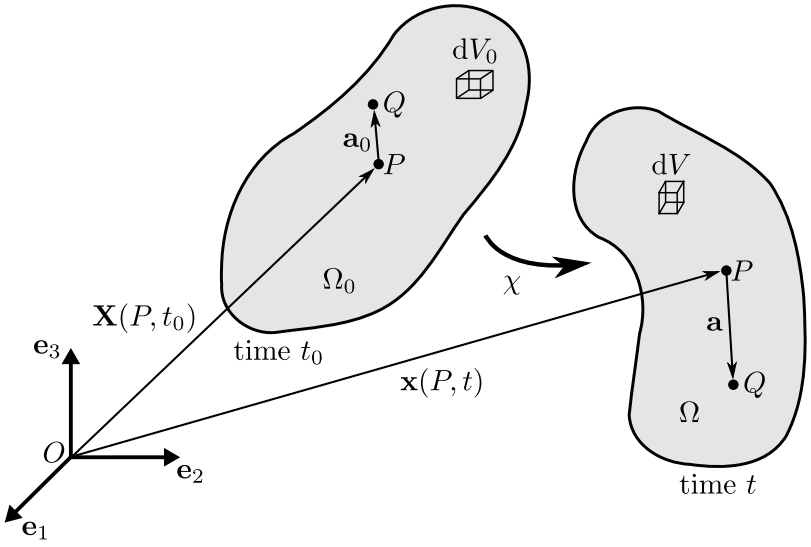

Figure 1.1.: Deformation of a continuum body $\mathcal{B}$ from the reference configuration Ω_0 to the deformed configuration Ω.

where $\mathbf{R}$ is a rotation tensor and $\mathbf{U}$ and $\mathbf{v}$ are the right and left stretch tensors, respectively. Thus, $\mathbf{F}$ is decomposed into a pure stretch and a pure rotation in which a line element at $\mathbf{X}$ may first be stretched by $\mathbf{U}$ and then rotated to $\mathbf{x}$ by $\mathbf{R}$, or first rotated to $\mathbf{x}$ by $\mathbf{R}$ followed by the stretch $\mathbf{v}$. The unique and proper orthogonal $\mathbf{R}$ has the properties $\mathbf{R}^{\mathrm{T}}\mathbf{R} = \mathbf{I}$ and $\det\mathbf{R} = 1$, where $\mathbf{I}$ is the second-order identity tensor. The unique and positive definite stretch tensors are symmetric, i.e. $\mathbf{U} = \mathbf{U}^{\mathrm{T}}$ and $\mathbf{v} = \mathbf{v}^{\mathrm{T}}$, and the square of these tensors are

$$\mathbf{C} = \mathbf{F}^{\mathrm{T}}\mathbf{F} = \mathbf{U}^2 \qquad \text{and} \qquad \mathbf{b} = \mathbf{F}\mathbf{F}^{\mathrm{T}} = \mathbf{v}^2, \tag{1.3}$$

which are called the right and left Cauchy-Green stretch tensors, respectively. Using these stretch tensors, the well known Green-Lagrange strain-tensor is now given by

$$\mathbf{E} = \frac{1}{2}(\mathbf{C} - \mathbf{I}), \tag{1.4}$$

which describes the strain in Ω_0 while the Euler-Almansi strain-tensor is given by

$$\mathbf{e} = \frac{1}{2}(\mathbf{I} - \mathbf{b}^{-1}), \tag{1.5}$$

which describes the strain in Ω. The push-forward and pull-back operations are defined, respectively, for covariant tensors as

$$\chi_*(\bullet)^\flat = \mathbf{F}^{-\mathrm{T}}(\bullet)^\flat\mathbf{F}^{-1} \qquad \text{and} \qquad \chi_*^{-1}(\bullet)^\flat = \mathbf{F}^{\mathrm{T}}(\bullet)^\flat\mathbf{F}, \tag{1.6}$$

and for contravariant tensors as

$$\chi_*(\bullet)^\sharp = \mathbf{F}(\bullet)^\sharp\mathbf{F}^{\mathrm{T}} \qquad \text{and} \qquad \chi_*^{-1}(\bullet)^\sharp = \mathbf{F}^{-1}(\bullet)^\sharp\mathbf{F}^{-\mathrm{T}}. \tag{1.7}$$

Examples of covariant tensors are $\mathbf{E}^\flat$, $\mathbf{C}^\flat$, $\mathbf{e}^\flat$ and $(\mathbf{b}^{-1})^\flat$ while examples of contravariant tensors are $(\mathbf{C}^{-1})^\sharp$, $\mathbf{b}^\sharp$ and many of the common stress tensors.

1.2.2. Stress measures

Considering an infinitesimal surface ds with a unit vector $\mathbf{n}$ normal to the surface on a part of the deformed body Ω and an infinitesimal force d$\mathbf{f}$, the Cauchy traction vector $\mathbf{t}$ is obtained through the relation $\mathrm{d}\mathbf{f} = \mathbf{t}\mathrm{d}s$. Cauchy's stress principle states further that

$$\mathbf{t} = \boldsymbol{\sigma}\mathbf{n}, \tag{1.8}$$

where $\boldsymbol{\sigma}$ is the second-order Cauchy stress tensor which is symmetric, i.e. $\boldsymbol{\sigma} = \boldsymbol{\sigma}^{\mathrm{T}}$. That $\boldsymbol{\sigma}$ is symmetric will be shown in Section 1.2.3. The often used engineering (first Piola-Kirchhoff) stress tensor, $\mathbf{P}$, may be retrieved using the Nanson's formula

$$\mathbf{P} = J\boldsymbol{\sigma}\mathbf{F}^{-\mathrm{T}} \tag{1.9}$$

and is, in general, not symmetric but instead fulfills the relation $\mathbf{P}\mathbf{F}^{\mathrm{T}} = \mathbf{F}^{\mathrm{T}}\mathbf{P}$. Other convenient stress measures that are often used are the symmetric Kirchhoff stress tensor

$$\boldsymbol{\tau} = J\boldsymbol{\sigma} \tag{1.10}$$

or the symmetric second Piola-Kirchhoff stress tensor obtained using the Piola transformation

$$\mathbf{S} = \mathbf{F}^{-1}\mathbf{P} = J\mathbf{F}^{-1}\boldsymbol{\sigma}\mathbf{F}^{-\mathrm{T}}. \tag{1.11}$$

The stress tensors $\mathbf{S}$ and $\boldsymbol{\tau}$ are both related using the pull-back and push-forward operators

$$\mathbf{S} = \chi_*^{-1}(\boldsymbol{\tau}^\sharp) = \mathbf{F}^{-1}\boldsymbol{\tau}\mathbf{F}^{-\mathrm{T}} \qquad \text{and} \qquad \boldsymbol{\tau} = \chi_*(\mathbf{S}^\sharp) = \mathbf{F}\mathbf{S}\mathbf{F}^{\mathrm{T}}, \tag{1.12}$$

respectively.

1.2.3. Balance laws

Based on experience, basic axioms are formulated called the balance laws. These laws relate the state variables of the continuum to influences of actions outside the continuum.

Reynolds' transport theorem. To formulate the balance laws, we first need to state the Reynolds' transport theorem. Let Ω be a closed spatial boundary region with a smooth boundary $\partial\Omega$. Also, assume we have a spatial scalar field $\phi = \phi(\mathbf{x},t)$ that is continuously differentiable in both $\mathbf{x}$ and t. Taking the time derivative of a volume integral of ϕ, i.e.

$$\frac{\mathrm{D}}{\mathrm{D}t}\int_{\Omega}\phi(\mathbf{x},t)\mathrm{d}v, \tag{1.13}$$

where V is the volume of Ω, is not straightforward as the region Ω depends on time. The quantities are, therefore, transformed to the referential configuration Ω_0 with volume V_0,

which is time independent, i.e. $\mathbf{x} = \chi(\mathbf{X},t)$ and $\mathrm{d}v = J(\mathbf{X},t)\,\mathrm{d}V$. Now, using the chain-rule, (1.13) can be reformulated as

$$\begin{aligned}\frac{\mathrm{D}}{\mathrm{D}t}\int_{\Omega}\phi(\mathbf{x},t)\mathrm{d}v &= \frac{\mathrm{D}}{\mathrm{D}t}\int_{\Omega_0}\phi(\chi(\mathbf{X},t),t)\,J(\mathbf{X},t)\,\mathrm{d}V\\ &= \int_{\Omega_0}\left[\frac{\partial\phi(\chi(\mathbf{X},t),t)}{\partial t}J(\mathbf{X},t)+\phi(\chi(\mathbf{X},t),t)\frac{\partial J(\mathbf{X},t)}{\partial t}\right]\mathrm{d}V\\ &= \int_{\Omega_0}\left[\dot{\phi}(\chi(\mathbf{X},t),t)\,J(\mathbf{X},t)+\phi(\chi(\mathbf{X},t),t)\,J(\mathbf{X},t)\,\mathrm{div}\,\mathbf{v}\right]\mathrm{d}V\\ &= \int_{\Omega}\left[\dot{\phi}(\mathbf{x},t)+\phi(\mathbf{x},t)\mathrm{div}\,\mathbf{v}\right]\mathrm{d}v, \end{aligned}\tag{1.14}$$

where $\partial J/\partial t = J\mathrm{div}\,\mathbf{v}$ is used and $\mathbf{v}(\mathbf{x},t)$ is a vector function in Ω. Equation (1.14) is called the Reynolds' transport theorem, which we here rewrite in another useful form. Utilizing that the material time derivative of $\phi(\mathbf{x},t)$ is

$$\dot{\phi}(\mathbf{x},t) = \frac{\partial\phi(\mathbf{x},t)}{\partial t}+\mathrm{grad}\phi\cdot\mathbf{v},\tag{1.15}$$

we can further reformulate $(1.14)_4$ as

$$\begin{aligned}\frac{\mathrm{D}}{\mathrm{D}t}\int_{\Omega}\phi(\mathbf{x},t)\mathrm{d}v &= \int_{\Omega}\left(\frac{\partial\phi(\mathbf{x},t)}{\partial t}+\mathrm{grad}\phi\cdot\mathbf{v}+\phi(\mathbf{x},t)\mathrm{div}\,\mathbf{v}\right)\mathrm{d}v\\ &= \int_{\Omega}\left\{\frac{\partial\phi(\mathbf{x},t)}{\partial t}+\mathrm{div}\left[\phi(\mathbf{x},t)\,\mathbf{v}\right]\right\}\mathrm{d}v,\end{aligned}\tag{1.16}$$

and using the divergence theorem on $(1.16)_2$, yields the well known Reynolds' transport theorem as

$$\frac{\mathrm{D}}{\mathrm{D}t}\int_{\Omega}\phi(\mathbf{x},t)\mathrm{d}v = \int_{\Omega}\frac{\partial\phi(\mathbf{x},t)}{\partial t}\mathrm{d}v+\int_{\partial\Omega}\phi(\mathbf{x},t)\,\mathbf{v}\cdot\mathbf{n}\,\mathrm{d}s,\tag{1.17}$$

where the first term on the right hand side of (1.17) denotes the rate of change of $\phi(\mathbf{x},t)$ within the region Ω, while the second term denotes the rate of the outward normal flux of $\phi(\mathbf{x},t)\,\mathbf{v}$ out of Ω across the surface $\partial\Omega$ and $\mathrm{d}s$ is an area element.

Conservation of mass. The mass m in a closed system can neither be created nor destroyed and is thus an invariant during motion for all times. This may be shown as

$$\dot{m} = \frac{\mathrm{D}m}{\mathrm{D}t} = \frac{\mathrm{D}}{\mathrm{D}t}\int_{\Omega}\rho_{\mathrm{m}}(\mathbf{x},t)\,\mathrm{d}v = 0,\tag{1.18}$$

where $\rho_{\mathrm{m}}(\mathbf{x},t)$ is the spatial mass density. Using the Reynolds' transport theorem (1.14), $\dot{m}$ can be rewritten as

$$\dot{m} = \int_{\Omega} [\dot{\rho}_m(\mathbf{x},t) + \rho_{\mathrm{m}}(\mathbf{x},t)\mathrm{div}\,\mathbf{v}]\,\mathrm{d}v, \tag{1.19}$$

and using the localization theorem it follows that

$$\dot{\rho}_m(\mathbf{x},t) + \rho_{\mathrm{m}}(\mathbf{x},t)\mathrm{div}\,\mathbf{v} = 0 \qquad \text{or} \qquad \frac{\partial \rho_{\mathrm{m}}(\mathbf{x},t)}{\partial t} + \mathrm{div}[\rho_{\mathrm{m}}(\mathbf{x},t)\,\mathbf{v}]. \tag{1.20}$$

The continuity of mass equation relates the mass density $\rho_{\mathrm{m0}}(\mathbf{X})$ in the reference configuration to the mass density $\rho_{\mathrm{m}}(\mathbf{x},t) = \rho_{\mathrm{m}}(\chi(\mathbf{X},t),t)$ in the current configuration as

$$\rho_{\mathrm{m0}}(\mathbf{X}) = \rho_{\mathrm{m}}(\chi(\mathbf{X},t),t)J(\mathbf{X},t). \tag{1.21}$$

Balance of linear and angular momentum. The balance of linear and angular momentum states that the change in linear momentum for a region Ω equals the external forces acting on that region and that the change in angular momentum equals the external moments acting on that region. In addition, the balance between external forces and moments and the rate of change in linear and angular momentums are valid for all parts of the continuum body. Let $\mathbf{b}_{\mathrm{F}} = \mathbf{b}_{\mathrm{F}}(\mathbf{x},t)$ be body forces, $\mathbf{t} = \mathbf{t}(\mathbf{x},t,\mathbf{n})$ be contact forces acting on a unit area with the surface normal $\mathbf{n}$ and $\mathbf{v} = \mathbf{v}(\mathbf{x},t)$ be a velocity field. In the following, the arguments of the tensors are dropped for notational simplicity. The balance of linear momentum takes the form

$$\frac{\mathrm{D}}{\mathrm{D}t}\int_{\Omega} \rho_{\mathrm{m}}\mathbf{v}\,\mathrm{d}v = \int_{\Omega} \rho_{\mathrm{m}}\mathbf{b}_{\mathrm{F}}\,\mathrm{d}v + \int_{\partial\Omega} \mathbf{t}\,\mathrm{d}s, \tag{1.22}$$

and the balance of angular momentum takes the form

$$\frac{\mathrm{D}}{\mathrm{D}t}\int_{\Omega} \mathbf{r}\times\mathbf{v}\,\mathrm{d}v = \int_{\Omega} \mathbf{r}\times\rho_{\mathrm{m}}\mathbf{b}_{\mathrm{F}}\,\mathrm{d}v + \int_{\partial\Omega} \mathbf{r}\times\mathbf{t}\,\mathrm{d}s, \tag{1.23}$$

where $\mathbf{r}$ is the position vector associated with the infinitesimal volume element. Through the relations (1.22) and (1.23), and in comparison with Eq. (1.17), it is seen that if $\mathbf{b}_{\mathrm{F}} = \mathbf{0}$ in the region Ω and $\mathbf{t} = \mathbf{0}$ on the surface $\partial\Omega$, the linear and angular momentum are conservative quantities in Ω. If instead $\mathbf{v} = \mathbf{0}$, the sum of internal and external forces and moments vanish, which is the condition in the classical statics equilibrium equations.

Cauchy's equations of motion. By using Cauchy's stress principle $\mathbf{t} = \boldsymbol{\sigma}\mathbf{n}$, see Eq. (1.8), and the divergence theorem, it is straightforward to show for the second term on the right hand side of (1.22) that

$$\int_{\partial\Omega} \mathbf{t}\,\mathrm{d}s = \int_{\partial\Omega} \boldsymbol{\sigma}\mathbf{n}\,\mathrm{d}s = \int_{\Omega} \mathrm{div}\boldsymbol{\sigma}\,\mathrm{d}v. \tag{1.24}$$

Substituting this into (1.22) and using the relation

$$\frac{\mathrm{D}}{\mathrm{D}t}\int_{\Omega}\rho_{\mathrm{m}}\mathbf{v}\,\mathrm{d}v=\int_{\Omega}\rho_{\mathrm{m}}\dot{\mathbf{v}}\,\mathrm{d}v \tag{1.25}$$

yields Cauchy's first equation of motion as

$$\int_{\Omega}(\mathrm{div}\boldsymbol{\sigma}+\mathbf{b}_{\mathrm{F}}-\rho_{\mathrm{m}}\dot{\mathbf{v}})\,\mathrm{d}v=\mathbf{0}. \tag{1.26}$$

As (1.26) holds (point-wise) for any volume V, it may also be rewritten in its local form as

$$\mathrm{div}\boldsymbol{\sigma}+\mathbf{b}_{\mathrm{F}}=\rho_{\mathrm{m}}\dot{\mathbf{v}}. \tag{1.27}$$

If there is no acceleration of the body, i.e. $\dot{\mathbf{v}}=\mathbf{0}$, Eq. (1.27) becomes

$$\mathrm{div}\boldsymbol{\sigma}+\mathbf{b}_{\mathrm{F}}=\mathbf{0}, \tag{1.28}$$

which is the classical Cauchy's equation of static equilibrium. Using the Cauchy stress principle on the second term on right hand side of Eq. (1.23) and using the divergence theorem yields

$$\int_{\partial\Omega}\mathbf{r}\times\mathbf{t}\,\mathrm{d}s=\int_{\partial\Omega}\mathbf{r}\times\boldsymbol{\sigma}\mathbf{n}\,\mathrm{d}s=\int_{\Omega}(\mathbf{r}\times\mathrm{div}\boldsymbol{\sigma}+\boldsymbol{\mathcal{E}}:\boldsymbol{\sigma}^{\mathrm{T}})\,\mathrm{d}v, \tag{1.29}$$

were $\boldsymbol{\mathcal{E}}$ is the third order permutation tensor. Using (1.29) together with (1.25), the equation for angular momentum (1.23) can be rewritten as

$$\int_{\Omega}\mathbf{r}\times(\rho_{\mathrm{m}}\dot{\mathbf{v}}-\mathrm{div}\boldsymbol{\sigma}-\mathbf{b}_{\mathrm{F}})\,\mathrm{d}v=\int_{\Omega}\boldsymbol{\mathcal{E}}:\boldsymbol{\sigma}^{\mathrm{T}}\,\mathrm{d}v, \tag{1.30}$$

which using (1.27) and the fact that (1.30) holds (point-wise) for any volume V, becomes

$$\boldsymbol{\mathcal{E}}:\boldsymbol{\sigma}^{\mathrm{T}}=\mathbf{0}. \tag{1.31}$$

Through Eq. (1.31) it is easy to show that the relations $\sigma_{12}-\sigma_{21}=0$, $\sigma_{13}-\sigma_{31}=0$ and $\sigma_{23}-\sigma_{32}=0$ must hold, which is satisfied if and only if

$$\boldsymbol{\sigma}=\boldsymbol{\sigma}^{\mathrm{T}}, \tag{1.32}$$

i.e. the Cauchy stress tensor is symmetric. The symmetry of the Cauchy stress tensor is thus retrieved using the angular momentum and is referred to as Cauchy's second equation of motion.

1.2.4. Constitutive equations

The relation between the deformation of a material, say represented by $\mathbf{F}$, and the stress in the material, say represented by $\boldsymbol{\sigma}$ or $\mathbf{P}$, is given by the constitutive relations. If we further consider hyperelastic materials, there must exist a Helmholtz free-energy (strain-energy) scalar-valued function $\Psi(\mathbf{F})$. A stress constitutive equation for a hyperelastic material can then be postulated as

$$\mathbf{P} = \frac{\partial \Psi(\mathbf{F})}{\partial \mathbf{F}}, \tag{1.33}$$

or

$$\boldsymbol{\sigma} = J^{-1} \frac{\partial \Psi(\mathbf{F})}{\partial \mathbf{F}} \mathbf{F}^{\mathrm{T}}. \tag{1.34}$$

There are many restriction on the constitutive equations. For example, it must be and invariant under rigid body motion (material objectivity), it must fulfill the balance laws (consistency) and it must be possible to write a function with a unique solution given initial values and boundary conditions (determinism). For a strain-energy function there is also the restriction that no energy is stored in the material if there is no deformation, i.e.

$$\Psi(\mathbf{F} = \mathbf{I}) = 0. \tag{1.35}$$

Also, the strain energy must be positive (or zero) for all deformations, i.e.

$$\Psi(\mathbf{F}) \geq 0. \tag{1.36}$$

In addition, the volume of a body can not be infinitely expanded or reduced to zero volume, i.e. the strain energy must go towards $+\infty$ according to

$$\Psi(\mathbf{F}) \to +\infty \qquad \text{as} \qquad \det\mathbf{F} \to +\infty, \tag{1.37}$$

$$\Psi(\mathbf{F}) \to +\infty \qquad \text{as} \qquad \det\mathbf{F} \to +0. \tag{1.38}$$

Changing the frame of reference from $\varphi(O, \mathbf{e}_i)$ to $\hat{\varphi}(\hat{O}, \hat{\mathbf{e}}_i)$ by using $\hat{\mathbf{x}} = \mathbf{c}(t) + \mathbf{Q}(t)\mathbf{x}$, where $\mathbf{c}(t)$ is a vector from O to $\hat{O}$ and $\mathbf{Q}(t)$ is the rigid body rotation between φ and $\hat{\varphi}$, it can be shown by using Eq. (1.1) that $\hat{\mathbf{F}} = \mathbf{Q}\mathbf{F}$ and that $\hat{\mathbf{C}} = \mathbf{C}$. As the strain-energy of a body $\mathcal{B}$ is indifferent to the observer, the principle of material frame indifference (material objectivity) implies that

$$\Psi(\hat{\mathbf{F}}) = \Psi(\mathbf{Q}\mathbf{F}) = \Psi(\mathbf{F}), \tag{1.39}$$

which must hold for all proper ortogonal rotations $\mathbf{Q}$. Using $\mathbf{Q} = \mathbf{R}^{\mathrm{T}}$ and Eq. (1.2) it is also follows that the strain-energy function may fulfill the relation

$$\Psi(\mathbf{F}) = \Psi(\mathbf{U}) = \tilde{\Psi}(\mathbf{C}). \tag{1.40}$$

Recalling Eq. (1.4), the material stress constitutive relations may be written in terms of $\mathbf{C}$ or $\mathbf{E}$ as

$$\mathbf{P} = 2\mathbf{F}\frac{\partial \Psi(\mathbf{C})}{\partial \mathbf{C}} \qquad \text{and} \qquad \mathbf{P} = \mathbf{F}\frac{\partial \Psi(\mathbf{E})}{\partial \mathbf{E}}, \tag{1.41}$$

$$\mathbf{S} = 2\frac{\partial \Psi(\mathbf{C})}{\partial \mathbf{C}} \qquad \text{and} \qquad \mathbf{S} = \frac{\partial \Psi(\mathbf{E})}{\partial \mathbf{E}}, \tag{1.42}$$

or

$$\boldsymbol{\sigma} = 2J^{-1}\mathbf{F}\frac{\partial \Psi(\mathbf{C})}{\partial \mathbf{C}}\mathbf{F}^{\mathrm{T}} \qquad \text{and} \qquad \boldsymbol{\sigma} = J^{-1}\mathbf{F}\frac{\partial \Psi(\mathbf{E})}{\partial \mathbf{E}}\mathbf{F}^{\mathrm{T}}. \tag{1.43}$$

1.2.5. Incompressibility and near incompressibility

Many soft biological tissues exhibit an incompressible, or nearly incompressible, behavior. As shown in [6], the strain-energy function for an incompressible material may be obtained by introducing the hydrostatic pressure p_{h} as

$$\Psi = \Psi(\mathbf{F}) - p_{\mathrm{h}}(J-1), \tag{1.44}$$

where p_{h} is determined from the boundary conditions. The Cauchy stress and the second Piola-Kirchhoff stress tensors for an incompressible material are thus, e.g., using $\Psi(\mathbf{C})$,

$$\boldsymbol{\sigma} = 2\mathbf{F}\frac{\partial \Psi(\mathbf{C})}{\partial \mathbf{C}}\mathbf{F}^{\mathrm{T}} - p_{\mathrm{h}}\mathbf{I} \qquad \text{and} \qquad \mathbf{S} = 2\frac{\partial \Psi(\mathbf{C})}{\partial \mathbf{C}} - p_{\mathrm{h}}\mathbf{C}^{-1}, \tag{1.45}$$

respectively. Although the formulations in (1.45) are convenient to use in an analytical setting, in a computational setting it is often more advantageous to use a compressible formulation, where the (near) incompressibility of biological tissues is achieved through a penalization of the volumetric terms. To separate the strain-energy function into a volumetric (volume changing) and an isochoric (volume preserving) term, a multiplicative decomposition of the deformation gradient is performed according to

$$\mathbf{F} = (J^{1/3}\mathbf{I})\overline{\mathbf{F}}, \tag{1.46}$$

where $J^{1/3}\mathbf{I}$ is associated with the volumetric deformation and $\overline{\mathbf{F}}$ is associated with the isochoric deformation. The isochoric right and left Cauchy-Green tensors may also be retrieved using $\overline{\mathbf{F}}$ by

$$\overline{\mathbf{C}} = \overline{\mathbf{F}}^{\mathrm{T}}\overline{\mathbf{F}} = J^{-2/3}\mathbf{C} \qquad \text{and} \qquad \overline{\mathbf{b}} = \overline{\mathbf{F}}\overline{\mathbf{F}}^{\mathrm{T}} = J^{-2/3}\mathbf{b}, \tag{1.47}$$

respectively. Often the strain energy function may be decoupled, as $\Psi(\mathbf{C}) = \Psi_{\mathrm{vol}}(J) + \Psi_{\mathrm{iso}}(\overline{\mathbf{C}})$, where the subscripts vol and iso stands for the volumetric and isochoric parts, respectively.

This enables an additive split of the second Piola-Kirchhoff stress tensor into a purely volumetric and a purely isochoric contribution according to

$$\mathbf{S} = \mathbf{S}_{\mathrm{vol}} + \mathbf{S}_{\mathrm{iso}}, \tag{1.48}$$

where

$$\mathbf{S}_{\mathrm{vol}} = 2\frac{\partial \Psi_{\mathrm{vol}}(J)}{\partial \mathbf{C}} = Jp_{\mathrm{h}}\mathbf{C}^{-1} \qquad \text{and} \qquad \mathbf{S}_{\mathrm{iso}} = 2\frac{\partial \Psi_{\mathrm{iso}}(\overline{\mathbf{C}})}{\partial \mathbf{C}} = J^{-2/3}\mathrm{Dev}\overline{\mathbf{S}}, \tag{1.49}$$

and where the hydrostatic pressure p_{h} and the fictitious second Piola-Kirchhoff stress tensor $\overline{\mathbf{S}}$ are defined by

$$p_{\mathrm{h}} = \frac{\mathrm{d}\Psi_{\mathrm{vol}}(J)}{\mathrm{d}J} \qquad \text{and} \qquad \overline{\mathbf{S}} = 2\frac{\partial \Psi_{\mathrm{iso}}(\overline{\mathbf{C}})}{\partial \overline{\mathbf{C}}}, \tag{1.50}$$

and where the Lagrangian deviatoric operator is defined by the relation $\mathrm{Dev}(\bullet) = (\bullet) - (1/3)[(\bullet) : \mathbf{C}]\mathbf{C}^{-1}$ so that $\mathrm{Dev}\overline{\mathbf{S}} : \mathbf{C} = 0$ is fulfilled, (the symbol : denotes the double contraction operation).

In terms of the Cauchy stress tensor, the same procedure is only possible for isotropic materials, where the decoupled strain-energy function may be formulated as $\Psi(\mathbf{b}) = \Psi_{\mathrm{vol}}(J) + \Psi_{\mathrm{iso}}(\overline{\mathbf{b}})$ and where an additive split of the Cauchy stress tensor leads to $\boldsymbol{\sigma} = \boldsymbol{\sigma}_{\mathrm{vol}} + \boldsymbol{\sigma}_{\mathrm{iso}}$. However, since none of the materials covered in this theses are isotropic, those terms will not be explicitly given here.

The Cauchy stress tensor for an anisotropic nearly incompressible material is instead given by a push-forward transformation, using (1.7), of the second Piola-Kirchhoff stress tensor, $\mathbf{S} = \mathbf{S}_{\mathrm{vol}} + \mathbf{S}_{\mathrm{iso}}$, according to

$$\boldsymbol{\sigma} = J^{-1}\chi_*(\mathbf{S}^\sharp) = 2J^{-1}\mathbf{F}\left(\frac{\partial \Psi_{\mathrm{vol}}(J)}{\partial \mathbf{C}} + \frac{\partial \Psi_{\mathrm{iso}}(\overline{\mathbf{C}})}{\partial \mathbf{C}}\right)\mathbf{F}^{\mathrm{T}} \tag{1.51}$$

which yields the components

$$\boldsymbol{\sigma}_{\mathrm{vol}} = p\mathbf{I} \qquad \text{and} \qquad \boldsymbol{\sigma}_{\mathrm{iso}} = J^{-1}\overline{\mathbf{F}}(\mathbb{P} : \overline{\mathbf{S}})\overline{\mathbf{F}^{\mathrm{T}}}, \tag{1.52}$$

where the projection tensor $\mathbb{P} = \mathbb{I} - 1/3\mathbf{C}^{-1} \otimes \mathbf{C}$ is used and $\mathbb{I}$ is the fourth-order identity tensor, (the symbol $\otimes$ denotes the dyadic (tensor) product operation).

The elasticity tensor, needed in computational solutions of nonlinear boundary-value problems, is in terms of $\mathbf{E}$, $\mathbf{C}$ or $\Psi(\mathbf{C})$ retrieved as

$$\mathbb{C} = \frac{\partial \mathbf{S}(\mathbf{E})}{\partial \mathbf{E}} = 2\frac{\partial \mathbf{S}(\mathbf{C})}{\partial \mathbf{C}} = 4\frac{\partial^2 \Psi(\mathbf{C})}{\partial \mathbf{C}\partial \mathbf{C}}. \tag{1.53}$$

In a decoupled form, $\mathbb{C} = \mathbb{C}_{\mathrm{vol}} + \mathbb{C}_{\mathrm{iso}}$ may be obtained, e.g., using $(1.53)_2$, by

$$\mathbb{C}_{\mathrm{vol}} = 2\frac{\partial \mathbf{S}_{\mathrm{vol}}}{\partial \mathbf{C}} \qquad \text{and} \qquad \mathbb{C}_{\mathrm{iso}} = 2\frac{\partial \mathbf{S}_{\mathrm{iso}}}{\partial \mathbf{C}}. \tag{1.54}$$

The elasticity tensor in the deformed configuration, labeled $\mathbb{c}$, may be obtained using the Piola transformation of $\mathbb{C}$ on each large index according to

$$\mathbb{c} = J^{-1}\chi_*(\mathbb{C}), \qquad \text{or in index notation} \qquad c_{abcd} = J^{-1}F_{aA}F_{bB}F_{cC}F_{dD}C_{ABCD}. \tag{1.55}$$

1.2.6. Invariant formulation

For an isotropic hyperelastic material the strain-energy function may be written in terms of the principal invariants as

$$\Psi(\mathbf{C}) = \Psi(I_1, I_2, I_3), \tag{1.56}$$

where these invariants are given by

$$I_1(\mathbf{C}) = \mathrm{tr}\mathbf{C} = \lambda_1^2 + \lambda_2^2 + \lambda_3^2, \tag{1.57}$$

$$I_2(\mathbf{C}) = \frac{1}{2}[(\mathrm{tr}\mathbf{C})^2 - \mathrm{tr}\mathbf{C}^2] = \lambda_1^2\lambda_2^2 + \lambda_1^2\lambda_3^2 + \lambda_2^2\lambda_3^2, \tag{1.58}$$

$$I_3(\mathbf{C}) = \det\mathbf{C} = \lambda_1^2\lambda_2^2\lambda_3^2. \tag{1.59}$$

For an anisotropic material with a directionally dependent orientation, say in a fiber family direction $\mathbf{a}_0$, a pseudo-invariant I_4 may be formulated as

$$I_4 = \mathbf{F}\mathbf{a}_0 \cdot \mathbf{F}\mathbf{a}_0 = \mathbf{a}_0 \cdot \mathbf{C}\mathbf{a}_0 = \mathbf{C} : \mathbf{A}_0 = \lambda_\mathrm{a}^2, \tag{1.60}$$

where $\mathbf{A}_0 = \mathbf{a}_0 \otimes \mathbf{a}_0$ is a structure tensor and λ_a is the stretch in the fiber direction. The invariant I_4 is thus equal to the square of the stretch in the direction of the fiber family. An additional invariant for the fiber family $\mathbf{a}_0$ is given by

$$I_5 = \mathbf{a}_0 \cdot \mathbf{C}^2\mathbf{a}_0 = \mathbf{C}^2 : \mathbf{A}_0, \tag{1.61}$$

although this invariant has no physical interpretation. If an additional fiber family is present, say in the direction $\mathbf{g}_0$, the equivalent invariants to (1.60) and (1.61) are given by

$$I_6 = \mathbf{C} : \mathbf{G}_0 = \lambda_\mathrm{g}^2 \qquad \text{and} \qquad I_7 = \mathbf{C}^2 : \mathbf{G}_0, \tag{1.62}$$

where λ_g is the stretch in the direction of the second fiber family and $\mathbf{G}_0 = \mathbf{g}_0 \otimes \mathbf{g}_0$. Further, a coupling invariant between these two fiber families may be defined as

$$I_8 = \mathbf{a}_0 \cdot \mathbf{C}\mathbf{g}_0. \tag{1.63}$$

A hyperelastic anisotropic material with two fiber families may thus be represented by the strain-energy function $\Psi = \Psi(\mathbf{C}, \mathbf{A}_0, \mathbf{G}_0) = \Psi(I_1, \ldots, I_8)$ and the stress response may thus be retrieved as

$$\mathbf{S} = 2\frac{\partial\Psi(I_1, \ldots, I_8)}{\partial\mathbf{C}} = 2\sum_{a=1}^{8} \frac{\partial\Psi(I_1, \ldots, I_8)}{\partial I_a}\frac{\partial I_a}{\partial\mathbf{C}}, \tag{1.64}$$

using the chain-rule. For some deformation modes, all eight invariants are not independent why the number of invariants used may be reduced. Also, through $(1.47)_1$, the isochoric counterpart of the invariants are simply retrieved as, e.g., $\bar{I}_4 = \overline{\mathbf{C}} : \mathbf{A}_0 = J^{-2/3}I_4$.

1.2.7. Strong and weak form of a boundary-value problem

The mechanical response of biological tissues is usually computed using the wak, finite element, formulation of the boundary value problem. In this section the used strong and corresponding weak formulations are presented. Thes are valid for passive cardiac as well as arterial mechanical simulations.

In left ventricular mechanical problems, the following static mechanical equilibrium mixed boundary-value problem, in the material (reference) configuration, is often posed,

$$\begin{aligned}
&\mathrm{Div}(\mathbf{FS}) = \mathbf{0} && \text{in} && \Omega_0 && (1.65a)\\
&\mathbf{FSN} = -pJ(\mathbf{F}^{-1})^{\mathrm{T}}\mathbf{N} && \text{on} && \partial\Omega_{0\mathbf{t}1} && (1.65b)\\
&\mathbf{FSN} = \mathbf{0} && \text{on} && \partial\Omega_{0\mathbf{t}2} && (1.65c)\\
&\mathbf{u}(\mathbf{X}) = \mathbf{0} && \text{on} && \partial\Omega_{0\mathbf{u}1} && (1.65d)
\end{aligned}$$

where $\mathrm{Div}(\bullet)$ denotes the divergence operator with respect to the reference configuration and $\mathbf{N}$ is the surface normal of the body Ω_0. Equation (1.65b) is the natural boundary condition where a pressure p is applied (the surface $\partial\Omega_{0\mathbf{t}1}$ is usually defined as the endocardial surface of the LV). Equation (1.65c) is the natural boundary condition which is traction free (the surface $\partial\Omega_{0\mathbf{t}2}$ is usually defined as the epicardial surface of the LV) and (1.65d) is the essential condition of a zero displacement surface (the surface $\partial\Omega_{0\mathbf{u}1}$ is often defined as the basal plane of an LV represented by a truncated ellipsoidal model). Also other more complex boundary conditions may be used where, e.g., the entire surface $\partial\Omega_{0\mathbf{u}1}$ is not displacement free or where displacements are prescribed in certain directions.

The pressure loading (1.65b) is a follower load, i.e. it is deformation dependent, and is, in general, not conservative and can then not be derived from a potential [7]. The principal of minimum potential energy is therefore not applicable as the basis for the finite element solution method. Instead, the weak formulation is derived directly from the strong formulation, i.e. the equations in (1.65), in the following manner; let $\boldsymbol{\phi} = \boldsymbol{\phi}(\mathbf{X})$ be a suitable vector-valued test function that satisfy homogeneous prescribed displacement boundary conditions, i.e. $\boldsymbol{\phi} = \mathbf{0}$, on $\partial\Omega_{0\mathbf{u}1}$. By forming the inner product of Eq. (1.65a) with $\boldsymbol{\phi}$ and integrating over the domain Ω_0, the weak equilibrium equations are obtained. By using the identity

$$\boldsymbol{\phi}\cdot\mathrm{Div}(\mathbf{FS}) = \mathrm{Div}\left[(\mathbf{FS})^{\mathrm{T}}\boldsymbol{\phi}\right] - \mathrm{Tr}\left[(\mathbf{FS})^{\mathrm{T}}\mathrm{Grad}\boldsymbol{\phi}\right], \tag{1.66}$$

we get

$$\int_{\Omega_0}\mathrm{Div}(\mathbf{FS})\cdot\boldsymbol{\phi}\,\mathrm{d}v = \int_{\Omega_0}\mathrm{Div}\left[(\mathbf{FS})^{\mathrm{T}}\boldsymbol{\phi}\right]\mathrm{d}v - \int_{\Omega_0}\mathrm{Tr}\left[(\mathbf{FS})^{\mathrm{T}}\mathrm{Grad}\boldsymbol{\phi}\right] = 0. \tag{1.67}$$

Further, by using Gauss' divergence theorem

$$\int_{\Omega_0}\mathrm{Div}\left[(\mathbf{FS})^{\mathrm{T}}\boldsymbol{\phi})\right]\mathrm{d}v = \int_{\partial\Omega_0}\left[(\mathbf{FS})^{\mathrm{T}}\boldsymbol{\phi}\right]\cdot\mathbf{N}\,\mathrm{d}A, \tag{1.68}$$

we get

$$\int_{\Omega_0} \mathrm{Tr}(\mathbf{S}\mathbf{F}^{\mathrm{T}}\mathrm{Grad}\boldsymbol{\phi})\,\mathrm{d}v - \int_{\partial\Omega_0} \mathbf{F}\mathbf{S}\mathbf{N}\cdot\boldsymbol{\phi}\,\mathrm{d}A = 0, \tag{1.69}$$

where the relations $\mathbf{S} = \mathbf{S}^{\mathrm{T}}$ and $[(\mathbf{F}\mathbf{S})^{\mathrm{T}}\boldsymbol{\phi}]\cdot\mathbf{N} = (\mathbf{F}\mathbf{S}\mathbf{N})\cdot\boldsymbol{\phi}$ are used. Given the load p (and potential boundary displacements), as well as the necessary material data specifying the material function in, e.g., (1.48) and (1.49), we obtain the weak equilibrium formulation by finding the displacement $\mathbf{u}$ such that

$$\int_{\Omega_0} \mathrm{Tr}\left[\mathbf{S}(\mathbf{F}^{\mathrm{T}}\mathrm{Grad}\boldsymbol{\phi})^{\mathrm{S}}\right]\,\mathrm{d}v + \int_{\partial\Omega_{0\mathbf{t}1}} pJ(\mathbf{F}^{-1})^{\mathrm{T}}\mathbf{N}\cdot\boldsymbol{\phi}\,\mathrm{d}A = 0 \quad \text{in} \quad \Omega_0 \tag{1.70a}$$

$$\mathbf{u}(\mathbf{X}) = \mathbf{0} \quad \text{on} \quad \partial\Omega_{0\mathbf{u}1} \tag{1.70b}$$

is satisfied. Note that only the symmetric part, denoted $(\bullet)^{\mathrm{S}}$, will remain of $\mathbf{F}^{\mathrm{T}}\mathrm{Grad}\boldsymbol{\phi}$ using a Cartesian decomposition. Furthermore, the discrete equations can instead be written in terms of the displacements as $\mathbf{F}(\mathbf{u}) = \mathbf{0}$, which is nonlinear in $\mathbf{u}$. By using an incremental iterative Newton-Raphson procedure, the solution $\mathbf{u}$, for a given p (and potential boundary displacements), is found. The total Lagrangian formulation in (1.70) may be used as a foundation for the finite element equations formed using, e.g., the multipurpose finite element software FEAP, but is often pushed forward to an updated Lagrangian formulation in the spatial (deformed) configuration, see [7, 8] for more details.

Regardless of which material that is studied, or which numerical solution scheme that is used to model it, the constitutive models should try to capture the material behavior to 'some' desired accuracy, and thus it is essential to understand the underlying mechanics of the material that is studied. The following two sections, therefore, describe the constituents and material behavior of a cerebral aneurysm and of the myocardium.

1.3. Cerebral Aneurysms

A cerebral aneurysm is an unhealthy dilation of the arterial vessels in the brain. In contrast to abdominal aneurysm, which are fusiform in shape, cerebral aneurysms are often saccular, or berry shaped. They are present in 2–5 % of the general population and if ruptured have a high mortality and morbidity rate [9]. However, most often a cerebral aneurysm grows in a stable manner and only ruptures in 1.3 % cases per year [10]. Cerebral aneurysms are generally found at arterial bifurcations, with the majority at the anterior part of the Circle of Willis [11].

1.3.1. Arterial wall

The artery surrounding the aneurysm is often healthy and consists of three layers as seen in Fig. 1.2, the intima which is the innermost layer, the media which is the middle and thickest layer and the adventitia which is the outermost layer. In healthy or young arteries, the

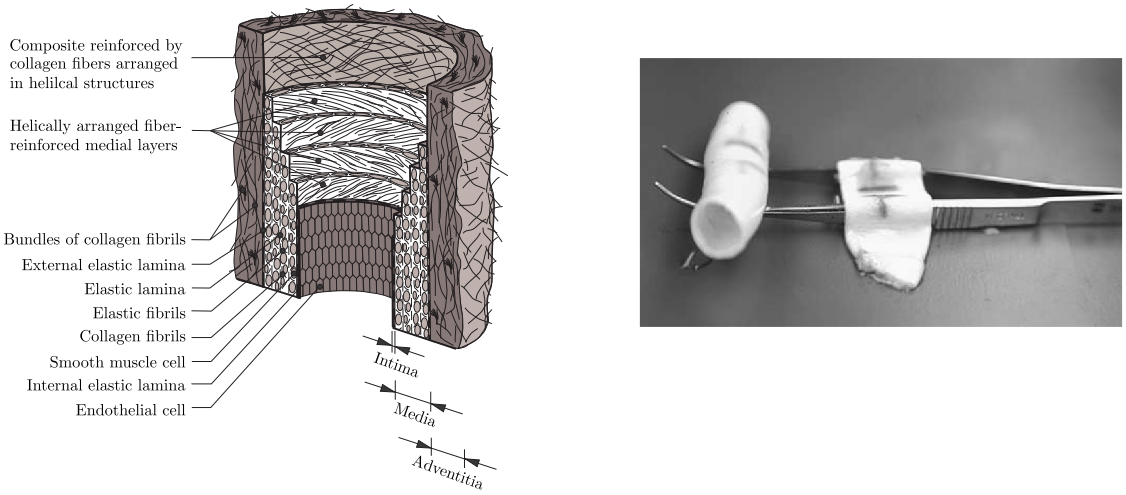

Figure 1.2.: Diagram showing the components of a healthy artery and the three layers intima, media and adventitia (left panel). Mechanically separated medial and adventitial layers (right panel) into a stiff medial tube, shown on the left side, and the limp adventitia, shown to the right, adapted from [12].

intimal layer is a very thin sheet consisting of endothelial cells laying on a basal membrane and is often considered not to carry any load. With age or disease, however, it becomes significantly thicker and the no-load carrying assumption is no longer valid [13]. The media is a relatively thick layer and consists of smooth muscle cells, elastin and collagen fibrils. The smooth muscles can contract and thus alter the diameter and flow through the artery. The collagen fibrils are arranged in a helical pathway, but with a small pitch, making them nearly circumferential in orientation [12]. The media is fairly stiff even at a load-free configurations, as seen in Fig. 1.2. The adventitia is composed mainly of collagen which are arranged in a helical structure to reinforce the arterial wall. The adventitia is soft at low loads, or a load-free state, as seen in Fig. 1.2, but stiffens significantly at higher loads and is thus thought to protect the artery from rupture at instances of increased blood pressure [12].

In addition, the arterial wall is residually stressed. However, as shown by Holzapfel et al. [14], each layer of the artery is stressed in different directions. Thus, a single material parameter, such as the opening angle suggested by Liu and Fung [15], is not enough to characterize the three-dimensional residual stress state of arteries.

1.3.2. Evolving aneurysm

Structural changes in arterial walls and, more specifically, structural evolution of developing aneurysms have been addressed in several studies. Different approaches are used, but the continuous turnover of collagen fibers is widely accepted to be the driving mechanism in the development of aneurysms. Humphrey and Rajagopal [16] suggest a general theoretical framework for growth and remodeling of soft tissues, incorporating collagen

turnover. This framework is utilized by Baek et al. [17], who model aneurysm growth and assume that the collagen production rate is governed by the current in-plane wall stress of the aneurysm. They also assume that the orientation of newly deposited collagen is governed by a specific criterion, based on the principal stresses or stretches in the aneurysm wall, and the outcome for different criteria is evaluated. Driessen et al. [18] also model collagen remodeling in an artery wall. In that study, the collagen fibers are assumed to be aligned in a few fiber directions, and these alignments are assumed to evolve depending on the principal stretches in the material.

Watton et al. [19] model aneurysm growth by assuming that collagen fibers are continuously attached in a pre-stretched state and configured such that the strain in these fibers at systole is constant. Kroon and Holzapfel [20] presented a theoretical model for the growth of a saccular cerebral aneurysm. The growth model was assessed for an axisymmetric problem, where the aneurysm was described as a circular membrane hinged along the boundary and exposed to an inflation pressure. The aneurysm wall was assumed to consist of a number of distinct collagen fiber layers. The continuous turnover of collagen in the layers was responsible for the growth of the aneurysm, and the collagen production in the layers was driven by a deformation measure. A parameter study was performed to outline the general behavior of the model, and a stability analysis was provided. In Chapter 2 of this thesis, this model is used to investigate the influence of an anisotropic medial layer on an evolving cerebral aneurysm and the effects of axial in situ stretch.

1.4. Cardiac Mechanics

The heart is a complex organ which essentially acts as an electro-mechanical pump of blood. It is comprised of four chambers, the right and left atrium and the right and left ventricles. Oxygen poor blood enters the right atrium from the superior and inferior vena cava, as well as the coronary sinus. The right atrium pumps the blood through the tricuspid valve into the right ventricle which in turn pumps the blood through the pulmonary valve and pulmonary trunk into the pulmonary artery and lungs where the blood gets reoxygenated. Oxygen rich blood enters the left atrium from the pulmonary veins and pumps it through the mitral valve to the left ventricle. Finally, the left ventricle pumps the blood through the aortic valve into the aorta where it continues throughout the body via the aortic tree. The heart itself is supplied by blood from the right coronary artery which is attached to the aortic branch.

The heart wall is comprised of three layers, the endocardium which is the innermost layer, the myocardium which is the middle layer and the epicardium which is the outermost layer. The heart is enclosed in a fluid which is contained in a doubled-walled sac (the pericardium), which keeps the motion of the heart frictionless against the surrounding tissue, where the innermost layer of the pericardium is connected to the epicardium which is a thin protective layer of connective tissue. Also the endocardium is a very thin layer but is comprised of cells similar to the endothelial cells of arteries. The myocardium, on

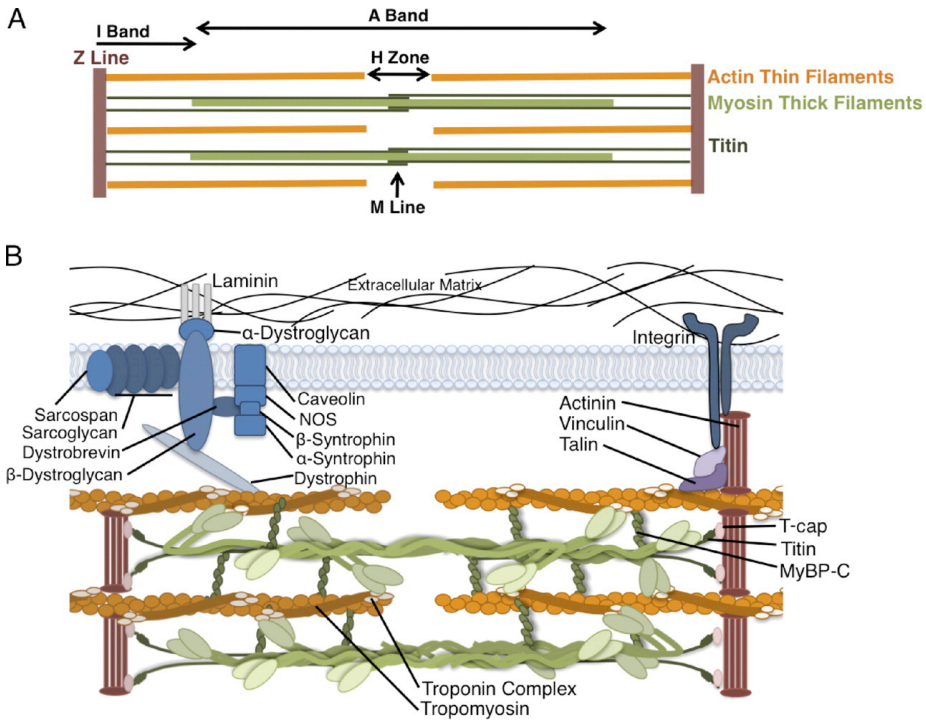

Figure 1.3.: Simplified model showing the basic organization of a sarcomere (top) and a representation of the major proteins of a sarcomere (bottom), adapted from [21].

the other hand, is by far the thickest of the three layers. It is comprised of striated muscle cells (myocytes), which work together to generate the contraction of the heart and is thus responsible for the large pumping force.

1.4.1. Contractile unit

Each myocyte is built up of myofibrils which in turn contains several sarcomeres. The sarcomeres, shown in Fig. 1.3, are the basic building blocks of the cardiac muscle and are what causes the heart to contract by sliding actin and myosin filaments (thin and thick filaments, respectively) along each other. In order for sliding to be achieved, calcium ions have to bind to the tropomyosin (on troponin-C molecules) which covers the actin filaments, thus altering the tropomyosin and exposing binding sites where cross-bridges can be formed between myosin heads and the actin filament. The myosin heads are bound to an adenosine diphosphate (ADP) and a phosphate ion in the resting position (a resting position is when the myosin head is not attached to the actin filament, but where the myosin head is in a high-energy configuration). The exposure of the binding site on the actin filament causes the myosin head to connect, forming a cross-bridge, and loose the attached phosphate. The remaining ADP is released causing the myosin head, still attached to the actin filament, to move in a power-stroke that also moves the actin filament. After the power-stroke, an adenosine triphosphate (ATP) molecule is attached to the myosin head, causing a release of the cross-bridge. The myosin head now hydrolyze the ATP into ADP

and a phosphate ion, causing a recovery stroke in which a release of energy moves the head back to its resting, but high-energy, configuration. This sequence of power-strokes and recovery strokes are repeated until the calcium ions are removed and the binding sites on the actin filaments are again covered by the tropomyosin.

The increase in calcium in a myocyte, responsible for the contraction, is triggered by a phenomenon called calcium-induced calcium release. An action potential travels through gap junctions to the contractile unit where it travels through the T-tubules in the Z-band (seen in Fig. 1.3 top panel). There, the potential triggers a flux of calcium ions through L-type calcium channels into the cell. Inside the cell, the sarcoplasmic reticulum contains a large storage of calcium ions and it has the possibility to sense the flux increase of calcium ions to the cytosol. When the sarcoplasmic reticulum senses this increase, it triggers an additional release of its stored calcium ions which can then bind to the troponin-C molecules. During muscle relaxation, the calcium ions in the cytosol are again retained in the sarcoplasmic reticulum.

The action potential is generated by the pacemaker cells located at the sinoatrial node in the right atrium. The pacemaker cells are modified myocytes which do not contract, but instead spontaneously discharge. The action potential travels from the sinoatrial node to the myocytes via a fast conduction network called the Purkinje system (PS). The Purkinje fibers comprising this complex three-dimensional system are modified myocytes which end at Purkinje-ventricular junctions. These sites may be viewed as point sources of electrical wavefronts to the myocardium. The electrical wavefront in the myocardium travels at different speeds determined by the structure of the myocardium (as described in Section 1.4.2) and is fastest along the myocyte fiber direction and slowest in the sheet-normal direction.

1.4.2. Structural organization of the myocardium

In general, myocyte orientation in the LV follows a right-handed helical pathway from the endocardium towards the mid-wall, and a left-handed helical pathway from the mid-wall towards the epicardium [22–24], as shown in Fig. 1.4 (a). As described by, e.g., Hort [26], the myocytes are further bundled into layers that are four to six cells thick creating sheets as shown in Fig. 1.4 (b). The orientation of the sheets vary both transmurally and in the apico-basal direction [24, 25, 27, 28]. Labeling the local myocyte direction as the fiber direction, we may thus characterize the myocardium as an orthotropic material with a fiber, sheet and sheet-normal direction labeled f, s and n, respectively.

In addition, the fiber alignment in the helical pathway is quite strong in a healthy heart where the angular dispersion (AD) is only $\sim$ 12-15°. In a diseased heart, e.g., with hypertrophic cardiomyopathy (HCM), the AD may locally increase to $\sim 25°$ [29–31]. An increased disarray in both collagen and muscle fiber orientation is also found in other diseases, such as myocardial infarction [32–34]. Experiments have further shown that in healthy hearts, the sheet direction is also locally dispersed [35–37] and although it has not

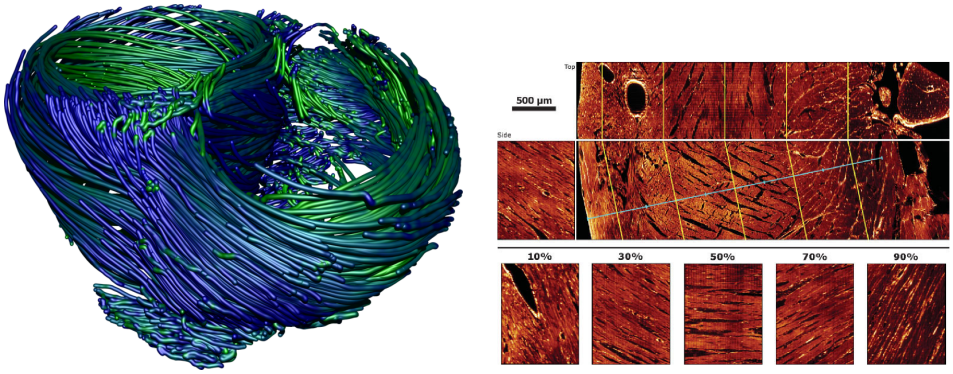

(a) DTMRI (b) Confocal microscopy

Figure 1.4.: Fiber and sheet orientation in the ventricular wall: (a) diffusion tensor magnetic resonance imaging (DTMRI) showing the helical structure of the myocyte orientation, adapted from [24]; (b) confocal microscopy showing the sheet structure (top) and the transmural change in the fiber structure (bottom), adapted from [25].

been studied in as great detail as that of the fiber direction, it may still play a significant role in the function of myocardium [38]. However, further experiments quantifying the sheet dispersion on diseased human hearts are needed as no data is available today.

1.4.3. Modeling cardiac mechanics

In its simplest form, the heart can be considered to act as a pump generating pressure and blood flow. This inspired early work to model the tension in the heart wall using the law of Laplace for thin walled spheres [39]. Although this method provides an easy way to calculate wall stresses based on pressure and dimension, it does not capture any mechanical properties of the myocardium. Small strain theory was later used in an attempt to capture the distribution of stresses within the ventricular wall [40], but as the deformations in many biological tissues can exceed 50–100 %, small strain theory has been shown to yield unrealistic stress values [41]. Nonlinear finite deformation theory has now become the common setting. Used together with the finite element method (FEM), it is possible to solve the complex boundary-value problem associated with the heart. It has enabled the incorporation of complex geometrical description, anisotropic fiber reinforcement and many different constitutive models.

Constitutive models for myocardium. For myocardium, constitutive models often assumed that the tissue is hyperelastic and thus can be characterized by a strain-energy function, as shown in Section 1.2.4. Models for myocardium that includes the muscle fiber response are either i) transversely isotropic models or ii) orthotropic models. As pointed out in an excellent review of cardiac models by Holzapfel and Ogden [42], the transversely isotropic models does not capture the orthotropic behavior of myocardium, but they may nevertheless be useful as they often contain fewer material parameters which may be more

easily determined in vivo [43]. Common transversely isotropic models are the exponential Fung-type models (based on [44]), e.g., the model developed by Omens et al. [45],

$$\Psi(\mathbf{E}) = \frac{1}{2}a[\exp(Q) - 1], \tag{1.71}$$

where

$$Q = b_1 E_{\mathrm{ff}}^2 + b_2(E_{\mathrm{ss}}^2 + E_{\mathrm{nn}}^2 + E_{\mathrm{sn}}^2) + 2b_3(E_{\mathrm{fs}}^2 + E_{\mathrm{fn}}^2), \tag{1.72}$$

or the model by Costa et al. [46] where Q changes to

$$Q = 2b_1(E_{\mathrm{ff}} + E_{\mathrm{ss}} + E_{\mathrm{nn}}) + b_2 E_{\mathrm{ff}}^2 + b_3(E_{\mathrm{ss}}^2 + E_{\mathrm{nn}}^2 + 2E_{\mathrm{sn}}^2) + 2b_4(E_{\mathrm{fs}}^2 + E_{\mathrm{fn}}^2), \tag{1.73}$$

and f, s and n pertain to the fiber, sheet and sheet-normal directions, respectively.

For models that can capture the orthotropic behavior of myocardium, a common exponential Fung-type models is, e.g., the model developed by Costa et al. [47], where $\Psi(\mathbf{E})$ is given by (1.71) and Q takes the form

$$Q = b_{\mathrm{ff}} E_{\mathrm{ff}}^2 + b_{\mathrm{ss}} E_{\mathrm{ss}}^2 + b_{\mathrm{nn}} E_{\mathrm{nn}}^2 + b_{\mathrm{fs}} E_{\mathrm{fs}}^2 + b_{\mathrm{fn}} E_{\mathrm{fn}}^2 + b_{\mathrm{sn}} E_{\mathrm{sn}}^2. \tag{1.74}$$

The advantage of this model is that it only has 7 material parameters, however, although interpretations for the material parameters where attempted by Costa et al. [47], those parameters are all coupled through a in (1.71), which means that their individual parameter interpretation is questionable. Other orthotropic models are motivated by equi-biaxial tension tests, e.g., the so-called pole-zero model develped by Hunter et al. [48],

$$\begin{aligned}\Psi(\mathbf{E}) = &\frac{k_{\mathrm{ff}} E_{\mathrm{ff}}^2}{|a_{\mathrm{ff}} - |E_{\mathrm{ff}}||^{b_{\mathrm{ff}}}} + \frac{k_{\mathrm{fn}} E_{\mathrm{fn}}^2}{|a_{\mathrm{fn}} - |E_{\mathrm{fn}}||^{b_{\mathrm{fn}}}} + \frac{k_{\mathrm{nn}} E_{\mathrm{nn}}^2}{|a_{\mathrm{nn}} - |E_{\mathrm{nn}}||^{b_{\mathrm{nn}}}} \\ &+ \frac{k_{\mathrm{fs}} E_{\mathrm{fs}}^2}{|a_{\mathrm{fs}} - |E_{\mathrm{fs}}||^{b_{\mathrm{fs}}}} + \frac{k_{\mathrm{ss}} E_{\mathrm{ss}}^2}{|a_{\mathrm{ss}} - |E_{\mathrm{ss}}||^{b_{\mathrm{ss}}}} + \frac{k_{\mathrm{ns}} E_{\mathrm{ns}}^2}{|a_{\mathrm{ns}} - |E_{\mathrm{ns}}||^{b_{\mathrm{ns}}}}.\end{aligned} \tag{1.75}$$

Here the material parameters are more easily related to the principal directions of the material, however, the obvious drawback is that the model needs 18 material parameters, see Schmid et al. [49, 50] for a discussion on the fit of these models to the experimental data of Dokos et al. [51].

Both the orthotropic 'Costa' model and the 'pole-zero model' uses the material strain to define the strain-energy function, and through the relations $2E_{ii} = I_{4i}$, where $i \in \{\mathrm{f}, \mathrm{s}, \mathrm{n}\}$ and $2E_{ij} = I_{8ij}$, where $i \neq j$, they may be seen as a special case of the model developed by Holzapfel and Ogden [42], which uses the strain (and pseudo) invariants according to

$$\begin{aligned}\Psi(I_1, I_{4\mathrm{f}}, I_{4\mathrm{s}}, I_{8\mathrm{fs}}) = &\frac{a}{2b}\{\exp[b(I_1 - 3)] - 1\} + \sum_{i=\mathrm{f,s}} \frac{a_i}{2b_i}\{\exp[b_i(I_{4i} - 1)^2] - 1\} \\ &+ \frac{a_{\mathrm{fs}}}{2b_{\mathrm{fs}}}[\exp(b_{\mathrm{fs}} I_{8\mathrm{fs}}^2) - 1].\end{aligned} \tag{1.76}$$

This model is micro-structurally based with only 8 material parameters and each term in the strain-energy function has a clear physical interpretation, see [42] for details.

Myocardial stress. Constitutive models are used to determine the passive stress in the myocardium, i.e. the stress in the tissue due to the deformation. This deformation, in turn, originates from the contraction of the myocytes and is often modeled using either the active strain approach or the active stress approach, see [52, 53] for a review of these approaches. In the active strain approach, the deformation gradient $\mathbf{F}$ is multiplicatively decomposed into an active part $\mathbf{F}_\mathrm{a}$, described by a constitutive relations that does not store energy, and an elastic part $\mathbf{F}_\mathrm{e}$, described by a passive constitutive model [54, 55]. In the active stress approach, the stress tensor $\boldsymbol{\sigma}$ (defined in Section 1.2.5) is additively decomposed into an active stress tensor $\boldsymbol{\sigma}_\mathrm{a}$ and a passive stress tensor $\boldsymbol{\sigma}_\mathrm{p}$ [56, 57]. The active stress can be modeled in several ways. A popular approach is to use a cellular tension model calculated either from the ionic concentrations [58, 59] or directly from the electrical potential [60]. It has also been proposed to additively separate the strain-energy function Ψ into an active part Ψ_a and a passive part Ψ_p [61]. However, as pointed out by Skallerud et al. [62], such a function Ψ_a is not a true strain-energy function but merely a term that generate the active stress tensor, see Trayanova and Rice [63] for an excellent review of active cardiac electro-mechanical models and coupling.

Cardiac electro-physiology. The myocardium is often approximated as a continuous media of electrical activation and repolarization. Two common models describing this behavior are the reaction-diffusion equations referred to as the bidomain or monodomain models [64]. Through a conductivity tensor present in these models, with the eigenaxes in the fiber, sheet and sheet-normal directions, the wavefront of electrical activation spreads with a ratio 3:2:1 along the three axis, respectively [65–67]. To generate the action potential, many generic models are based on the famous Hodgkin-Huxley model for currents in an axon [68], which was reduced to a two-variable model in the FitzHugh-Nagumo model [69]. Phenomenological models, such as the Fenton-Karma or the Mahajan models [70, 71], are also used because of the simplicity to fit these models directly to experimental data, see Clayton et al. [72] for a review of models for cardiac tissue electrophysiology.

Electro-mechanical coupling. To couple the multi-scale tissue models and the biophysical models a variety of techniques are available. Perhaps the simplest and most often used technique is the weakly coupled approach [73]. In this approach, it is assumed that the mechanics has a limited influence on the electrophysiology so the electrical quantities are first calculated separately and then relevant parameters are fed into a mechanical simulation of deformation and stress. The main advantages of the weakly coupled approach is its simplicity, stability and low computation time [74]. In the strongly coupled approach it is instead assumed that the mechanical quantities influence the electrophysiology. The mechanical quantities are, therefore, continuously passed back to the electrical simulation which enables the modeling of subtle effects such as myocardial mechano-electrical feedback [60, 75]. The strongly coupled approach is more complex than the weakly coupled approach and it is prone to numerical instabilities, although those issues are being

addressed [58, 76], see Nordsletten et al. [77] for a review on issues of coupling the multi-physics models to cardiac mechanics.

Pressure calculations. The pressure volume relation in cardiac ventricular simulations are often modeled to follow the classical pressure volume loops as defined by experiments, see, e.g., [78]. This entails that the follower type pressure load p is calculated in five consecutive steps. The first step is an initialization load, where the pressure is increased linearly to the end diastolic pressure. This represent the filling of blood into the ventricle, which at this point is in a relaxed state. The second step involves an isochoric (volume preserving) contraction as both the mitral and aortic valves are considered to be closed while the ventricle is contracting. The third load step is the ejection phase. This represent the release of blood from the ventricle as the aortic valve opens. The fourth load step is again an isochoric deformation, this time as the ventricle is relaxing, while the aortic valve is closed to hinder regurgitation (back-flow). In the fifth and final step, the pressure and volume is increasing again as the mitral valve opens and blood enters the ventricle. In simtulations of several heart beats, the cycle then starts over from the second load step.

The first and fifth load steps are usually simulated using a linear increase of pressure. The two isochoric loads, steps 2 and 4, may be calculated iteratively for each time step to keep the volume V constant using $p_{n+1} = p_n + (V_{n+1} - V_n)/C_\mathrm{p}$ as described in [79], where C_p is a penalty parameter. The value of C_p is then set to give a computationally efficient convergence for the isochoric solution.

The ejection phase, load step 3, is often calculated using the 2, 3 or 4-element Windkessel models. The two element Windkessel model [80], for example, is described as

$$C\frac{\mathrm{d}p}{\mathrm{d}t} + \frac{p}{R} = -\frac{\mathrm{d}v}{\mathrm{d}t}, \tag{1.77}$$

where C and R relate to arterial compliance and resistance, respectively. Most often C and R are considered constants, and do not account for the nonlinear behavior of arteries [81, 82]. Equation (1.77) may, e.g., be solved iteratively as described in Kerckhoffs et al. [83], or alternatively, to achieve both the isochoric deformation and the Windkessel deformations, the pressure and volume change can directly be prescribed in the finite deformation elasticity equations, i.e., make them part of Eq. (1.70).

1.5. Organization of the Thesis

The thesis is a compilation of five scientific papers, which focus on different computational aspects in biomechanics. The papers span from modeling the growth of a cerebral aneurysm to simulating the behavior of the left ventricle with an emphasis on the material behavior. The papers are presented in the following chapters:

2. *'Influence of Medial Collagen Organization and Axial In Situ Stretch on Saccular Cerebral Aneurysm Growth'*, T.S.E. Eriksson, M. Kroon and G.A. Holzapfel, ASME Journal of Biomechanical Engineering, 131:101010 (7 pages), 2009

   The study focuses on the influence of an anisotropic medial layer on an evolving cerebral aneurysm. The middle cerebral artery is modelled as a two-layered cylinder, where the layers correspond to the media and the adventitia. Local and instant loss of media is considered responsible for the aneurysm growth. The adventitia is composed of several distinct layers with collagen fibers that are the only load bearing constituent in the aneurysm wall. Their production and degradation are depending on the stretch of the wall and are also responsible for the growth of the aneurysm. The anisotropy of the medial layer is modeled using a strain-energy function valid for an elastic material with two families of fibers. The results shows that including fiber reinforcement in the medial layer reduces the maximum principal stress, thickness increase and shear stress in the aneurysm wall. A variation of the initial fiber angles is shown to have little effect whereas the axial in situ stretch has a much larger effect in terms of shape and stresses in the aneurysm wall.

3. *'Tensors Needed for Finite Element Implementation of an Invariant Based Constitutive Model for Passive Myocardium'*, T.S.E. Eriksson and G.A. Holzapfel

   The study focuses on the constituents needed for implementation of an invariant based orthotropic model for passive myocardium. The stress and elasticity tensors are shown together with a fit of the model to experimental data. A comparison is made between the proposed invariant based model and a commonly used Green-Lagrange strain based model and it is shown that using material parameters retrieved when both models are fitted to a simple shear mode experiment, the proposed model is better suited to predict the stress in the myocardium for other modes of deformation. In addition, the finite element implementation is used on a model of the left ventricle and it is shown that passively increasing the pressure on the endocardial wall results in steep stress gradients through the wall thickness. This suggests that residual stresses may need to be included in future models.

4. *'Influence of Spatial Heterogeneity in Tissue Orthotropy upon Mechanical Contraction in the Left Ventricle'*, T.S.E. Eriksson, A.J. Prassl, G. Plank and G.A. Holzapfel

   The study focuses on spatial heterogeneity in myocardial tissue. A coupled model of the left ventricle is presented where pressure is calculated as a response to change in internal volume. The passive behavior is modeled as a hyperelastic material using an orthotropic strain-energy function and an evolution equation is used to generate the active stresses. The influence of myocardial fiber and sheet distributions is investigated by using two different fiber and sheet distribution setups, a generic setup and one based on experiments. It was found that spatial heterogeneity may play a

critical role in mechanical contraction of the LV and that geometrical descriptions of deformations are needed when evaluating the accuracy of a ventricular model.

5. *'Modeling the Disarray in Cardiac Fiber and Sheet Orientations'*, T.S.E. Eriksson, A.J. Prassl, G. Plank and G.A. Holzapfel

   The study focuses on a novel approach to model the disarray of both fiber and sheet orientations in cardiac tissue. A material structure parameter describing the relation between an isotropic invariant and a directionally dependent invariant is fitted to experimental data of angular disperison in both the fiber and sheet direction. The parameter is used to model the dispersion in myocardial tissue by augmenting an invariant based orthotropic strain-energy function and in a structure tensor used to determine the direction of active stress. Simulations shows that dispersion has a large effect on myocardial stress and deformation development as well as on pressure volume loops of a left ventricle.

6. *'On Tension-Compression Switching in Dispersed Fiber-Reinforced Constitutive Models'*, T.S.E. Eriksson, D.M. Pierce and G.A. Holzapfel

   The study focuses on tension-compression switching of a dispersed fiber-reinforced constitutive model. Large-strain, fiber-reinforced constitutive models are commonly used for solving complex boundary-value problems in the context of the finite element method. Although the mathematical and physical motivation for including a tension-compression fiber 'switch' may be clear when using models which do not include fiber dispersion, neither the mathematical nor physical motivation for tension-compression fiber switching is so clear for cases where fiber-reinforced models are extended to include the effect of distributed fiber orientations. Here we explore methods to study such switching mechanisms by analyzing six potential switching cases, and draw some conclusions about the mathematical robustness and physical interpretation of the different possible approaches. We propose using two different permeations of the dispersed fiber-reinforced models, depending on whether one can assume that the fibers are (nearly) uncoupled or strongly coupled to the isotropic ground matrix.

The following conference proceedings and accepted (extended) abstracts where also part of the thesis:

- W. Rachowicz, A. Zdunek and T.S.E. Eriksson: Application of the adaptive FEM to computational biomechanics. 6^{th} European Congress on Computational Methods in Applied Sciences and Engineering (ECCOMAS), Vienna, Austria, September 10–14, 2012.
- G.A. Holzapfel, T.S.E. Eriksson, A.J. Prassl and G. Plank: An electro-mechanically computational model for the myocardium including fiber and sheet disarray. 23^{rd}

International Congress of Theoretical and Applied Mechanics, Beijing (ICTAM), China, August 19–24, 2012.

- T.S.E. Eriksson, G. Plank and G.A. Holzapfel: A structurally motivated model for myocardial fiber and sheet disarray. 8^{th} European Solid Mechanics Conference (ESMC), Graz, Austria, July 9–13, 2012.
- C. Augustin, E. Hoetzl, T.S.E. Eriksson, A.J. Prassl, G.A. Holzapfel, O. Steinbach and G. Plank: Application of advanced bidomain solver techniques to cardiac electromechanics. 8^{th} European Solid Mechanics Conference (ESMC), Graz, Austria, July 9–13, 2012.
- G.A. Holzapfel, T.S.E. Eriksson and M. Unterberger: Structurally-based computation of the biomechanical response of cardiovascular tissues. 11^{th} International Conference on Computational Plasticity. Fundamentals and Applications (COMPLAS XI), Barcelona, Spain, September 7–9, 2011.
- W. Rachowicz, A. Zdunek and T.S.E. Eriksson: Application of hp-adaptive FEM to medical diagnostics. Higher Order Finite Element and Isogeometric Methods (HOFEIM), Krakow, Poland, June 27-29, 2011.
- T.S.E. Eriksson, G. Plank and G.A. Holzapfel: A coupled model for the left ventricle including regional differences in structure and function, *Proceedings in Applied Mathematics and Mechanics (PAMM)*, 11:85–86, 2011.
- T.S.E. Eriksson, G. Plank and G.A. Holzapfel: A coupled model of the left ventricle including regional differences in structure and function. 82nd Annual Meeting of the Internatonal Association of Applied Mathematics and Mechanics (GAMM), Graz University of Technology, Austria, April 18-22, 2011.
- T.S.E. Eriksson, R. Höller, G. Plank and G.A. Holzapfel: New material model for the passive response of the myocardium: numerical realization and new experimental data. 6^{th} World Congress on Biomechanics, Singapore, August 1-6, 2010.
- T.S.E. Eriksson, G. Plank and G.A. Holzapfel: A new invariant-based constitutive model for the passive response of the myocardium and constituents needed for FE implementation. 1^{st} International Conference on Material Modelling (ICMM), Dortmund, Germany, September 15–17, 2009.

2. INFLUENCE OF MEDIAL COLLAGEN ORGANIZATION AND AXIAL IN SITU STRETCH ON SACCULAR CEREBRAL ANEURYSM GROWTH

Abstract A model for saccular cerebral aneurysm growth, proposed by Kroon and Holzapfel *(J. Theor. Biol., 2007, 247:775–787; J. Biomech. Eng., 2008, 130:051012)*, is further investigated. A human middle cerebral artery is modeled as a two-layer cylinder, where the layers correspond to the media and the adventitia. The immediate loss of media in the location of the aneurysm is taken to be responsible for the initiation of the aneurysm growth. The aneurysm is regarded as a development of the adventitia, which is composed of several distinct layers of collagen fibers perfectly aligned in specified directions. The collagen fibers are the only load bearing constituent in the aneurysm wall; their production and degradation depend on the stretch of the wall and are responsible for the aneurysm growth. The anisotropy of the surrounding media was modeled using the strain-energy function proposed by Holzapfel et al. (J. Elasticity, 2000, 61:1–48) valid for an elastic material with two families of fibers. It was shown that the inclusion of fibers in the media reduced the maximum principal Cauchy stress and the maximum shear stress in the aneurysm wall. The thickness increase of the aneurysm wall due to material growth was also decreased. Varying the fiber angle in the media from a circumferential direction to a deviation of 10° from the circumferential direction did, however, only show a little effect. Altering the axial in situ stretch of the artery had a much larger effect in terms of the steady-state shape of the aneurysm and the resulting stresses in the aneurysm wall. The peak values of the maximum principal stress and thickness increase, both became significantly higher for larger axial stretches.

2.1. Introduction

Saccular cerebral aneurysms are detected in less than 5% of the human population, and are usually diagnosed in elder people between the fifth and the seventh decade. High blood pressure, which is rather specific for man, appears to have some influence on the development of cerebral aneurysms [84]. A subarachnoid hemorrhage due to the rupture of an intracranial aneurysm is a devastating event associated with high rates of morbidity and mortality. Approximately 12% of patients die before receiving medical attention, 40% of hospitalized patients die within one month after the event, and more than one third of those who survive have major neurological deficits [85].

Cerebral aneurysms generally form and grow at arterial bifurcations in connection to the Circle of Willis, where the internal elastic membrane is partially destroyed, and where the media is diminished [11]. Approximately 80% of all these aneurysms occur at one of three main sites, i.e. the carotid/posterior communicating respectively anterior choroidal artery junction, the anterior communicating artery, and the middle cerebral artery main bifurcation [86].

Determination of the structure of the aneurysm wall is a necessary precursor to establish suitable constitutive relations for this type of tissue. For this purpose, experimental investigations of aneurysmal tissue, for example, in terms of tensile testing and histological examinations, are necessary, but theoretical modeling may also provide important insights. Structural changes of artery walls and, more specifically, structural evolution of developing aneurysms have been addressed in previous theoretical studies [16–20, 87]. Kroon and Holzapfel [20, 87] proposed a theoretical model for the growth of a saccular cerebral aneurysm. In this model, the aneurysm wall was assumed to consist of a number of distinct collagen fiber layers. The continuous turnover of collagen in the layers was responsible for the growth of the aneurysm, and the collagen production in the layers was governed by the embedded fibroblasts.

In the present paper, this aneurysm model is further developed. A realistic 3D setting is now employed in the form of a human middle cerebral artery. More specifically, the middle cerebral artery is modeled as a two-layer cylinder, where the layers correspond to the media and the adventitia. The constitutive behavior of the adventitia is governed by the aneurysm growth model, and the media is modeled as a neo-Hookean material reinforced by two families of collagen fibers [12]. The structural integrity of an artery or aneurysm is to a large extent determined by the organization of the collagen fabric. The collagen of the adventitia or an aneurysm wall is mainly Type I [11,88], whereas the collagen of the media is mainly of Type III [89, 90]. In a previous study, the influence of the organization of the Type I collagen fabric of the adventitia was investigated [87]. Instead, the present study focuses on the influence of the orientation of the medial collagen on aneurysm growth. In addition, the consequences of different axial *in situ* stretches are studied. The influence is quantified in terms of stress distributions, wall thickness distributions and aneurysm shape at steady-state.

A short review of the aneurysm growth model is given in the next section. The current problem is then formulated, followed by a presentation of the numerical model and the numerical results. Finally, a discussion and some concluding remarks are provided.

2.2. Growth Model of a Saccular Cerebral Aneurysm

The saccular cerebral aneurysmal wall is considered to be the development of the adventitia of the originally healthy parent artery. The aneurysm wall is modeled as a hyperelastic

material and is characterized by a strain-energy function Ψ. The only load-bearing constituent is the collagen that is produced by fibroblasts, spread throughout the collagen network. The aneurysm wall is assumed to consist of n distinct and discrete layers of collagen fibers that can be considered as plies forming a laminate. The collagen fibers within layer i are perfectly aligned in direction ϕ_i, and as the fibroblasts are aligned in the same direction as the collagen fibers, newly produced collagen will be deposited at this angle as well during the growth process. The collagen mass production rate per unit reference volume, say $\dot{m}_i$, depends on both the stretching of individual fibroblasts and the proliferation of fibroblasts which are taken to be governed by the global stretching of the aneurysm wall. The mass production rate in layer i at time t is [20]

$$\dot{m}_i(t) = \beta_0 C_i^{\alpha}, \tag{2.1}$$

where β_0 is the normal mass production rate in a reference configuration of a healthy artery considered to be the density of fibroblasts multiplied by the collagen production rate per fibroblast [17]. In (2.1) C_i is a scalar defined as $C_i = \mathbf{C} : \mathbf{A}(\phi_i)$, where $\mathbf{C}$ is the right Cauchy-Green tensor, $\mathbf{A}(\phi_i) = \mathbf{M} \otimes \mathbf{M}$ is a structure tensor and the unit vector $\mathbf{M}$ has components $\cos\phi_i$ and $\sin\phi_i$, [12]. Thus, C_i is the projection of $\mathbf{C}$ in the direction ϕ_i of the fibers, and the influence of C_i on the mass production rate $\dot{m}_i(t)$ is modulated by the exponent α.

Fiber deposition occurs at time t_{dp} and at any time between $-\infty$ and current time t. The related deformation gradient is then $\mathbf{F}(t_{\text{dp}}) = \mathbf{R}(t_{\text{dp}})\mathbf{U}(t_{\text{dp}})$, where $\mathbf{R}(t_{\text{dp}})$ is the rotation tensor, with $\det\mathbf{R}(t_{\text{dp}}) = 1$, and $\mathbf{U}(t_{\text{dp}})$ is the right stretch tensor at time t_{dp}, with $\mathbf{U} = \mathbf{U}^{\text{T}}$, [6]. Decomposing the current deformation gradient at t yields $\mathbf{F}(t) = \mathbf{R}'(t, t_{\text{dp}})\mathbf{U}_{\text{loc}}(t, t_{\text{dp}})\mathbf{U}(t_{\text{dp}})$, where $\mathbf{U}_{\text{loc}}(t, t_{\text{dp}})$ is the current local material stretch to which collagen, deposited at time t_{dp}, is exposed, and $\mathbf{R}'(t, t_{\text{dp}})$ is another rotation tensor. Thus, the local right Cauchy-Green tensor $\mathbf{C}_{\text{loc}}$ is

$$\mathbf{C}_{\text{loc}}(t, t_{\text{dp}}) = \mathbf{U}_{\text{loc}}^2(t, t_{\text{dp}}) = \mathbf{U}^{-1}(t_{\text{dp}})\mathbf{C}(t)\mathbf{U}^{-1}(t_{\text{dp}}), \tag{2.2}$$

where $\mathbf{C}(t) = \mathbf{F}^{\text{T}}(t)\mathbf{F}(t) = \mathbf{U}(t)^2$.

Collagen fibers are deposited by the fibroblasts with a pre-stretch λ_{pre}. An expression of the resulting deformation of individual fibers is, therefore, made according to

$$C_{\text{fib}} = \lambda_{\text{pre}}^2 \mathbf{C}_{\text{loc}} : \mathbf{A}(\phi_i). \tag{2.3}$$

A simple polynomial characterizes the strain-energy function ψ_{fib} per unit mass stored in the collagen fibers, namely

$$\psi_{\text{fib}} = \mu_c (C_{\text{fib}} - 1)^3, \quad C_{\text{fib}} \geq 1, \tag{2.4}$$

where $\mu_c > 0$ is a positive material parameter that is governed by the stiffness of collagen fibers. The fibers are considered to have no stiffness in compression ($C_{\text{fib}} < 1$) so that ψ_{fib} is only active when the fibers are in tension.

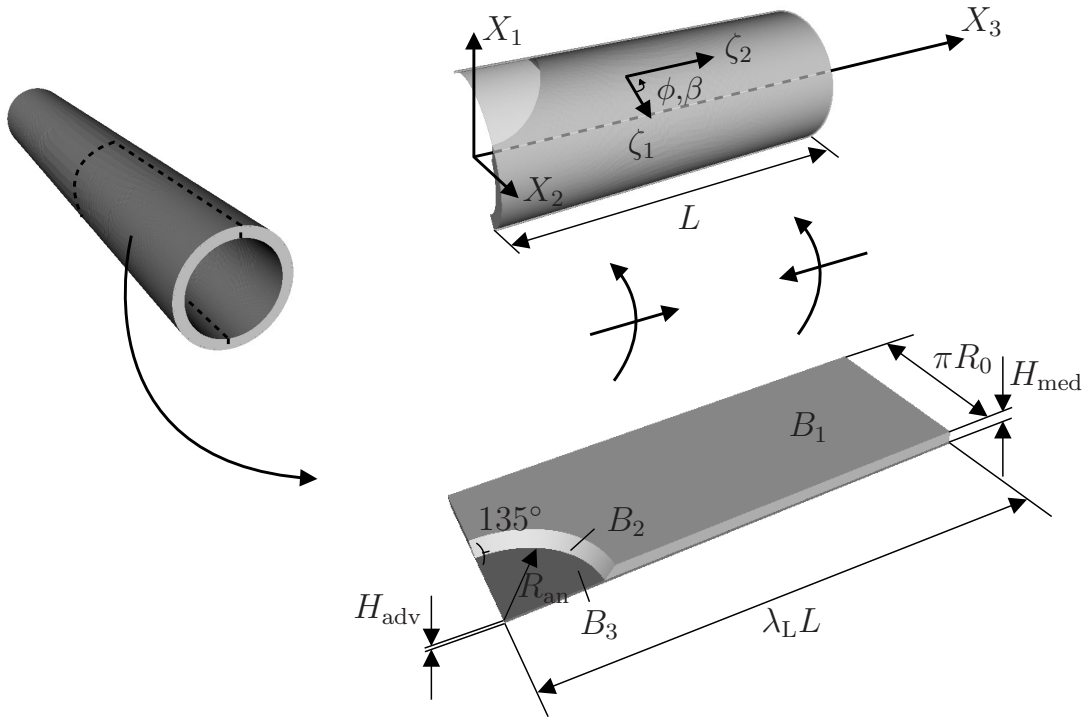

Figure 2.1.: Middle cerebral artery modeled as a two-layer cylinder (media and adventitia). The cylindrical structure (top right figure) constitutes the reference configuration of the posed problem.

The initial thickness of each collagen layer H_{adv}/n is assumed to be the same for all n layers, where H_{adv} is the total initial thickness of the adventitia. The total strain energy Ψ for all plies is integrated according to

$$\Psi(t) = \frac{1}{n}\sum_{i=1}^{n}\Psi_i(t) = \frac{1}{n}\sum_{i=1}^{n}\int_{-\infty}^{t} g(t,t_{\text{dp}})\dot{m}_i(t_{\text{dp}})\,\psi_{\text{fib}}(t,t_{\text{dp}})\,\mathrm{d}t_{\text{dp}}, \tag{2.5}$$

where the turnover of collagen is accounted for by the use of a pulse function $g(t,t_{\text{dp}})$, which is equal to 1 for $t_{\text{dp}} \in [t-t_{\text{lf}},t]$ and 0 otherwise; t_{lf} is the life-time of the collagen fibers.

2.3. Problem Formulation

2.3.1. Model geometry, boundary and loading conditions

The intima is not considered to contribute significantly to the mechanics of the arterial wall. Hence, the artery is modeled as a two-layered cylinder, i.e. media and adventitia, see Fig. 2.1. Due to symmetry only one quarter of a cylinder needs to be modeled. The

model geometry is first defined as a plane sheet with a total thickness of $H_{\text{med}} + H_{\text{adv}}$ and side lengths πR_0 and $\lambda_{\text{L}} L$. The thicknesses of the media and the adventitia are denoted by H_{med} and H_{adv}, respectively. Aneurysm growth is initiated by the removal of the media in a circular region, characterized by the radius R_{an}, as shown in Fig. 2.1. The angle between the exposed adventitia in this circular region, plane B_3, and the cut in the remaining media, plane B_2, is 135°. This plane sheet is then mapped onto a cylindrical surface with outer radius R_0. In that mapping, the geometry is also scaled in the X_3-direction by a factor $1/\lambda_{\text{L}}$, giving the cylindrical structure the length L. Thus, the cylindrical structure, as shown at the top right in Fig. 2.1, constitutes the reference configuration of the posed problem.

The external loading imposed on the model aneurysm consists of an internal pressure p and an axial stretch λ_{L}. Boundary conditions in terms of tractions $\mathbf{t}$ and prescribed displacements $\mathbf{u}$ are thus imposed at time $t = 0^+$ according to (accounting for symmetry)

$$B_1, B_2, B_3 : t_{\text{n}} = -p, \qquad X_1 = -R_0 : u_1 = 0, \qquad X_2 = 0 : u_2 = 0,$$
$$X_3 = 0 : u_3 = 0, \qquad X_3 = L : u_3 = (\lambda_{\text{L}} - 1)L, \tag{2.6}$$

where B_1, B_2, B_3 are the surfaces defined in Fig. 2.1 on which the pressure acts and t_{n} is the normal component of the traction vector $\mathbf{t}$.

2.3.2. Stress response

Aneurysm growth is initiated by a local loss of media. This damage process occurs in a loaded state in which the artery is exposed to a blood pressure and an axial *in situ* stretch. Subsequently we model the following process: (i) a healthy (undamaged) artery is exposed to an (internal) pressure p and an axial stretch λ_{L}; (ii) a local loss of media occurs in a region defined by the radius R_{an}; (iii) growth of the aneurysm starts. In order to model this process, the reference geometry is initially defined as a plane sheet with length $\lambda_{\text{L}} L$ and with a circular damage zone; and this plane sheet is then scaled in the axial direction by the factor $1/\lambda_{\text{L}}$ (and mapped onto a cylindrical shape) to obtain the mentioned reference configuration.

The adventitia of a healthy artery (and the aneurysm wall) is not able to withstand any (or very little) bending, whereas the media of healthy arteries has a significant bending stiffness. Therefore, the adventitia is modeled as a membrane and the media as a three-dimensional continuum (tetrahedral solid elements). The adventitia is built up of n layers with distinct collagen fiber angle ϕ_i for each layer i, where $i = 1, \ldots, n$. The fiber angles are defined by the 2D reference coordinate system ζ_1-ζ_2, as shown in Figs 2.1,2.2, in which ζ_1 follows the circumferential direction of the artery and ζ_2 the axial direction; X_3 and ζ_1-ζ_2 is a local coordinate system defined in every point on the artery surface. As shown in Fig. 2.2, the fiber distribution is uniform and the fiber direction ϕ_1 is taken to coincide with the ζ_1-axis, see Fig. 2.1.

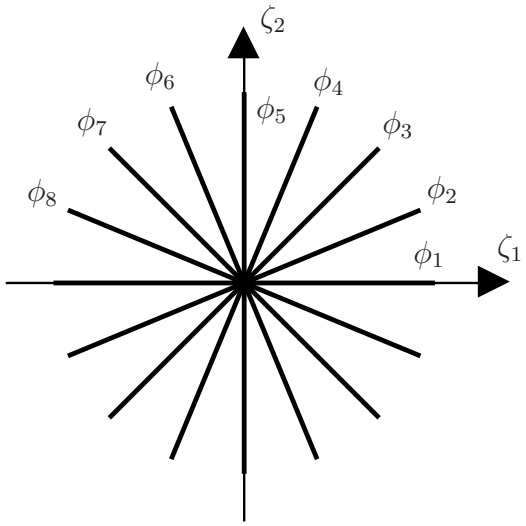

Figure 2.2.: Uniform fiber distribution in the aneurysm wall shown for eight layers; the coordinate system ζ_1-ζ_2 corresponds to the tangential and axial directions, as shown in Fig. 2.1.

For the strain-energy function (2.5) that governs the constitutive response of the adventitia the in-plane second Piola-Kirchhoff stress components $S_{\alpha\beta}$ are given as

$$S_{\alpha\beta} = \frac{2}{n}\sum_{i=1}^{n}\frac{\partial \Psi_i}{\partial C_{\alpha\beta}} = \frac{2}{n}\sum_{i=1}^{n}\int_{-\infty}^{t} g(t,t_{\mathrm{dp}})\dot{m}_i(t_{\mathrm{dp}})\frac{\partial \psi_{\mathrm{fib}}}{\partial C_{\alpha\beta}}\mathrm{d}t_{\mathrm{dp}}, \quad \alpha,\beta = 1,2, \tag{2.7}$$

where $C_{\alpha\beta}$ are the components of the 2D right Cauchy-Green tensor, and indices α and β pertain to the local 2D in-plane reference coordinate system ζ_1-ζ_2 in the plane of the adventitial membrane.

When modeling the media, the components are smooth muscle cells, elastin and collagen (Type III), [91,92]. Elastin and smooth muscle cells are expected to have a fairly linear response. As both the smooth muscle cells and the collagen tend to be aligned approximately in the circumferential direction, the total response of the media is, in general, anisotropic, see [13, 89, 93–95]. In order to model the anisotropic mechanical behavior of the media, the strain-energy function as proposed by Holzapfel et al. [12] was adopted. Thus,

$$\Psi_{\mathrm{med}} = \frac{\mu_{\mathrm{M}}}{2}(I_1 - 3) + \frac{k_{1,\mathrm{med}}}{2k_{2,\mathrm{med}}}\sum_{i=4,6}\{\exp[k_{2,\mathrm{med}}(I_i - 1)^2] - 1\}, \tag{2.8}$$

where the parameter μ_{M} denotes the shear modulus of the media describing the isotropic non-collagenous matrix material (mainly elastin and passive response of smooth muscle). The anisotropic part is related to the response of the collagen and described by $k_{1,\mathrm{med}}$ and $k_{2,\mathrm{med}}$, where $k_{1,\mathrm{med}} > 0$ is a stress-like parameter and $k_{2,\mathrm{med}} > 0$ is dimensionless. They

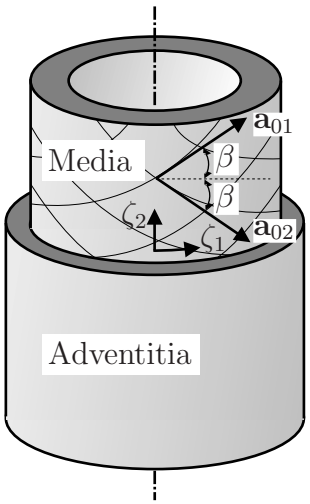

Figure 2.3.: Orientations $\mathbf{a}_{01}$ and $\mathbf{a}_{02}$ of two families of fibers in the media symmetrically disposed with respect to the cylinder axis. The parameter β is the angle between the collagen fiber and the circumferential direction ζ_1.

do not depend on the geometry or fiber angle; those effects are instead introduced through the invariants I_4 and I_6, and are defined as

$$I_1 = \mathbf{C} : \mathbf{I}, \qquad I_4 = \mathbf{C} : \mathbf{A}_1, \qquad I_6 = \mathbf{C} : \mathbf{A}_2. \tag{2.9}$$

The structure tensors $\mathbf{A}_1$ and $\mathbf{A}_2$ are

$$\mathbf{A}_1 = \mathbf{a}_{01} \otimes \mathbf{a}_{01}, \qquad \mathbf{A}_2 = \mathbf{a}_{02} \otimes \mathbf{a}_{02}, \tag{2.10}$$

where the column matrices $[\mathbf{a}_{01}] = [\cos\beta,\ \sin\beta,\ 0]^{\mathrm{T}}$ and $[\mathbf{a}_{02}] = [\cos\beta,\ -\sin\beta,\ 0]^{\mathrm{T}}$ collect the components of the unit vectors $\mathbf{a}_{01}$ and $\mathbf{a}_{02}$, respectively, with 2β being the angle between the collagen fibers, as shown in Fig. 2.3. The principal values of the second Piola-Kirchhoff stress that corresponds to the media are calculated as [6],

$$S_a = \frac{1}{\lambda_a}\frac{\partial \Psi_{\mathrm{med}}}{\partial \lambda_a}, \tag{2.11}$$

where the three principal directions are indexed $a = 1,2,3$.

A stress measure that is physically relevant for the aneurysm wall is the co-rotated Cauchy-like stress measure $\sigma^{\star}_{\alpha\beta}$, [6]. The in-plane membrane stress is defined as

$$\sigma^{\star}_{\alpha\beta} = \frac{1}{J^{\star}} U^{\star}_{\alpha\gamma} S^{\star}_{\gamma\delta} U^{\star}_{\delta\beta} = \frac{2}{\lambda_3 J^{\star}} U^{\star}_{\alpha\gamma} \frac{1}{n} \sum_{i=1}^{n} \frac{\partial \Psi_i}{\partial C^{\star}_{\gamma\delta}} U^{\star}_{\delta\beta}, \tag{2.12}$$

where α and β again pertain to the local 2D in-plane reference coordinate system. The deformation tensor $\mathbf{C}^{\star}$ with components $C^{\star}_{\gamma\delta}$ are given as $\mathbf{C}^{\star}(t) = \mathbf{C}_{\mathrm{loc}}(t, t_{\mathrm{dp}} = t - t_{\mathrm{lf}})$,

where $\mathbf{C}^{\star}(t) = \mathbf{U}^{\star 2}(t)$ and $J^{\star}(t) = \det\mathbf{U}^{\star}(t)$. This is the deformation experienced by the 'oldest' and most stretched fibers in the aneurysm wall. The components $S^{\star}_{\gamma\delta}$ are seen as modified second Piola-Kirchhoff stress components that result from a differentiation of the strain-energy function with respect to $C^{\star}_{\gamma\delta}$. In addition, the thickness change of the membrane (due to material growth) is introduced as λ_3, which is defined as the ratio between the current and initial aneurysm wall thickness. This ratio is estimated as

$$\lambda_3 = \frac{1}{n\lambda_1\lambda_2}\sum_{i=1}^{n}\frac{m_i}{m_0}, \tag{2.13}$$

where λ_1 and λ_2 are the total principal in-plane stretches of the membrane, and m_i and m_0 denote the current and reference collagen mass content, respectively. It is important to emphasize that it is the production of new tissue that is described by the entity λ_3 and *not* an actual stretching. Thus, material parameters that need to be supplied are: $\beta_0\mu_c t_{\mathrm{lf}}$, α, λ_{pre}, n, $\phi_1,\ldots,\phi_n$ (adventitia); μ_{M}, $k_{1,\mathrm{med}}$, $k_{2,\mathrm{med}}$ (media).

In the half-closed interval $t \in (-\infty, 0]$, the modeled reference configuration is unloaded which for the adventitia corresponds to a uniform deformation $\mathbf{C} = \mathbf{I}$, where $\mathbf{I}$ is the 2D identity tensor. A uniform deformation in turn corresponds to a constant collagen production rate $\dot{m}_i(t \le 0) = \beta_0$, a constant fiber deformation of $C_{\mathrm{fib}}(t \le 0) = \lambda^2_{\mathrm{pre}}$, and a constant strain energy per unit reference volume, i.e. $\Psi(t \le 0) = \mu_c\beta_0(\lambda^2_{\mathrm{pre}} - 1)^3 t_{\mathrm{lf}}$. At time $t = 0^+$, prescribed boundary conditions are imposed and the aneurysm starts to evolve.

2.3.3. Model specification, numerics

The considered model geometry is according to a healthy human middle cerebral artery [96, 97]: $R_0 = 1.2\,\mathrm{mm}$, $H_{\mathrm{med}} = 0.25\,\mathrm{mm}$, $H_{\mathrm{adv}} = 0.30\,\mu\mathrm{m}$. The size of the damage region, where the media is absent, is characterized by the radius R_{an} set to be $\pi R_0/2$. On the basis of investigations conducted by Monson et al. [96], material stiffness parameters are set to $\mu_{\mathrm{M}} = 0.3\,\mathrm{MPa}$ and $\beta_0\mu_c t_{\mathrm{lf}} = 14\,\mathrm{MPa}$ (in [96] there is a substantial variation in results and the parameters chosen are from test specimens with a relatively low stiffness). The parameters $k_{1,\mathrm{med}}$ and $k_{2,\mathrm{med}}$ are based on material parameters for a carotid artery from a rabbit [98], for which $k^{\mathrm{r}}_{1,\mathrm{med}} = 2.3632\,\mathrm{kPa}$, $k^{\mathrm{r}}_{2,\mathrm{med}} = 0.8393$, $\mu^{\mathrm{r}}_{\mathrm{M}} = 3.0\,\mathrm{kPa}$, where the superscript 'r' stands for 'rabbit'. The non-dimensional parameter is taken to be the same for a human middle cerebral artery as for the rabbit ($k_{2,\mathrm{med}} = k^{\mathrm{r}}_{2,\mathrm{med}}$), whereas $k_{1,\mathrm{med}}$ for a human cerebral artery is estimated by assuming that the relation

$$\frac{k_{1,\mathrm{med}}}{\mu_{\mathrm{M}}} \approx \frac{k^{\mathrm{r}}_{1,\mathrm{med}}}{\mu^{\mathrm{r}}_{\mathrm{M}}} \tag{2.14}$$

holds, leading to the estimation $k_{1,\mathrm{med}} = 0.24$ MPa. The length of the (quarter) model is $L = 8R_0$, which is considered to be sufficient in order for the ends of the artery not to have any influence on the stress distribution in the aneurysm wall.

The stability properties of the aneurysm model were investigated by Kroon and Holzapfel [20]. It was found that the stabilization of the evolving aneurysmal wall was drastically increased when the parameter α was in the range $1.5 < \alpha < 2$. Therefore, in the present study α is set to 1.7, as most aneurysms do grow in a stabilizing manner. It was also found that the pre-stretching of fibers in the aneurysm wall λ_{pre} should be set to a relatively low value when compared to the *in situ* stretch of arteries. Hence, the pre-stretch is, therefore, set to $\lambda_{\text{pre}} = 1.02$. The influence of the number of layers n in the media was also investigated by Kroon and Holzapfel [20, 87], and it was found that as long as $n \geq 4$, the number of layers does not influence the model behavior to a large degree. Hence, the number of layers n is, therefore, set to $n = 8$.

The internal pressure p is set to 7 kPa which is in accordance to the internal pressure for human carotid arteries [99]. The axial *in situ* stretch of human arteries depends on the location and is in the range 1.0-1.5 [100, 101]. An *in situ* mean stretch for cerebral arteries of 1.31 was found by Monson et al. [102]. Three axial stretches are investigated, namely $\lambda_{\text{L}} = 1.0$, $\lambda_{\text{L}} = 1.2$ and $\lambda_{\text{L}} = 1.4$.

The open source finite element analysis program FEAP [8] is used to analyze the problem, and the growth model of the aneurysm was implemented as a user membrane element. Three different finite element meshes are used in the study pertaining to the different axial stretches. The resulting mesh sizes are 13 492, 13 608, and 13 886 finite elements. Collapsed, 4-node, bi-linear, membrane elements are used to model the adventitia which includes the developing aneurysm wall, and 4-node, tri-linear, tetrahedral solid elements are used for the media. On the surfaces B_1,B_2, B_3, surface pressure elements are used to impose the pressure p which acts on the deformed configuration. In the region of the aneurysmal expansion, the mesh is refined and the elements there have a characteristic size of $\pi R_0/80$ which is sufficient to obtain converging results. In the solution scheme, a time-independent procedure calculating the steady state solution directly, is used.

2.4. Numerical Results

In the present numerical study we investigate the influence of the medial collagen organization, i.e. the fiber angle β, and the axial *in situ* stretch λ_{L} of the artery on the growth of the saccular cerebral aneurysm.

2.4.1. Influence of medial collagen organization

In Fig. 2.4 the distributions of the maximum principal Cauchy stress σ_1^* are displayed. Solutions are shown for the cases with $\beta = 0^\circ$, 5°, 10° (Figs 2.4(a)–(c)), and, as a reference, the solution with no medial collagen fibers is also included (Fig. 2.4(d)). The axial stretch is $\lambda_{\text{L}} = 1.2$. For all cases the stress distribution varies smoothly over the aneurysm surface with a peak value at the fundus. When fibers are included in the media, the peak value is lower when compared to a model without fibers. For an axial stretch of $\lambda_{\text{L}} = 1.2$ and $\beta = 0^\circ$, the maximum principal stress reaches a peak value of 0.622 MPa (Fig. 2.4 (a)).

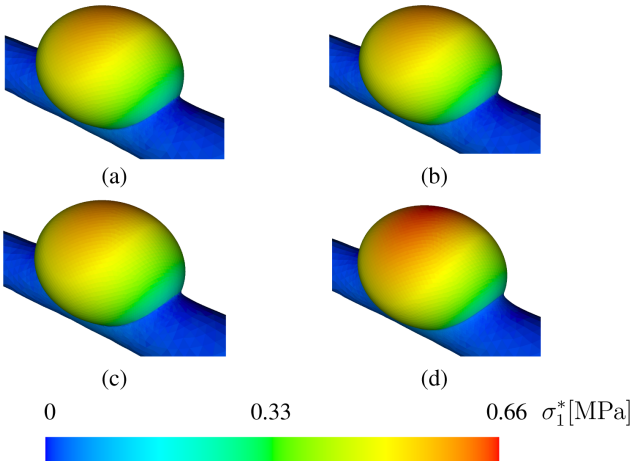

Figure 2.4.: Distributions of maximum principal Cauchy stress σ_1^* (axial *in situ* stretch $\lambda_L = 1.2$). The fiber angle of the medial collagen varies according to: (a) $\beta = 0°$; (b) $5°$; (c) $10°$; in (d) no collagen fibers are included in the media, and the related aneurysm size is noticeably larger. Including collagen fibers in the media decreases the peak stress of 7.2%. The peak values are at the fundus.

When the fiber angle in the media is increased to $5°$ and $10°$, the maximum principal stress becomes 0.624 MPa for both cases (Figs 2.4 (b),(c)). This is a very small change when compared to the model without medial fibers, where the maximum principal stress is 0.670 MPa (Fig. 2.4 (d)). Thus, including collagen fibers in the media decreases the peak stress of 7.2% compared to the solution without medial fibers. The size of the aneurysm does not differ much between the cases with fibers (Figs 2.4(a)–(c)), but the aneurysm without medial fibers is noticeably larger.

The corresponding distributions of the steady-state thickness change λ_3, i.e. according to Eq. (2.13), are shown in Fig. 2.5. For the three cases $\beta = 0°; 5°; 10°$ the largest thickness increase is 4.34 and occurs at the fundus (Figs 2.5 (a)–(c)). This value is lower when compared to the case with no fibers in the media (Fig. 2.5 (d)) which has a thickness increase of 4.56 at the fundus.

The maximum in-plane Cauchy shear stress τ for the four investigated cases is plotted in Fig. 2.6. The maximum values are 0.093 MPa, 0.094 MPa and 0.095 MPa for the cases with fibers in the media, as shown in Figs 2.6 (a)–(c), respectively. These values are all lower compared to the case with no fibers in the media, which experienced a maximum shear stress of 0.102 MPa (Fig. 2.6 (d)). The peak values do not appear at the fundus but are located close to the neck at the long side of the aneurysm, as can be seen in Fig. 2.6. The largest shear stress are about 15% of the largest maximum principal stresses. The minimum values are located between the fundus and the neck in the plane $X_2 = 0$. It may be noted that the maximum shear stress quantifies the difference between the two in-plane principal stresses. Thus, we may conclude that the maximum difference between

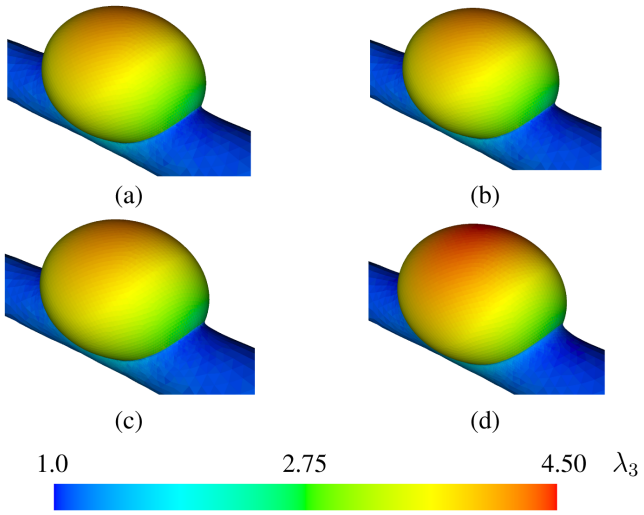

Figure 2.5.: Distributions of the thickness increase λ_3 (axial *in situ* stretch $\lambda_L = 1.2$), i.e. according to Eq. (2.13). The fiber angle varies: (a) $\beta = 0°$; (b) 5°; (c) 10°; in (d) no fibers are included in the media. The largest thickness increases occur at the fundus; 4.34 for (a)–(c) and 4.56 for (d).

the principal stresses is about 0.2 MPa and occurs close to the neck of the aneurysm. We emphasize that the stress distributions in Fig. 2.6 are symmetric with respect to the X_1-X_3-plane, even though this is not obvious from Fig. 2.6.

2.4.2. Influence of axial in situ stretch

In this part of the study a constant fiber angle $\beta = 0°$ is used, and solutions for three different axial stretches $\lambda_L = 1.0$, 1.2 and 1.4 are compared. For the different axial stretches, the maximum principal Cauchy stress σ_1^* (again occurring at the fundus) is found to be 0.580, 0.622, 0.626 MPa, as shown in the Figs 2.7 (a)–(c), respectively. The difference in the resulting steady-state geometry of these three cases are clearly shown in Fig. 2.7. No axial stretch ($\lambda_L = 1.0$) results in a more spherical shape (Fig. 2.7(a)), whereas an axial stretch of $\lambda_L = 1.4$ results in a more elliptic shape (Fig. 2.7(c)).

The thickness increases λ_3 for the cases with the three axial stretches reach values of 4.07, 4.34 and 4.55 at the fundus, see Figs 2.8 (a)–(c), respectively. However, the maximum thickness increase is not always at the fundus. For $\lambda_L = 1.4$, for example, the maximum value of λ_3 is not located in the aneurysm but rather in the intact artery close to the neck of the aneurysm. The value of the maximum thickness increase in that point is 5.64.

The resulting maximum in-plane Cauchy shear stress τ reaches the maximum values 0.115, 0.0933, 0.116 MPa, respectively (Figs 2.9 (a)–(c)). As can be seen, the maximum shear stress is lowest for $\lambda_L = 1.2$, whereas the peak values are almost identical for $\lambda_L = 1.0$ and $\lambda_L = 1.4$. The location of the maximum value also changes when altering the stretch. The

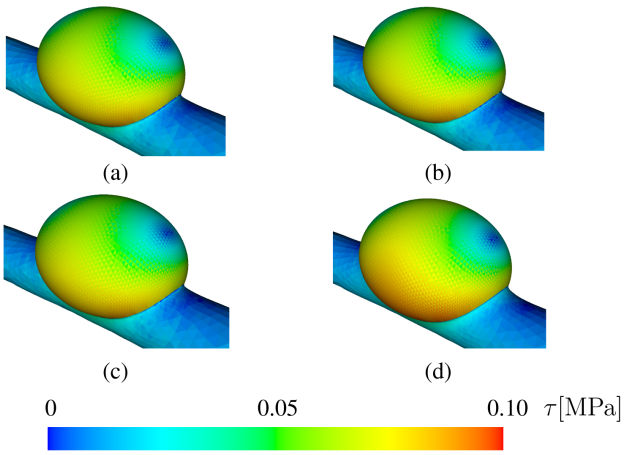

Figure 2.6.: Distributions of maximum in-plane Cauchy shear stress τ (axial *in situ* stretch $\lambda_L = 1.2$). The fiber angle varies: (a) $\beta = 0°$; (b) 5°; (c) 10°; in (d) no fibers are included in the media. The peak values are located close to the neck at the long side of the aneurysm (0.093, 0.094, 0.095 MPa for (a)–(c) and 0.102 MPa for (d)). The minimum values are located between the fundus and the neck in the plane $X_2 = 0$.

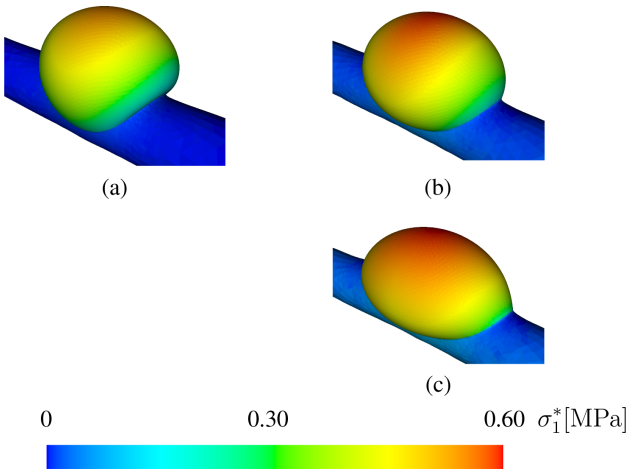

Figure 2.7.: Distributions of maximum principal Cauchy stress σ_1^* (fiber angle $\beta = 0°$). The axial stretch varies: (a) $\lambda_L = 1.0$; (b) 1.2; (c) 1.4. The peak values are at the fundus. No axial stretch results in a more spherical shape, whereas an axial stretch of 1.4 results in a more elliptic shape.

location of the maximum values for $\lambda_L = 1.0$ and 1.2 is at the long side of the aneurysm, whereas it is on the short side for $\lambda_L = 1.4$, see Fig. 2.9.

2.5. Discussion

In the process of saccular cerebral aneurysm growth several stages can be identified. During the initial stage, wall shear stress, which are induced by the blood flow, act on the intima

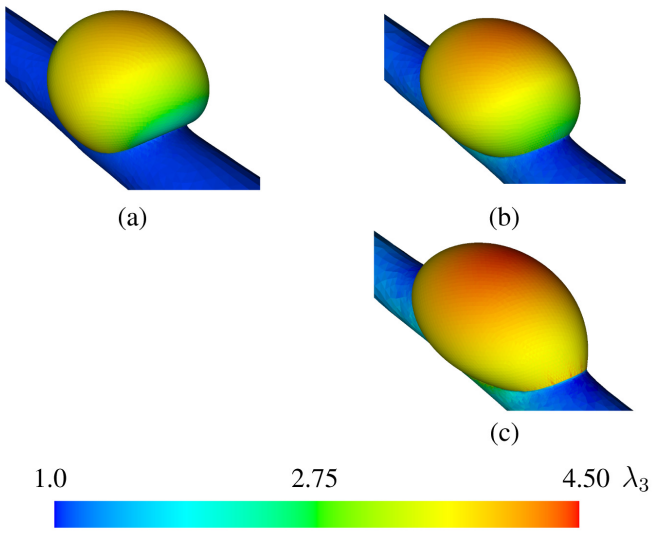

Figure 2.8.: Distributions of the thickness increase λ_3 (fiber angle $\beta = 0°$). The axial stretch varies: (a) $\lambda_L = 1.0$; (b) 1.2; (c) 1.4. The increase in λ_3 is not always at the fundus. For $\lambda_L = 1.4$ the maximum value of λ_3 is located in the intact artery close to the neck of the aneurysm, with value 5.64.

and may cause degradation of the media and the internal elastic lamina of the artery. As a result, an increased load has to be carried by the adventitia, which is triggered to dilate. If this process is continued, this dilatation may develop into a saccular aneurysm. In the present aneurysm model, processes that relate to fluid dynamics and mechanochemical processes leading to aneurysm growth initiation are not considered explicitly. Instead, an initial and instant loss of the media and the internal elastic lamina is assumed to occur initiating aneurysm growth. In previous works, the proposed aneurysm growth model has been assessed for axisymmetric growth [20] and also for a more realistic 3D setting in the form of a human middle cerebral artery [87]. In the present paper the saccular aneurysm growth model is extended to include collagen fibers in the media of the parent artery surrounding the aneurysm. A parameter study is performed to investigate the influence of collagen fiber organization in the media and axial *in situ* stretch of the artery on the on aneurysm growth. The driving mechanism for the aneurysm growth is the continuous turnover of collagen fibers in the aneurysm wall. The model response is quantified in terms of the principal Cauchy stresses, the thickness increase of the aneurysm wall and the maximum in-plane Cauchy shear stresses. The model parameters are chosen on the basis of experiments and previous numerical results.

By introducing fibers in the media, the size of the developed aneurysm decreased noticeably. However, in terms of aneurysm size, there was no significant difference between the models with different medial fiber angles. It was also noted that the maximum stress, appearing at the fundus of the aneurysm, decreased by introducing fibers in the media. Fibers add stiffness to the vessel and, thereby, reduce the compliance at the boundary be-

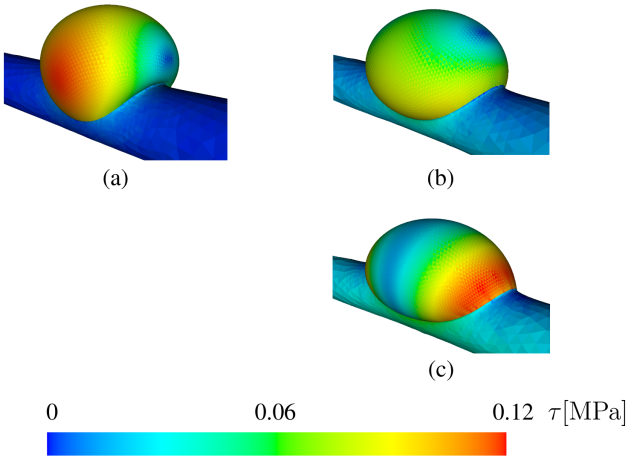

Figure 2.9.: Distributions of maximum in-plane Cauchy shear stress τ (fiber angle $\beta = 0°$). The axial stretch varies: (a) $\lambda_L = 1.0$; (b) 1.2; (c) 1.4. The maximum value is lowest for $\lambda_L = 1.2$, whereas the peak values are almost identical for $\lambda_L = 1.0$ and 1.4. The location of the maximum values for $\lambda_L = 1.0$ and 1.2 is at the long side of the aneurysm and on the short side for 1.4.

tween the aneurysm and the artery. With a decreased boundary compliance, the resulting aneurysm size becomes smaller and the aneurysm wall stresses decrease. By increasing the fiber angle β the peak value of the maximum principal Cauchy stress $\sigma_1^\star$ increases somewhat. When β increases, the compliance in the circumferential direction of the artery increases, and this results in a slightly wider aneurysm neck. This may in turn explain why the aneurysm wall stress increases with increasing β.

The most drastic change in the aneurysm geometry is, however, seen by altering the axial stretch imposed on the model. The case with no axial stretch ($\lambda_L = 1.0$) produced a berry-shaped aneurysm with a very sharp neck. For the largest stretch investigated ($\lambda_L = 1.4$), the neck was much less pronounced, and the aneurysm clearly became less berry-shaped. Due to the loss of media in the aneurysm region, there is a localization in the remaining media below the aneurysm. The reference geometry and the modeling method correspond to an instant loss of media in a circular damage region. The size of this damage region is defined by the radius R_{an} which is independent of the axial stretch. However, it should be noted that the level of applied axial stretch will still affect how strong the localization becomes in the remaining media below the aneurysm. The character of this localization will strongly affect the shape of the aneurysm, where a higher axial stretch tends to enhance the localization and make the aneurysm more ellipsoidal.

The axial *in situ* stretch of arteries is known to vary, and the values used here are in accordance with clinical observations [102]; $\lambda_L = 1.31$ has been observed for cerebral arteries. The axial *in situ* stretch had a stronger influence on the maximum principal stress in the aneurysm than the fiber angle; higher stretches resulted in higher stresses. The surface area of the aneurysm on which the internal pressure acts is larger for larger axial stretches,

which explains the higher stresses. The stress, however, is also influenced by the thickness increase of the aneurysmal wall, which is larger for higher axial stretches and thereby reduces the stress to some extent. The strength of cerebral aneurysmal tissue has been experimentally estimated to 0.5-2.0 MPa [103, 104]. The peak stresses in our model for the various axial stretches and the medial collagen fiber angles are 0.58-0.63 MPa, and are of the same order.

Adding fibers in the media reduced the maximum thickness at the fundus from 137 μm ($\lambda_3 = 4.56$) to 130 μm ($\lambda_3 = 4.34$) for $\lambda_L = 1.2$. As the thickness increase is governed by the total stretch of the material (with respect to the reference configuration) and as the inclusion of medial fibers reduced the aneurysmal stretching by stiffening the borders between aneurysm and artery, this is an expected outcome. Changing the fiber angle in the media resulted in a minimal increase in stretch and, thereby, a minimal increase in thickness of the adventitia, whereas increasing the axial stretch of the artery resulted in relatively large stretches in the aneurysm, leading to increasing thickness. For the lowest axial stretch considered ($\lambda_L = 1.0$), the thickness was 122 μm, and for the largest ($\lambda_L = 1.4$) 137 μm. The thickness increases are in the range of experimentally determined values [104], where the thickness of larger cerebral aneurysms is between 116 and 212 μm.

In summary, saccular cerebral aneurysm growth has been modeled. In particular, the influences of the medial collagen organization (fiber angles) and the axial *in situ* stretch on the aneurysm growth have been investigated. The previously proposed aneurysm model was extended to include fibers in the media of the parent artery surrounding the aneurysm, and a parameter study was performed by changing the collagen fiber angle in the media and the axial *in situ* stretch of the artery. When collagen fibers were included in the media, the peak stress in the aneurysm was reduced by 7.2% (compared to a case without fibers). Increasing axial stretch led to increasing steady-state aneurysm wall stresses. The numerical results predicted by the model are in good agreement with experimental data documented in the literature. The present study indicates that improved estimations of the mechanical properties of the medial collagen and, in particular, of the axial *in situ* stretches of arteries are necessary for a refined prediction of aneurysm growth.

Acknowledgement

Financial support for this research was partly provided by @neurIST, an Integrated EU Project (Call Identifier FP6-2004-IST-4). This support is gratefully acknowledged.

3. TENSORS NEEDED FOR FINITE ELEMENT IMPLEMENTATION OF AN INVARIANT BASED CONSTITUTIVE MODEL FOR PASSIVE MYOCARDIUM

Abstract In this paper constituents needed for implementation of a new structurally based constitutive law describing the behavior of passive myocardium is shown. The model aims at capturing the orthotropic behavior of passive myocardium with respect to its three orthogonal fiber, sheet and sheet-normal directions. Both the structure of the material model, in particular the separation of invariants into separate terms, and the coordinate frame independence caused by the invariants, leads to stress and elasticity tensors which may be implemented in a finite element software with relative ease when compared, for example, a material model based on Green-Lagrange strain components. The analytical Cauchy and second Piola-Kirchhoff stress expressions of the model are also shown for uniaxial, biaxial and simple shear deformation modes. The model is fitted against experimental data of passive myocardium and a near perfect fit is shown. The sensitivity of the material parameters retrieved from the fit is examined where parameter b_s is found to be the most sensitive for the fit against a simple shear test. In addition, a comparison is made between the newly proposed invariant based model and a commonly used Green-Lagrange strain based model. Using material parameters retrieved when both models was fitted against a simple shear mode experiment, the newly proposed model was better suited to predict the stress in myocardium for a biaxial deformation when compared to experimental data. The finite element implementation was tested on a model with an ellipsoidal geometry which is a commonly used geometrical model to represent the left ventricle of the heart. In the geometrical model, the fiber, sheet and sheet-normal directions were included and for a simple case with internal pressure, a gradient of the fiber stress component is evident through the wall thickness which suggests that also residual stresses may need to be included in a future model describing the heart. It is also shown that the gradient is steeper if all fibers are all aligned in the circumferential direction of the ellipsoid which also results in a much larger deformation at the apex.

3.1. Introduction

Heart failure is the major cause of morbidity and mortality in the industrialized world. A large percentage of patients suffers from dilated cardiomyopathy and many of these individuals develop left ventricular dyssynchrony where the electrical activation sequence of the heart, which orchestrates mechanical contraction, is disturbed. This entails a less

synchronized and thus less efficient mechanical contraction of the ventricles which impairs the heart's ability to drive blood through the circulatory system.

Inquiries into these regulatory mechanisms by experimental means are hampered by the inability of currently available methodology to simultaneously record electrical and mechanical activity in 3D with sufficient spatio-temporal resolution. Further, the multi-scale nature of the phenomenon exacerbates the reintegration of disparate experimental data into comprehensive models of cardiac electromechanics. For instance, the regulation of active tension generation occurs at cellular and subcellular spatial scales, however, important regulatory input is provided via mechanical deformation of the myocardial walls, which is governed by spatial scales at the tissue and organ level.

Computational modeling almost naturally suggests itself as a complementary approach to tackle these multi-scale challenges by facilitating the explicit representation of interactions across multiple temporal and spatial scales within a single comprehensive computational model. Such biophysically detailed multiscale models of ventricular electromechanics may play a pivotal role in the quest of conceiving better therapeutical strategies by enabling basic research to fully elucidate underlying mechanisms with high spatio-temporal resolution. Although the cardiac modeling community was striving for developing such modeling tools since more than three decades [105], the methodological complexities involved and the lack of adequate computational resources prevented major progress for many years.

Over the past few years, multi-scale computational models of ventricular electrical activity have been routinely used in numerous studies [106–108] where models have been discretized at a paracellular resolution [109, 110] using highly detailed representations of cellular dynamics with integrated models of excitation-contraction coupling and mitochondrial energetics [111]. In comparison, a fairly small number of studies employed organ level models of ventricular cardiac mechanics, and, even less frequent, models of ventricular electromechanics. In most of the cardiac organ level mechanics studies researchers resorted to simplifications by using electrical-only models to predict effects on mechanical performance [112], by employing simplified models of cellular dynamics [75, 113] and active tension [114], by simplified representation of organ geometry [113, 115] and by neglecting orthotropic properties of tissue structure [75, 113] and, finally, by largely neglecting the impact of pathological alterations onto ventricular electromechanics, although execptions do exist [116]. Evidence of the progress made in the field of computational modeling is the introduction of models into clinical application as an additional modality which supports clinical decisions in treating ischemic heart disease [117], the assessment of effects of heart surgery [118] and ventricular pacing [114, 116, 119]. Undoubtedly, despite the computational complexity of the current state of the art, current models are still in their infancy and, clearly, many of the physiological mechanisms which are aimed at to be modeled need to be further investigated. Nonetheless, these studies provide a first glimpse

into future applications and nicely highlight the high potential and the predictive power of biophysically detailed multi-scale models of ventricular electromechanics.

From an organ level modeling point of view, the constitutive laws which describe the mechanical properties of the myocardial wall are of pivotal importance for quantitatively realistic predictions of deformation feedback which serves as input to cellular regulatory loops. In this context the fibrous and laminar arrangement of intracellular and extracellular matrices composing the myocardial wall is of particular importance. There is accumulating evidence that rotationally isotropic material descriptions overly simplify biophysical reality. This notion is strongly supported by the observation that such models fail to quantitatively reproduce myocardial wall thickening during systole [120]. Further, it is becoming increasingly more apparent that local variations in material properties are an imporant factor in itself to understand the fundamental mechanisms underlying ventricular mechanics. For instance, a recent experimental study demonstrated that myocardial wall thickening is highly heterogeneous despite the absence of any heterogeneity in systolic fiber shortening [121]. These findings support the hypothesis put forward in earlier studies by numerous authors [120, 122, 123] that rearrangement of laminar sheets of fibers, and thus, the presence of tissue orthotropy, is a key contributor which amplifies systolic fiber shortening into adequate myocardial wall thickening. Finally, the constitutive descriptions are not only spatially varying throughout the heart, they are also temporally varying due to pathologies such as myocardial infarction [124] or dilated cardiomyopathy [125]. Such events clearly alter passive mechanical tissue properties significantly as a disease progresses.

It is expected that current advances made in computational modeling and the advent of the next generation petaflops supercomputers will help to leverage a new generation of electromechanically coupled multi-scale models of the ventricles which, eventually, enable novel investigations of cardiac function at an unprecedented level of physiological detail. At the very core of coupling organ level mechanics to cellular signaling is a mechancally sound representation of the constitutive material parameters of the myocardium which allow accurate prediction of stresses throughout the myocardial wall. The present study describes a numerical realization of a recently published novel constitutive law for the myocardial wall which is a further important step towards predictive computational models of ventricular electromechanics.

Passive myocardium has been found to be a nearly incompressible, pseudo-elastic and anisotropic material [126], with a hyperelastic stress response often modeled by a strain-energy function [47]. The myocytes in the myocardium of the left ventricle of the heart is in general organized in a right-handed helical pathway from the endocoardium towards the midwall, and a left-handed helical pathway from the midwall towards the epicardium, [22–24]. Furthermore, the myocytes are bundled and form layers with a direction that vary through the thickness of the ventricle wall, [24, 25, 27, 28]. This organization of the myocyte, in both a fiber and sheet direction, is responsible for the twisting motion of the

heart during systole [127]. Orthotropic models are available that have shown a good fit against experimental data. However, as the material parameters are coupled in many of those models, for instance the model proposed by Costa et al. [47], it is often difficult to find a clear physical interpretation what those material parameters relate to. For models with uncoupled material parameters, as for instance the Pole-Zero model proposed by Hunter et al. [128], the problem is the total number of parameters, in this case 18. Such a high number of material parameters may lead to non-uniqueness when fitting the model to experimental data.

For a recent review of both transversally isotropic and orthotropic constitutive models describing the passive behavior of myocardium, see Holzapfel and Ogden [42], where a structurally based constitutive model for myocardium was introduced that includes the orthotropic structure of the myocardium and for which the material parameters have a clear physical interpretation. In this paper the full expression of the constituents needed for implementation of this model in a finite element framework is shown. Also, analytical expressions needed for fitting the model to experimental data as well as the fit against two available experiments is shown. Further, the model is compared to the often used constitutive model showed by Costa et al. [47], and an example is made calculating the stress response when applying internal pressure on an ellipsoidal geometry which represents the left ventricle of the heart.

3.2. Material Model

As described earlier, myocardium, the material in the left ventricle midwall, may be characterized by a strain-energy function, Ψ, where the deformation has a hyperelastic stress response. In this section the volumetric and isochoric expressions of the newly proposed model for left ventricular myocardium [42] is shown together with the resulting stress and elasticity tensors in both the Lagrangian and Eulerian description.

3.2.1. Volume-preserving continuum mechanical framework

We introduce the deformation gradient $\mathbf{F}$ and its multiplicative decomposition into a volume-changing part $J^{1/3}\mathbf{I}$ and a volume-preserving part $\overline{\mathbf{F}}$ so that $\mathbf{F} = J^{1/3}\overline{\mathbf{F}}$, where $J = \det\mathbf{F} > 0$ is the volume ratio, and $\mathbf{I}$ is the second-order unit tensor (see, for example, [6]). The right and left Cauchy-Green tensors follow as $\mathbf{C} = J^{2/3}\overline{\mathbf{C}}$ and $\mathbf{b} = J^{2/3}\overline{\mathbf{b}}$, respectively, where $\overline{\mathbf{C}} = \overline{\mathbf{F}}^{\mathrm{T}}\overline{\mathbf{F}}$ and $\overline{\mathbf{b}} = \overline{\mathbf{F}}\overline{\mathbf{F}}^{\mathrm{T}}$ denote the modified tensor quantities. Additionally we are introducing three modified invariants as

$$\bar{I}_1 = \mathrm{Tr}\overline{\mathbf{C}}, \quad \bar{I}_{4\mathrm{a}} = \mathbf{a}_0 \cdot (\overline{\mathbf{C}}\mathbf{a}_0), \quad \bar{I}_{8\mathrm{ab}} = \mathbf{a}_0 \cdot (\overline{\mathbf{C}}\mathbf{b}_0) = \mathbf{b}_0 \cdot (\overline{\mathbf{C}}\mathbf{a}_0), \tag{3.1}$$

where $\mathbf{a}_0$ and $\mathbf{b}_0$ are unit vectors along the undeformed directions. The related derivatives of $\bar{I}_1$, $\bar{I}_{4\mathrm{a}}$ and $\bar{I}_{8\mathrm{ab}}$ with respect to $\overline{\mathbf{C}}$ are given by

$$\frac{\partial \bar{I}_1}{\partial \overline{\mathbf{C}}} = \mathbf{I}, \quad \frac{\partial \bar{I}_{4\mathrm{a}}}{\partial \overline{\mathbf{C}}} = \mathbf{a}_0 \otimes \mathbf{a}_0, \quad \frac{\partial \bar{I}_{8\mathrm{ab}}}{\partial \overline{\mathbf{C}}} = \frac{1}{2}(\mathbf{a}_0 \otimes \mathbf{b}_0 + \mathbf{b}_0 \otimes \mathbf{a}_0), \tag{3.2}$$

where the symbol $\otimes$ denotes the (dyadic) tensor product. The three invariants I_1, $I_{4\mathrm{a}}$ and $I_{8\mathrm{ab}}$ are defined in an analogous way to (3.1) and read $I_1 = \mathrm{Tr}\mathbf{C}$, $I_{4\mathrm{a}} = \mathbf{a}_0 \cdot (\mathbf{C}\mathbf{a}_0)$ and $I_{8\mathrm{ab}} = \mathbf{a}_0 \cdot (\mathbf{C}\mathbf{b}_0) = \mathbf{b}_0 \cdot (\mathbf{C}\mathbf{a}_0)$ so that the relations

$$\bar{I}_1 = J^{-2/3} I_1, \quad \bar{I}_{4\mathrm{a}} = J^{-2/3} I_{4\mathrm{a}}, \quad \bar{I}_{8\mathrm{ab}} = J^{-2/3} I_{8\mathrm{ab}} \tag{3.3}$$

hold.

3.2.2. Strain-energy function for the passive mechanical response of the myocardium

Myocardial tissue is an orthotropic material with fiber, sheet and sheet-normal directions denoted by the direction vectors $\mathbf{f}_0$, $\mathbf{s}_0$ and $\mathbf{n}_0$, respectively, as shown in Fig. 3.1.

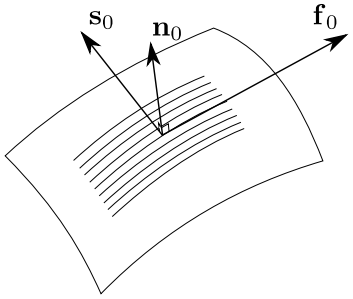

Figure 3.1.: Orthotropic myocardial tissue showing the vectors in the fiber, sheet and sheet-normal directions ($\mathbf{f}_0$, $\mathbf{s}_0$, $\mathbf{n}_0$).

We postulate here a unique *decoupled* representation of the strain-energy function Ψ (per unit reference volume). It is based on the kinematic assumption as introduced above, and is of the specific form

$$\Psi = \Psi_{\mathrm{vol}}(J) + \Psi_{\mathrm{iso}}(\bar{I}_1, \bar{I}_{4\mathrm{f}}, \bar{I}_{4\mathrm{s}}, \bar{I}_{8\mathrm{fs}}), \tag{3.4}$$

where Ψ_{vol} and Ψ_{iso} are given scalar-valued functions of J and the modified invariants $\bar{I}_1, \bar{I}_{4\mathrm{f}}, \bar{I}_{4\mathrm{s}}, \bar{I}_{8\mathrm{fs}}$, respectively. Note that these invariants are according to (3.1) where $\mathbf{a}_0$ and $\mathbf{b}_0$ are replaced by $\mathbf{f}_0$ and $\mathbf{s}_0$, as shown in Fig. 3.1. The two scalar-valued functions then describe the volumetric and isochoric elastic responses of the material.

The function Ψ_{vol} is treated as a penalty function enforcing the incompressibility constraint $J = 1$. We use here

$$\Psi_{\mathrm{vol}} = \frac{\mu_{\mathrm{K}}}{2}(J-1)^2, \tag{3.5}$$

where μ_{K} is the bulk modulus, which serves as a user-specified penalty parameter. With increasing μ_{K} the violation of the constraint is reduced. If the restriction on the value $\mu_{\mathrm{K}} \to \infty$ is taken, the constraint condition is exactly enforced, and then (3.4) represents a

functional for an incompressible material with $J = 1$. The specification of the strain-energy function Ψ_{iso} is based on the formulation of Holzapfel and Ogden [42], and has the form

$$\Psi_{\text{iso}} = \frac{a}{2b}\{\exp[b(\bar{I}_1 - 3)] - 1\} + \sum_{i=\text{f,s}} \frac{a_i}{2b_i}\{\exp[b_i(\bar{I}_{4i} - 1)^2] - 1\} + \frac{a_{\text{fs}}}{2b_{\text{fs}}}[\exp(b_{\text{fs}}\bar{I}_{8\,\text{fs}}^2) - 1]. \tag{3.6}$$

As discussed in [42], the eight material parameters a, b, a_{f}, b_{f}, a_{s}, b_{s}, a_{fs} and b_{fs} are all positive and the terms containing the directionally dependent invariants are included in Eq. (3.6) only if $\bar{I}_{4\,\text{f}} > 1$ and $\bar{I}_{4\,\text{s}} > 1$ is fulfilled.

3.2.3. Stress tensors

According to the form of the strain-energy function (3.4) the second Piola-Kirchhoff stress tensor $\mathbf{S} = 2\partial\Psi/\partial\mathbf{C}$ is also separated into a purely volumetric part ($\mathbf{S}_{\text{vol}}$) and a purely isochoric ($\mathbf{S}_{\text{iso}}$) part, i.e. $\mathbf{S} = \mathbf{S}_{\text{vol}} + \mathbf{S}_{\text{iso}}$. The volumetric part is

$$\mathbf{S}_{\text{vol}} = J p_{\text{h}} \mathbf{C}^{-1} \qquad \text{where} \qquad p_{\text{h}} = \frac{\mathrm{d}\Psi_{\text{vol}}(J)}{\mathrm{d}J} = \mu_{\text{K}}(J - 1) \tag{3.7}$$

is the hydrostatic pressure, and the function (3.5) has been introduced. From (3.6), by using the chain rule, the isochoric second Piola-Kirchhoff stress tensor takes on the form

$$\mathbf{S}_{\text{iso}} = 2\frac{\partial\Psi_{\text{iso}}}{\partial\mathbf{C}} = 2\left(\overline{\psi}_1\frac{\partial\bar{I}_1}{\partial\mathbf{C}} + \overline{\psi}_{4\,\text{f}}\frac{\partial\bar{I}_{4\,\text{f}}}{\partial\mathbf{C}} + \overline{\psi}_{4\,\text{s}}\frac{\partial\bar{I}_{4\,\text{s}}}{\partial\mathbf{C}} + \overline{\psi}_{8\,\text{fs}}\frac{\partial\bar{I}_{8\,\text{fs}}}{\partial\mathbf{C}}\right), \tag{3.8}$$

where we have introduced the definitions

$$\overline{\psi}_1 = \frac{\partial\Psi_{\text{iso}}}{\partial\bar{I}_1} = \frac{a}{2}\exp[b(\bar{I}_1 - 3)], \tag{3.9}$$

$$\overline{\psi}_{4i} = \frac{\partial\Psi_{\text{iso}}}{\partial\bar{I}_{4i}} = a_i(\bar{I}_{4i} - 1)\exp[b_i(\bar{I}_{4i} - 1)^2], \quad i = \text{f,s}, \tag{3.10}$$

$$\overline{\psi}_{8\,\text{fs}} = \frac{\partial\Psi_{\text{iso}}}{\partial\bar{I}_{8\,\text{fs}}} = a_{\text{fs}}\bar{I}_{8\,\text{fs}}\exp(b_{\text{fs}}\bar{I}_{8\,\text{fs}}^2), \tag{3.11}$$

which are the derivatives of (3.6) with respect to the four modified invariants $\bar{I}_1$, $\bar{I}_{4\,\text{f}}$, $\bar{I}_{4\,\text{s}}$ and $\bar{I}_{8\,\text{fs}}$. For (3.8) we have to specify the derivatives of the modified invariants with respect to $\mathbf{C}$. For the first modified invariant $\bar{I}_1 = J^{-2/3}\text{Tr}\mathbf{C}$ we may write by using the product rule

$$\frac{\partial\bar{I}_1}{\partial\mathbf{C}} = -\frac{1}{3}J^{-2/3}\mathbf{C}^{-1}\text{Tr}\mathbf{C} + J^{-2/3}\mathbf{I} = J^{-2/3}[\mathbf{I} - \frac{1}{3}(\text{Tr}\mathbf{C})\mathbf{C}^{-1}] = J^{-2/3}\text{Dev}\mathbf{I}, \tag{3.12}$$

where $\text{Dev}(\bullet) = (\bullet) - (1/3)[(\bullet) : \mathbf{C}]\mathbf{C}^{-1}$ is the deviatoric operator in the Lagrangian description so that $\text{Dev}(\partial\Psi_{\text{iso}}/\partial\overline{\mathbf{C}}) : \mathbf{C} = 0$. Next we need to specify the term $\partial\bar{I}_{4\,\text{f}}/\partial\mathbf{C}$. By

using $\bar{I}_{4\mathrm{f}} = J^{-2/3} I_{4\mathrm{f}}$ and by taking into consideration that $\partial I_{4\mathrm{f}}/\partial \mathbf{C} = \mathbf{f}_0 \otimes \mathbf{f}_0$ we get

$$\begin{aligned}\frac{\partial \bar{I}_{4\mathrm{f}}}{\partial \mathbf{C}} &= J^{-2/3}\frac{\partial I_{4\mathrm{f}}}{\partial \mathbf{C}} + I_{4\mathrm{f}}\frac{\partial J^{-2/3}}{\partial \mathbf{C}} = J^{-2/3}\mathbf{f}_0 \otimes \mathbf{f}_0 + I_{4\mathrm{f}}(-\frac{1}{3}J^{-2/3}\mathbf{C}^{-1}) \\ &= J^{-2/3}(\mathbf{f}_0 \otimes \mathbf{f}_0 - \frac{1}{3}I_{4\mathrm{f}}\mathbf{C}^{-1}) = J^{-2/3}(\mathbf{f}_0 \otimes \mathbf{f}_0 - \frac{1}{3}\bar{I}_{4\mathrm{f}}\overline{\mathbf{C}}^{-1}) \\ &= J^{-2/3}\mathrm{Dev}(\mathbf{f}_0 \otimes \mathbf{f}_0). \end{aligned} \tag{3.13}$$

In an analogous manner we may write

$$\frac{\partial \bar{I}_{4\mathrm{s}}}{\partial \mathbf{C}} = J^{-2/3}\mathrm{Dev}(\mathbf{s}_0 \otimes \mathbf{s}_0), \quad \frac{\partial \bar{I}_{8\mathrm{fs}}}{\partial \mathbf{C}} = \frac{1}{2}J^{-2/3}\mathrm{Dev}(\mathbf{f}_0 \otimes \mathbf{s}_0 + \mathbf{s}_0 \otimes \mathbf{f}_0). \tag{3.14}$$

Hence, by substituting (3.12)–(3.14) into (3.8) and by adding $(3.7)_1$ we get the explicit expression for the second Piola-Kirchhoff stress tensor, i.e.

$$\begin{aligned}\mathbf{S} = Jp_{\mathrm{h}}\mathbf{C}^{-1} + 2J^{-2/3}[&\overline{\psi}_1\mathrm{Dev}\mathbf{I} + \overline{\psi}_{4\mathrm{f}}\mathrm{Dev}(\mathbf{f}_0 \otimes \mathbf{f}_0) + \overline{\psi}_{4\mathrm{s}}\mathrm{Dev}(\mathbf{s}_0 \otimes \mathbf{s}_0) \\ &+ \frac{1}{2}\overline{\psi}_{8\mathrm{fs}}\mathrm{Dev}(\mathbf{f}_0 \otimes \mathbf{s}_0 + \mathbf{s}_0 \otimes \mathbf{f}_0)]. \end{aligned} \tag{3.15}$$

In order to get the spatial version of this expression, we need to perform a push-forward operation of the second Piola-Kirchhoff stress tensors to the current configuration which is $\boldsymbol{\sigma} = J^{-1}\mathbf{F}(\mathbf{S}_{\mathrm{vol}} + \mathbf{S}_{\mathrm{iso}})\mathbf{F}^{\mathrm{T}}$. By using (3.15) and $\mathbf{b} = J^{2/3}\overline{\mathbf{b}}$ it is straightforward to get the Cauchy stress tensor $\boldsymbol{\sigma}$ as

$$\begin{aligned}\boldsymbol{\sigma} = p_{\mathrm{h}}\mathbf{I} + 2J^{-1}[&\overline{\psi}_1\,\mathrm{dev}\overline{\mathbf{b}} + \overline{\psi}_{4\mathrm{f}}\,\mathrm{dev}(\bar{\mathbf{f}} \otimes \bar{\mathbf{f}}) + \overline{\psi}_{4\mathrm{s}}\,\mathrm{dev}(\bar{\mathbf{s}} \otimes \bar{\mathbf{s}}) \\ &+ \frac{1}{2}\overline{\psi}_{8\mathrm{fs}}\,\mathrm{dev}(\bar{\mathbf{f}} \otimes \bar{\mathbf{s}} + \bar{\mathbf{s}} \otimes \bar{\mathbf{f}})], \end{aligned} \tag{3.16}$$

where we have introduced the spatial vectors

$$\bar{\mathbf{f}} = \overline{\mathbf{F}}\mathbf{f}_0, \quad \bar{\mathbf{s}} = \overline{\mathbf{F}}\mathbf{s}_0, \tag{3.17}$$

describing the fiber and sheet vectors in teh spatial configuration repsectively and $\mathrm{dev}(\bullet) = (\bullet) - (1/3)[(\bullet) : \mathbf{I}]\mathbf{I}$ is the deviatoric operator in the Eulerian description.

3.2.4. Elasticity tensor in the Lagrangian description

The elasticity tensor in the Lagrangian description is also separated into its volumetric and isochoric parts, i.e.

$$\mathbb{C} = 2\frac{\partial \mathbf{S}}{\partial \mathbf{C}} = \mathbb{C}_{\mathrm{vol}} + \mathbb{C}_{\mathrm{iso}}, \tag{3.18}$$

where the volumetric part may be expressed as

$$\mathbb{C}_{\mathrm{vol}} = 2\frac{\partial (Jp_{\mathrm{h}}\mathbf{C}^{-1})}{\partial \mathbf{C}} = J\tilde{p}_{\mathrm{h}}\mathbf{C}^{-1} \otimes \mathbf{C}^{-1} - 2Jp_{\mathrm{h}}\mathbf{C}^{-1} \odot \mathbf{C}^{-1}, \tag{3.19}$$

with $\tilde{p}_{\mathrm{h}} = p_{\mathrm{h}} + J\mathrm{d}p_{\mathrm{h}}/\mathrm{d}J$ and $\mathbf{C}^{-1} \odot \mathbf{C}^{-1} = -\partial \mathbf{C}^{-1}/\partial \mathbf{C}$ (for details see [6]).

Due to the additive composition of the terms in (3.6), the isochoric part $\mathbb{C}_{\mathrm{iso}}$ of the elasticity tensor also becomes a sum,

$$\mathbb{C}_{\mathrm{iso}} = 2\frac{\partial \mathbf{S}_{\mathrm{iso}}}{\partial \mathbf{C}} = \sum_{i=1,4\mathrm{f},4\mathrm{s},8\mathrm{fs}} \mathbb{C}_{\mathrm{iso}}^{\bar{I}_i}, \tag{3.20}$$

where the superscript refers to the invariant that is included in the tensor expression (3.15). Thus, by using the product rule we obtain the four expressions

$$\mathbb{C}_{\mathrm{iso}}^{\bar{I}_i} = 4\frac{\partial}{\partial \mathbf{C}}\left(\overline{\psi}_i \frac{\partial \bar{I}_i}{\partial \mathbf{C}}\right) = 4\overline{\psi}_{ii}\frac{\partial \bar{I}_i}{\partial \mathbf{C}} \otimes \frac{\partial \bar{I}_i}{\partial \mathbf{C}} + 4\overline{\psi}_i \frac{\partial^2 \bar{I}_i}{\partial \mathbf{C}\partial \mathbf{C}}, \quad i = 1, 4\mathrm{f}, 4\mathrm{s}, 8\mathrm{fs}, \tag{3.21}$$

where the four terms $\partial \bar{I}_i/\partial \mathbf{C}$ are provided in (3.12)–(3.14) and where the definition $\overline{\psi}_{ii} = \partial^2 \Psi_{\mathrm{iso}}/\partial \bar{I}_i \partial \bar{I}_i$ is introduced. With the strain-energy function (3.6) we get the specifications for $\overline{\psi}_{ii}$, i.e.

$$\overline{\psi}_{11} = \frac{\partial^2 \Psi_{\mathrm{iso}}}{\partial \bar{I}_1 \partial \bar{I}_1} = \frac{ab}{2}\exp[b(\bar{I}_1 - 3)], \tag{3.22}$$

$$\overline{\psi}_{4j4j} = \frac{\partial^2 \Psi_{\mathrm{iso}}}{\partial \bar{I}_{4\,j} \partial \bar{I}_{4\,j}} = a_j[1 + 2b_j(\bar{I}_{4\,j} - 1)^2]\exp[b_j(\bar{I}_{4\,j} - 1)^2], \quad j = \mathrm{f}, \mathrm{s}, \tag{3.23}$$

$$\overline{\psi}_{8\mathrm{fs}\,8\mathrm{fs}} = \frac{\partial^2 \Psi_{\mathrm{iso}}}{\partial \bar{I}_{8\,\mathrm{fs}} \partial \bar{I}_{8\,\mathrm{fs}}} = a_{\mathrm{fs}}(1 + 2b_{\mathrm{fs}}\bar{I}_{8\,\mathrm{fs}}^2)\exp(b_{\mathrm{fs}}\bar{I}_{8\,\mathrm{fs}}^2). \tag{3.24}$$

In addition, in $(3.21)_2$ we need to specify the second derivative of the modified invariants with respect to $\mathbf{C}$. For the modified invariant $\bar{I}_1$ we obtain with $(3.12)_3$ that

$$\begin{aligned}
\frac{\partial^2 \bar{I}_1}{\partial \mathbf{C}\partial \mathbf{C}} &= \frac{\partial (J^{-2/3}\mathrm{Dev}\mathbf{I})}{\partial \mathbf{C}} \\
&= -\frac{1}{3}J^{-2/3}\mathbf{C}^{-1} \otimes \mathrm{Dev}\mathbf{I} - \frac{1}{3}J^{-2/3}\left(\mathbf{I} \otimes \mathbf{C}^{-1} + \mathrm{Tr}\mathbf{C}\frac{\partial \mathbf{C}^{-1}}{\partial \mathbf{C}}\right) \\
&= -\frac{1}{3}J^{-2/3}(\mathbf{C}^{-1} \otimes \mathrm{Dev}\mathbf{I} + \mathrm{Dev}\mathbf{I} \otimes \mathbf{C}^{-1}) + \frac{1}{3}J^{-2/3}I_1\tilde{\mathbb{P}},
\end{aligned} \tag{3.25}$$

where

$$\tilde{\mathbb{P}} = \mathbf{C}^{-1} \odot \mathbf{C}^{-1} - \frac{1}{3}\mathbf{C}^{-1} \otimes \mathbf{C}^{-1} \tag{3.26}$$

is a modified projection tensor of fourth-order [6]. In an analogous manner we may derive the second derivative of $\bar{I}_{4\mathrm{f}}$ with respect to $\mathbf{C}$, i.e.

$$\frac{\partial^2 \bar{I}_{4\mathrm{f}}}{\partial \mathbf{C}\partial \mathbf{C}} = -\frac{1}{3}J^{-2/3}[\mathbf{C}^{-1} \otimes \mathrm{Dev}(\mathbf{f}_0 \otimes \mathbf{f}_0) + \mathrm{Dev}(\mathbf{f}_0 \otimes \mathbf{f}_0) \otimes \mathbf{C}^{-1}] + \frac{1}{3}J^{-2/3}I_{4\mathrm{f}}\tilde{\mathbb{P}}, \tag{3.27}$$

and $\partial^2 \bar{I}_{4\mathrm{s}}/\partial\mathbf{C}\partial\mathbf{C}$ which we get by writing s instead of f in Eq. (3.27). Finally, taking the derivative of $(3.14)_2$ with respect to $\mathbf{C}$ in an analogous way, we get

$$\begin{aligned}\frac{\partial^2 \bar{I}_{8\,\mathrm{fs}}}{\partial\mathbf{C}\partial\mathbf{C}} = &-\frac{1}{6}J^{-2/3}[\mathbf{C}^{-1}\otimes\mathrm{Dev}(\mathbf{f}_0\otimes\mathbf{s}_0+\mathbf{s}_0\otimes\mathbf{f}_0)\\ &+\mathrm{Dev}(\mathbf{f}_0\otimes\mathbf{s}_0+\mathbf{s}_0\otimes\mathbf{f}_0)\otimes\mathbf{C}^{-1}]+\frac{1}{3}J^{-2/3}I_{8\,\mathrm{fs}}\tilde{\mathbb{P}}.\end{aligned} \tag{3.28}$$

Hence, substituting $(3.12)_3$ and $(3.25)_3$ into $(3.21)_2$ we get the final expression for the isochoric elasticity tensor with respect to the isotropic invariant, i.e.

$$\mathbb{C}^{\bar{I}_1}_{\mathrm{iso}} = 4J^{-4/3}\overline{\psi}_{11}\mathrm{Dev}\mathbf{I}\otimes\mathrm{Dev}\mathbf{I}-\frac{4}{3}J^{-2/3}\overline{\psi}_1(\mathbf{C}^{-1}\otimes\mathrm{Dev}\mathbf{I}+\mathrm{Dev}\mathbf{I}\otimes\mathbf{C}^{-1}-I_1\tilde{\mathbb{P}}). \tag{3.29}$$

Using $(3.13)_5$ and (3.27) in $(3.21)_2$ gives

$$\begin{aligned}\mathbb{C}^{\bar{I}_{4\mathrm{f}}}_{\mathrm{iso}} = &\,4J^{-4/3}\overline{\psi}_{4\mathrm{f}4\mathrm{f}}\mathrm{Dev}(\mathbf{f}_0\otimes\mathbf{f}_0)\otimes\mathrm{Dev}(\mathbf{f}_0\otimes\mathbf{f}_0)\\ &-\frac{4}{3}J^{-2/3}\overline{\psi}_{4\mathrm{f}}[\mathbf{C}^{-1}\otimes\mathrm{Dev}(\mathbf{f}_0\otimes\mathbf{f}_0)+\mathrm{Dev}(\mathbf{f}_0\otimes\mathbf{f}_0)\otimes\mathbf{C}^{-1}-I_{4\mathrm{f}}\tilde{\mathbb{P}}],\end{aligned} \tag{3.30}$$

while the isochoric elasticity tensor $\mathbb{C}^{\bar{I}_{8\,\mathrm{fs}}}_{\mathrm{iso}}$ follows from $(3.21)_2$ by means of $(3.14)_2$ and (3.28), i.e.

$$\begin{aligned}\mathbb{C}^{\bar{I}_{8\,\mathrm{fs}}}_{\mathrm{iso}} = &\,J^{-4/3}\overline{\psi}_{8\,\mathrm{fs}\,8\,\mathrm{fs}}\mathrm{Dev}(\mathbf{f}_0\otimes\mathbf{s}_0+\mathbf{s}_0\otimes\mathbf{f}_0)\otimes\mathrm{Dev}(\mathbf{f}_0\otimes\mathbf{s}_0+\mathbf{s}_0\otimes\mathbf{f}_0)\\ &-\frac{2}{3}J^{-2/3}\overline{\psi}_{8\,\mathrm{fs}}[\mathbf{C}^{-1}\otimes\mathrm{Dev}(\mathbf{f}_0\otimes\mathbf{s}_0+\mathbf{s}_0\otimes\mathbf{f}_0)\\ &+\mathrm{Dev}(\mathbf{f}_0\otimes\mathbf{s}_0+\mathbf{s}_0\otimes\mathbf{f}_0)\otimes\mathbf{C}^{-1}-2I_{8\,\mathrm{fs}}\tilde{\mathbb{P}}].\end{aligned} \tag{3.31}$$

Note that the elasticity tensor $\mathbb{C}^{\bar{I}_{4\mathrm{s}}}_{\mathrm{iso}}$ is simply achieved by writing s instead of f in eq. (3.30). Hence, with the relations (3.29)–(3.31) we have now an explicit expression for the isochoric elasticity tensor $(3.20)_2$ expressed in terms of material quantities.

3.2.5. Elasticity tensors in the Eulerian description

The elasticity tensor $\mathbb{c}$ in the Eulerian description may be calculated by using the push-forward operation of $\mathbb{C}$, i.e. $[\mathbb{c}]_{abcd} = F_{aA}F_{bB}F_{cC}F_{dD}[\mathbb{C}]_{ABCD}$, so that $\mathbb{c} = \mathbb{c}_{\mathrm{vol}} + \mathbb{c}_{\mathrm{iso}}$, which is the analogue of eq. $(3.18)_2$. In the following we show each term of the Eulerian elasticity tensor.

The volumetric elasticity tensor $\mathbb{c}_{\mathrm{vol}}$ in the Eulerian description may be written as the push-forward operation of $(3.19)_2$ which is

$$\mathbb{c}_{\mathrm{vol}} = J(\tilde{p}_{\mathrm{h}}\mathbf{I}\otimes\mathbf{I}-2p_{\mathrm{h}}\mathbb{I}), \tag{3.32}$$

where $\mathbb{I}$ is the fourth-order unit tensor. It is also straightforward to provide the spatial version of $(3.20)_2$, i.e. the isochoric elasticity tensor

$$\mathbb{c}_{\text{iso}} = \sum_{i=1,4\text{f},4\text{s},8\text{fs}} \mathbb{c}_{\text{iso}}^{\bar{I}_i}, \tag{3.33}$$

with the four contributions which may be derived from (3.29)-(3.31). By using the modified left Cauchy-Green tensor $\overline{\mathbf{b}} = \overline{\mathbf{F}}\overline{\mathbf{F}}^{\text{T}}$ and the definitions (3.3) and (3.17) we obtain the isochoric elasticity tensors which are needed in (3.33), i.e.

$$\mathbb{c}_{\text{iso}}^{\bar{I}_1} = 4\overline{\psi}_{11}\text{dev}\overline{\mathbf{b}} \otimes \text{dev}\overline{\mathbf{b}} - \frac{4}{3}\overline{\psi}_1(\mathbf{I} \otimes \text{dev}\overline{\mathbf{b}} + \text{dev}\overline{\mathbf{b}} \otimes \mathbf{I} - \bar{I}_1 \mathbb{P}), \quad \mathbb{P} = \mathbb{I} - \frac{1}{3}\mathbf{I} \otimes \mathbf{I}, \tag{3.34}$$

$$\begin{aligned}\mathbb{c}_{\text{iso}}^{\bar{I}_{4\text{f}}} &= 4\overline{\psi}_{4\text{f}4\text{f}}\text{dev}(\bar{\mathbf{f}} \otimes \bar{\mathbf{f}}) \otimes \text{dev}(\bar{\mathbf{f}} \otimes \bar{\mathbf{f}}) \\ &\quad - \frac{4}{3}\overline{\psi}_{4\text{f}}[\mathbf{I} \otimes \text{dev}(\bar{\mathbf{f}} \otimes \bar{\mathbf{f}}) + \text{dev}(\bar{\mathbf{f}} \otimes \bar{\mathbf{f}}) \otimes \mathbf{I} - \bar{I}_{4\text{f}} \mathbb{P}],\end{aligned} \tag{3.35}$$

$$\begin{aligned}\mathbb{c}_{\text{iso}}^{\bar{I}_{8\text{fs}}} &= \overline{\psi}_{8\text{fs}\,8\text{fs}}\text{dev}(\bar{\mathbf{f}} \otimes \bar{\mathbf{s}} + \bar{\mathbf{s}} \otimes \bar{\mathbf{f}}) \otimes \text{dev}(\bar{\mathbf{f}} \otimes \bar{\mathbf{s}} + \bar{\mathbf{s}} \otimes \bar{\mathbf{f}}) \\ &\quad - \frac{2}{3}\overline{\psi}_{8\text{fs}}[\mathbf{I} \otimes \text{dev}(\bar{\mathbf{f}} \otimes \bar{\mathbf{s}} + \bar{\mathbf{s}} \otimes \bar{\mathbf{f}}) + \text{dev}(\bar{\mathbf{f}} \otimes \bar{\mathbf{s}} + \bar{\mathbf{s}} \otimes \bar{\mathbf{f}}) \otimes \mathbf{I} - 2\bar{I}_{8\text{fs}} \mathbb{P}].\end{aligned} \tag{3.36}$$

Note that in this form the volume ratio J does not appear explicitly.

3.3. Analytical Expression of the Stress Tensor

When implementing a new material model in a finite element framework, the implementation itself needs to be verified. For that reason, analytical expressions of the material model is presented in this section. Expressions are shown for uniaxial deformation, biaxial deformation and simple shear. The same analytical expressions may also be used for retrieving the material parameters of the model by fitting them to experimental data.

3.3.1. General analytical expression for incompressible material

For an incompressible material there is no change of volume which means the volume ratio $J = 1$ and there is no deviatoric part. The analytical expression of the Cauchy stress shown in (3.6) is thus

$$\boldsymbol{\sigma} = p_{\text{h}}\mathbf{I} + 2\left(\psi_1 \mathbf{b} + \psi_{4\text{f}}\mathbf{f} \otimes \mathbf{f} + \psi_{4\text{s}}\mathbf{s} \otimes \mathbf{s}\right) + \psi_{8\text{fs}}\left(\mathbf{f} \otimes \mathbf{s} + \mathbf{s} \otimes \mathbf{f}\right). \tag{3.37}$$

Here, p_{h} is the hydrostatic pressure and may be seen as a Lagrange multiplier for the volume constraint. It is determined by the boundary conditions. Using

$$[\mathbf{b}] = \begin{bmatrix} \text{b}_{11} & \text{b}_{12} & \text{b}_{13} \\ \text{b}_{21} & \text{b}_{22} & \text{b}_{23} \\ \text{b}_{31} & \text{b}_{32} & \text{b}_{33} \end{bmatrix} \qquad \text{and} \qquad \begin{aligned}[\mathbf{f}] &= [\text{f}_1\,\text{f}_2, \text{f}_3]^{\text{T}} \\ [\mathbf{s}] &= [\text{s}_1, \text{s}_2, \text{s}_3]^{\text{T}} \\ [\mathbf{n}] &= [\text{n}_1, \text{n}_2, \text{n}_3]^{\text{T}}\end{aligned} \tag{3.38}$$

the components of the symmetric Cauchy stress tensor (3.37) are

$$\sigma_{11} = p_{\mathrm{h}} + 2\,(\psi_1 \mathrm{b}_{11} + \psi_{4\mathrm{f}} \mathrm{f}_1^2 + \psi_{4\mathrm{s}} \mathrm{s}_1^2 + \psi_{8\,\mathrm{fs}} \mathrm{f}_1 \mathrm{s}_1), \tag{3.39}$$

$$\sigma_{22} = p_{\mathrm{h}} + 2\,(\psi_1 \mathrm{b}_{22} + \psi_{4\mathrm{f}} \mathrm{f}_2^2 + \psi_{4\mathrm{s}} \mathrm{s}_2^2 + \psi_{8\,\mathrm{fs}} \mathrm{f}_2 \mathrm{s}_2), \tag{3.40}$$

$$\sigma_{33} = p_{\mathrm{h}} + 2\,(\psi_1 \mathrm{b}_{33} + \psi_{4\mathrm{f}} \mathrm{f}_3^2 + \psi_{4\mathrm{s}} \mathrm{s}_3^2 + \psi_{8\,\mathrm{fs}} \mathrm{f}_3 \mathrm{s}_3), \tag{3.41}$$

$$\sigma_{12} = 2\,(\psi_1 \mathrm{b}_{12} + \psi_{4\mathrm{f}} \mathrm{f}_1 \mathrm{f}_2 + \psi_{4\mathrm{s}} \mathrm{s}_1 \mathrm{s}_2) + \psi_{8\,\mathrm{fs}} (\mathrm{f}_1 \mathrm{s}_2 + \mathrm{f}_2 \mathrm{s}_1), \tag{3.42}$$

$$\sigma_{13} = 2\,(\psi_1 \mathrm{b}_{13} + \psi_{4\mathrm{f}} \mathrm{f}_1 \mathrm{f}_3 + \psi_{4\mathrm{s}} \mathrm{s}_1 \mathrm{s}_3) + \psi_{8\,\mathrm{fs}} (\mathrm{f}_1 \mathrm{s}_3 + \mathrm{f}_3 \mathrm{s}_1), \tag{3.43}$$

$$\sigma_{23} = 2\,(\psi_1 \mathrm{b}_{23} + \psi_{4\mathrm{f}} \mathrm{f}_2 \mathrm{f}_3 + \psi_{4\mathrm{s}} \mathrm{s}_2 \mathrm{s}_3) + \psi_{8\,\mathrm{fs}} (\mathrm{f}_2 \mathrm{s}_3 + \mathrm{f}_3 \mathrm{s}_2). \tag{3.44}$$

If not stated otherwise in the following, the undeformed fiber, sheet and sheet-normal directions are assumed to coincide with the global cartesian axis, $[\mathbf{f}_0] = [1, 0, 0]^{\mathrm{T}}$, $[\mathbf{s}_0] = [0, 1, 0]^{\mathrm{T}}$ and $[\mathbf{n}_0] = [0, 0, 1]^{\mathrm{T}}$. Further, we are assuming the material is incompressible and we are considering a plain stress state.

3.3.2. Uniaxial stretch

For a uniaxial stretch, λ_{ff} in the $\mathbf{f}_0$ direction, the deformation gradient and left Cauchy Green tensor are

$$[\mathbf{F}] = \begin{bmatrix} \lambda_{\mathrm{ff}} & 0 & 0 \\ 0 & 1/\sqrt{\lambda_{\mathrm{ff}}} & 0 \\ 0 & 0 & 1/\sqrt{\lambda_{\mathrm{ff}}} \end{bmatrix}, \quad [\mathbf{b}] = \begin{bmatrix} \lambda_{\mathrm{ff}}^2 & 0 & 0 \\ 0 & 1/\lambda_{\mathrm{ff}} & 0 \\ 0 & 0 & 1/\lambda_{\mathrm{ff}} \end{bmatrix}, \tag{3.45}$$

Remembering that the terms correlating to the fiber and sheet direction in the strain energy function are only active if they are in tension, i.e., $\lambda_{\mathrm{s}} < 1$, $\psi_{4\mathrm{s}} = 0$, the components of the Cauchy stress are

$$\sigma_{11} = 2\psi_1(\lambda_{\mathrm{ff}}^2 - 1/\lambda_{\mathrm{ff}}) + 2\psi_{4\mathrm{f}}\lambda_{\mathrm{ff}}^2, \tag{3.46}$$

$$\sigma_{22} = p_{\mathrm{h}} + 2\psi_1(1/\lambda_{\mathrm{ff}}) = 0, \tag{3.47}$$

$$\sigma_{33} = p_{\mathrm{h}} + 2\psi_1(1/\lambda_{\mathrm{ff}}) = 0, \tag{3.48}$$

$$\sigma_{12} = \sigma_{13} = \sigma_{23} = 0, \tag{3.49}$$

where p_{h} have been calculated from (3.47) or (3.48) and inserted in (3.46). The derivatives used in (3.46)–(3.48) are

$$\psi_1 = \frac{a}{2}\exp[b(\lambda_{\mathrm{ff}}^2 + \frac{2}{\lambda_{\mathrm{ff}}} - 3)] \qquad \text{and} \qquad \psi_{4\mathrm{f}} = a_{\mathrm{f}}(\lambda_{\mathrm{ff}}^2 - 1)\exp[b_{\mathrm{f}}(\lambda_{\mathrm{ff}}^2 - 1)^2]. \tag{3.50}$$

3.3.3. Biaxial stretch

For an equibiaxial stretch, λ_{ff} and λ_{ss} in the $\mathbf{f}_0$ and $\mathbf{s}_0$ directions respectively, the deformation gradient and left Cauchy Green tensor are

$$[\mathbf{F}] = \begin{bmatrix} \lambda_{\mathrm{ff}} & 0 & 0 \\ 0 & \lambda_{\mathrm{ss}} & 0 \\ 0 & 0 & 1/(\lambda_{\mathrm{ff}}\lambda_{\mathrm{ss}}) \end{bmatrix} \qquad \text{and} \qquad [\mathbf{b}] = \begin{bmatrix} \lambda_{\mathrm{ff}}^2 & 0 & 0 \\ 0 & \lambda_{\mathrm{ss}}^2 & 0 \\ 0 & 0 & 1/(\lambda_{\mathrm{ff}}\lambda_{\mathrm{ss}})^2 \end{bmatrix}. \tag{3.51}$$

The components of the Cauchy stress tensor are

$$\sigma_{11} = 2\psi_1(\lambda_{\mathrm{ff}}^2 - \frac{1}{\lambda_{\mathrm{ff}}^2\lambda_{\mathrm{ss}}^2}) + 2\psi_{4\mathrm{f}}\lambda_{\mathrm{ff}}^2, \tag{3.52}$$

$$\sigma_{22} = 2\psi_1(\lambda_{\mathrm{ss}}^2 - \frac{1}{\lambda_{\mathrm{ff}}^2\lambda_{\mathrm{ss}}^2}) + 2\psi_{4\mathrm{s}}\lambda_{\mathrm{ss}}^2, \tag{3.53}$$

$$\sigma_{33} = p_{\mathrm{h}} + 2\psi_1\frac{1}{\lambda_{\mathrm{ff}}^2\lambda_{\mathrm{ss}}^2} = 0, \tag{3.54}$$

$$\sigma_{12} = \sigma_{13} = \sigma_{23} = 0, \tag{3.55}$$

where p_{h} is calculated from (3.54) and inserted into (3.52) and (3.53). The derivatives used in (3.52)–(3.54) are

$$\psi_1 = \frac{a}{2}\exp[b(\lambda_{\mathrm{ff}}^2 + \lambda_{\mathrm{ss}}^2 + \frac{1}{\lambda_{\mathrm{ff}}^2\lambda_{\mathrm{ss}}^2} - 3)], \tag{3.56}$$

$$\psi_{4\mathrm{f}} = a_{\mathrm{f}}(\lambda_{\mathrm{ff}}^2 - 1)\exp[b_{\mathrm{f}}(\lambda_{\mathrm{ff}}^2 - 1)^2], \tag{3.57}$$

$$\psi_{4\mathrm{s}} = a_{\mathrm{s}}(\lambda_{\mathrm{ss}}^2 - 1)\exp[b_{\mathrm{s}}(\lambda_{\mathrm{ss}}^2 - 1)^2]. \tag{3.58}$$

3.3.4. Simple shear

For an analytical expression of simple shear, γ in the 21-plane, i.e. shearing the X_2 plane in the X_1 direction (see Fig. 3.2), the deformation gradient and corresponding left Cauchy Green tensor are

$$[\mathbf{F}] = \begin{bmatrix} 1 & \gamma & 0 \\ 0 & 1 & 0 \\ 0 & 0 & 1 \end{bmatrix}, \qquad [\mathbf{b}] = \begin{bmatrix} 1+\gamma^2 & \gamma & 0 \\ \gamma & 1 & 0 \\ 0 & 0 & 1 \end{bmatrix}. \tag{3.59}$$

This deformation gradient is valid for both *plain strain* and *plain stress*. It is volume preserving (isochoric), i.e. $J = \det(\mathbf{F}) = 1$, exactly.

Adding some complexity to the analytical case, the undeformed fiber and sheet directions may vary with an angle α with respect to the global X_1-axis, as shown in Fig. 3.2. The direction vectors for the fiber, sheet and sheet-normal axes are then

$$[\mathbf{f_0}] = \begin{bmatrix} \cos\alpha \\ \sin\alpha \\ 0 \end{bmatrix}, \qquad [\mathbf{s_0}] = \begin{bmatrix} -\sin\alpha \\ \cos\alpha \\ 0 \end{bmatrix}, \qquad [\mathbf{n_0}] = \begin{bmatrix} 0 \\ 0 \\ 1 \end{bmatrix}, \tag{3.60}$$

and the deformed direction vectors are

$$[\mathbf{f}] = \begin{bmatrix} \cos\alpha + \gamma\sin\alpha \\ \sin\alpha \\ 0 \end{bmatrix}, \quad [\mathbf{s}] = \begin{bmatrix} -\sin\alpha + \gamma\cos\alpha \\ \cos\alpha \\ 0 \end{bmatrix}, \quad [\mathbf{n}] = \begin{bmatrix} 0 \\ 0 \\ 1 \end{bmatrix}. \tag{3.61}$$

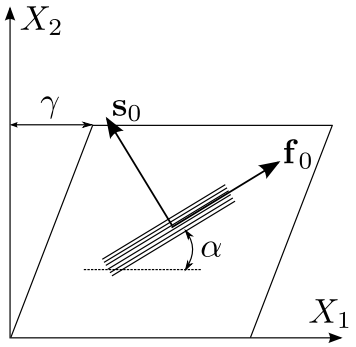

Figure 3.2.: Shear of a square block in the 21-plane with γ. The fiber direction is at angle α with respect to the global 1-axis, and the sheet axis is perpendicular to the fiber axis.

Using $\mathrm{s} = \sin\alpha$, $\mathrm{c} = \cos\alpha$ for a more simple notation, the Cauchy stress components, as shown in (3.39)–(3.44), are now

$$\sigma_{11} = 2\left[\psi_1\gamma^2 + \psi_{4\mathrm{f}}(\mathrm{c}+\gamma\mathrm{s})^2 + \psi_{4\mathrm{s}}(-\mathrm{s}+\gamma\mathrm{c})^2 + \psi_{8\mathrm{fs}}(\mathrm{c}+\gamma\mathrm{s})(-\mathrm{s}+\gamma\mathrm{c})\right], \tag{3.62}$$

$$\sigma_{22} = 2\left(\psi_{4\mathrm{f}}\mathrm{s}^2 + \psi_{4\mathrm{s}}\mathrm{c}^2 + \psi_{8\mathrm{fs}}\mathrm{sc}\right), \tag{3.63}$$

$$\sigma_{33} = p_\mathrm{h} + 2\psi_1 = 0, \tag{3.64}$$

$$\sigma_{12} = 2[\psi_1\gamma + 2\psi_{4\mathrm{f}}\mathrm{s}(\mathrm{c}+\gamma\mathrm{s}) + 2\psi_{4\mathrm{s}}\mathrm{c}(-\mathrm{s}+\gamma\mathrm{c})] + \psi_{8\mathrm{fs}}(2\gamma\mathrm{sc} + 2\mathrm{c}^2 - 1), \tag{3.65}$$

$$\sigma_{13} = \sigma_{23} = 0. \tag{3.66}$$

Again, p_h is calculated from (3.64) and is inserted in (3.62) and (3.63). For the special case where $\alpha = 0$ the stress components are

$$\sigma_{11} = 2(\psi_1\gamma^2 + \psi_{4\mathrm{s}}\gamma^2 + \psi_{8\mathrm{fs}}\gamma), \tag{3.67}$$

$$\sigma_{22} = 2\psi_{4s}, \tag{3.68}$$

$$\sigma_{33} = 0, \tag{3.69}$$

$$\sigma_{12} = 2(\psi_1 + \psi_{4\mathrm{s}})\gamma + \psi_{8\mathrm{fs}}, \tag{3.70}$$

$$\sigma_{13} = \sigma_{23} = 0, \tag{3.71}$$

and for this case the derivatives used in (3.67), (3.68) and (3.70) are

$$\psi_1 = \frac{a}{2}\exp(b\,\gamma^2), \tag{3.72}$$

$$\psi_{4\mathrm{f}} = 0, \tag{3.73}$$

$$\psi_{4\mathrm{s}} = a_\mathrm{s}\gamma^2\exp(b_\mathrm{s}\,\gamma^4), \tag{3.74}$$

$$\psi_{8\mathrm{fs}} = a_\mathrm{fs}\gamma\exp(b_\mathrm{fs}\,\gamma^2). \tag{3.75}$$

These equations may be used for both validating an implementation of the proposed model in a finite element software as well as when fitting the model against experimental data to retrieve material parameters as shown in the next section.

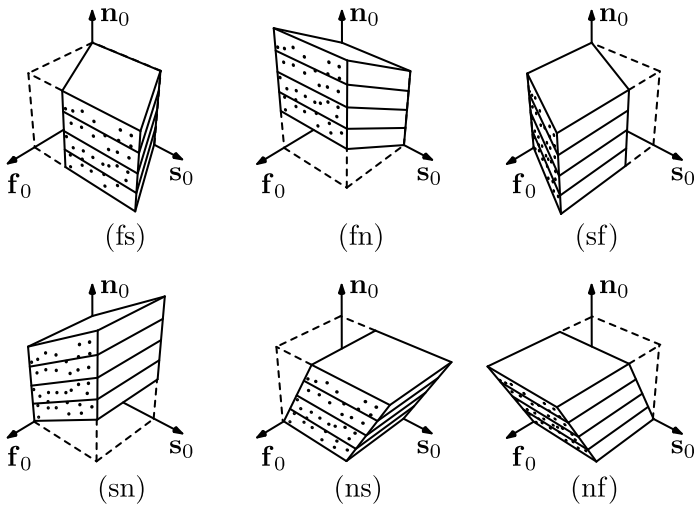

Figure 3.3.: Six possible shear directions of a cube with respect to fiber, sheet and sheet-normal directions $\mathbf{f}_0$, $\mathbf{s}_0$, $\mathbf{n}_0$ aligned in the global X_1, X_2, X_3 coordinate system.

3.4. Model Fit to Experimental Data

To verify that our model describes the behavior of myocardial tissue, it is fitted against experimental data using the nonlinear least squares MATLAB lsqnonlin function. Using the large-scale option in this function, it is possible to set lower bounds on the fitting procedure which may be needed, as previously described in Section 3.2.2 and [42], to ensure that all material parameters are larger than zero.

3.4.1. Fit to a simple shear experiment

Plain stress, shear tests was performed by Dokos et al. [51], where cubic pieces was excised from porcine myocardium. In the experiments, the fiber, sheet and sheet-normal directions of the myocardial cubes were identified and positioned in the global X_1, X_2 and X_3 directions respectively. Thus, the undeformed direction vectors are $\mathbf{f}_0 = [1, 0, 0]^{\mathrm{T}}$, $\mathbf{s}_0 = [0, 1, 0]^{\mathrm{T}}$ and $\mathbf{n}_0 = [0, 0, 1]^{\mathrm{T}}$. The cubes were then sheared in all six possible shearing directions as shown in Fig. 3.3. The shear stress corresponding to shear displacement were shown for each direction, see for instance Fig. 6 in [51]. Note however, that the ordering of the labels (fs) and (fn) in that figure is inconsistent with other figures in their paper. This is corrected by switching the roles of these labels in the fitting procedure. We are assuming the deformation mode is simple shear, and thus the analytical equations for the shear stress

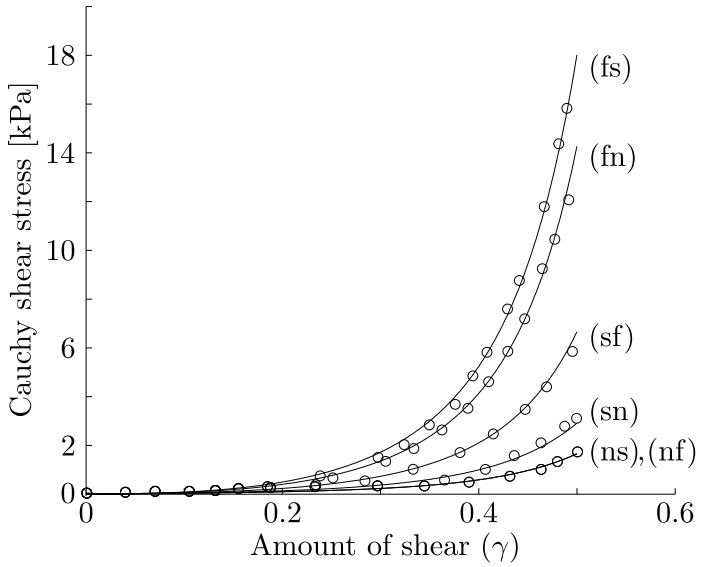

Figure 3.4.: Fit to data presented by Dokos et al. [51] where cubes of myocardial tissue was sheared in 6 different directions according to: fiber to sheet (fs); fiber to sheet-normal (fn); sheet to fiber (sf); sheet to sheet-normal (sn); sheet-normal to sheet (ns) and sheet-normal to fiber (nf).

are

$$\sigma_{12}^{(\mathrm{fs})} = 2(\psi_1 + \psi_{4\mathrm{f}})\gamma + \psi_{8\mathrm{fs}}, \tag{3.76}$$

$$\sigma_{13}^{(\mathrm{fn})} = 2(\psi_1 + \psi_{4\mathrm{f}})\gamma, \tag{3.77}$$

$$\sigma_{21}^{(\mathrm{sf})} = 2(\psi_1 + \psi_{4\mathrm{s}})\gamma + \psi_{8\mathrm{fs}}, \tag{3.78}$$

$$\sigma_{23}^{(\mathrm{sn})} = 2(\psi_1 + \psi_{4\mathrm{s}})\gamma, \tag{3.79}$$

$$\sigma_{32}^{(\mathrm{ns})} = 2\psi_1\gamma, \tag{3.80}$$

$$\sigma_{31}^{(\mathrm{nf})} = 2\psi_1\gamma. \tag{3.81}$$

It may be noted that the expressions (3.78) and (3.70) are the same as it is the same case. The fit of the stress Eqs. (3.76)-(3.81) is shown in Fig. 3.4 and as may be seen the procedure leads to a near perfect fit with the corresponding values in Table 3.1. Except for (3.80) and (3.81), the expressions for shear stress all look different and thus individual stresses may be calculated for all shear stresses. The small difference between the stresses of (3.80) and (3.81), as seen in the test performed by Dokos et al. [51], motivates that they have a similar expression. However, if a variation is needed, it could easily be achieved by adding the following additional term to (3.6),

$$\Psi_{8\,\mathrm{sn}} = \frac{a_{\mathrm{sn}}}{2b_{\mathrm{sn}}}[\exp(b_{\mathrm{sn}}\bar{I}_{8\,\mathrm{sn}}^2) - 1]. \tag{3.82}$$

This term would lead to the addition $\overline{\psi}_{8\,\mathrm{sn}}$, to equations (3.79) and (3.80) which result in a total separation of all values, see [42] for more details. The meaning of the indices for the invariant and material parameters in (3.82) are consistent with those previously shown.

experimental type	a (kPa)	b (-)	a_f (kPa)	b_f (-)	a_s (kPa)	b_s (-)	a_fs (kPa)	b_fs (-)
shear	0.330	9.242	18.535	15.972	2.564	10.446	0.417	11.602
biaxial	2.280	9.726	1.685	15.779	0.000	0.000	-	-

Table 3.1.: Material parameters retrieved when fitting the model against shear experimental data by Dokos et al. [51] shown in Fig. 3.4 and biaxial experimental data by Yin et al. [129] shown in Fig. 3.5.

3.4.2. Fit to a biaxial experiment

A biaxial test was made by Yin et al. [129], and the result is shown in Fig. 4 in that paper, where they expressed the the second Piola Kirchhoff stress tensor $\mathbf{S}$ as a function of the Green-Lagrange strain $\mathbf{E} = (\mathbf{C}-\mathbf{I})/2$. Described briefly, they cut slices of myocardial tissue, identified the fiber direction, and stretched the slices in the fiber and cross-fiber direction. They also varied the stretch ratio between the two directions of stretch, here labeled $v = E_{\mathrm{ff}}/E_{\mathrm{ss}}$. Since $I_{8\,\mathrm{fs}} = 0$, always in a biaxial test (when stretching in the fiber and sheet direction, with $[\mathbf{f}_0] = [1,0,0], [\mathbf{s}_0] = [0,1,0]$), the $\psi_{8\,\mathrm{fs}}$ term may be excluded from the stress formulation, and using the pull-back operation $\mathbf{S} = J\mathbf{F}^{-1}\boldsymbol{\sigma}\mathbf{F}^{-\mathrm{T}}$ to retrieve the second Piola-Kirchhoff stress tensor from the Cauchy stress tensor (3.52) and (3.53), the following non-zero components are obtained

$$S_{11} = 2\psi_1(1-\frac{\lambda_{\mathrm{nn}}^2}{\lambda_{\mathrm{ff}}^2}) + 2\psi_{4\,\mathrm{f}} \qquad \text{and} \qquad S_{22} = 2\psi_1(1-\frac{\lambda_{\mathrm{nn}}^2}{\lambda_{\mathrm{ss}}^2}) + 2\psi_{4\,\mathrm{s}}, \tag{3.83}$$

where $\lambda_{\mathrm{nn}} = (\lambda_{\mathrm{ff}}\lambda_{\mathrm{ss}})^{-1}$. Expressing the stretch λ_i, $i \in \{\mathrm{ff}, \mathrm{ss}, \mathrm{nn}\}$, in the Green-Lagrange strain E_{ff}, results in

$$\lambda_{\mathrm{ff}}^2 = 2E_{\mathrm{ff}} + 1, \qquad \lambda_{\mathrm{ss}}^2 = 2E_{\mathrm{ff}}/v + 1 \qquad \text{and} \qquad \lambda_{\mathrm{nn}}^2 = \frac{1}{(2E_{\mathrm{ff}}+1)(2E_{\mathrm{ff}}/v+1)}. \tag{3.84}$$

The non-zero second Piola-Kirchhoff stress components, in terms of Green-Lagrange strains, are then

$$S_{11} = 2\psi_1\left[1 - \frac{1}{(2E_{\mathrm{ff}}+1)^2(2E_{\mathrm{ff}}/v+1)}\right] + 2\psi_{4\,\mathrm{f}}, \tag{3.85}$$

$$S_{22} = 2\psi_1\left[1 - \frac{1}{(2E_{\mathrm{ff}}+1)(2E_{\mathrm{ff}}/v+1)^2}\right] + 2\psi_{4\,\mathrm{s}}, \tag{3.86}$$

where the derivatives used in Eqs. (3.85) and (3.86) are

$$\psi_1 = \frac{a}{2}\exp\left\{b\left[2(E_{\mathrm{ff}} + E_{\mathrm{ff}}/v) + \frac{2}{(2E_{\mathrm{ff}}+1)(2E_{\mathrm{ff}}/v+1)} - 1\right]\right\}, \tag{3.87}$$

$$\psi_{4\,\mathrm{f}} = 2\,a_\mathrm{f} E_{\mathrm{ff}} \exp\left(b_\mathrm{f} 4\,E_{\mathrm{ff}}^2\right), \tag{3.88}$$

$$\psi_{4\,\mathrm{s}} = 2\,a_\mathrm{s}\frac{E_{\mathrm{ff}}}{v}\exp\left(b_\mathrm{s} 4\,\frac{E_{\mathrm{ff}}^2}{v^2}\right). \tag{3.89}$$

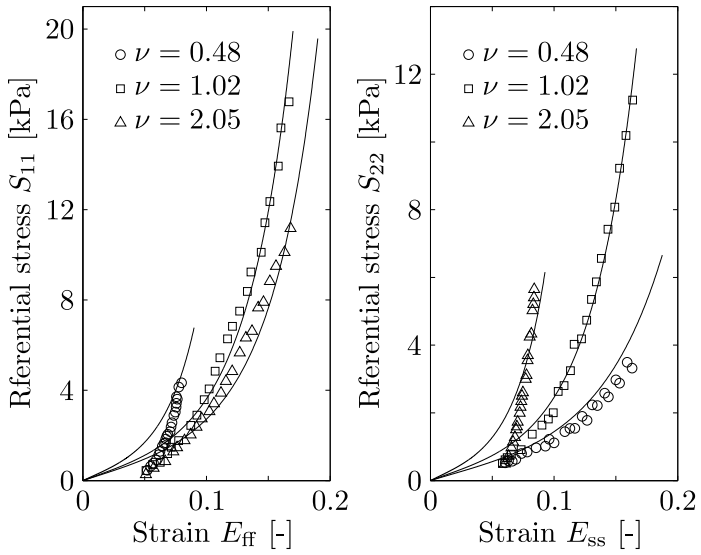

Figure 3.5.: Solid curves represent the fit to data presented by Yin et al. [129], where the circles, squares and triangles represent data points at varying ratios $v = E_{\mathrm{ff}}/E_{\mathrm{ss}}$.

These equations were fitted against the biaxial test by Yin et al. [129], and the fit is shown in Fig. 3.5. The corresponding values of the material parameters are shown in Table 3.1 and as seen, the value for $a_s = 0$, which implies that the material parameters are expressed for a transversally isotropic material. This shows that to retrieve accurate material parameters a biaxial fit alone may not be sufficient to describe the orthotropic behavior which we know is evident in myocardium. Furthermore, due to the size of the specimen in a biaxial fit it is, to the authors knowledge, not possible to extract a test specimen that is aligned in both the fiber and sheet direction. Therefore, without knowing the underlying variation of the sheet structure in the specimen tested, it is, therefore, not really possible to fit a model that has a specified sheet direction incorporated.

3.4.3. Comparison to available model

A commonly used orthotropic model for the passive behavior of myocardial tissue that has been shown to give a good fit against experimental data, [49,50,130], is a Fung-type model based on Green-Lagrange strains, shown by Costa et al. [47],

$$\Psi(\mathbf{E}) = \frac{C}{2}[\exp(Q) - 1], \tag{3.90}$$

$$Q = c_1 E_{\mathrm{ff}}^2 + c_2 E_{\mathrm{ss}}^2 + c_3 E_{\mathrm{nn}}^2 + 2c_4 E_{\mathrm{fs}} E_{\mathrm{sf}} + 2c_5 E_{\mathrm{sn}} E_{\mathrm{ns}} + 2c_4 E_{\mathrm{fn}} E_{\mathrm{nf}}. \tag{3.91}$$

To compare this Costa-model with our new model, we use the same fitting procedure against the experimental data presented by Dokos et al. [51] as was shown previously in Section 3.4.1. The Cauchy stress is calculated (for $J = 1$) by

$$\boldsymbol{\sigma} = \mathbf{F}\frac{\partial \Psi(\mathbf{E})}{\partial \mathbf{E}}\mathbf{F}^{\mathrm{T}}, \tag{3.92}$$

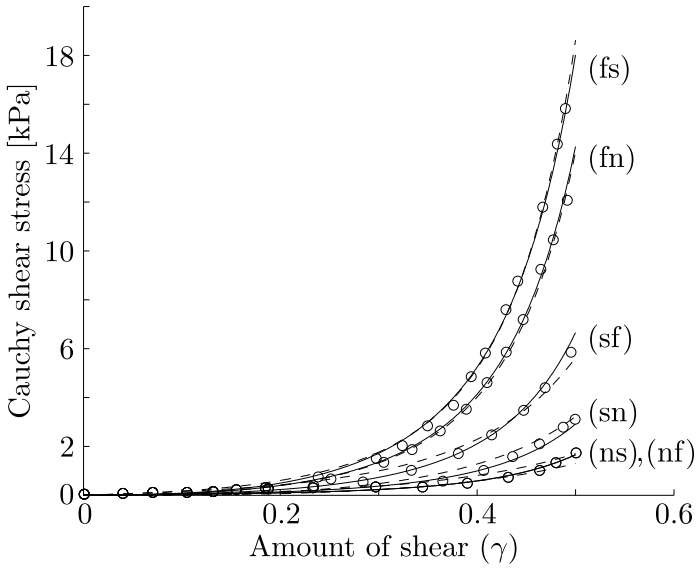

Figure 3.6.: Fit to data presented by Dokos et al. [51]. The fit of the Costa model is shown with dashed curves, and the fit of our new proposed model is shown with solid curves.

and the fit of this equation on all experimentally retrieved shear stresses is shown in Fig. 3.6 with the corresponding material parameters shown in Table 3.2. We omit here to write the full expression of the equations used for the fit. As seen in Fig. 3.6 the Costa model is also capable of capturing a near perfect fit against these experimental data. A very simple measure of the goodness of fit is the R^2 value, which is calculated as $R^2 = 1.0 - SS_{\text{reg}}/SS_{\text{tot}}$, where SS_{reg} is the sum of squares of the distances of the data points to the best fitted curve and SS_{tot} is the sum of squares of the distances from the data points to a horizontal line through the mean of all data points. An R^2 value of 1 means a perfect fit, and an R^2 value of 0 means that the curve have no fit at all.

The overall fit of our model using this measure gives $R^2 = 0.981344$ and for the Costa model $R^2 = 0.955929$. Our model shows a slightly higher R^2 value then the Costa model, but both models are well within the expected error in measurements of the experiment and thus it is not possible to say which model fits the material behavior best with this measure.

C (kPa)	c_1 (-)	c_2 (-)	c_3 (-)	c_4 (-)	c_5 (-)	c_6 (-)
1.193	62.354	27.947	14.021	2.236	0.000	0.698

Table 3.2.: Material parameters retrieved when fitting the Costa model shown in [47], to the data by Dokos et al. [51].

Ultimately, the perfect set of material parameters for a constitutive material model is able to predict, for example, the stress in another state of deformation then in the experiment from which the material parameters were retrieved. We therefore use the material parameters,

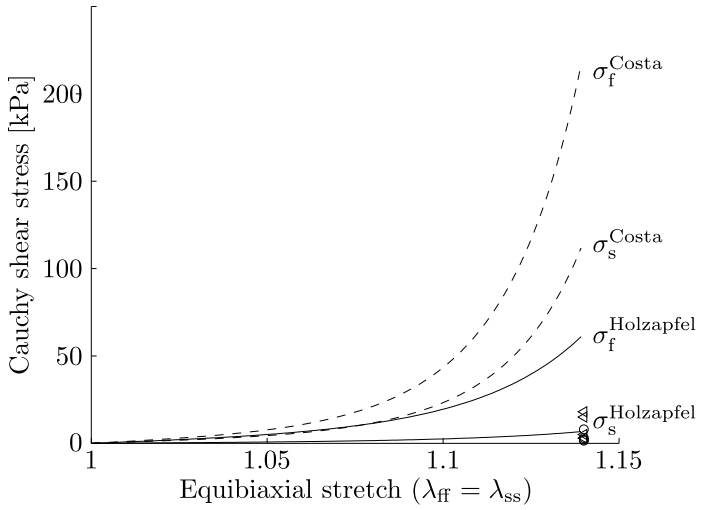

Figure 3.7.: Analytical stress for a biaxial deformation using our model (solid curves) and the Costa model (dashed curves). Various experimental values from biaxial tests [45, 131–133] are plotted where triangles represent stresses in the fiber direction and circles represent stresses in the sheet direction.

retrieved from the shear experiment and shown in Table 3.1 and 3.2, for our model and the Costa model, and calculate the analytical stress for a biaxial deformation where a unit cube is stretched equally in the fiber and sheet direction and is free to deform in the sheet-normal direction.

The analytical stress for both models is shown in Fig. 3.7 and there is a clear difference in the predicted stress response for the two models. To the authors knowledge, there have been no experiments made quantifying the biaxial stress-strain relationship for porcine myocardium in the fiber and cross-fiber direction. Instead in Fig. 3.7 the experimental values of the stresses in the fiber and cross-fiber direction for different materials are plotted as triangles and circles respectively. The materials tested and shown here are bovine, rabbit, rat and canine [45, 131–133]. Our model predicts much more conservatively the stresses in the fiber and sheet direction and when compared to the data from Yin et al. [129], the stress in the fiber direction is about three times that what Yin reported, $\sigma_f \sim 3\,\sigma_f^{Yin}$, and in the sheet direction it is almost exactly the same as their reported values for the cross-fiber direction, $\sigma_s \sim \sigma_s^{Yin}$. Whereas for the Costa model, the predicted fiber stress is about twelve times that of the reported values, $\sigma_f^{Costa} \sim 12\,\sigma_f^{Yin}$, and for the sheet direction about fourteen times those reported, $\sigma_s^{Costa} \sim 14\,\sigma_s^{Yin}$. One needs to remember that the material parameters were retrieved from shear tests on porcine myocardium [51] and the comparison is again canine myocardium [129] which are two different materials. However, for all experiments found in the literature our model is more accurate then the Costa model by an order of magnitude, as shown in Fig. 3.7.

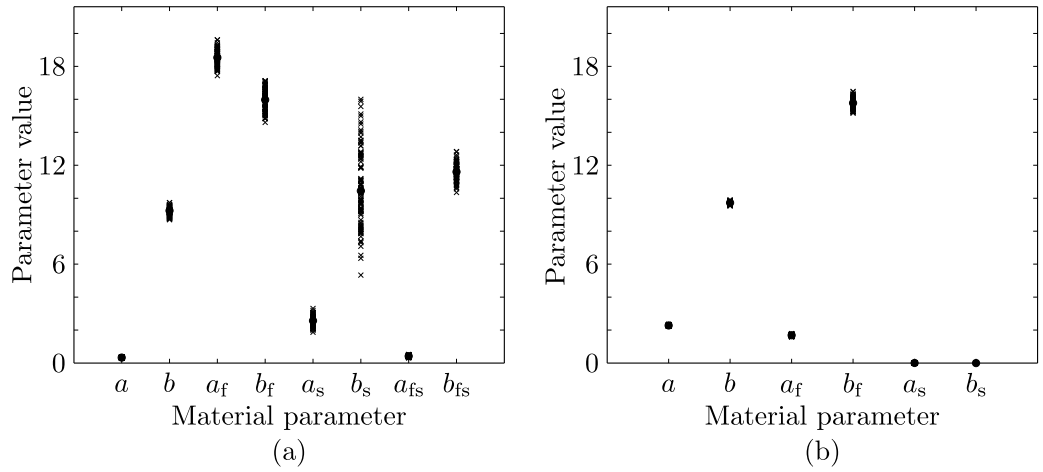

Figure 3.8.: Dispersion of one hundred best fitted material parameters when individually varying the experimental data points arbitrary by $\pm$0-2 % in: (a) simple shear experiment by Dokos et al. [51]; (b) biaxial experiment by Yin et al. [129].

3.5. Model Sensitivity

In this section a brief investigation into how sensitive the model response is to individual changes of the material parameters is presented as well as the sensitivity of the fit. As a measure of the sensitivity when fitting the material parameters, the stress datapoints used as input parameters for the fit of the model are changed randomly with $\pm$0-2 % of its original value, and the model is fitted again. This may also be considered as the sensitivity to a poorly performed experiment. A plot of the material parameters from one hundred such fits are shown in Fig. 3.8(a), where the fit against the data by Dokos et al. [51] shows that the material parameter b_s is the most sensitive. For the fit against the data by Yin et al. [129], shown in Fig. 3.8(b), the material parameter b_f shows the highest sensitivity.

Another example showing the model sensitivity is made by changing the material parameters retrieved from the fit against both experiments individually by $\pm$10 % of their original value, and look at the respective response in the change in peak stress. As seen in Table 3.3, the peak stress for σ_{ns} and σ_{nf} have the largest change for the shear experiment, about 25 %, when changing the material parameter b. For the biaxial experiment, the largest change in stress is in the σ_{11} direction, by about 36 %, when changing the material parameter b_f.

3.6. Ellipsoidal Model

In order to predict the response of the LV, the constitutive euqation is implemented into a FE software. The correctness of the implementation is verified using the material test cases. A geometrical model that is often used in computational modelling of the left ventricle is an ellipsoid truncated at the base [23, 127, 134, 135]. Here we use such a model to test the implementation of the passive material model (3.6).

	Peak stress change in % for a 10 % change in the material parameter							
	Shear stress						Biaxial stress	
Material parameter	σ_{fs}	σ_{fn}	σ_{sf}	σ_{sn}	σ_{ns}	σ_{nf}	σ_{11}	σ_{22}
a	± 0.9	± 1.2	± 2.5	± 5.7	± 10.0	± 10.0	± 0.2	± 2.2
b	$+2.3$ -1.9	$+3.0$ -2.4	$+6.3$ -5.0	$+14.5$ -11.5	$+25.5$ -20.3	$+25.5$ -20.3	$+0.6$ -0.5	$+8.5$ -6.1
a_f	± 7.0	± 8.8	-	-	-	-	± 9.8	-
b_f	$+7.5$ -6.8	$+9.4$ -8.5	-	-	-	-	$+36.3$ -26.5	-
a_s	-	-	± 1.9	± 4.3	-	-	-	± 7.8
b_s	-	-	$+1.5$ -1.4	$+3.4$ -3.2	-	-	-	$+20.8$ -16.4
a_{fs}	± 2.1	-	± 5.6	-	-	-	-	-
b_{fs}	$+2.0$ -1.8	-	$+5.5$ -5.0	-	-	-	-	-

Table 3.3.: Material parameters retrieved from the fit to the shear data from Dokos et al. [51] and biaxial data from Yin et al. [129] are changed individually by $\pm 10\%$ and the corresponding change in the peak stress values are shown.

The ellipsoid is characterized by its major and minor radii, $a_{i,o}$ and $b_{i,o}$ respectively, where the indexes 'i,o' stands for inner or outer surface of the ellipsoid. The geometry of the ellipsoid is described using prolate spheroidal coordinates ξ_1, ξ_2 and ξ_3, see Fig. 3.9. Those may be be expressed in a cartesian coordinate system by

$$x_1 = d\cosh\xi_1\cos\xi_2, \tag{3.93}$$
$$x_2 = d\sinh\xi_1\sin\xi_2\cos\xi_3, \tag{3.94}$$
$$x_3 = d\sinh\xi_1\sin\xi_2\sin\xi_3, \tag{3.95}$$

where d is the focal length, defined as $d^2_{i,o} = a^2_{i,o} - b^2_{i,o}$. The inner radii chosen are $a_i = 42\,\text{mm}$ and $b_i = 19\,\text{mm}$, and the outer radii are $a_o = 47\,\text{mm}$ and $b_o = 28\,\text{mm}$, consistent with the data for a canine heart shown in [136] and references therein. The longitudinal coordinate ξ_2 varies from 2^o to 120^o in 15 steps and the circumferential coordinate ξ_3 varies from 0^o to 180^o, also in 15 steps. Using (3.95), ξ_1 is simply calculated with the relation $a = d\cosh\xi_1$ or $b = d\sinh\xi_1$ and is determined in 4 steps between the inner and outer values, ξ_{1i} and ξ_{1o}. This leads to an ellipsoidal model with 14 elements in the longitudinal direction, 15 elements in the circumferential direction and 5 elements through the thickness in the radial direction. The geometrical model consists of 1350 nodes and 1050 hexahedral elements.

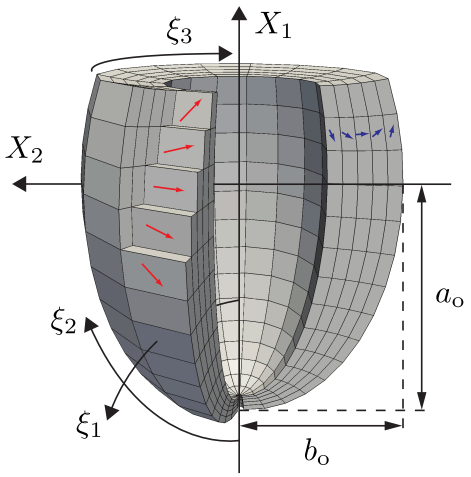

Figure 3.9.: Ellipsoidal geometrical model representing the left ventricle of the heart. A section is removed in the figure as well as selected elements, enabling visualization of sheet and fiber directions. The orientation of the fiber directions are shown in red, projected at the surface of five elements with a norm in the ξ_1-direction. The sheet directions are shown in blue projected on the surface of five elements with a norm in the ξ_3-direction.

To have an easily interpretable geometrical model, the fiber and sheet directions are set to vary linearly throughout the material. The fiber direction varies between $+60^{\text{o}}$ and -60^{o} in the ξ_2-ξ_3 plane and the sheet direction vary between $+85^{\text{o}}$ and -85^{o} in the ξ_1-ξ_2 plane, both going from the subepicardial side towards the subendocardial side. The fiber directions are shown in red in Fig. 3.9, and the sheet directions are projected on the cut surface and shown in blue in the same figure. Bear in mind that the sheet direction is in fact orthogonal to the fiber direction. Internal pressure is applied as a follower load on 210 pressure elements located on the inner surfaces of the subepicardial elements. All nodes located at the base of the ellipsoid is fixed against translation in all directions. Three pressure levels are shown which are in accordance with the physiological pressure levels for the canine left ventricle, [137–140]. The pressure levels are 7 mmHg which was reported for end diastole, 116 mmHg as reported for end systole and an intermediate pressure of 70 mmHg.

The result of the simulation is shown in Fig. 3.10, where contour plots of the stress component in the fiber direction is shown, and in Fig. 3.11, where the shear stress component between the fiber and sheet direction is shown as contour plots. Contour plots for the stress in the sheet direction is omitted as they show zero values for all pressure levels. For (d) in Figs. 3.10 and 3.11 the initial geometry is changed with respect to the fiber direction. Instead of a varying fiber angle from the epicardium to the endocardium as described earlier, we now set the fiber angle to zero degrees, i.e. the fibers are in the circumferential direction for all elements, and a pressure of 116 mmHg is applied. Notable first of all, in Fig. 3.10 is the much higher displacement at the apex when comparing (d) with (c). Also the stress gradient for (d) is much steeper than for (c). Evident in Fig. 3.11(a)–(c) is a difference

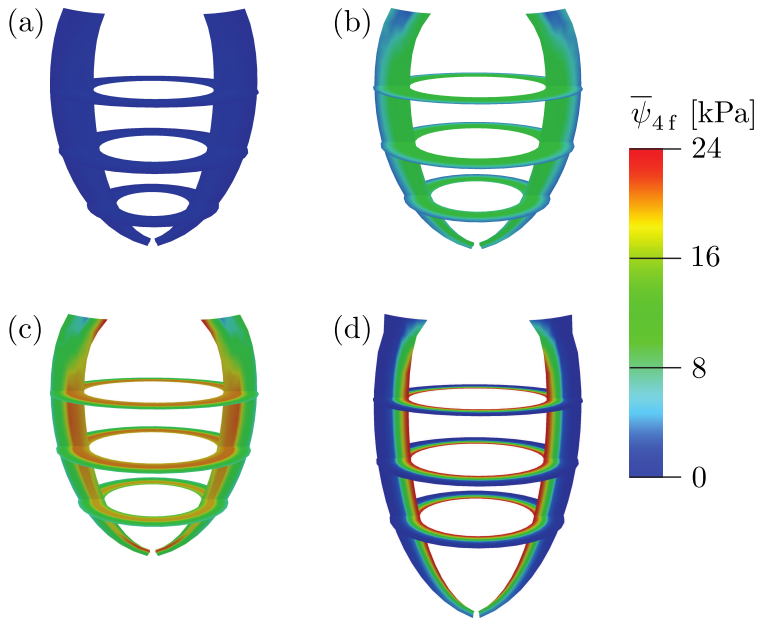

Figure 3.10.: Contour plots of the fiber stress component $\overline{\psi}_{4\,\mathrm{f}}$ for different levels of internal pressure. The pressure levels for (a) to (c) are 7, 70 and 116 mmHg, respectively. In (d) the fiber angle with respect to the circumferential direction is set to zero throughout the thickness of the ellipsoidal and the pressure level is 116 mmHg.

of positive and negative values of the shear stress. The difference is on either side of the midwall element where the fiber angle is in the circumferential direction and where the shear stress component is zero. This is also seen in Fig. 3.11(d) where the fiber direction is circumferential for all element and thus the shear stress component is zero throughout the geometry.

3.7. Concluding Remarks

In this paper we have shown the full expressions of the stress and elasticity tensors needed for implementing the recently proposed constitutive model for passive myocardium. We have shown that relatively simple expression of the stress and elasticity tensor may be derived as the invariants in the strain energy function comprising the material model are all separated in different terms. Such simple expressions are easy to implement in any finite element software. Basing the model on invariants, not only contributes to the simple implementation, but also ensures coordinate frame independence and thus only locally preferred directions of the material is needed when calculating the stress and elasticity tensor.

Analytical expressions for three modes of deformation was presented which may be used, not only to verify the implementation of the model, but also when fitting the model to experimental data which was shown for a simple shear and a biaxial experiment. The model

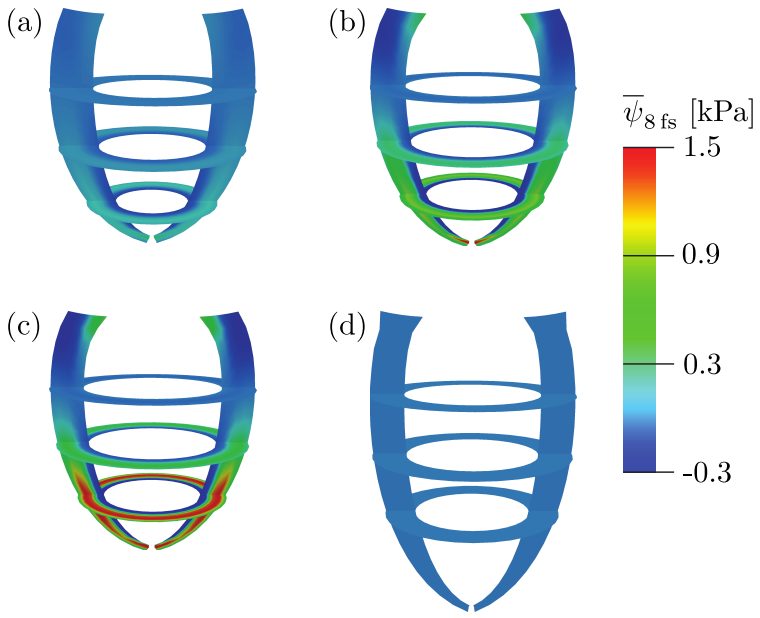

Figure 3.11.: Contour plots of the shear stress component $\overline{\psi}_{8\,\mathrm{fs}}$ for different levels of internal pressure. The pressure levels for (a) to (c) are 7, 70 and 116 mmHg, respectively. In (d) the fiber angle with respect to the circumferential direction is set to zero throughout the thickness of the ellipsoidal and the pressure level is 116 mmHg.

has a near perfect fit against the shear experiments and a reasonable fit against the biaxial experiment. As already discussed by Holzapfel and Ogden [42], the quality of the biaxial experiment is limited and there is a need for more complete experimental data. The sensitivity of the material parameters of the constitutive model was investigated and the parameters in the exponents were the most sensitive. For the simple shear deformation the model was most sensitive in the sheet-normal to sheet and sheet-normal to fiber direction, which is reasonable as those directions of shear have the lowest stress and are only governed by the isotropic part of the strain-energy function and thus only by two material parameters. In the comparison made between our newly proposed model and that of Costa et al. [47], both models displays a near perfect fit against experimental shear data of porcine myocardium. But, when using the material parameters retrieved from that fit, our model seems to be better at predicting the stress for a biaxial mode of deformation. This is a statement made with caution as the species, and thus the materials, are not the same in the comparison. The reason for this is that, to the authors knowledge, there exists no biaxial experiments of porcine myocardium in the literature today. However, looking at the range of stress values retrieved from biaxial experiments found in the literature for different species, our model is closer on all by an order of magnitude than that of the model by Costa et al. [141] and it is unlikely that stress values from a biaxial experiment on porcine myocardium will be that much higher.

In a numerical example the results of internal pressure on an ellipsoidal geometry was

investigated. A stress gradient through the thickness of the ellipsoid was found which is natural when applying internal pressure. It may be noted, however, that in vivo the situation is different as it is not pressurized from within and extended outwards, but rather it is the active compression of the wall that leads to an increase in pressure on the endocardial surface. Furthermore, a strong stress gradient in a living tissue might be physically unrealistic and would be compensated by the residual stresses that are evident in the ventricular wall [141]. Interestingly, the stress gradient is less steep when the fiber direction in the wall varies through the thickness as is seen when comparing (c) and (d) in Fig. 3.10. An explanation for this may be that the fiber angles generate a twisting motion in different direction at the subepicardial and subendocardial site and therefore the shear stress evident in Fig. 3.11(c) as opposed to (d), leads to the reduction of the stress gradient through the thickness. The large difference in the displacement at the apex may be explained by the lack of a fiber component in the longitudinal direction anywhere in the geometry for (d), together with the much lower stiffness in the sheet direction than the fiber direction due to a lower value of the material parameter a_{s} compared to a_{f}. The kink seen at the base of the ellipsoid in Figs. 3.10(d) and 3.11(d) arises from the boundary condition on the nodes at the base. This is not evident in Figs. 3.10(c) and 3.11(c) as the displacements are not as large due to the fiber orientation, as discussed earlier.

With internal pressure on the ellipsoid and a sheet angle that varies through the thickness, the sheet component of stress was found to be near zero. This is not surprising when only applying internal pressure, since the wall thickness will decrease with an increasing pressure. This results in a compression in the sheet direction and thus the sheet component of the stress is set to zero in accordance to the requirement for material stability previously explained in Section 3.2.2.

Acknowledgements

This project is in part supported by the SFB Research Center ‘Mathematical Optimization and Applications in Biomedical Sciences’, project F3210-N18 granted by the Austrian Science Fund. This support is gratefully acknowledged.

4. INFLUENCE OF MYOCARDIAL FIBER/SHEET ORIENTATIONS ON LEFT VENTRICULAR MECHANICAL CONTRACTION

Abstract At any point in space the material properties of the myocardium are characterized as orthotropic, that is, there are three mutually orthogonal axes along which both electrical and mechanical parameters differ. To investigate the role of spatial structural heterogeneity in an orthotropic material, electro-mechanically coupled models of the left ventricle (LV) were used. The implemented models differed in their arrangement of fibers and sheets in the myocardium, but were identical otherwise: (i) a generic homogeneous model, where a rule-based method was applied to assign fiber and sheet orientations, and (ii) a heterogeneous model, where the assignment of the orthotropic tissue structure was based on experimentally obtained fiber/sheet orientations. While both models resulted in pressure-volume loops and metrics of global mechanical function that were qualitatively and quantitatively similar and matched well with experimental data, the predicted deformations were strikingly different between these models, particularly with regard to torsion. Thus, the simulation results strongly suggest that heterogeneous structure properties are playing an important non-negligible role in LV mechanics and, consequently, should be accounted for in computational models.

4.1. Introduction

The capability of the heart to efficiently pump blood around the circulatory system is of vital importance. The underlying electro-mechanical function is governed by an interwoven cascade of events that interact across a broad range of spatial and temporal scales. Comprehensive, biophysically-detailed computer models of these multi-scale and multi-physics phenomena play an important role in a better understanding of integrated electro-mechanical function in health and disease. A key factor in such models is the accurate representation of the myocardial tissue structure, in particular of the left ventricle (LV), which is the main pumping chamber.

In the LV the prevailing myocyte orientations, usually referred to as fibers, follows a right-handed helical pathway from the endocardium towards the mid-wall, and a left-handed helical pathway from the mid-wall towards the epicardium, see, e.g., [22, 24]. In addition to this transmural change in the inclination angle of the fiber, termed 'fiber rotation', myocytes are bundled and form layers of four to six cells, which are referred to as laminae or sheets. Sheet orientations vary as well, not only transmurally, but also in the apico-basal

direction [24, 27]. At any point in space, the LV is characterized by an orthotropic material with three preferred eigendirections, oriented along fibers, transverse to the fibers but within a sheet, and orthogonal to the sheets.

Orthotropic material properties in the LV influence both the spread of electrical activation and re-polarization and the mechanical response to pressure load and active contraction. Electrically, wavefronts travel fastest along the fibers and slowest in the sheet normal direction, with velocity ratios of roughly $3 : 2 : 1$ along the three axes [67]. Via electro-mechanical coupling these spatio-temporal patterns of electrical activity trigger active stress transients in the myocytes, which are either modeled as active stresses or strains [52] acting along the orientation of the fibers in a current configuration [58]. The resulting mechanical deformations are then largely determined by both the passive hyperelastic orthotropic properties of the tissue and the generated active stresses.

Many numerical studies of ventricular mechanics use a simple generic rule-based approach to define the fiber and sheet angles, see, e.g., [22, 43, 53, 111, 113, 119, 142–145]. In these studies, the fibers often vary linearly between the endocardium and the epicardium. When orthotropic models are used, the sheet angles either follow the radial direction or also vary linearly between the endocardium and the epicardium. It is with good reason that these studies have chosen such a simple fiber/sheet structure; as it is often difficult to obtain good detailed fiber/sheet data *in vivo*. However, it has been shown that using fiber/sheet angles that do not vary linearly through the thickness yields more realistic mechanical responses [23, 146].

In the present study we investigate the mechanical effect of models when based on experimentally obtained fiber/sheet orientations and on generic rule-based fiber/sheet orientations, as frequently used in the literature. We compare the two model results and use an invariant-based orthotropic constitutive equation [42]. A weakly coupled electromechanical model of the LV is employed where the LV anatomy is approximated as a truncated ellipsoid [73, 113]. The model is equipped with two sets of fiber and sheet arrangements. In the first arrangement, a generic rule-based dataset is used where fiber/sheet angles vary linearly in the transmural direction, as seen previously in, e.g., [22, 43, 53, 111, 113, 119, 142–145]. Several values for the linear change of fiber/sheet angles are examined. In the second arrangement, an experimentally-obtained dataset is used [24], where fiber/sheet angles vary spatially throughout the LV. Simulation results reveal that the generic fiber-sheet setup predicts an incorrect torsion up to five times larger than what is observed experimentally [147,148], as opposed to an experiment-based orthotropic setup where the torsion is found to be close to the expected range. However, lumped parameter results such as PV loops and cardiac output show only a small difference between the two setups.

4.2. Material and Methods

4.2.1. Electrophysiological modeling

The spread of electrical activation and re-polarization is described by the mono-domain equation

$$\beta_{\mathrm{m}} C_{\mathrm{m}} \frac{\partial V_{\mathrm{m}}}{\partial t} + \beta_{\mathrm{m}} I_{\mathrm{ion}}(V_{\mathrm{m}}, \boldsymbol{\eta}) = \nabla \cdot (\mathbf{g}_{\mathrm{m}} \nabla V_{\mathrm{m}}) + I_{\mathrm{tr}}, \tag{4.1}$$

where β_{m} is the membrane surface to volume ratio, C_{m} is the membrane capacitance, V_{m} is the transmembrane potential, I_{ion} is the density of the total ionic current which is a function of V_{m} and a set of state variables, $\boldsymbol{\eta}$, I_{tr} is a transmembrane stimulus current, and $\mathbf{g}_{\mathrm{m}}$ is the mono-domain conductivity tensor given by

$$\mathbf{g}_{\mathrm{m}} = g_{\mathrm{m,f}} (\mathbf{f}_0 \otimes \mathbf{f}_0) + g_{\mathrm{m,s}} (\mathbf{s}_0 \otimes \mathbf{s}_0) + g_{\mathrm{m,n}} (\mathbf{n}_0 \otimes \mathbf{n}_0), \tag{4.2}$$

with the eigenaxes $\mathbf{f}_0$ oriented along the fibers, $\mathbf{s}_0$ perpendicular to the fibers, but within a laminar sheet, and $\mathbf{n}_0$ perpendicular to the sheets, and $\mathrm{diag}(g_{\mathrm{m,f}}, g_{\mathrm{m,s}}, g_{\mathrm{m,n}})$ are the corresponding conductivities along the tensor axes. The model by Mahajan et al. [71], as developed for the rabbit ventricular myocytes, is employed to describe cellular dynamics.

4.2.2. Active and passive mechanical modeling

The Cauchy stress tensor $\boldsymbol{\sigma}$ is additively decomposed by

$$\boldsymbol{\sigma} = \boldsymbol{\sigma}_{\mathrm{p}} + \boldsymbol{\sigma}_{\mathrm{a}}, \tag{4.3}$$

where $\boldsymbol{\sigma}_{\mathrm{p}}$ refers to passive stresses, and $\boldsymbol{\sigma}_{\mathrm{a}}$ are active stresses intrinsically generated by the myocytes.

Passive stress component

With regard to the mechanical deformation the myocardium is characterized as an orthotropic material with the eigenaxes $\mathbf{f}_0$, $\mathbf{s}_0$ and $\mathbf{n}_0$ in the Lagrangian description. Using the multiplicative decomposition of the deformation gradient $\mathbf{F}$, into a volumetric $J^{1/3}\mathbf{I}$ and an isochoric $\overline{\mathbf{F}}$ part so that $\mathbf{F} = (J^{1/3}\mathbf{I})\overline{\mathbf{F}}$, where $J = \det\mathbf{F} > 0$ is the volume ratio, the Lagrangian direction vectors are transformed into their isochoric Eulerian counterparts by $\bar{\mathbf{f}} = \overline{\mathbf{F}}\mathbf{f}_0$, $\bar{\mathbf{s}} = \overline{\mathbf{F}}\mathbf{s}_0$ and $\bar{\mathbf{n}} = \overline{\mathbf{F}}\mathbf{n}_0$. An orthotropic, invariant-based strain-energy function [42] is used for describing the nonlinear passive behavior of the myocardium, which yields a frame-independent stress tensor. The strain-energy function described in [42] is here extended to include the multiplicative decomposition of the deformation gradient. Hence, the strain-energy function $\Psi = U(J) + \overline{\Psi}_{\mathrm{iso}}(\bar{I}_1) + \overline{\Psi}_{\mathrm{aniso}}(\bar{I}_{4\mathrm{f}}, \bar{I}_{4\mathrm{s}}, \bar{I}_{8\mathrm{fs}})$ is separated into a volumetric function $U(J)$ and two volume preserving functions $\overline{\Psi}_i$, $i \in \{\mathrm{iso}, \mathrm{aniso}\}$, which relate to the isotropic and the anisotropic behavior, respectively. A standard volumetric

function $U(J) = \mu_K \ln(J)^2/2$ is used, where the bulk modulus μ_K serves as a penalty parameter for enforcing incompressibility. The volume preserving functions $\overline{\Psi}_{\text{iso}}$ and $\overline{\Psi}_{\text{aniso}}$ are described as

$$\overline{\Psi}_{\text{iso}} = \frac{a}{2b}\{\exp[b(\bar{I}_1 - 3)] - 1\}, \tag{4.4}$$

and

$$\overline{\Psi}_{\text{aniso}} = \sum_{i=\text{f,s}} \frac{a_i}{2b_i}\{\exp[b_i(\bar{I}_{4i} - 1)^2] - 1\} + \frac{a_{\text{fs}}}{2b_{\text{fs}}}[\exp(b_{\text{fs}}\bar{I}_{8\,\text{fs}}^2) - 1], \tag{4.5}$$

respectively, where in total eight material parameters (a, b, $a_{(\text{f,s,fs})}$ and $b_{(\text{f,s,fs})}$) are needed to describe the isochoric orthotropic material behavior. By using the modified volume-preserving right Cauchy-Green tensor $\overline{\mathbf{C}} = \overline{\mathbf{F}}^{\text{T}}\overline{\mathbf{F}}$, the isochoric invariants in (4.4) and (4.5) are defined as $\bar{I}_1 = \text{tr}(\overline{\mathbf{C}})$, $\bar{I}_{4\,\text{f}} = \mathbf{f}_0 \cdot (\overline{\mathbf{C}}\mathbf{f}_0)$, $\bar{I}_{4\,\text{s}} = \mathbf{s}_0 \cdot (\overline{\mathbf{C}}\mathbf{s}_0)$ and $\bar{I}_{8\,\text{fs}} = \mathbf{f}_0 \cdot (\overline{\mathbf{C}}\mathbf{s}_0)$. As shown in [42], necessary conditions on (4.4) and (4.5) for material stability are $a, b, a_{(\text{f,s,fs})}, b_{(\text{f,s,fs})} \geq 0$ and $\bar{I}_{4\,\text{f}}, \bar{I}_{4\,\text{s}} > 1$. If any of the invariants are less than one, the term containing it is dropped from Eq. (4.5). The passive Cauchy stress tensor is then given by $\boldsymbol{\sigma}_{\text{p}} = 2J^{-1}\mathbf{F}(\partial\Psi/\partial\mathbf{C})\mathbf{F}^{\text{T}}$, which results into

$$\boldsymbol{\sigma}_{\text{p}} = p_{\text{h}}\mathbf{I} + 2J^{-1}[\overline{\psi}_1 \text{dev}\overline{\mathbf{b}} + \overline{\psi}_{4\,\text{f}}\text{dev}(\bar{\mathbf{f}} \otimes \bar{\mathbf{f}}) + \overline{\psi}_{4\,\text{s}}\text{dev}(\bar{\mathbf{s}} \otimes \bar{\mathbf{s}}) + \frac{1}{2}\overline{\psi}_{8\,\text{fs}}\text{dev}(\bar{\mathbf{f}} \otimes \bar{\mathbf{s}} + \bar{\mathbf{s}} \otimes \bar{\mathbf{f}})], \tag{4.6}$$

where $p_{\text{h}} = \text{d}U(J)/\text{d}J$ is used, $\overline{\mathbf{b}} = \overline{\mathbf{F}}\overline{\mathbf{F}}^{\text{T}}$ is the isochoric modified left Cauchy-Green tensor and $\text{dev}(\bullet) = (\bullet) - (1/3)[(\bullet) : \mathbf{I}]\mathbf{I}$ is the deviatoric operator in the Eulerian description [6]. Furthermore, in (4.6), the definitions

$$\overline{\psi}_i = \frac{\partial\Psi}{\partial\bar{I}_i}, \quad i = 1, 4\,\text{f}, 4\,\text{s}, 8\,\text{fs} \tag{4.7}$$

have been used.

Active stress component

The active stress tensor $\boldsymbol{\sigma}_{\text{a}}$ is defined as

$$\boldsymbol{\sigma}_{\text{a}} = J^{-1}S_{\text{a}}(\hat{\mathbf{f}} \otimes \hat{\mathbf{f}}), \tag{4.8}$$

where S_{a} is an active second Piola-Kirchhoff stress component, and $\hat{\mathbf{f}} = \bar{\mathbf{f}}/|\bar{\mathbf{f}}|$ is the normalized fiber direction vector. Following [60], in this study S_{a} is calculated using the single ordinary differential equation of the form

$$\dot{S}_{\text{a}} = \varepsilon(V_{\text{m}})(k_{S_{\text{a}}}\Delta V_{\text{m}} - S_{\text{a}}), \tag{4.9}$$

where $\varepsilon(V_{\text{m}})$ is a delay function controlling the rate of activation and relaxation of S_{a}, and $k_{S_{\text{a}}}$ regulates the amplitude of S_{a} as a function of the deviation of the transmembrane potential V_{m} from the myocyte resting potential V_{r}, i.e. $\Delta V_{\text{m}} = V_{\text{m}} - V_{\text{r}}$. Instead of the Heaviside function proposed in [60], we follow [144] and use a smoother delay function

$$\varepsilon(V_{\text{m}}) = \varepsilon_0 + (\varepsilon_\infty - \varepsilon_0)\exp\{-\exp[-\zeta_{\text{r}}(V_{\text{m}} - V_{\text{s}})]\}, \tag{4.10}$$

where ε_0 and ε_∞ are upper and lower bounds for the transmembrane potential $V_m \ll V_s$ and $V_m \gg V_s$, respectively, where V_s is a given phase shift, and ζ_r is the transition rate. Note, however, that there is an erratum in the delay function shown in Eq. (23) of [60].

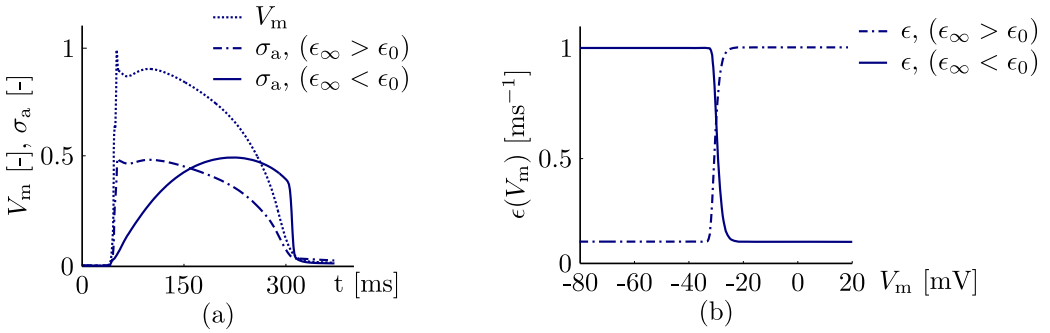

Figure 4.1.: (a) Transmembrane potential V_m, dotted curve, and corresponding delay in the active stress value using $\varepsilon_\infty > \varepsilon_0$, dash-dotted curve, and $\varepsilon_\infty < \varepsilon_0$, solid curve; for clarity the values are scaled in the image; (b) shape of the delay function $\varepsilon(V_m)$ using $\varepsilon_\infty > \varepsilon_0$, dash-dotted curve, and $\varepsilon_\infty < \varepsilon_0$, solid curve, when shifted by $V_s = -30\,\mathrm{mV}$ with the parameter $\zeta_r = 0.3\,\mathrm{mV}^{-1}$

With the choice $\varepsilon_\infty = 10\varepsilon_0$ an electro-mechanical delay between an upstroke of the action potential and the peak active stress, as illustrated in Figure 2 in [60], cannot be obtained. In order to reproduce the reported time course of S_a the relation $\varepsilon_\infty < \varepsilon_0$ must hold. The authors in [144] have used the original parameter relation, i.e. $\varepsilon_\infty = 10\varepsilon_0$, resulting in a delay function that goes from lower to higher values and, thus, to an active stress transient with non-physiologically short electro-mechanical delay (see Figure 3 in [144]). The resulting differences in the shape of $\varepsilon(V_m)$ and the active stress transients are illustrated in Figure 4.1.

4.2.3. Geometry

A simplified LV geometry is modeled as an ellipsoid truncated at the base using prolate spheroidal coordinates ξ_1, ξ_2 and ξ_3, see Figure 4.2. Using the focal position $d_i = \sqrt{a_i^2 - b_i^2}$, $i \in \{\mathrm{endo}, \mathrm{epi}\}$, where a_i and b_i are the polar and equatorial axes for the endocardial and epicardial borders, respectively, the prolate spheroidal coordinates is expressed in a Cartesian coordinate system by $x_1 = d_i \sinh\xi_1 \sin\xi_2 \cos\xi_3$, $x_2 = d_i \sinh\xi_1 \sin\xi_2 \sin\xi_3$ and $x_3 = d_i \cosh\xi_1 \cos\xi_2$. Epicardial and endocardial dimensions are chosen as $a_{\mathrm{epi}} = 19.3\,\mathrm{mm}$, $b_{\mathrm{epi}} = 12.7\,\mathrm{mm}$ and $a_{\mathrm{endo}} = 18.0\,\mathrm{mm}$, $b_{\mathrm{endo}} = 6.9\,\mathrm{mm}$, respectively, to arrive at a good match with an available image-based rabbit LV geometry [132]. The ξ_2-angle has a maximum value of 120° at the endocardial surface. When going in the ξ_1-direction along the epicardial surface the maximum ξ_2-angle is decreased so that the basal surface remains flat in the global X_3-direction.

Model *I* – Generic fiber-sheet setup

In model *I* a generic fiber-sheet setup is implemented. Fibers rotate linearly from α_{endo} at the endocardial border to α_{epi} at the epicardial border along the transmural axis ξ_1, with

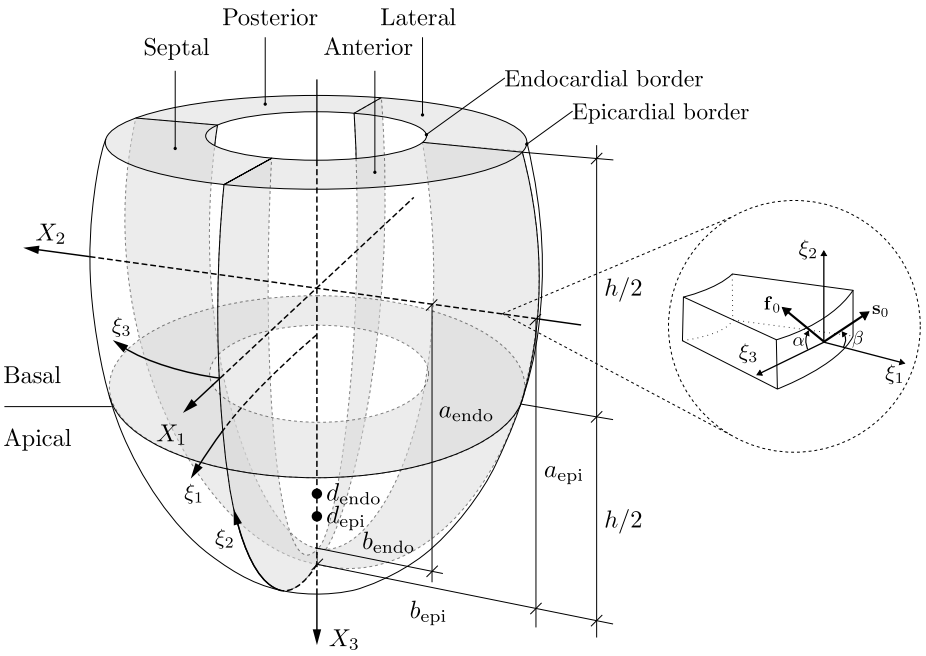

Figure 4.2.: Ellipsoidal model representing a rabbit LV with both the global X_1, X_2 and X_3 coordinates and the prolate spheroidal coordinates ξ_1, ξ_2 and ξ_3; where a_{endo}, b_{endo}, a_{epi}, b_{epi} are the polar and equatorial axes, and d_{endo} and d_{epi} are the focal positions for the endocardial and epicardial borders, respectively. The plane separating the basal and apical regions is half of the LV height h. The septal region lies in the X_1, X_2 quadrant, the anterior region lies in the $X_1, -X_2$ quadrant, the lateral region lies in the $-X_1, -X_2$ quadrant and the posterior region lies in the $-X_1, X_2$ quadrant. The fiber and sheet directions (Lagrangian form) are characterized by $\mathbf{f}_0$ and $\mathbf{s}_0$, respectively. The inclination angle, measured in the (ξ_2, ξ_3) plane, and the sheet angle, measured in the (ξ_1, ξ_2) plane, are characterized by α and β, respectively.

the inclination angle α measured in the (ξ_2, ξ_3) plane, see Figure 4.2. Similarly, a linear rotation of sheet angles from β_{endo} at the endocardial border to β_{epi} at the epicardial border is imposed in the transmural direction ξ_1 with the sheet angle β measured in the (ξ_1, ξ_2) plane, see Figure 4.2. Since both fiber and sheet orientations vary only along the transmural direction ξ_1, this setup is homogeneous in the circumferential and longitudinal directions ξ_2 and ξ_3. We, therefore, label this setup as *homogeneous*. Different combinations of fiber/sheet orientations, taken from the existing literature, is examined, see, e.g., [22, 43, 53, 111, 113, 119, 142–145]. The cases examined in this study are as follows:

(i) $\alpha_{\text{endo}} = -60^\circ$, $\alpha_{\text{epi}} = +60^\circ$, $\beta_{\text{endo}} = 0^\circ$, $\beta_{\text{epi}} = 0^\circ$,

(ii) $\alpha_{\text{endo}} = -45^\circ$, $\alpha_{\text{epi}} = +45^\circ$, $\beta_{\text{endo}} = 0^\circ$, $\beta_{\text{epi}} = 0^\circ$,

(iii) $\alpha_{\text{endo}} = -60^\circ$, $\alpha_{\text{epi}} = +85^\circ$, $\beta_{\text{endo}} = 0^\circ$, $\beta_{\text{epi}} = 0^\circ$,

(iv) $\alpha_{\text{endo}} = -60^\circ$, $\alpha_{\text{epi}} = +60^\circ$, $\beta_{\text{endo}} = -85^\circ$, $\beta_{\text{epi}} = +85^\circ$,

(v) $\alpha_{\text{endo}} = -45^\circ$, $\alpha_{\text{epi}} = +45^\circ$, $\beta_{\text{endo}} = -85^\circ$, $\beta_{\text{epi}} = +85^\circ$,

(vi) $\alpha_{\text{endo}} = -60°$, $\alpha_{\text{epi}} = +85°$, $\beta_{\text{endo}} = -45°$, $\beta_{\text{epi}} = +45°$.

We have here attempted to cover values which are commonly used in the literature, including sheet directions that are aligned in the radial direction ξ_1 (i.e. $\beta = 0°$) and inclination angles α which lead to a non-symmetry, as seen in the cases (iii) and (vi).

Model *II* – Experimentally-based LV fiber-sheet setup

To study the influence of structural heterogeneity, a fiber-sheet setup, which is based on experimental data, is implemented in model *II*. The fiber and sheet orientations are here assigned to fit the diffusion MRI data of Rohmer et al. [24] (Figure 4.3), which reported fiber and sheet angles in eight different regions corresponding to four circumferential segments of the LV, *septal, anterior, lateral* and *posterior* in each of the two apico-basal segments, *basal* and *apical*.

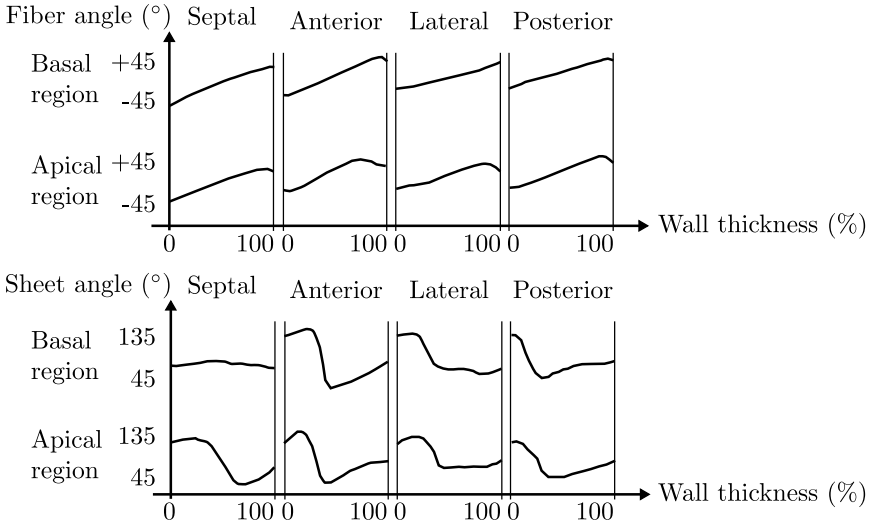

Figure 4.3.: Fiber and sheet angles through the wall thickness of the LV starting from the endocardium, adapted from [24].

A linear weighting function is used in between these regions to ensure a smooth transition of fiber and sheet angles. In contrast to model *I*, model *II* is spatially heterogeneous in all directions, not only in the transmural direction. We, therefore, label this setup as *heterogeneous*.

Torsion

To analyze the torsion of the LV we define the long axis to be aligned with the main direction of the septal wall and the short axis to be perpendicular to the long axis, and chosen to be close to the endocardial apex. Aligning the centroid of the cavity in the short axis images, taken from end diastolic and end systolic volumes, the torsion is calculated by tracking the movement of the mesh between these two configurations.

4.2.4. Material parameters

The mono-domain bulk conductivities in Eq. (4.2) are chosen to be $g_{\mathrm{m,f}} = 0.204\,\mathrm{Sm}^{-1}$, $g_{\mathrm{m,s}} = 0.102\,\mathrm{Sm}^{-1}$ and $g_{\mathrm{m,n}} = 0.037\,\mathrm{Sm}^{-1}$, which lead to conduction velocities of $0.6\,\mathrm{ms}^{-1}$, $0.4\,\mathrm{ms}^{-1}$ and $0.2\,\mathrm{ms}^{-1}$ along the principal tensor axes. Standard values of $C_{\mathrm{m}} = 1\,\mu\mathrm{F\,cm}^{-2}$ and $\beta_{\mathrm{m}} = 1400\,\mathrm{cm}^{-1}$ are chosen for the membrane capacitance and the membrane surface to volume ratio, respectively.

Mechanical material parameters are summarized in Table 4.1. Passive material parameters are adapted from [42] where the constitutive model was fitted to experimental data reported by Dokos et al. [51]. Active material parameters are in part adapted from [60] and in part

Passive stress	Active stress	Pressure term
$\mu_{\mathrm{K}} = 3333\,\mathrm{kPa}$	$k_{S_{\mathrm{a}}} = 0.50\,\mathrm{kPa\,mV}^{-1}$	$C = 0.2\,\mathrm{ml\,mmHg}^{-1}$
$a = 0.333\,\mathrm{kPa}$	$V_{\mathrm{r}} = -86.796\,\mathrm{mV}$	$R = 750\,\mathrm{mmHg\,ms\,ml}^{-1}$
$b = 9.242$ (-)	$V_{\mathrm{s}} = -80.0\,\mathrm{mV}$	$C_{\mathrm{p}} = -900\,\mathrm{mmHg\,ml}^{-1}$
$a_{\mathrm{f}} = 18.535\,\mathrm{kPa}$	$\varepsilon_0 = 1.0\,\mathrm{ms}^{-1}$	
$b_{\mathrm{f}} = 15.972$ (-)	$\varepsilon_\infty = 0.1\,\mathrm{ms}^{-1}$	
$a_{\mathrm{s}} = 2.564\,\mathrm{kPa}$	$\zeta_{\mathrm{r}} = 0.1\,\mathrm{mV}^{-1}$	
$b_{\mathrm{s}} = 10.446$ (-)		
$a_{\mathrm{fs}} = 0.417\,\mathrm{kPa}$		
$b_{\mathrm{fs}} = 11.602$ (-)		

Table 4.1.: Material parameters used in both analytical and numerical calculations. The parameters for the passive state are adapted from [42], the parameters for the active state are adapted from [60], and the pressure term is chosen to give a realistic pressure-volume response.

to achieve an electro-mechanical delay of 110 ms between the peak action potential and the peak active stress [149], which leads the parameter relation of the delay function to be $\varepsilon_\infty = \varepsilon_0/10$. The pressure parameters (see Section 4.2.6) are tuned such that realistic pressure-volume loops are obtained, and to keep the pressure calculations numerically stable.

4.2.5. Numerical solution

The finite element method is employed for the spatial discretization of the mono-domain equation (4.1). Two overlapping finite element meshes of the same ellipsoidal LV geometry are generated, a fully structured coarser hexahedral mesh for solving the mechanics, and a fully unstructured hybrid mesh with an average resolution of $\sim 200\,\mu\mathrm{m}$, using an image-based mesh generation technique [150], as implemented in the commercial mesh generator Tarantula (CAE Software Solution, Eggenberg, Austria) for solving the electrics. In both meshes, fiber and sheet orientations are interpolated onto the barycenters of the finite elements. The mechanical mesh consists of 5 406 nodes and 5 310 hexahedral mixed $Q1/P0$ finite elements (see, e.g., [151]), whereas the electrical mesh consists of 1 054 146 nodes and 1 201 507 hybrid finite elements using linear weighting functions [152].

Using overlapping grids of different resolutions is a natural choice when considering the vastly different constraints imposed by the physics of the electrical and the mechanical problems. Electrical transients are fast and act on time scales in the μs range, which translates into steep depolarization wavefronts of small spatial extent in the sub-millimeter range, thus necessitating the use of fine spatial resolutions $\ll 250\,\mu$m to compute solutions with reasonable accuracy. On the other hand, mechanical processes tend to occur at larger space and slower time scales, and, thus, coarser spatial discretizations can be used. In the weakly coupled approach applied in this study, Eq. (4.1) is solved on the electrical mesh first, and electrical quantities required for computing the active stress transients, i.e. V_{m}, are then transferred to the integration points of the mechanical mesh.

The temporal discretization of the mono-domain equations relies on an implicit-explicit (IMEX) scheme where the diffusion term is treated implicitly and the reaction term explicitly, using a time step of $20\,\mu$s. The linear system is solved in parallel by employing a block Jacobi pre-conditioner with an iterative Conjugate Gradient solver, using an Incomplete LU (ILU(0)) factorization as a sub-block pre-conditioner [153]. The system of ODEs in the model by Mahajan et al. [71] is solved using the Rush-Larsen method [154] with several optimizations [111]. The Cardiac Arrhythmia Research Package (CARP) [155], which is built on top of the MPI-based library PETSc [153], is employed to solve Eq. (4.1). Numerical aspects have been described in detail elsewhere [156]. The equations (4.3) together with (4.6) and (4.8) are implemented and solved using the finite element software FEAP [8]. Both grids are partitioned for parallel execution using parMETIS [157].

4.2.6. Initial values and boundary conditions

Electrics

An initial state vector is computed for the model by Mahajan et al. [71] by pacing a single cell at a pacing cycle length of 350 ms until arriving at a stable limit cycle. The state vector $\boldsymbol{\eta}$ is then used to populate the LV model. Transmembrane current injection applied to the endocardial surface at $t = 0$ ms initiates a transmural activation wavefront. With this protocol, the whole endocardium activates synchronously. Electrical activation delays within the endocardium, as observed in the presence of a Purkinje system, and remains unaccounted for. Here 350 ms of activity is simulated to cover one full depolarization and re-polarization cycle throughout the entire LV.

Mechanics, circulatory components and pressure-volume loops

All finite elements on the endocardial surface of the LV are subjected to a follower pressure load p. Displacement boundary conditions (BCs) are imposed over the entire base of the LV, i.e. where $\xi_2 = \xi_{2\,\mathrm{max}}$ for all ξ_3 and ξ_1 (the subindex max denotes the maximum coordinate value), preventing any movement in the ξ_2-direction. Additional displacement BCs are imposed on a subset of nodes which are located in the basal plane along the epicardial surface, i.e. where $\xi_1 = \xi_{1\,\mathrm{max}}$, $\xi_2 = \xi_{2\,\mathrm{max}}$ and for all ξ_3, to restrict the movement in the ξ_3-direction. These BCs are summarized in Table 4.2.

BC	Coordinates		Description
$t_\mathrm{n} = -p$	$\xi_1 = \xi_{1\,\mathrm{min}}$	for all ξ_2, ξ_3	Endocardial surface
$u_{\xi_2} = 0$	$\xi_2 = \xi_{2\,\mathrm{max}}$	for all ξ_1, ξ_3	Basal surface
$u_{\xi_3} = 0$	$\xi_1 = \xi_{1\,\mathrm{max}}$ $\xi_2 = \xi_{2\,\mathrm{max}}$	for all ξ_3	Outer boundary at the basal surface

Table 4.2.: Mechanical boundary condition (BC) for the LV in terms of prescribed traction $\mathbf{t}$ and displacement $\mathbf{u}$. The component t_n of $\mathbf{t}$ is the normal to the endocardial surface on which the pressure p acts. The components u_{ξ_1}, u_{ξ_2}, u_{ξ_3} of $\mathbf{u}$ are the displacements in the directions ξ_1, ξ_2, ξ_3 shown in Figure 4.2, where the index max and min denotes the maximum and minimum possible coordinate in the respective direction.

The endocardial pressure load p is calculated in five consecutive steps (i)–(v): (i) initialization phase with linear increase in p to the end diastolic pressure (EDP); before the electrical activation has started, the pressure increases first linearly from 0 to 20 mmHg, which is considered the EDP [78]. (ii) Isochoric LV contraction phase: electrical activation starts the isochoric contraction phase where both mitral and aortic valves are closed. Following [79] this is implemented by using the iteration

$$p_{n+1} = p_n + (V_{n+1} - V_n)/C_\mathrm{p}, \tag{4.11}$$

where C_p serves as a penalty parameter that is chosen to give a robust convergence. The iteration is considered to be converged using the criterion $\|V_{n+1} - V_n\|/\|V_n\| < 0.01$. (iii) Ejection phase where p reaches 95 mmHg [78]. The ejection phase starts in response to the opening of the aortic valve. The pressure is modeled using a two element Windkessel model described as

$$C\frac{\mathrm{d}p}{\mathrm{d}t} + \frac{p}{R} = -\frac{\mathrm{d}V}{\mathrm{d}t}, \tag{4.12}$$

where C and R relate to the arterial compliance and resistance, respectively. (iv) Isochoric LV relaxation phase: when $\mathrm{d}V/\mathrm{d}t$ becomes positive (reversed blood flow), the aortic valve closes. The pressure at the instant of flow reversal is considered the end systolic pressure that starts isochoric relaxation, again modeled by using the pressure iteration given through Eq. (4.11). (v) Filling phase with linear pressure increase to EDP: finally, when p dropped to 12.5 mmHg [78], the mitral valve opens and passive filling starts. Again, this phase is modeled as a linear increase of p up to EDP.

The specific parameters C, R and C_p used in the subsequent analyses are provided in Table 4.1.

4.2.7. Lumped parameters

The average thickness of the LV wall is calculated using the Gauss divergence theorem. Defining h_ed and h_es as the wall thickness corresponding to end diastolic volume (EDV)

and the end systolic volume (ESV), respectively, the fractional thickening h_f is calculated as $h_\mathrm{f} = 100 \cdot (h_\mathrm{es} - h_\mathrm{ed})/h_\mathrm{ed}$. As a coarse measure for examining incompressibility the fractional change in the myocardial volume, say V_f, is calculated as $V_\mathrm{f}(t) = 100 \cdot (V_\mathrm{wall}(t) - V^0_\mathrm{wall})/V^0_\mathrm{wall}$, where $V_\mathrm{wall}(t)$ and V^0_wall are the volumes of the myocardial wall at time t and in the initial unloaded configuration, respectively. The largest change in the volume fraction $V_\mathrm{f}(t)$ is denoted by $V_\mathrm{f}^\mathrm{max}$, which may be used as an approximate metric to gauge how well the incompressibility constraint is enforced in the simulation. Furthermore, stroke volume SV is defined as $\mathrm{SV} = \mathrm{EDV} - \mathrm{ESV}$, cardiac output CO is defined as $\mathrm{CO} = \mathrm{SV} \cdot \mathrm{HR}$, where HR is the heart rate, and the ejection fraction EF is defined as $\mathrm{EF} = 100 \cdot \mathrm{SV}/\mathrm{EDV}$. Although only one heart beat is simulated, HR is assumed to follow the simulated activity time of 350 ms, giving a HR of about 171 beats per minute.

4.3. Results

4.3.1. Validation of the implementation

To test the numerical framework, an analytical test case is designed and explored. A unit myocardium tissue cube with mean material directions is considered. The cube has the fiber, sheet and sheet-normal directions along the global coordinate system (X,Y,Z), and the material directions are according to $[\mathbf{f}_0] = [1,0,0]^\mathrm{T}$, $[\mathbf{s}_0] = [0,1,0]^\mathrm{T}$ and $[\mathbf{n}_0] = [0,0,1]^\mathrm{T}$, as shown in Figure 4.4(a). The cube can freely deform, and it is subjected to an active stress S_a resulting in a contraction in the global X-direction, i.e. the fiber direction. The material is assumed to be incompressible and, therefore, the cube must expand in the global Y and Z-directions. Thus, the corresponding deformation gradient is $\mathbf{F} = \mathrm{diag}(\lambda_\mathrm{f}, \lambda_\mathrm{s}, \lambda_\mathrm{n})$, where the stretch λ_f in the fiber direction is $\lambda_\mathrm{f} < 1$ and the stretches in the sheet and sheet-normal directions are $\lambda_\mathrm{s} > 1$ and $\lambda_\mathrm{n} > 1$, respectively. As the unit cube is free to deform, the stress

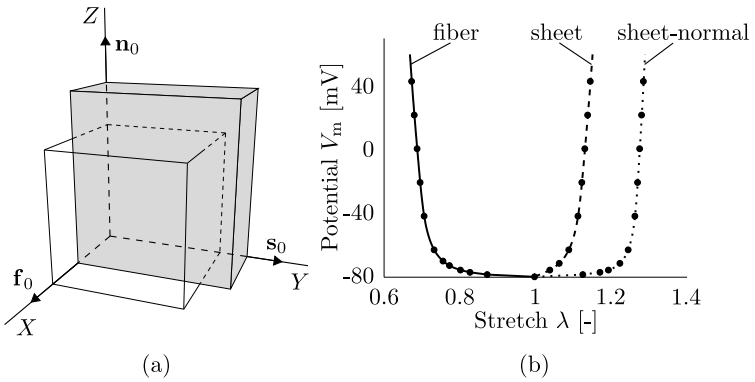

Figure 4.4.: (a) Deformation of a unit cube before deformation and after activation in the fiber direction (X), shown in gray; (b) stretch responses as a function of the membrane potential V_m. Fiber, sheet and sheet-normal stretches are illustrated by solid, dashed and dotted curves, respectively, and the circles show the corresponding finite element results.

at equilibrium is zero for all components of the Cauchy stress matrix and the Lagrange

multiplier p_{h} is readily determined from the relation $\sigma_{33} = 0$. Using the condition of a volume preserving incompressible material ($J = \det\mathbf{F} = 1$), the following nonlinear system of equations may be obtained as

$$\sigma_{11} = 2\overline{\psi}_1(\lambda_{\mathrm{f}}^2 - \lambda_{\mathrm{n}}^2) + 2\overline{\psi}_{4\mathrm{f}}\lambda_{\mathrm{f}}^2 + S_{\mathrm{a}} = 0, \tag{4.13}$$

$$\sigma_{22} = 2\overline{\psi}_1(\lambda_{\mathrm{s}}^2 - \lambda_{\mathrm{n}}^2) + 2\overline{\psi}_{4\mathrm{s}}\lambda_{\mathrm{s}}^2 = 0, \tag{4.14}$$

$$\lambda_{\mathrm{f}}\lambda_{\mathrm{s}}\lambda_{\mathrm{n}} = 1. \tag{4.15}$$

Keeping in mind that $\overline{\psi}_{4\mathrm{f}}$ vanishes if $\lambda_{\mathrm{f}} < 1$ (see [42]), which is always the case in this particular example, the system of Eqs. (4.13)–(4.15) can be solved for λ_{f}, λ_{s} and λ_{n} for a given value of the active stress S_{a}. This system is solved using the MATLAB function *fsolve()* (Matlab R2012a, The Mathworks, Nantucket, USA). The material parameters used are taken from Table 4.1. The same problem is solved with FEAP, using $Q1/P0$ finite elements, and the resulting stretches are compared to the analytical solution for several values of the active stress S_{a} computed using a linear increase of the transmembrane potential V_{m} from the resting potential $V_{\mathrm{m}} = V_{\mathrm{r}}$ to $V_{\mathrm{m}} = +50\,\mathrm{mV}$. The results are summarized in Figure 4.4(b) and show a good agreement between the analytical result and the numerical solution; the different stretches in the figure are abbreviated by λ.

4.3.2. Effect of fiber/sheet arrangement upon mechanical contraction

To study the effect of the arrangement of fibers and laminae, pressure-volume (PV) loops are computed for a full cardiac cycle by using the models *I* and *II*. Both models are subjected to the same stimulation protocol and boundary conditions; the only difference is the fiber and sheet arrangement.

The PV loops predicted by the models *I* and *II* are in good agreement with those observed experimentally [78]. Figure 4.5(a) shows a comparison between model *II* and experimental data. Volume transients for this comparison are normalized to account for the difference in the initial LV volumes. Figure 4.5(b) compares the PV loops predicted by model *I* (case (i), Section 4.2.3, chosen as a representative case for the generic distributions), and model *II*. Overall, both models predict very similar PV loops. The only minor difference is that model *II* exhibits a noticeably larger EDV while no significant differences are found in ESV. Moreover, no major differences are observed in other lumped metrics that characterize the mechanical performance globally. A comparison of the parameters h_{f}, $V_{\mathrm{f}}^{\max}$, HR, SV, EF and CO is summarized in Table 4.3, again using case (i), Section 4.2.3, as a representative case for model *I*. The stroke volume SV is slightly lower with model *I*, and thus, since HR is the same, CO is lower too. The relatively small change in the volume fraction $V_{\mathrm{f}}^{\max}$ of the wall indicates that the chosen bulk modulus is large enough to enforce the prescribed incompressibility constraint.

While PV loops and some other metrics of the global mechanical function are qualitatively and quantitatively similar, in several other aspects the model predictions are strikingly different. In the model *I* the apex moves only along the apico-basal direction, aligned with

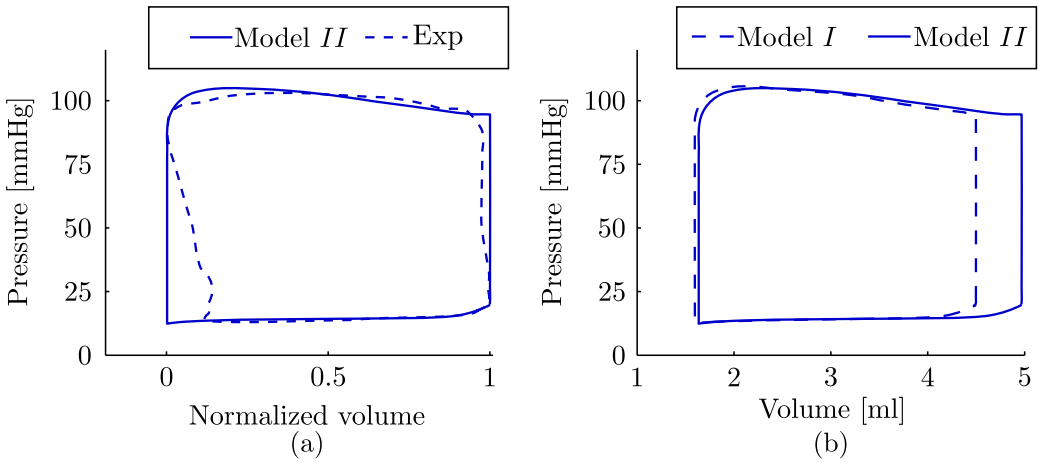

Figure 4.5.: (a) Comparison of pressure-volume (PV) loops between model *II* and experimental data [78]. Volume transients for this comparison are normalized to account for the difference in the initial LV volumes; (b) comparison of PV loops between the models *I* and *II*. As a representative case for model *I* the fibers and sheets vary linearly between $\alpha_{\text{endo}} = -60^\circ$, $\alpha_{\text{epi}} = +60^\circ$ while $\beta_{\text{endo}} = \beta_{\text{epi}} = 0^\circ$, respectively (case (i), Section 4.2.3).

Result	Model *I*	Model *II*	Experiment
h_{f} (%)	33	29	35.2[a]
$V_{\text{f}}^{\max}$ (%)	−0.42	−0.51	−7.2[b]
HR (bmp)	171	171	198[c]
SV (ml)	2.7	3.1	1.8[c]
EF (%)	61	63	53[c]
CO (l/min)	0.46	0.53	0.421[c]

Table 4.3.: Comparison of results between the models *I*, *II* and the experimental data: h_{f} = fractional thickening, $V_{\text{f}}^{\max}$ = largest change in volume fraction of the wall, HR = heart rate, SV = stroke volume, EF = ejection fraction, CO = cardiac output. Experimental values are taken from: [a] [158]; [b]average value of the through-the-thickness volume change [159]; [c] [160].

the global X_3-direction in our setup, whereas in the model *II* a significant shift of the apex towards the septal wall occurs, see Figure 4.6(b). A significant quantitative difference is observed with regard to torsion. While the average torsion, measured in the short axis plane, predicted by model *II* is 4.5° (Figure 4.6(c)), a vastly larger torsion is predicted by the generic fiber and sheet setups used in model *I*, which results in, e.g., a torsion of 51° for case (i), Section 4.2.3 (see Figure 4.6(d)). A summary of the torsion which results from all generic fiber/sheet setups is shown in Table 4.4, where the values range from 33–72°. The radial contractions from EDV to ESV, i.e. the local changes of the endocardium and epicardium in the radial direction visible in Figure 4.6(c)-(d), are analyzed along the septal-lateral and posterior-anterior directions. In both models *I* and *II*, this contraction is quite similar and match experimental data quite well [161], except in the septal-lateral direction at the epicardial border where model *II* is significantly closer to the experimental

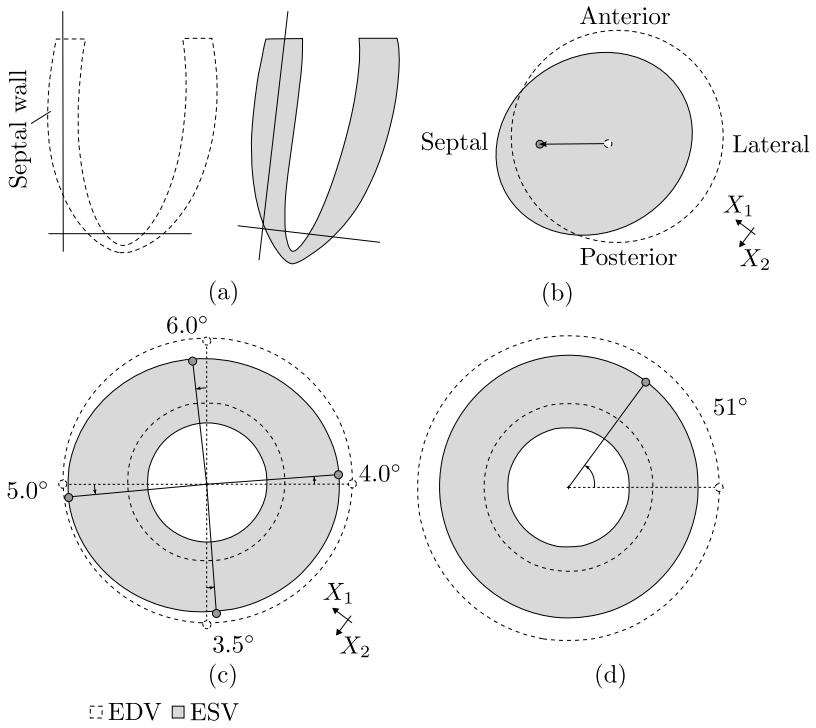

Figure 4.6.: Geometries at EDV shown by dashed curves, and at ESV shown by solid curves filled with gray areas: (a) the short axis plane is perpendicular to the long axis plane, which is always aligned with the main direction of the septal wall; (b) the outlined epicardial surface viewed from the apex towards the base of the LV. The apex in both EDV and ESV are marked with a circle and show the movement of the apex towards the septal region; (c) torsion at the short axis plane for the model *II*. The average torsion is 4.5°; (d) torsion at the short axis plane for the model *I*, case (i) (Section 4.2.3). The torsion is the same for all regions and is 51°.

values than model *I* (all cases).

Case (i)	Case (ii)	Case (iii)	Case (iv)	Case (v)	Case (vi)
51°	72°	35°	47°	62°	33°

Table 4.4.: Resulting torsion using the cases as outlined in Section 4.2.3.

A further fundamental difference is observed with regard to the first principal stress σ_I. Model *I* predicts a higher stress in the mid-myocardial band, whilst model *II* predicts a gradient of stress from lower to higher transmurally from endocardium to epicardium. This is illustrated in Figure 4.7, which visualizes σ_I in a cross section through the septal and lateral wall, again using case (i), as a representative case for model *I*.

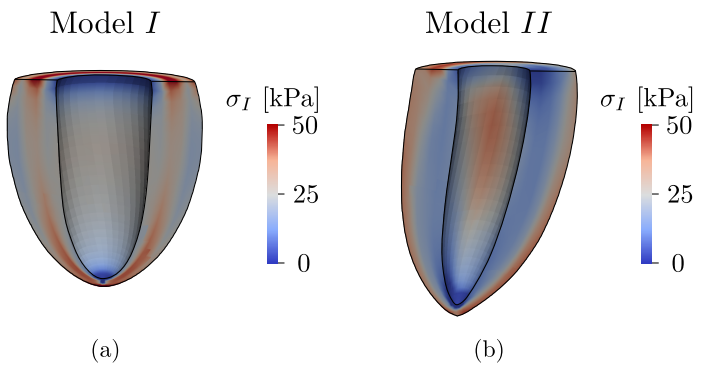

(a) (b)

Figure 4.7.: First principal stress σ_I: (a) in model I; (b) in model II.

4.4. Discussion

A computational model of LV electro-mechanics has been used to investigate the influence of spatial heterogeneity of the structural (orthotropic) components on mechanical contraction. Two models (I and II) are designed so that they differed only in terms of the fiber and sheet arrangements. As in virtually all recent modeling studies of ventricular electromechanics, see, e.g., [58, 60, 113], several simplifying assumptions are made, which may result in model predictions that deviate from experimental observations in one or the other aspect. While these shortcomings warrant caution when drawing general physiological conclusions, it is possible to study whether a given factor is a relevant contributor to the overall response of the system or not.

Although the notion that tissue orthotropy and its spatial structural heterogeneity may play an important role in ventricular mechanics is widely accepted [77], most organ-scale modeling studies reported in the literature refrained from accounting the inherent heterogeneity. To the best of our knowledge, there are only a handful of studies that model the LV as an orthotropic material, see [42] for a review. In fact, most of the modeling studies represent both electrophysiology and mechanics of the ventricles as transversely isotropic materials and, thus, ignore the influence of orthotropy. One reason for this may be the inherent difficulty in the measurements of electrical conductivity and mechanical stress, which has led to an ongoing debate on the 'exact' ratios between the eigenvalues and the material parameters along the axes $\mathbf{f}_0$, $\mathbf{s}_0$ and $\mathbf{n}_0$. However, due to the convincing evidence provided by various studies using histological [28, 36, 66] and MRI-based imaging techniques [24, 162], and measuring the mechanical properties of the passive ventricular myocardium [51], there is a broad consensus that electrical and mechanical properties of cardiac tissue are best characterized as orthotropic.

In this work we studied the relative influence of heterogeneous orthotropic fiber/sheet structures on mechanical contraction. While the predictions of both models (homogeneous and heterogeneous) are similar and matched fairly well with the experimental data in terms of most lumped system parameters such as PV loops, strikingly different mechan-

ical responses are observed in several other aspects. Most notably, this is the case with torsion, which turns out to be significantly smaller when the structure is considered as heterogeneous.

The simulation results strongly suggest that heterogeneity of the fiber/sheet structure plays an important (non-negligible) role in the mechanical LV contraction and, consequently, should be accounted for in computational models.

4.4.1. Effects of structural heterogeneity

Simulations using model *I* predicted a torsion which is much higher than the average torsion of 4.5° predicted by model *II*. For example, case (i) (Section 4.2.3), predicted an end systolic torsion of 51°. Experimental measurements suggest that the end systolic torsion is in the range of $\sim$ 8-12° [147, 148]; hence model *II* slightly underestimates torsion whereas model *I* led to a significant overestimation.

When compared to physiological measurements both models suffered from shortcomings. The pronounced torsion predicted by model *I* may be attributed to the simplified representation of the LV geometry and the absence of the right ventricle, which would likely restrain torsion significantly, particularly in the septal region. On the other hand, despite the more realistic end systolic torsion in model *II*, it led to some non-physiological predictions that are not present in model *I*. In particular, model *II* predicted a longitudinal elongation of the LV, which is in contradiction to the longitudinal shortening, as it is observed in experiments [163]. Potential reasons are: (i) the fiber angles according to Rohmer et al. [24], as used in the model *II*, tend to be smaller than those observed in histological studies [22] upon which most approaches are built upon. Thus, due to the reduced fiber component along the long axis of the LV the maximum active stress generated, regulated by the parameter k_{S_a}, was not sufficiently large and the cavitary pressure of the LV may have been the dominating factor; (ii) the mapping of orthotropic data from an anatomically realistic model onto a simplified ellipsoidal model may have led to distortions due to the geometrical differences between an idealized ellipsoid and a real ventricular geometry. This difficulty could be circumvented by using a dataset that provides both anatomical accurate representations of the ventricles obtained via high-resolution MRI, and structural information acquired by, e.g., diffusion tensor MRI. A further potential discrepancy stems from the fact that the complex trabeculation of the endocardium remains unaccounted for in our model, a limitation that is shared with all other modeling studies on ventricular mechanics; (iii) the mean values as presented in [24] are used and they are linearly interpolated, however, the noise and variance in these data are big. The data were averaged over large sectors of the ventricles – more detailed data on a per voxel base is not available.

A further difference between the models is the first principal stress σ_I , as illustrated in Figure 4.7. This seems to be an indirect effect of the reduced torsion in the model *II*, which, in turn, attenuated the influence of the applied boundary conditions.

Stroke volume SV, ejection fraction EF and cardiac output CO are all close to experimentally obtained values, as seen in Table 4.3. Thus, similar to the argument concerning the PV loops, with these values it is only possible to partially differentiate between, or determine the accuracy of, the models. The discrepancy between experimentally observed and simulated values for the compressibility of wall volume $V_{\mathrm{f}}^{\max}$ is explained by the fact that ventricular vascularization is not represented in the model. While myocardial tissue is nearly incompressible and, therefore, it is modeled as an incompressible material, the ventricles as a whole are not since the wall volume reduces during systole due to blood being squeezed out of the coronary arteries [159].

4.4.2. Limitations of the study

In our models we have made a few simplifying assumptions and these have to be considered when interpreting the reported results. One limitation is the use of a stylized geometry in which the LV anatomy is approximated by an ellipsoidal shape. Further, a mono-ventricular, not a bi-ventricular geometry is used, thus, the LV is modeled in absence of the right ventricle. Apart from the simplified representation of the macro-anatomy, the complex structure of the ventricular endocardium, consisting of structures such as trabeculae and papillary muscles, is approximated by a smooth endocardial surface. Unlike in electrophysiological modeling studies, where these structures are included in models [110], there have not been any reports yet in the mechanical modeling. Most likely this is due the significant increase in mesh density required to resolve these finer anatomical details, which entails a substantial increase in computational costs [164]. Considering the limited performance of current solver techniques used in modeling ventricular mechanics it suggests that this is not feasible yet.

In the literature a simplified phenomenological model of electro-mechanical coupling is proposed where the generated active stress depends only on the transmembrane potential [60, 144], ignoring all major physiological factors implicated in the process of active stress generation such as calcium transients, the interactions of calcium with myofilaments and metabolic aspects as well as length and velocity dependencies [63]. Finally, as in most previous studies [43, 73, 79], the electrical and mechanical models are weakly coupled. While strongly coupled approaches are likely to be key when subtle electro-mechanical effects have to be captured, most modeling studies opted for implementing a weak coupling approach. This is mainly due to the increased complexity of computation schemes and potential problems with numerical instabilities, although those issues are being addressed [58].

In this study, we have focused on the heterogeneity of the myocardial structure components. Another factor which may alter the simulation results significantly is a heterogeneity of the myocardial material parameters. Such varying material properties, both transmurally, longitudinally and circumferentially could be included in a future study. However, due to the lack of experimental data available on regional-specific myocardial material properties such a study is not feasible at the moment. Despite the numerous limitations,

which are shared with most contemporary modeling studies on cardiac electro-mechanics the relative difference due to a change in the myocardium structure, namely the use of rule-based versus experiment-based data on fiber and sheet arrangements, is a clear indication that heterogeneity in the orthotropic structure property is a relevant factor and as such it should be accounted for in computational models of ventricular mechanics.

Acknowledgement

This project was partly supported by the SFB Research Center 'Mathematical Optimization and Applications in Biomedical Sciences', project F3210-N18, granted by the Austrian Science Fund. This support is gratefully acknowledged.

5. MODELING THE DISPERSION IN CARDIAC FIBER AND SHEET ORIENTATIONS

Abstract We present an approach to model the dispersion of fiber and sheet orientations in the myocardium. By utilizing structure parameters an existing orthotropic and invariant-based constitutive model developed to describe the passive behavior of the myocardium is augmented. Two dispersion parameters are fitted to experimentally-observed angular dispersion data of the myocardial tissue. Computations are performed on a unit myocardium tissue cube and on a slice of the left ventricle (LV) indicating that the dispersion parameter has an effect on the myocardial deformation and the stress development. The use of fiber dispersions relating to a pathological myocardium had a rather big effect. The final example represents an ellipsoidal model of the LV indicating the influence of fiber and sheet dispersions upon contraction over a cardiac cycle. While only a minor shift in the pressure-volume loops between the cases with no dispersions and with fiber and sheet dispersions for a healthy myocardium was observed, a remarkably different behavior is obtained with a fiber dispersion relating to a diseased myocardium. In future simulations this dispersion model for myocardial tissue may advantageously be used together with models of, e.g., growth and remodeling of various cardiac diseases.

5.1. Introduction

The left ventricle (LV) is the main pumping chamber of the heart supplying blood through the circulatory system to the entire body. The LV builds up the necessary pressure by active contraction where the electrical activation of the heart triggers a cascade of events leading to a shortening of the cardiac myocytes. Myocytes are arranged in a highly organized fashion, following a right-handed helical pathway from the endocardium towards the mid-wall, and a left-handed helical pathway from the mid-wall towards the epicardium [22–24]. This prevailing myocyte orientation is usually referred to as 'fiber orientation'. In addition, fiber bundles are arranged into laminar sheets of four to six cell layers, where the prevailing sheet orientation also varies in the transmural and apico-basal directions [24,25,27,28]. At any point in the LV, the structural arrangement of myocytes is reflected by three orthogonal directions along which both electrical and mechanical material parameters are different, thus requiring to model the electrical and mechanical responses of the myocardium as an *orthotropic* material. These preferred directions are along the fibers, transverse to the fibers but within a laminar sheet, and perpendicular to the sheets; these directions are thus called the fiber, sheet and sheet-normal directions, respectively.

In a healthy heart, the fiber alignment follows very closely this helical structure with only small angular dispersion (AD) in the range of $\sim$ 12-15°, whereas in a diseased heart such as hypertrophic cardiomyopathy (HCM) or myocardial infarction (MI) the AD may locally increase by $\sim$ 65% (at foci points within the septal wall) [29–31] or $\sim$ 50% (at the site of infarction) [32–34]. Furthermore, the dispersion of the fibers has been shown to have a circular distribution, they are not located in plane [165]. Less is known about the structural arrangement of laminae. Due to the importance of sheet orientation in myocardial wall thickening it has been speculated that the dispersion of sheet orientations may play a significant physiological role [38]. There are a few studies available discussing quite a large dispersion of the sheet structure, even in healthy hearts [35–37]. Although to our knowledge there are no experimental reports available that quantify sheet dispersion in the diseased myocardium, it is likely the case that dispersion is also elevated when compared with healthy conditions. To the authors' knowledge there are no recently published biomechanical cardiac models available that consider dispersion, the latest are [23, 31]; none of them include sheet dispersion. Hence, the present study focuses on the development of an approach to model fiber and sheet dispersions using an invariant-based framework. A previously published orthotropic and invariant-based model which characterizes the nonlinear passive behavior of myocardium [42] is here augmented with structure parameters allowing the quantification of the degree of dispersion based on measured fiber and sheet angle data. The structure parameters are based on a distribution function developed for the collagen structure of arteries [166], and is here used for the fiber and sheet dispersions.

Cardiac simulations have electrical and mechanical components rendering the modeling to a multi-physics problem. Electro-mechanical models need high spatio-temporal resolution, making the entire problem computationally expensive; advanced numerics and highly optimized parallel implementations are needed to keep simulations tractable. Therefore, a natural choice is the use of overlapping grids of different resolution because the constraints differ significantly between the imposed physics of the electrical and the mechanical problem. The electrical transients are fast, acting on time scales in the μs range, which translates into steep depolarization wavefronts of small spatial extent in the sub-millimeter range, thus requiring the use of fine spatial resolutions $\ll 250\mu$m to compute solutions with reasonable accuracy. On the other hand, mechanical processes tend to occur at larger space and slower time scales, and, thus, coarser spatial discretizations can be used. The electromechanical coupling of the spatio-temporal patterns of the electrical activity and the active stress transients in the myocytes are either modeled as active stresses or strains [52] acting along the fiber's orientation in an Eulerian description [58]. The resulting mechanical deformations in our model is largely determined by the passive hyperelastic properties of the tissue and the generated active stresses both incorporating the dispersed structure of the tissue.

Our simulation indicates that the dispersion has a relevant influence on the mechanical response of the myocardium both during passive deformation and active contraction, by reducing the stress response and changing the deformation pattern. When including the

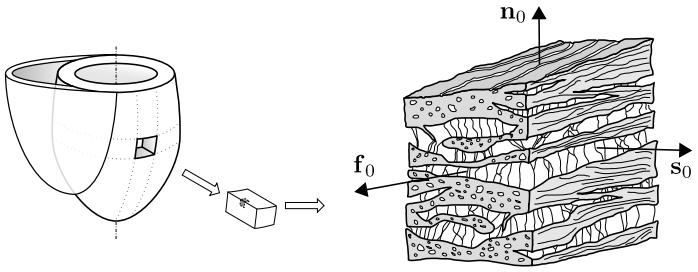

Figure 5.1.: Schematic representation of the structure of the myocardium showing the fiber-reinforced laminar composite that comprises the averaged fiber, sheet and sheet-normal directions in a continuum model, characterized by $\mathbf{f}_0$, $\mathbf{s}_0$ and $\mathbf{n}_0$, respectively.

dispersion parameter in a ventricular simulation incorporating electrical activation the pressure volume loop is considerably altered. Since the degree of dispersion is significantly elevated under various cardiac pathologies there is a need to consider dispersion when modeling myocardial tissue in diseased states.

5.2. Modeling Framework

5.2.1. Kinematics

The structure of the myocardium may be described by three orthogonal direction vectors $\mathbf{f}_0$, $\mathbf{s}_0$ and $\mathbf{n}_0$ corresponding to the mean fiber, sheet and sheet-normal directions, respectively, in the Lagrangian description (Fig. 5.1). In a continuum setting, this fiber and sheet direction vectors are considered as averaged quantities over several fibers and sheets.

The isochoric Eulerian counterpart of these direction vectors are given by the relations $\bar{\mathbf{f}} = J^{-1/3}\mathbf{F}\mathbf{f}_0$, $\bar{\mathbf{s}} = J^{-1/3}\mathbf{F}\mathbf{s}_0$ and $\bar{\mathbf{n}} = J^{-1/3}\mathbf{F}\mathbf{n}_0$, where $\mathbf{F}$ is the deformation gradient and $J = \det\mathbf{F} > 0$ is the volume ratio. The displacement field $\mathbf{u}$ between the two points $\mathbf{X}$ and $\mathbf{x}$ at time t is given by $\mathbf{u} = \mathbf{x} - \mathbf{X}(\mathbf{x},t)$. The circular dispersion of the fiber and sheet direction vectors around their mean orientations may be modeled using the structure tensors

$$\mathbf{H}_\mathrm{f} = \kappa_\mathrm{f}\mathbf{I} + (1-3\kappa_\mathrm{f})\mathbf{f}_0 \otimes \mathbf{f}_0, \qquad \mathbf{H}_\mathrm{s} = \kappa_\mathrm{s}\mathbf{I} + (1-3\kappa_\mathrm{s})\mathbf{s}_0 \otimes \mathbf{s}_0, \tag{5.1}$$

$$\bar{\mathbf{h}}_\mathrm{f} = \kappa_\mathrm{f}\bar{\mathbf{b}} + (1-3\kappa_\mathrm{f})\bar{\mathbf{f}} \otimes \bar{\mathbf{f}}, \qquad \bar{\mathbf{h}}_\mathrm{s} = \kappa_\mathrm{s}\bar{\mathbf{b}} + (1-3\kappa_\mathrm{s})\bar{\mathbf{s}} \otimes \bar{\mathbf{s}}, \tag{5.2}$$

as similarly described in [166], where $\mathbf{H}_i$ are the Lagrangian structure tensors and $\bar{\mathbf{h}}_i = J^{-2/3}\mathbf{F}\mathbf{H}_i\mathbf{F}^\mathrm{T}$ are the isochoric Eulerian structure tensors where $i \in \{\mathrm{f},\mathrm{s}\}$ correlates to the fiber and sheet directions. The second-order identity tensor is denoted by $\mathbf{I}$ while the modified isochoric left Cauchy Green tensor is denoted by $\bar{\mathbf{b}} = J^{-2/3}\mathbf{F}\mathbf{F}^\mathrm{T}$.

The formulation of the dispersion parameters κ_i is described in detail in [166]. Briefly, the range of valid values for κ_i are $\in [0, 1/3]$, where $\kappa_i = 0$ means perfect alignment and

$\kappa_i = 1/3$ means isotropy. A formulation of κ_i may be derived through the probability density function (PDF) $\rho_i(\Theta)$, using the relation

$$\kappa_i = \frac{1}{4}\int_0^{\pi} \rho_i(\Theta)\sin^3\Theta \mathrm{d}\Theta, \tag{5.3}$$

where Θ is the distribution angle centered around $\Theta = 0$. The PDF used is given by

$$\rho(\Theta) = 4\sqrt{\frac{b}{2\pi}}\frac{\exp\{b[\cos(2\Theta)+1]\}}{\mathrm{erfi}(\sqrt{2b})}, \tag{5.4}$$

where b is a concentration parameter and $\mathrm{erfi}(x) = -\mathrm{i}\,\mathrm{erf}(x)$ denotes an imaginary error function. The function $\rho(\Theta)$ is the standard π-periodic von Mises PDF, normalized by

$$\frac{1}{4\pi}\int_{\omega} \rho(\Theta)\mathrm{d}\omega = 1, \tag{5.5}$$

where ω is the unit sphere.

The values for κ_i may thus be fitted to the histograms of the dispersion of fiber and sheet angles for the myocardial tissue. To fit the PDF (5.4) to histogram data (fiber angles), the fiber angle Θ is shifted to $\bar{\Theta}$ to center around $\Theta = 0^\circ$ (the bar on the Θ variable denotes the shifted value), and the maximum likelihood method in Matlab, i.e. *mle()*, is used together with a custom function describing Eq. (5.4). The parameter b is thus retrieved with a 95% confidence interval, and by using (5.3), the parameters κ_i are obtained.

The fit of the PDF to the fiber dispersion is shown in Fig. 5.2 for both a healthy myocardial tissue (see Fig. 5.2(a)), and a diseased tissue (see Fig. 5.2(b)), where the dispersion data were adapted from [29]. The fit of the PDF to the sheet dispersion is only shown for a healthy sub-epicardium (see Fig. 5.2(c)), where the dispersion data were adapted from [35]. To the authors' knowledge the structure of sheet orientations in a diseased myocardium has never been investigated. The fitting produced the dispersion parameters $\kappa_\mathrm{f} = 0.00765$ and $\kappa_\mathrm{s} = 0.0249$ for the healthy myocardial tissue, and $\kappa_\mathrm{f} = 0.0886$ for the diseased tissue; compare with Fig. 5.2.

In the proposed framework, the dispersion parameters for the fiber and sheet directions are uncoupled, and we assume that the mean orientation of these directions are kept orthogonal. Furthermore, the dispersion of the sheet-normal direction is not considered; it is excluded to match the strain-energy function developed in [42], as shown in Section 5.2.2.

5.2.2. Constitutive relations

The anisotropy, generated by the preferred directions of the material (Fig. 5.1), can be modeled by using the isochoric invariants $\bar{I}_{4\mathrm{f}} = \mathbf{f}_0 \cdot \overline{\mathbf{C}}\mathbf{f}_0$, $\bar{I}_{4\mathrm{s}} = \mathbf{s}_0 \cdot \overline{\mathbf{C}}\mathbf{s}_0$ and $\bar{I}_{4\mathrm{n}} = \mathbf{n}_0 \cdot \overline{\mathbf{C}}\mathbf{n}_0$,

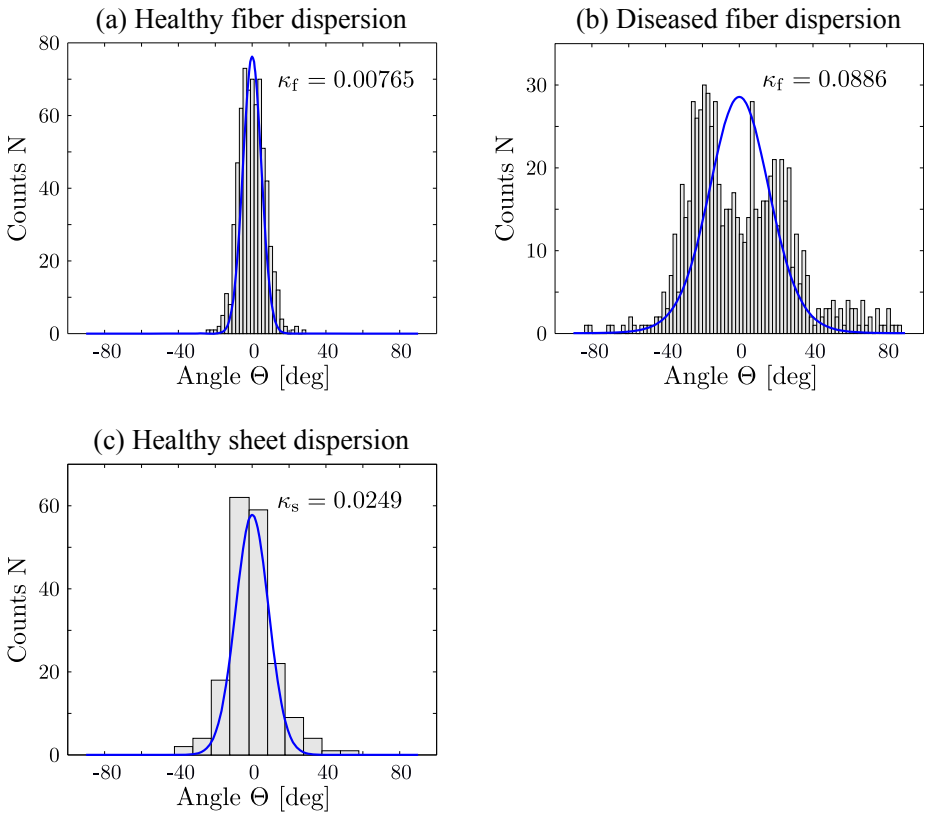

Figure 5.2.: Fit of histogram data for fiber and sheet dispersions adapted from [29, 35] : (a) fiber dispersion in a healthy tissue ($\kappa_f = 0.00765$); (b) fiber dispersion in a diseased tissue ($\kappa_f = 0.0886$); (c) sheet dispersion in a healthy tissue ($\kappa_s = 0.0249$).

where $\overline{\mathbf{C}} = J^{-2/3}\mathbf{C}$ is the modified right Cauchy-Green tensor and $\mathbf{C} = \mathbf{F}^{\mathrm{F}}\mathbf{F}$ denotes the right Cauchy-Green tensor [6].

By using the first invariant of $\overline{\mathbf{C}}$, namely $\bar{I}_1 = \overline{\mathbf{C}} : \mathbf{I}$, we may define the two modified invariants $\bar{I}^*_{4\mathrm{f}}$ and $\bar{I}^*_{4\mathrm{s}}$ as a linear combination of $\bar{I}_1$, $\bar{I}_{4\mathrm{f}}$ and $\bar{I}_{4\mathrm{s}}$. Thus,

$$\bar{I}^*_{4i} = \kappa_i \bar{I}_1 + (1 - 3\kappa_i)\bar{I}_{4i}, \qquad i \in \{\mathrm{f}, \mathrm{s}\}, \tag{5.6}$$

similar to [166–168]. To characterize the orthotropic behavior of the myocardium we modify the strain-energy function suggested by Holzapfel & Ogden [42], by writing

$$\Psi = U(J) + \overline{\Psi}_{\mathrm{p}}(\bar{I}_1, \bar{I}^*_{4\mathrm{f}}, \bar{I}^*_{4\mathrm{s}}, \bar{I}_{8\mathrm{fs}}), \tag{5.7}$$

where $\bar{I}_{8\mathrm{fs}} = \mathbf{f}_0 \cdot \overline{\mathbf{C}}\mathbf{s}_0$ is the modified invariant which couples $\mathbf{f}_0$ with $\mathbf{s}_0$, U is a volumetric function, and $\overline{\Psi}_{\mathrm{p}}$ is an isochoric strain-energy function describing the passive behavior of the myocardium. For the volumetric function we use

$$U(J) = \frac{\mu_{\mathrm{K}}}{2}(\ln J)^2, \tag{5.8}$$

where μ_{K} servers as a user-specified penalty parameter. In an analogous manner to [42] the isochoric strain-energy function for the passive myocardium tissue is given by

$$\overline{\Psi}_{\mathrm{p}} = \frac{a}{2b}\{\exp[b(\bar{I}_1 - 3)] - 1\} + \sum_{i=\mathrm{f,s}} \frac{a_i}{2b_i}\{\exp[b_i(\bar{I}^*_{4i} - 1)^2] - 1\} + \frac{a_{\mathrm{fs}}}{2b_{\mathrm{fs}}}[\exp(b_{\mathrm{fs}}\bar{I}^2_{8\,\mathrm{fs}}) - 1]. \tag{5.9}$$

Note that in the limiting case, where $\kappa_i = 0$, the original model, as described in [42], is retrieved.

The material parameters needed in (5.8) and (5.9) are μ_{K}, a, b, $a_{(\mathrm{f,s,fs})}$ and $b_{(\mathrm{f,s,fs})}$, and the two dispersion parameters κ_{f} and κ_{s}. The passive Cauchy stress tensor is given by $\boldsymbol{\sigma}_{\mathrm{p}} = 2J^{-1}\mathbf{F}(\partial\Psi/\partial\mathbf{C})\mathbf{F}^{\mathrm{T}}$, and by using the notation

$$\overline{\psi}_j = \frac{\partial\overline{\Psi}_{\mathrm{p}}}{\partial\bar{I}_j}, \quad j = 1, 8\,\mathrm{fs}, \qquad \overline{\psi}^*_{4i} = \frac{\partial\overline{\Psi}_{\mathrm{p}}}{\bar{I}^*_{4i}}, \quad i = \mathrm{f,s}, \tag{5.10}$$

this results into

$$\boldsymbol{\sigma}_{\mathrm{p}} = p_{\mathrm{h}}\mathbf{I} + 2J^{-1}[\overline{\psi}_1\,\mathrm{dev}\bar{\mathbf{b}} + \sum_{i=\mathrm{f,s}} \overline{\psi}^*_{4i}\,\mathrm{dev}\bar{\mathbf{h}}_i + \frac{1}{2}\overline{\psi}_{8\,\mathrm{fs}}\,\mathrm{dev}(\bar{\mathbf{f}}\otimes\bar{\mathbf{s}} + \bar{\mathbf{s}}\otimes\bar{\mathbf{f}})], \tag{5.11}$$

where $p_{\mathrm{h}} = \mathrm{d}U(J)/\mathrm{d}J$ is used, and $\mathrm{dev}(\bullet) = (\bullet) - (1/3)[(\bullet) : \mathbf{I}]\mathbf{I}$ denotes the deviatoric operator in the Eulerian description [6].

The evolution of an active second Piola-Kirchhoff stress term S_{a}, which originates from [60], is given by

$$\frac{\partial S_{\mathrm{a}}}{\partial t} = \varepsilon(V_{\mathrm{m}})(k_{S_{\mathrm{a}}}\Delta V_{\mathrm{m}} - S_{\mathrm{a}}), \tag{5.12}$$

where $\varepsilon(V_{\mathrm{m}})$ is a delay function controlling the rate of activation and relaxation of S_{a}. The parameter $k_{S_{\mathrm{a}}}$ regulates the amplitude of S_{a}, $\Delta V_{\mathrm{m}} = V_{\mathrm{m}} - V_{\mathrm{r}}$ is the difference in the transmembrane potential where V_{m} is the current action potential and V_{r} is the myocyte resting potential. A smooth delay function $\varepsilon = \varepsilon(V_{\mathrm{m}})$, as proposed in [144], is used, which is given by

$$\varepsilon(V_{\mathrm{m}}) = \varepsilon_0 + (\varepsilon_\infty - \varepsilon_0)\exp\{-\exp[-\zeta_{\mathrm{r}}(V_{\mathrm{m}} - V_{\mathrm{s}})]\}, \tag{5.13}$$

where ε_0 and ε_∞ are the limiting values of the delay function when the action potential V_{m} is larger or lower than a given phase shift V_{s}. Further, the transition rate of the delay function is controlled by the parameter ζ_{r}. However, in contradiction to what is written in [144], the relation between the limiting values must follow $\varepsilon_0 > \varepsilon_\infty$ in order to achieve the delay of peak active stress with respect to the upstroke of the action potential. An active second Piola-Kirchhoff stress tensor $\mathbf{S}_{\mathrm{a}}$ is retrieved by introducing a dispersed structure tensor $\hat{\mathbf{H}}_{\mathrm{a}}$ according to

$$\mathbf{S}_{\mathrm{a}} = S_{\mathrm{a}}\hat{\mathbf{H}}_{\mathrm{a}}, \tag{5.14}$$

where

$$\hat{\mathbf{H}}_{\mathrm{a}} = \frac{\kappa_{\mathrm{f}}}{1-2\kappa_{\mathrm{f}}}\mathbf{C}^{-1} + \frac{1-3\kappa_{\mathrm{f}}}{1-2\kappa_{\mathrm{f}}} I_{4\mathrm{f}}^{-1}\mathbf{f}_0 \otimes \mathbf{f}_0, \tag{5.15}$$

with $I_{4\mathrm{f}} = J^{2/3}\bar{I}_{4\mathrm{f}}$. The active Cauchy stress tensor $\boldsymbol{\sigma}_{\mathrm{a}}$ is now retrieved by the push-forward operation according to $\boldsymbol{\sigma}_{\mathrm{a}} = J^{-1}\mathbf{F}\mathbf{S}_{\mathrm{a}}\mathbf{F}^{\mathrm{T}}$ which yields

$$\boldsymbol{\sigma}_{\mathrm{a}} = J^{-1} S_{\mathrm{a}} \hat{\mathbf{h}}_{\mathrm{a}}, \tag{5.16}$$

where

$$\hat{\mathbf{h}}_{\mathrm{a}} = \frac{\kappa_{\mathrm{f}}}{1-2\kappa_{\mathrm{f}}}\mathbf{I} + \frac{1-3\kappa_{\mathrm{f}}}{1-2\kappa_{\mathrm{f}}}\hat{\mathbf{f}} \otimes \hat{\mathbf{f}}, \tag{5.17}$$

where $\hat{\mathbf{f}} = \mathbf{f}/|\mathbf{f}|$ is the normalized fiber direction vector. The structure tensor (5.15) is formulated so that (5.17) may be seen as a normalization of $(5.2)_1$ where the length change of the mean fiber orientation does not affect the magnitude of the applied stress so that the condition $\hat{\mathbf{f}} \cdot \hat{\mathbf{h}}_{\mathrm{a}} \hat{\mathbf{f}} = 1$ holds, which together ensures that (5.16) is a true Cauchy stress tensor. The Cauchy stress tensor $\boldsymbol{\sigma}$ is now simply given by the additive decomposition

$$\boldsymbol{\sigma} = \boldsymbol{\sigma}_{\mathrm{p}} + \boldsymbol{\sigma}_{\mathrm{a}}. \tag{5.18}$$

The elasticity tensors needed for implementing the passive stress $\boldsymbol{\sigma}_{\mathrm{p}}$ in the finite element package FEAP [8] have previously been shown in [166], and for the active stress $\boldsymbol{\sigma}_{\mathrm{a}}$ the elasticity tensor in the Lagrangian and the Eulerian descriptions is shown in the Appendix A.1.

5.2.3. Modeling electro-mechanically coupled myocardial tissue

The computation of electrical activation and re-polarization and their coupling to passive tissue mechanics is here briefly described. The spread of electrical activation and re-polarization is described by a reaction-diffusion equation referred to as the mono-domain equation, given by

$$\beta C_{\mathrm{m}} \frac{\partial V_{\mathrm{m}}}{\partial t} + \beta I_{\mathrm{ion}}(V_{\mathrm{m}}, \boldsymbol{\eta}) = \nabla \cdot (\mathbf{g}_{\mathrm{m}} \nabla V_{\mathrm{m}}) + I_{\mathrm{tr}}, \tag{5.19}$$

where β is the membrane surface to volume ratio, C_{m} is the membrane capacitance, V_{m} is the transmembrane potential, I_{ion} is the density of the total ionic current which is a function of V_{m} and a set of state variables $\boldsymbol{\eta}$, I_{tr} is the transmembrane stimulus current, and $\mathbf{g}_{\mathrm{m}}$ is the mono-domain conductivity tensor with the eigenaxes $\zeta = f$ along the fibers, $\zeta = s$ perpendicular to the fibers, but within a laminar sheet, and $\zeta = n$ is perpendicular to the sheets. No dispersion parameters are here included in the formulation of the electrical activation. The eigenvalues of $\mathbf{g}_{\mathrm{m}}$ are chosen as the harmonic mean of the intracellular and interstitial conductivities, which renders the mono-domain equation axially equivalent to the more general bi-domain equation [169, 170].

We employ the finite element method for the spatial discretization of the mono-domain equation (5.19). A ventricular geometry is modeled using two overlapping finite element meshes, a fully structured coarser hexahedral mesh for solving the mechanics, and a fully unstructured hybrid mesh with an average resolution of $\sim$200 μm, using an image-based mesh generation technique [150], as implemented in the commercial mesh generator Tarantula (CAE Software Solution, Eggenberg, Austria) for solving electrics. Fiber and sheet orientations are interpolated onto the barycenters of the finite elements in both meshes. Both grids were partitioned for parallel execution using parMETIS [157]. By treating the diffusion terms implicitly and the reaction terms explicitly, the temporal discretization of the mono-domain equation relies on an implicit-explicit (IMEX) scheme, using the time step of 20 μs. Blocked Jacobi pre-conditioner with an iterative Conjugate Gradient (CG) solver is used to solve the linear system in parallel, using an Incomplete LU (ILU(0)) factorization as a sub-block pre-conditioner [153].

The electrical and mechanical models are weakly coupled, i.e. the solution of the electrical quantities (5.19) is calculated on a static mesh first, using the Cardiac Arrhythmia Research Package (CARP) [155], which is built on top of the MPI-based library PETSc [153]. Numerical aspects of this approach have been described in detail elsewhere [156]. Relevant parameters, i.e. V_{m}, required for computing the active stress transients are transferred to the integration points of the mechanical mesh and fed into a separate subsequent simulation of deformation and stress analysis using FEAP [8].

In this study, however, the electrical quantities are either calculated according to (5.19), as it is the case in the model of a left ventricle, Section 5.3.5, or the transmembrane potential V_{m} is prescribed directly as an input to the mechanical deformation analysis.

5.3. Representative Numerical Examples

To illustrate the effect of the myocardial model considering dispersion five representative numerical examples are carried out. In order to elucidate how the dispersion parameters κ_{f} and κ_{s} influence the myocardium model behavior they are appropriately modified; for example, isotropic fiber distribution was considered while keeping a small dispersion in the sheet orientation and *vice versa*. Such relations between fiber and sheet dispersion are non-physiological, but are used to provide more insight into the proposed model.

The five examples are as follows: (i) in Section 5.3.1 a unit cube of myocardial tissue is electrically activated to generate active tension. The influence of the dispersion on the mechanical deformation (stretch) is studied by varying the dispersion parameters κ_{f} and κ_{s}; (ii) a second example, see Section 5.3.2, aims to predict the influence of the dispersion on simple shear; (iii) a FE model of a cube of myocardial tissue is used in Section 5.3.3 to investigate the relative influence of electrically-generated active stress in the presence of dispersion of the fiber orientation; (iv) in Section 5.3.4 a passive inflation experiment on a ventricular section is performed to study the transmural change in stress as a function of

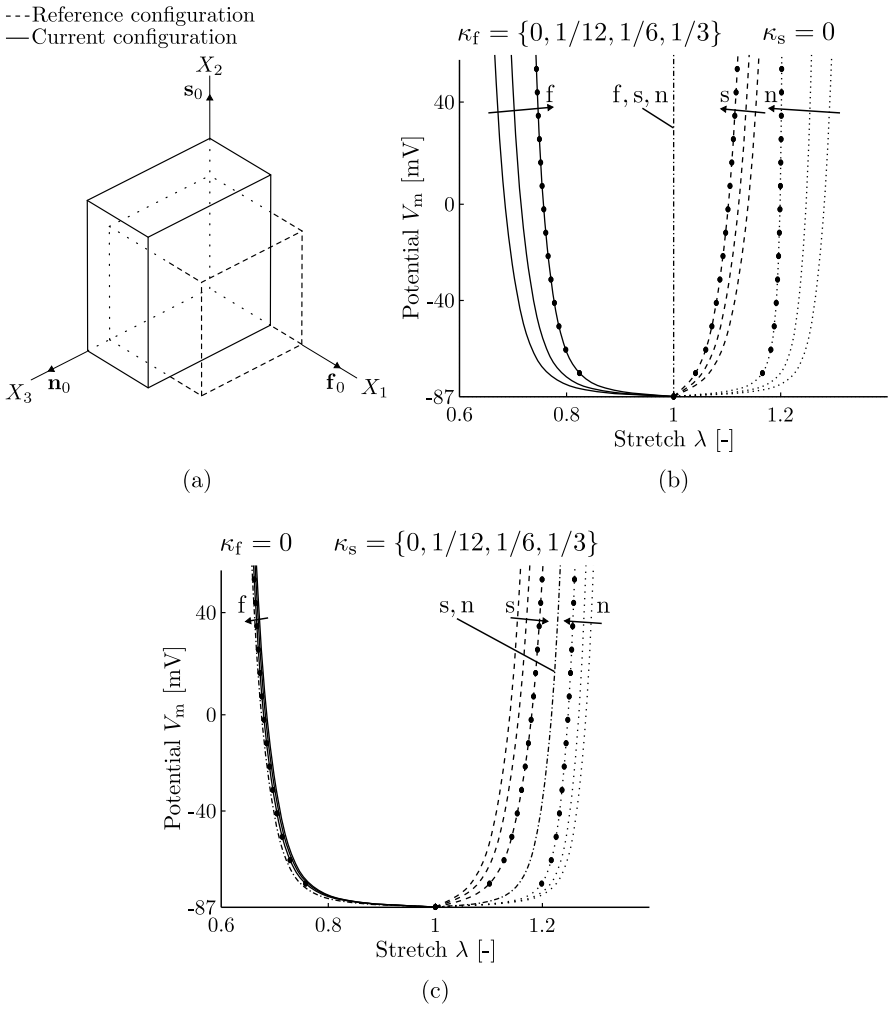

Figure 5.3.: (a) Deformation of a unit cube when activated in the fiber direction; analytical results along the fiber, sheet and sheet-normal directions using different values for the distribution parameters κ_f in (b) and κ_s in (c). The fiber, sheet and sheet-normal responses are shown by solid, dashed and dotted curves, respectively, and the circles show the FE results for comparison reasons using either $\kappa_f = 1/6$, see (b), or $\kappa_s = 1/6$, see (c). Using the limiting case $\kappa_f = 1/3$ or $\kappa_s = 1/3$, the dash-dotted curves show the stretch responses for all three f, s and n-directions, see (b), and for the s and n-directions, see (c).

the altered dispersion parameters related to the fiber and sheet directions; (v) an electromechanically coupled LV model is used in Section 5.3.5 to study the influence of fiber and sheet dispersions upon contraction on pressure-volume loops over a cardiac cycle where dispersion parameters are chosen to account for both healthy and pathological conditions. The related numerical results were obtained by using mixed $Q1/P0$ displacement/pressure finite elements.

Passive stress		
$\mu_{\mathrm{K}} = 3333$ kPa	$a = 0.333$ kPa	$b = 9.242$ (-)
	$a_{\mathrm{f}} = 18.535$ kPa	$b_{\mathrm{f}} = 15.972$ (-)
	$a_{\mathrm{s}} = 2.564$ kPa	$b_{\mathrm{s}} = 10.446$ (-)
	$a_{\mathrm{fs}} = 0.417$ kPa	$b_{\mathrm{fs}} = 11.602$ (-)
Active stress		
$k_{S_{\mathrm{a}}} = 0.50$ kPa mV^{-1}	$V_{\mathrm{r}} = -86.796$ mV	$V_{\mathrm{s}} = -80.0$ mV
$\varepsilon_0 = 1.0$ ms^{-1}	$\varepsilon_\infty = 0.1$ ms^{-1}	$\zeta_{\mathrm{r}} = 0.1$ mV^{-1}

Table 5.1.: Material parameters used for both analytical and numerical calculations, except for the dispersion values of κ_{f} and κ_{s} which are provided in the respective section. The material parameters for the passive tissue behavior are taken from [42], while the parameters for the active stress are taken from [60].

5.3.1. Electrically activated cube with dispersion

A unit myocardium tissue cube with mean material directions is considered. By introducing a global coordinate system (X_1, X_2, X_3) the material directions are according to $[\mathbf{f}_0] = [1,0,0]^{\mathrm{T}}$, $[\mathbf{s}_0] = [0,1,0]^{\mathrm{T}}$ and $[\mathbf{n}_0] = [0,0,1]^{\mathrm{T}}$. The cube is fixed against rigid body movement but can otherwise freely deform. The reference configuration of the cube is shown by the dashed lines in Fig. 5.3(a). The cube is activated by increasing the transmembrane potential V_{m} generating a contraction in the fiber direction. The corresponding deformation gradient is given by $\mathbf{F} = \mathrm{diag}(\lambda_{\mathrm{f}}, \lambda_{\mathrm{s}}, \lambda_{\mathrm{n}})$, where λ_{f}, λ_{s} and λ_{n} are the stretches in the fiber, sheet and sheet-normal directions, respectively. Since the activation in the fiber direction leads to a contraction of the fiber, the stretches follow the relations $\lambda_{\mathrm{f}} < 1$, $\lambda_{\mathrm{s}} > 1$ and $\lambda_{\mathrm{n}} > 1$. A deformed configuration (at $V_{\mathrm{m}} = 50$ mV, with $\kappa_{\mathrm{f}} = \kappa_{\mathrm{s}} = 0$) is shown by the solid lines in Fig. 5.3(a). The components of the Cauchy stress tensor $\boldsymbol{\sigma} = \boldsymbol{\sigma}_{\mathrm{p}} + \boldsymbol{\sigma}_{\mathrm{a}}$ can now be calculated from (5.11) and (5.16) by using $J = 1$. Thus,

$$\sigma_{11} = p_{\mathrm{h}} + 2[\overline{\psi}_1 + \overline{\psi}^*_{4\mathrm{f}}(1-2\kappa_{\mathrm{f}}) + \overline{\psi}^*_{4\mathrm{s}}\kappa_{\mathrm{s}}]\lambda_{\mathrm{f}}^2 + S_{\mathrm{a}}, \tag{5.20}$$

$$\sigma_{22} = p_{\mathrm{h}} + 2[\overline{\psi}_1 + \overline{\psi}^*_{4\mathrm{f}}\kappa_{\mathrm{f}} + \overline{\psi}^*_{4\mathrm{s}}(1-2\kappa_{\mathrm{s}})]\lambda_{\mathrm{s}}^2 + S_{\mathrm{a}}\frac{\kappa_{\mathrm{f}}}{1-2\kappa_{\mathrm{f}}}, \tag{5.21}$$

$$\sigma_{33} = p_{\mathrm{h}} + 2(\overline{\psi}_1 + \overline{\psi}^*_{4\mathrm{f}}\kappa_{\mathrm{f}} + \overline{\psi}^*_{4\mathrm{s}}\kappa_{\mathrm{s}})\lambda_{\mathrm{n}}^2 + S_{\mathrm{a}}\frac{\kappa_{\mathrm{f}}}{1-2\kappa_{\mathrm{f}}}, \tag{5.22}$$

$$\sigma_{12} = \sigma_{13} = \sigma_{23} = 0. \tag{5.23}$$

Since the cube can freely deform, the stress components σ_{11}, σ_{22} and σ_{33} are zero, and p_{h} may be determined by, e.g., $\sigma_{33} = 0$. The unknowns are the stretches λ_{f}, λ_{s} and λ_{n}. By the use of the incompressibility condition $\lambda_{\mathrm{f}}\lambda_{\mathrm{s}}\lambda_{\mathrm{n}} = 1$, the nonlinear system (5.20)–(5.22) can be solved with respect to λ_{f}, λ_{s} and λ_{n} by using the function *fsolve()* in Matlab. The given values are the dispersion parameters κ_{f} and κ_{s}, and the active stress S_{a} which is computed from the given transmembrane potential V_{m}.

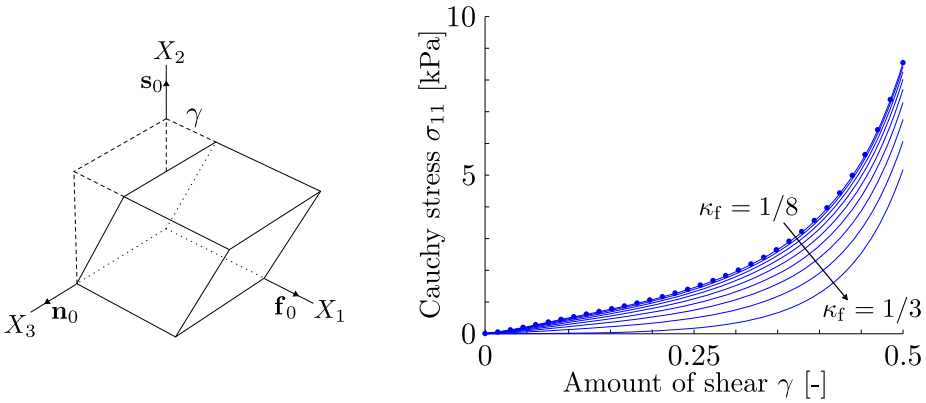

(a) (b)

Figure 5.4.: (a) Simple shear deformation of a unit cube with the deformation gradient $\mathbf{F} = \mathbf{I} + \gamma \mathbf{f}_0 \otimes \mathbf{s}_0$; (b) Cauchy stress σ_{11} versus the amount of shear γ for values κ_f between $1/8$ and $1/3$. The circles show FE results for comparison reasons using $\kappa_f = 1/8$.

With the material parameters from Table 5.1, and a linear increase in the transmembrane potential from $V_m = V_r$ to $V_m = +50\,\text{mV}$, the resulting stretches can be plotted as a function of the transmembrane potential V_m, see Figs. 5.3(b) and 5.3(c) for different sets of the dispersion parameters κ_f and κ_s. The fiber, sheet and sheet-normal responses are shown by solid, dashed and dotted curves, respectively (the stretches in Fig. 5.3 are abbreviated by λ). In addition, a comparison is shown with finite element (FE) results obtained for the same model setup where $\kappa_f = 1/6$ in Fig. 5.3(b) and $\kappa_s = 1/6$ in Fig. 5.3(c) (the FE results are shown as circles). For the limiting case $\kappa_f = 1/3$ the active stress acts in all direction, and due to the incompressibility the cube cannot deform, resulting in a straight line at $\lambda = 1$ for all directions, as shown by the dash-dotted line in Fig. 5.3(b). For the limiting case $\kappa_s = 1/3$ (the sheet direction is isotropic) the stretch responses in the sheet and sheet-normal directions are shown by the dash-dotted curves in Fig. 5.3(c). Note that the sheet and sheet-normal responses are indistinguishable. For $\kappa_s = 1/3$ the material model can be viewed as transversely isotropic.

5.3.2. Influence of dispersion on simple shear

Consider the same unit myocardium tissue cube with the same material directions as formulated in the previous example but subjected to a simple shear deformation in the 21-plane caused by the deformation gradient $\mathbf{F} = \mathbf{I} + \gamma \mathbf{f}_0 \otimes \mathbf{s}_0$ (see Fig. 5.4(a)). Thereby, γ denotes the amount of shear. In addition, let us consider a plane stress state throughout the myocardium tissue in the sense that the face of the cube normal to the direction $\mathbf{n}_0$ is free of surface traction ($\sigma_{13} = \sigma_{23} = \sigma_{33} = 0$). For that particular set-up the nonzero Cauchy stress components can be derived from (5.11) and (5.16). After some lengthy but

straightforward computation we obtain

$$\sigma_{11} = 2\{\overline{\psi}_1\gamma^2 + \overline{\psi}^*_{4\mathrm{f}}[1+(\gamma^2-3)\kappa_\mathrm{f}] + \overline{\psi}^*_{4\mathrm{s}}(1-2\kappa_\mathrm{s})\gamma^2 + \overline{\psi}_{8\mathrm{fs}}\gamma\} + S_\mathrm{a}\frac{1-3\kappa_\mathrm{f}}{1-2\kappa_\mathrm{f}}, \quad (5.24)$$

$$\sigma_{22} = 2\overline{\psi}^*_{4\mathrm{s}}(1-3\kappa_\mathrm{s}), \quad (5.25)$$

$$\sigma_{12} = \sigma_{21} = 2[\overline{\psi}_1 + \overline{\psi}^*_{4\mathrm{f}}\kappa_\mathrm{f} + \overline{\psi}^*_{4\mathrm{s}}(1-2\kappa_\mathrm{s})]\gamma + \frac{1}{2}\overline{\psi}_{8\mathrm{fs}}. \quad (5.26)$$

Note that although the applied active stress is dispersed along the fiber direction there are no components of the active stress in the two other orthogonal directions ($\mathbf{s}_0$ and $\mathbf{n}_0$). The Cauchy stress σ_{11} is shown in Fig. 5.4(b) as a function of the amount of shear γ for values κ_f between $1/8$ and $1/3$ (isotropy). As can clearly be seen from the plots an increased fiber dispersion decreases the Cauchy stress σ_{11}. In this example the active stress is zero in the reference configuration and increases with the increase of shear. Also here a comparison is shown with FE results (the circles in Fig. 5.4(b)) where $\kappa_\mathrm{f} = 1/8$.

5.3.3. Influence of myocyte dispersion on the mechanical tissue response

The influence of the myocyte dispersion on the mechanical tissue response is shown by using the same unit myocardium tissue cube (with 10 mm size) as in the previous examples. The cube is discretized by $10 \times 10 \times 10$ finite elements with fixed displacement boundary conditions in all degrees of freedom on the faces of the cube at $X_2 = 0$ and $X_2 = 10$ mm.

The dispersion parameter κ_s was set to zero. Four different values for κ_f are used (0, 0.1, 0.2, 0.3) whilst keeping κ_s constant. The cube is activated by a potential of $V_\mathrm{m} = +30$ mV and the corresponding first principal stress σ_I is shown in Fig. 5.5. As can be seen in the figure, an increase in the κ_f-value towards isotropy lowers the value of σ_I, and also decreases the contraction in the fiber direction. This is due to the increased dispersion of the fiber direction which leads to an increase in active stress components along the X_2 and X_3-directions, and due to the incompressibility of the material which reduces the influence of the active stress in the fiber direction in that particular example.

5.3.4. Passive inflation of a ventricular section

A left ventricular slice model is generated by approximating the cross section of the LV by a cylinder, as illustrated in Fig. 5.6(a). Two models, say A and B, of the same geometry but with different fiber and sheet arrangements are created. In model A, the average fiber angle α varies from $+60^\circ$ to -60° and the average sheet angle β varies from $+85^\circ$ to -85° transmurally from the epicardium to the endocardium, where the fiber and sheet angles α and β are defined in Fig. 5.6(b). In Model B, the fiber and sheet angles are assumed to be zero. The slice geometry is meshed with 400 hexahedral finite elements which are fixed against translation in the ξ_2-direction at the cut surfaces, and in the ξ_3-direction at the epicardial border to hinder rigid body movements. No electrical stimulus was applied, i.e. the tissue remained electrically quiescent and thus no active stresses were generated. Instead, the slice is passively inflated by applying a pressure load of 100 mmHg

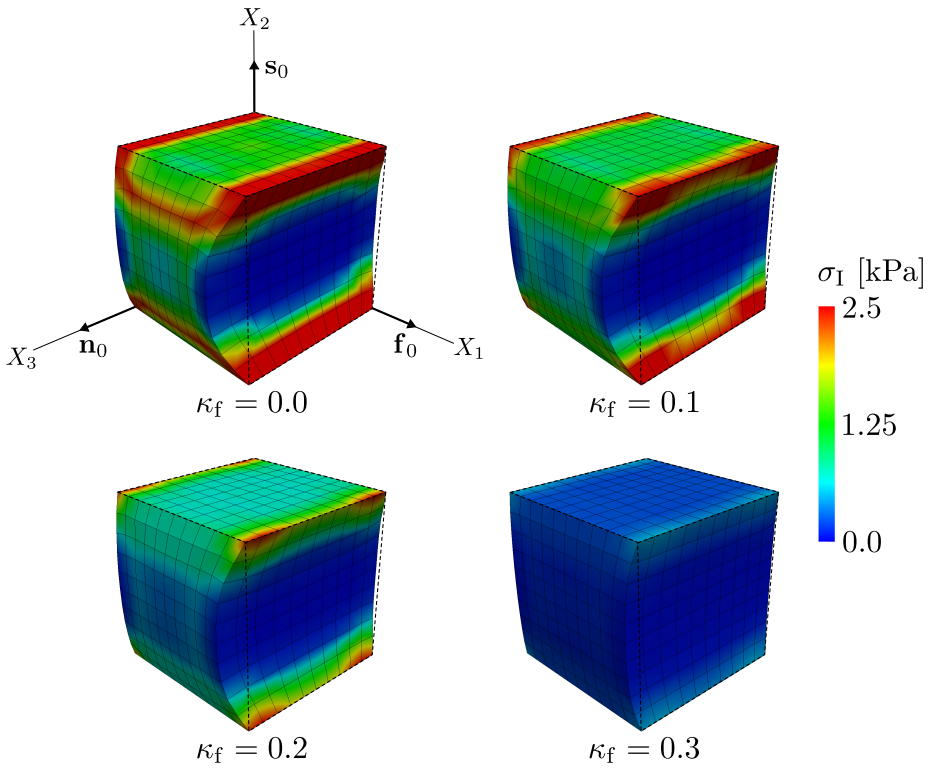

Figure 5.5.: Cube of myocardial tissue subjected to an active stress corresponding to a potential of $+30\,\mathrm{mV}$ with the dispersion parameters $\kappa_f = \{0, 0.1, 0.2, 0.3\}$ and $\kappa_s = 0$. The images illustrate the corresponding first principal stress σ_I.

to the endocardial surface in 200 incremental load steps of equal size. The influence of the dispersion parameters κ_f and κ_s on the distribution of the first principal stress σ_I is investigated by either using the dispersion parameters for healthy and diseased tissues, as provided in Fig. 5.2, or by using the dispersion parameters $\kappa_f = 0.2$ (strongly dispersed) and $\kappa_s = 0$ (perfect alignment), and *vice versa*.

In Fig. 5.7 the resulting first principal Cauchy stress σ_I at the applied pressure load of $100\,\mathrm{mmHg}$ is shown for different dispersion parameters. Figure 5.7(a) shows the stress distribution by using the dispersion parameters for a healthy myocardium resulting in a band of higher stresses in the middle region of the myocardium. This band is noticeably reduced by using the dispersion parameters for the fibers related to a diseased myocardium, as shown in Fig. 5.7(b). Instead, stresses are more spread out radially, and at the endocardial border stresses are higher relative to the setup of Fig. 5.7(a). This suggests that the fiber dispersion alone induces a radial stress gradient where the highest stresses arise at the inner wall, as commonly seen in, e.g., pressurized thick-walled isotropic tubes. This is exactly the case when using aligned sheets and a pronounced fiber dispersion, as can be seen in Fig. 5.7(c). In the opposite case, i.e. with fiber alignment and a pronounced sheet dispersion, there is an increased stress gradient visible in the middle region of the

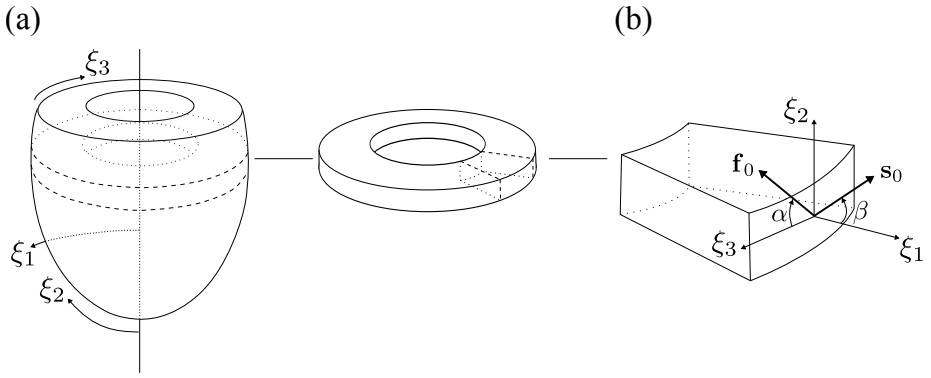

Figure 5.6.: (a) Coordinate system of a LV model and a section of the LV; (b) average fiber orientation defined by the angle α in the (ξ_2, ξ_3)-plane and average sheet orientation defined by the angle β in the (ξ_1, ξ_2)-plane. The arrows point in the positive directions of the angles.

myocardium, as seen in Fig. 5.7(d).

For the sake of comparison, for model *B* the first principal Cauchy stress σ_{I} at 100 mmHg was computed and the related results are shown in the Figs. 5.7(e) and (f) for two sets of dispersion parameters. For the case of a higher dispersion parameter κ_{f} (relates to a diseased myocardium) the first principal Cauchy stress is slightly higher at the endocardial border. This effect is not so pronounced when comparing Fig. 5.7(a) with (b).

5.3.5. LV model indicating the influence of fiber and sheet dispersions upon contraction

To study the influence of fiber and sheet dispersions upon contraction over a cardiac cycle an ellipsoidal model of a LV was constructed; the dimensions correlate with a rabbit LV [132]. The coordinates of the LV are described in prolate spheroidal coordinates with the axes ξ_1, ξ_2 and ξ_3, pointing in the radial, longitudinal and circumferential direction, respectively. The coordinate system is illustrated in Fig. 5.6(a). The arrangements of the fibers and the sheets correspond to the model *A*, as described in Section 5.3.4. Pressure boundary conditions, as imposed by the ventricular deformation and the response of the vascular system, are applied on the endocardial surface. The pressure p in the cavity is governed as follows:

(i) Non-physiological initial phase with linear pressure increase starting from $p = 0$ to the end diastolic pressure (EDP) ($p = 20$ mmHg).

(ii) Isochoric LV compression phase, p increases from EDP up to 95 mmHg.

(iii) Ejection phase where the pressure-volume relationship is governed by a Windkessel model, i.e.

$$C\frac{\mathrm{d}p}{\mathrm{d}t} + \frac{p}{R} = -\frac{\mathrm{d}V}{\mathrm{d}t}, \tag{5.27}$$

until reversed blood flow.

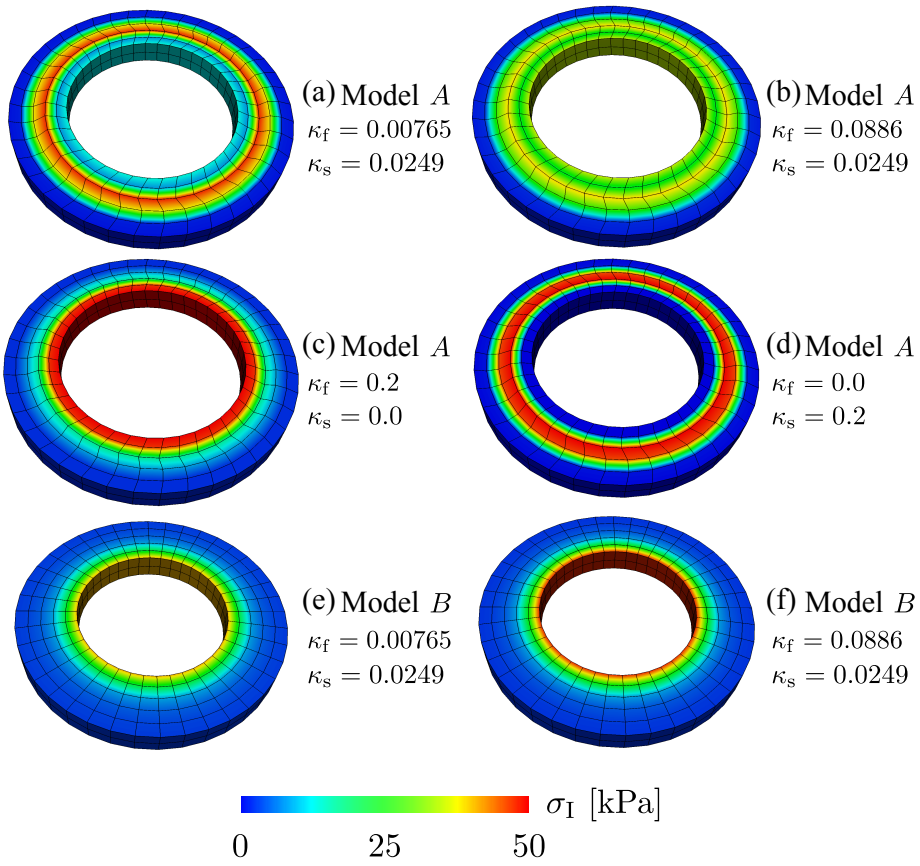

Figure 5.7.: Distribution of the first principal stress σ_I at applied pressure load of 100 mmHg in a section of a ventricular model. Models A and B pertain to different fiber and sheet-orientations; model A: $-60^\circ \leq \alpha \leq +60^\circ$ and $-85^\circ \leq \beta \leq +85^\circ$; model B: $\alpha = \beta = 0$ (α and β denote fiber and sheet angles, respectively, as defined in Fig. 5.6(b)). For some dispersion parameters see Fig. 5.2.

(iv) Isochoric LV relaxation phase, p drops down to 12.5 mmHg.

(v) Filling phase with linear pressure increase to EDP.

In the steps (ii) and (iv), the pressure p is computed using the iterative relation $p_{n+1} = p_n + (V_{n+1} - V_n)/C_p$ to keep the cavitary volume V of the LV constant, where C_p serves as a penalty parameter [79]. In the step (iii), where a two-element Windkessel model is used, the parameters C and R relate to the arterial compliance and the resistance, respectively. The values for C and R are chosen to generate pressure-volume (PV) loops which match with experimental data of rabbits [78]. Parameters required for calculating the pressure are: $C = 0.2\,\mathrm{ml\,mmHg^{-1}}$, $R = 700\,\mathrm{mmHg\,ms\,ml^{-1}}$ and $C_p = -900\,\mathrm{ml\,mmHg^{-1}}$. The parameters used to describe both active and passive mechanical behaviors of the model are summarized in Table 5.1, except for κ_f and κ_s which correspond to the dispersion parameters given in Fig. 5.2. The mechanical boundary conditions for the LV are described in Table 5.2. The mesh consists of 5310 hexahedral (mixed) finite elements used to solve

BCs	Coordinates		Description
$t_{\mathrm{n}} = -p$	$\xi_1 = \xi_{1\mathrm{min}}$	for all ξ_2, ξ_3	Endocardial surface
$u_{\xi_2} = 0$	$\xi_2 = \xi_{2\mathrm{max}}$	for all ξ_1, ξ_3	Basal surface
$u_{\xi_3} = 0$	$\xi_1 = \xi_{1\mathrm{max}}$ $\xi_2 = \xi_{2\mathrm{max}}$	for all ξ_3	Outer boundary at the base surface

Table 5.2.: Mechanical boundary conditions (BCs) for the LV in terms of the prescribed traction $\mathbf{t}$, where t_n is a component of $\mathbf{t}$ normal to the endocardial surface on which the pressure p acts, and the displacement $\mathbf{u}$ with components u_{ξ_1}, u_{ξ_2}, u_{ξ_3} in the direction of the coordinates given in Fig. 5.6(a).

the mechanics and of 1 201 507 linear hybrid finite elements to solve the electrics [152]. The model by Mahajan et al. [71] is employed to describe cellular dynamics, where the system of ODEs is solved using the Rush-Larsen algorithm [154] with several optimizations [111]. The model was initialized by pacing a single cell at a pacing cycle length of 350 ms until a stable limit cycle was observed.

The state vector $\boldsymbol{\eta}$ at the end of this pre-pacing procedure was used to populate the LV model with an initial state vector $\boldsymbol{\eta}_0$. Transmembrane current injection applied to the endocardial surface at $t = 0$ ms initiated the propagation of the action potentials at the endocardium to approximate a predominantly transmural activation sequence, as induced by activation via the Purkinje system. In this approximation the whole endocardium was activated synchronously, electrical activation delays within the endocardium remained unaccounted for. We simulated 350 ms of activity to cover one depolarization and repolarization cycle over the entire LV. This spread of electrical activation and re-polarization is modeled using Eq. (5.19).

By using the dispersion parameters that relate to the healthy and the diseased tissue, as seen in Fig. 5.2, the resulting deformations are quite different. This is illustrated at both the end diastolic volume (EDV) and the end systolic volume (ESV), as shown in the Figs. 5.8(a) and (b), respectively. Thereby, the distribution of the magnitude of the difference $|\mathbf{u}_{\mathrm{H}} - \mathbf{u}_{\mathrm{D}}|$ between the displacements is shown (H stands for healthy tissue and D for diseased). The resulting pressure-volume (PV) loops obtained from the simulations for different sets of dispersion parameters are shown in Fig. 5.8(c); also the case for no dispersion is illustrated ($\kappa_{\mathrm{f}} = \kappa_{\mathrm{s}} = 0$). While only a minor shift in the PV loops between the cases with no dispersions and with fiber and sheet dispersions for a healthy myocardium was observed, a remarkably different behavior is obtained with a fiber dispersion κ_{f} relating to a diseased myocardium; thereby the end diastolic and systolic volumes are much larger.

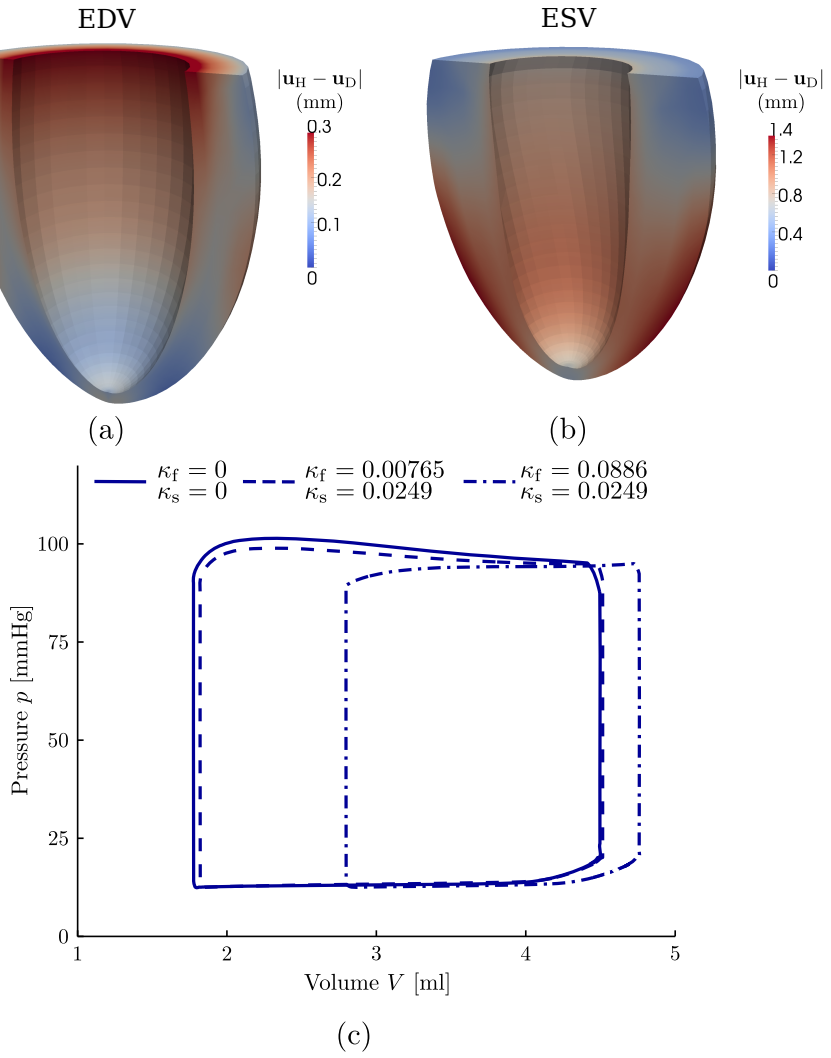

Figure 5.8.: Magnitude of the difference $|\mathbf{u}_H - \mathbf{u}_D|$ between the displacements (H stands for healthy tissue and D for diseased) for (a) the end diastolic volume (EDV) and (b) the end systolic volume (ESV). (c) Pressure-volume loops for different sets of dispersion parameters κ_f and κ_s.

5.4. Discussion

There are several reports in the literature which provide evidence for the presence of dispersion in the fiber and the sheet orientation in myocardial tissues. Under healthy conditions dispersion is rather mild, but under certain pathologies such as HCM [165, 171, 172] dispersion can be quite pronounced. In the vast majority of modeling studies, however, dispersion and its influence upon the mechanical response of the myocyardium has been largely ignored. In this study, a mechanical model of myocardial tissue has been proposed which explicitly accounts for the dispersion of fibers and sheets. By changing two scalar (dispersion) parameters, introduced as κ_f and κ_s, the dispersion along the fiber and the

sheet direction can be steered independently, thus allowing mechanistic investigations of pathological changes. The independence of the fiber and sheet directions is a reasonable approximation, despite the microstructural interaction. An approach which couples the fiber and sheet orientations is feasible, however, specific data are missing. The dispersion parameters κ_f, κ_s determine the blend between the isotropy (characterized by the invariant I_1) and the transverse isotropy (characterized by the invariants I_{4f}, I_{4s}). Thus, together, they give a dispersed orthotropic structure response where an increased dispersion leads to a more isotropic active and passive mechanical response.

The analytical and numerical examples investigated in this study suggest that dispersion may be an important factor in cardiac electro-mechanics. The increase in the dispersion along the fiber direction showed the most striking effect. This is illustrated in, e.g., Fig. 5.5 where the increase in the dispersion reduces contraction and the first principal stress. The enforced incompressibility condition is responsible for this reduced contraction, as can be seen from the analytical expressions (5.20)–(5.22) and (5.24)–(5.26). From a physiological point of view there is also an interpretation. As the dispersion increases, the orientation of myocytes, which are responsible for active contraction, becomes more evenly distributed. When dispersion is large enough, there is no preferred myocyte orientation anymore. This would entail an isotropic contraction, which is, however, impossible without altering the volume. Moreover, besides distributing the direction of active contraction, fiber dispersion also has a major impact on the passive myocardial response. This is illustrated in the Fig. 5.7(a) through (c) where the fiber dispersion is increased in a ventricular slice model. During passive inflation of the slice the first principal stress changes from being elevated in a mid-myocardial band for low fiber dispersion to being elevated at the endocardial border for high fiber dispersion. This shift is similar to what is commonly seen when inflating a thick-walled tube.

Although the effects of dispersion in the fiber direction on the mechanical myocardial response is more striking, numerical results indicate that increases in the sheet dispersion lead to significant alterations in the model behavior as well. The overall material response changes gradually from orthotropic towards transversely isotropic where the sheet response becomes indistinguishable from the sheet-normal response. This can be seen either in the analytical part of the first example discussed in Section 5.3.1, see eqs. (5.21) and (5.22), where $\kappa_s = 1/3$ gives identical expressions for the Cauchy stresses σ_{22} and σ_{33}, or, alternatively, from Fig. 5.3(c) where the behavior is identical along the sheet and sheet-normal directions. The difference in the passive stress response between a (nearly) transversely isotropic and an orthotropic material can be appreciated by comparing Fig. 5.7(d) with Fig. 5.7(a), where the stress in the middle region of the myocardial is even more elevated for the (nearly) transversely isotropic material. This large difference in the stress response also highlights the importance of the orthotropic structure as a factor which has to be considered when simulating ventricular electro-mechanical problems. Residual stresses, however, has not been included in the simulation, why the particular stress

distribution, as shown in Fig. 5.7, should not be considered as the true stress in a ventricle. It merely shows how the fiber and sheet dispersions affect the stress distribution.

Section 5.3.5 illustrates the numerical results for an electro-mechanically coupled model of a LV from a rabbit for a healthy and a pathological myocardium. While the effects of using fiber and sheet dispersion parameters for the healthy myocardium were fairly minor, the use of fiber dispersions relating to a pathological myocardium had a rather big effect. As can be seen by comparing the pressure-volume (PV) loops in Fig. 5.8(c), a significant shift of the entire PV loop towards larger end diastolic and end systolic LV cavity volumes occurred. While the PV loops show that there is a difference in volume of the ventricular lumen, Figs. 5.8(a) and (b) also illustrate that the remaining ventricular wall undergoes different patterns of deformation when using different dispersion parameters.

In summary, our modeling results identified the fiber and sheet dispersions as important determinants for the electro-mechanics of the myocardium. Distributed fiber and sheet orientations should be considered for more reliable predictions of, e.g., stress, deformation and volume change, in particular when compared with experimental data obtained from a pathological myocardium.

Limitations of the study. Due to the lack of structural data of pathological myocardium it is difficult to find suitable comparisons on which we may validate our approach. Therefore, we have focused on the description of the dispersion model and have attempted to show the related mechanisms. Once adequate structural data exist, future work is needed to validate and modify the model if necessary.

The fit of the histogram data to the PDF assumes a bell-shaped data distribution. This may not be suitable in pathological cases with increased fiber dispersion. As shown in Fig. 5.2(b), which displays the fiber dispersion of a HCM-diseased tissue, there may exist two predominant myocyte orientations in the region of interest. It is certainly possible to retrieve individual dispersion parameters, however, the increased dispersion obtained from the HCM sample was only seen within small focal islands throughout the myocardial wall [29, 30]. To appropriately account for the bimodal distribution of orientations, higher spatial resolutions would be required than those commonly used within FE studies, including this study. Since the spatial extent of a single finite element in the models used exceeds the size of a focal island in which increased dispersion can be found, we opted to only use one average direction which corresponds to a fit of the bell-shaped function over both predominant orientations.

In the LV model discussed in Section 5.3.5, the dispersion parameters corresponding to the tissue diseased by HCM were used throughout the entire LV wall. This is not a realistic assumption as the dispersion in the smaller focal islands seems only to be approximately 25% of the overall LV volume [29, 30]. Available data show sheet and fiber dispersions averaged over all islands found in a given ventricle, but no data on the spatial distribution and morphology of such islands are available. Therefore, simulation results show an overly

diseased case which can be considered as a limiting case for the dispersion effects. However, the focus of this study is mainly on the description of the modeling procedure and the potential effects of fiber dispersion, and not on the development of a model that strives for a perfect patho-physiological match for a HCM-diseased LV. In future higher resolution FE-modeling studies, dispersion parameters may easily be set to vary from finite element to element, however, by considering the paucity of available data on the spatial dispersion variation such a detailed investigation would appear to be premature. Experimental studies which characterize spatial and morphological aspects of the dispersion over the entire myocardium in health and disease are, therefore, of utmost need to provide a more solid basis for a more detailed study aiming to provide more specific predictions.

Furthermore, in the LV model the parameters κ_f and κ_s affected only the mechanical response of the LV, but not the electrical activation sequence since dispersion remained unaccounted for in the mono-domain equation. That is, the orthotropy in the propagation of the action potential in the LV model was governed by the mean orientation of the fibers and the sheets. A consideration of the dispersion in the electrical model would also reduce the orthotropy. However, the chosen activation sequence, which approximates a normal beat where the entire endocardium is activated almost simultaneously, leads to a strongly transmural activation where effects of electrical orthotropy are strongly attenuated. Under such conditions the consequence of electrical dispersion is minor and can be neglected, particularly when considering the rather large uncertainty in the experimental reports on conductivity values, which vary up to 300% [173].

Acknowledgement

The authors wish to thank Professor Ray W. Ogden from the University of Glasgow for the productive discussions. This project was partly supported by the SFB Research Center 'Mathematical Optimization and Applications in Biomedical Sciences', project F3210-N18 granted by the Austrian Science Fund. This support is gratefully acknowledged.

6. ON TENSION-COMPRESSION SWITCHING IN DISPERSED FIBER-REINFORCED CONSTITUTIVE MODELS

Abstract Large-strain, fiber-reinforced constitutive models are commonly used for solving complex boundary value problems in the context of the finite element method. In such models which do not include fiber dispersion, the mathematical and physical motivation for including a tension-compression fiber 'switch' (e.g., in which some portion of the model is not used if the fibers are in compression) is clear. In cases where fiber-reinforced models are extended to include the effect of distributed fiber orientations (i.e. models which include a parameter intended to capture fiber dispersion about a principal fiber direction, e.g., Gasser, Ogden and Holzapfel, Journal of the Royal Society Interface, 3:15-35, 2006) neither the mathematical nor physical motivation for tension-compression fiber switching is so clear, and in fact several choices exist for the material modeler. Here we explore methods to study such switching mechanisms by analyzing six potential switching cases, and draw some conclusions about the mathematical robustness and physical interpretation of the different possible approaches. We propose using two different permeations of the dispersed fiber-reinforced models, depending on whether one can assume that the fibers are (nearly) uncoupled or strongly coupled to the isotropic ground matrix.

6.1. Introduction

Fiber-reinforced constitutive models for soft tissue materials are commonly used for solving complex large-strain boundary value problems using the finite element method. Such materials are often considered to be hyperelastic and are modeled using a strain-energy function in the framework of continuum mechanics. Because soft biological tissues are commonly reinforced with collagen fibers, fiber-reinforced constitutive models play a crucial role in, e.g., determining the mechanical state of biological tissues.

The directions of collagen fiber-reinforcement in soft biological materials generally vary inhomogeneously within the tissues, and fibers are often bundled together to create fiber-families, in which the fibers are (to some degree) dispersed around a mean, or principal, fiber direction. Several models for fiber-reinforced materials are presented in the mechanics literature that incorporate a principal fiber direction, e.g., [174, 175], and many models have been presented for specific biological tissues, e.g., arteries [12, 176, 177], myocardium [42, 47, 128], and cartilage [178, 179]. Some of these models have been extended to further incorporate a measure of dispersion in the fibers orientations (i.e. they capture the distribution of the fiber orientations about a principal direction of reinforcement) [31, 166, 168, 180–183].

Although it is fairly straightforward to model fiber behavior under tension, it is not so clear what to do once the fibers go into compression. While a fiber, say a collagen fiber found in arterial tissue, bears load while in tension, it may buckle under compression and would thus not bear any compressive load alone. A common approach is to view the fiber as a tension-only quantity and superimpose this behavior with an isotropic matrix material which may handle compressive loads.

This approach is used in, e.g., the strain-energy function developed by Holzapfel, Gasser and Ogden [12], which is separated into two terms related to matrix and fiber behaviors of arterial tissue, i.e. $\Psi = \Psi_{\mathrm{m}} + \Psi_{\mathrm{f}}$, respectively. Here, the matrix material is considered to be isotropic and incompressible and can be modeled as a neo-Hookean material $\Psi_{\mathrm{m}} = \mu(I_1 - 3)/2$, where μ is the shear modulus in the reference configuration and $I_1 = \mathrm{tr}\mathbf{C}$ is an isotropic invariant of the right Cauchy-Green tensor $\mathbf{C} = \mathbf{F}^{\mathrm{T}}\mathbf{F}$. The behavior of arterial tissue related to the collagen fiber structure is modeled using a directionally dependent pseudo-invariant $I_4 = \mathbf{C} : \mathbf{A}_0 = \lambda_{\mathrm{f}}^2$ (the square of the stretch in the fiber direction), where $\mathbf{A}_0 = \mathbf{a}_0 \otimes \mathbf{a}_0$ is a material structure tensor for the fiber reinforcement with direction $\mathbf{a}_0$ in the reference configuration.

Assuming that the embedded collagen fibers are not highly-constrained in the matrix material, these fibers buckle under compression and thus the overall material response in compression is isotropic and captured by Ψ_{m} alone. Simplifying the strain-energy function for the fibers given in [12] to account for only one fiber family, Ψ_{f} may be written as

$$\Psi_{\mathrm{f}} = \begin{cases} \Psi_{\mathrm{f}}^{\mathrm{t}} = \dfrac{k_1}{2k_2}\left\{\exp\left[k_2(I_4-1)^2\right]-1\right\} & \text{if } I_4 > 1, \\ \Psi_{\mathrm{f}}^{\mathrm{c}} = 0 & \text{if } I_4 \leq 1, \end{cases} \tag{6.1}$$

where the superscript t and c stand for tension and compression respectively, $k_1 > 0$ is a stress-like material parameter and $k_2 > 0$ is a dimensionless parameter, both which control the nonlinear, equilibrium fiber fabric response. As discussed, e.g., in [12, 42], for both convexity and strong ellipticity to be fulfilled in tension, the material parameters in Ψ_{f} must fulfill the relations $k_1 > 0$ and $k_2 > 0$. Beyond the physical motivation for the compression 'switch' (the fibers buckle), there is also a mathematical reason for switching to $\Psi_{\mathrm{f}}^{\mathrm{c}} = 0$ in compression. Strong ellipticity can not be guaranteed without this switch, which may have a negative impact on numerical stability of the corresponding finite element implementations of the constitutive equations.

As the strain-energy function Ψ is separated into two terms, the Cauchy stress tensor

$$\boldsymbol{\sigma} = 2\mathbf{F}\frac{\partial \Psi}{\partial \mathbf{C}}\mathbf{F}^{\mathrm{T}} - p_{\mathrm{h}}\mathbf{I}, \tag{6.2}$$

can similarly be separated into $\boldsymbol{\sigma} = \boldsymbol{\sigma}_{\mathrm{m}} + \boldsymbol{\sigma}_{\mathrm{f}} - p_{\mathrm{h}}\mathbf{I}$, where $\boldsymbol{\sigma}_{\mathrm{m}}$ is the matrix contribution, $\boldsymbol{\sigma}_{\mathrm{f}}$ is the fiber contribution and $p_{\mathrm{h}}\mathbf{I}$ is a term used to enforce incompressibility via a Lagrange multiplier p_{h} (a non-physical penalty parameter) and the second order identity tensor $\mathbf{I}$.

Thus, assuming a neo-Hookean matrix contribution, the stress tensors $\boldsymbol{\sigma}_\mathrm{m}$ and $\boldsymbol{\sigma}_\mathrm{f}$ can be written as

$$\boldsymbol{\sigma}_\mathrm{m} = 2\mathbf{F}\frac{\partial \Psi_\mathrm{m}}{\partial \mathbf{C}}\mathbf{F}^\mathrm{T} = \mu \mathbf{b}, \tag{6.3}$$

and

$$\boldsymbol{\sigma}_\mathrm{f} = 2\mathbf{F}\frac{\partial \Psi_\mathrm{f}}{\partial \mathbf{C}}\mathbf{F}^\mathrm{T} = \begin{cases} \boldsymbol{\sigma}_\mathrm{f}^\mathrm{t} = 2k_1(I_4-1)\exp[k_2(I_4-1)^2]\mathbf{A} & \text{if } I_4 > 1, \\ \boldsymbol{\sigma}_\mathrm{f}^\mathrm{c} = 0 & \text{if } I_4 \leq 1, \end{cases} \tag{6.4}$$

where $\mathbf{b} = \mathbf{F}\mathbf{F}^\mathrm{T}$ is the left Cauchy-Green tensor and $\mathbf{A} = \mathbf{F}\mathbf{A}_0\mathbf{F}^\mathrm{T} = \mathbf{F}\mathbf{a}_0 \otimes \mathbf{F}\mathbf{a}_0 = \mathbf{a} \otimes \mathbf{a}$ is an Eulerian structure tensor associated with the fibers (characterized by the reference direction vector $\mathbf{a}_0$, $|\mathbf{a}_0| = 1$) with direction $\mathbf{a}$ in the Eulerian configuration.

In order to visualize the effects of fiber-term switching from tension to compression, we compare the Cauchy stresses $\boldsymbol{\sigma} = \boldsymbol{\sigma}_\mathrm{m} + \boldsymbol{\sigma}_\mathrm{f} - p_\mathrm{h}\mathbf{I}$ and $\tilde{\boldsymbol{\sigma}}_\mathrm{f} = \boldsymbol{\sigma}_\mathrm{f} - p_\mathrm{h}\mathbf{I}$ under uniaxial deformation of an incompressible material with the fiber orientation $\mathbf{a}_0$ in the global 11–direction. The material is stretched/compressed by λ_f in the global 11–direction and is free to deform (i.e. traction free) in the 22 and 33–directions. Thus the deformation gradient is $\mathbf{F} = \mathrm{diag}(\lambda_\mathrm{f}, \lambda_\mathrm{f}^{-1/2}, \lambda_\mathrm{f}^{-1/2})$ which assumes both transverse (in-plane) isotropy and material incompressibility, i.e. $\det\mathbf{F} = 1$. The Lagrange multiplier p is determined from the 33–component of the stress tensor.

Without loss of generality, the material parameters are chosen for a representative case as $\mu = 5\,\mathrm{kPa}$, $k_1 = 10\,\mathrm{kPa}$ and $k_2 = 15\,[\text{-}]$, and are not matched to any experimental material data. In Fig. 6.1(a) we compare the 11–components of the stresses (coincident with the fiber direction by design); the fiber stress $\tilde{\boldsymbol{\sigma}}_\mathrm{f}$ does not contribute to the total stress while the fibers are in compression, i.e. at $\lambda_\mathrm{f} < 1$. In compression the total stress tensor $\boldsymbol{\sigma}$ is instead completely governed by the matrix contribution which yields the appropriate negative stresses. In Fig. 6.1(b) we show the invariants I_1 and I_4 during tension-compression

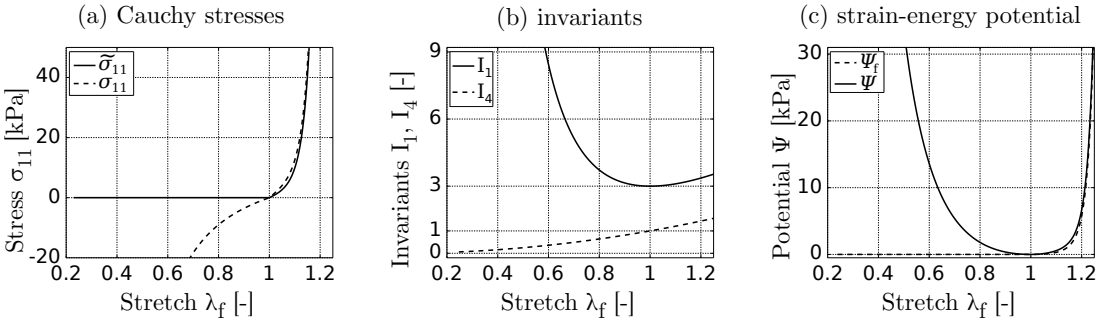

Figure 6.1.: Uniaxial tension-compression results for the fiber-reinforced model presented in [12]: (a) Cauchy stresses in the fiber direction for $\boldsymbol{\sigma}$ and $\tilde{\boldsymbol{\sigma}}_\mathrm{f}$; (b) invariants relating to isotropy, I_1, and fiber-reinforcement, I_4; (c) strain-energy potentials, both the total Ψ and the fiber contribution Ψ_f.

loading in the fiber direction. It is apparent that $I_4 \leq 1$ at $\lambda_\mathrm{f} \leq 1$, while $I_1 = 3$ at $\lambda_\mathrm{f} = 1$, and $I_1 > 3$ otherwise. In Fig. 6.1(c) we show the corresponding strain-energy response. Thus,

setting the fiber-component of the strain-energy function to zero during compression, i.e. $\Psi_{\mathrm{f}}^{\mathrm{c}} = 0$ when $I_4 \leq 1$, is motivated in part from physical considerations and in part from numerical considerations.

For constitutive models with distributed fiber orientations, cf. [31, 166, 180–182], stability of the fiber-terms in compression is still problematic, but a physical motivation to switch off fiber terms is now less clear. With fibers dispersed from the principal direction, single fibers oriented far from this principal direction may be in tension while the principal fiber direction is in compression (see, e.g., [167] for a related discussion on a dispersed model in tension). It must be noted though that such an assumption requires a very large dispersion or a very large compressions, both which are often outside the physiological range.

Nevertheless, a non-trivial choice must be made on how to handle compression in models with distributed fiber orientations. Here we analyze such a model, which includes a mixture of isotropic and transversely isotropic terms, for six different tension-compression switching assumptions. In Section 6.2 we outline our mathematical methods, in Section 6.3 we show results, and in Section 6.4 we provide a discussion and conclusion.

6.2. Mathematical methods

We examine the popular fiber dispersion model developed by Gasser, Holzapfel and Ogden [166]. It includes a dispersion parameter κ, based on the circular von Mises probability density function, which admits a physical interpretation. This dispersion parameter κ takes values in the range $\kappa \in [0, 1/3]$ and is used in the combined pseudo-invariant

$$I_4^* = \kappa I_1 + (1 - 3\kappa) I_4, \tag{6.5}$$

which is a mixture of the isotropic invariant I_1 and the directionally dependent pseudo-invariant I_4.

We generalize the presentation of the constitutive model from [166] to include six switching cases, which encompass different possible pseudo-invariants to trigger the tension-compression changes (Table 6.1, column 2; subsequently labeled as Table 6.1_2) and different possible strain-energy formulations for use in generalized compression $\Psi_{\mathrm{f}}^{\mathrm{c}i*}$, where the superscript i denotes the Case number, i.e. $i \in \{0, \ldots, 6\}$ (Table 6.1_4). Note that each Case thus represent a different material model. The combined invariant I_4^* replaces I_4 in (6.1) according to

$$\Psi_{\mathrm{f}}^* = \begin{cases} \Psi_{\mathrm{f}}^{\mathrm{t}*} = \dfrac{k_1}{2k_2}\left(\exp\left[k_2(I_4^* - 1)^2\right] - 1\right) & \text{if (Table } 6.1_2) > 1, \\ \Psi_{\mathrm{f}}^{\mathrm{c}i*} = (\text{Table } 6.1_4) & \text{if (Table } 6.1_2) \leq 1, \end{cases} \tag{6.6}$$

where again, for simplicity, we consider only one fiber direction. Note that when $\kappa = 0$ the fibers are perfectly aligned and $\Psi_{\mathrm{f}}^{\mathrm{t}*} = \Psi_{\mathrm{f}}^{\mathrm{t}}(I_4)$, but when $\kappa = 1/3$ the distribution is isotropic

and $\Psi_{\mathrm{f}}^{\mathrm{t}*} = \Psi_{\mathrm{f}}^{\mathrm{t}*}(I_1)$. As discussed in [166], for numerical stability (6.6) in tension needs to be modified for use in compression. Therefore, we investigate six possible switching cases shown in Table 6.1, where cases 1, 2 and 3 use as a 'switch' $I_4 \leq 1$, and cases 4, 5 and 6 use the combined invariant $I_4^* \leq 1$ as a 'switch'. A zeroth case, where $\Psi_{\mathrm{f}}^* = \Psi_{\mathrm{f}}^{\mathrm{t}*}$ for both tension and compression, i.e. no switch in compression, is also shown for illustrative purposes.

Case i	Switch	$I_{\mathrm{c}i}$	$\Psi_{\mathrm{f}}^{\mathrm{c}i*}$	$\boldsymbol{\sigma}_{\mathrm{f}}^{\mathrm{c}i*}$
0	-	I_4^*	$\frac{k_1}{2k_2}\left\{\exp\left[k_2(I_4^*-1)^2\right]-1\right\}$	$2k_1(I_4^*-1)\exp[k_2(I_4^*-1)^2]\mathbf{h}$
1	$I_4 \leq 1$	κI_1	$\frac{k_1}{2k_2}\left\{\exp\left[k_2(\kappa I_1-1)^2\right]-1\right\}$	$2k_1(\kappa I_1-1)\exp[k_2(\kappa I_1-1)^2]\kappa\mathbf{b}$
2	$I_4 \leq 1$	–	0	0
3	$I_4 \leq 1$	$\frac{1}{3}I_1$	$\frac{k_1}{2k_2}\left\{\exp\left[k_2(\frac{1}{3}I_1-1)^2\right]-1\right\}$	$2k_1(\frac{1}{3}I_1-1)\exp[k_2(\frac{1}{3}I_1-1)^2]\frac{1}{3}\mathbf{b}$
4	$I_4^* \leq 1$	κI_1	$\frac{k_1}{2k_2}\left\{\exp\left[k_2(\kappa I_1-1)^2\right]-1\right\}$	$2k_1(\kappa I_1-1)\exp[k_2(\kappa I_1-1)^2]\kappa\mathbf{b}$
5	$I_4^* \leq 1$	–	0	0
6	$I_4^* \leq 1$	$\frac{1}{3}I_1$	$\frac{k_1}{2k_2}\left\{\exp\left[k_2(\frac{1}{3}I_1-1)^2\right]-1\right\}$	$2k_1(\frac{1}{3}I_1-1)\exp[k_2(\frac{1}{3}I_1-1)^2]\frac{1}{3}\mathbf{b}$

Table 6.1.: Six possible choices for tension-compression switching of the dispersed fiber-reinforced constitutive model presented in [166]. The columns represent: the Case number, the criteria for tension-compression switching, the invariant term used in compression, the corresponding strain-energy function for compression and the corresponding Cauchy stress for compression, N.B., all Cases use the same combined invariant, strain-energy and corresponding Cauchy stress in tension. Case zero, shown for comparative purposes, does not switch from tension to compression.

As seen in Table 6.1_4, exclusion of directional (i.e. fiber orientation) dependence for the strain-energy function in compression may be achieved by simply removing I_4 from the equation, as shown in Cases 1 and 4, or by assigning $\kappa = 1/3$ for the dispersion parameter, as shown in Cases 3 and 6, or alternatively, and in accordance with (6.1), the entire strain-energy function associated with the fibers may be removed (i.e. $\Psi_{\mathrm{f}}^{\mathrm{c}i*} = 0$), as shown in Cases 2 and 5. Note that all Cases use the same combined invariant, strain-energy and corresponding Cauchy stress in tension.

It is now straightforward to write the Cauchy stress for the fiber contribution as

$$\boldsymbol{\sigma}_{\mathrm{f}}^* = 2\mathbf{F}\frac{\partial \Psi_{\mathrm{f}}^*}{\partial \mathbf{C}}\mathbf{F}^{\mathrm{T}} = \begin{cases} \boldsymbol{\sigma}_{\mathrm{f}}^{\mathrm{t}*} = 2k_1(I_4^*-1)\exp[k_2(I_4^*-1)^2]\mathbf{h} & \text{if (Table } 6.1_2) > 1, \\ \boldsymbol{\sigma}_{\mathrm{f}}^{\mathrm{c}i*} = (\text{Table } 6.1_5) & \text{if (Table } 6.1_2) \leq 1, \end{cases} \tag{6.7}$$

where $\mathbf{h} = \kappa\mathbf{b} + (1-3\kappa)\mathbf{a}\otimes\mathbf{a}$ is an Eulerian structure tensor incorporating the dispersed fiber structure.

We examine two loading conditions: uniaxial tension-compression in the principal fiber direction and simple shear (with a range of principal fiber directions). We use the material parameters from Section 6.1 (i.e., $k_1 = 10$ kPa and $k_2 = 15$ [-]), with the additional dispersion parameter κ [-] that is allowed to vary in the uniaxial tension-compression deformation state, and is set arbitrary to 0.15 in the shear deformation state. Given (6.7), we can determine the Cauchy stress analytically in terms of the applied deformations, i.e. the applied stretch λ_f or the shear γ. Full expressions for these stresses are given in Appendix B.1. For the uniaxial tension-compression loading state, we investigate the six switching cases in terms of (i) Cauchy stresses and (ii) the combined tension-compression invariant. For the simple shear loading state the switching cases are investigated in terms of (iii) the Cauchy stresses only.

6.3. Results

(i) The Cauchy stress – uniaxial tension-compression. Fig. 6.2 compares the fiber component of the Cauchy stress $\tilde{\boldsymbol{\sigma}}^*_\mathrm{f} = \boldsymbol{\sigma}^*_\mathrm{f} - p_\mathrm{h}\mathbf{I}$ which aligns with the 11–direction by design, i.e. $\tilde{\sigma}^*_\mathrm{ff} = [\tilde{\boldsymbol{\sigma}}^*_\mathrm{f}]_{11}$, for Cases 0–6. The solid black line in Fig. 6.2(a)–(f) highlight the stress behavior at $\kappa = 0.15$ for illustrative purposes. The effect of dispersion in tension is shown in all cases (the behavior in tension is always the same) where increasing values of κ decreases the tensile stress response (although it is always positive for $\lambda_\mathrm{f} > 1$). Case 0, as seen in Fig. 6.2(a), is used as a reference to show the effect of not changing the strain-energy function used in compression from that used in tension. For low κ-values and increased compressive stretches (λ_f increasingly < 1) the stress response will first turn strongly negative followed by a large positive stress. For very large values of κ the stress response will only be negative. Fig. 6.2(b) illustrates both cases 1 and 4 as they give a nearly identical stress response. Following the black line in compression, Cases 1 and 4 show a large positive stress in compression until $\lambda_\mathrm{f} \sim 0.3$ where it becomes negative. For Case 2, Fig. 6.2(c), the stress in compression is always zero. For Case 3, Fig. 6.2 d), the compressive stress is always negative and independent of the κ-value, and increased compression leads to increasingly negative stresses. In Fig. 6.2(e), Case 5, we see the effects of using $I^*_4 \leq 1$ as a switch. The stress in compression for Case 5 is zero until $\lambda_\mathrm{f} \sim 0.3$ where it turns negative, and note that increasing κ shifts the point where Case 5 yields negative stresses towards lower levels of compression. Lastly, following the black line for Case 6 in Fig. 6.2(f) shows that the fiber stress will drop to large negative values when initially compressed, but that further increasing compression will cause the stress to increase again.

(ii) The combined invariant – uniaxial tension-compression. Fig. 6.3(a)–d) compares the combined invariant I^*_4 for cases 0, 1, 3 and 4, respectively. A black line is again used

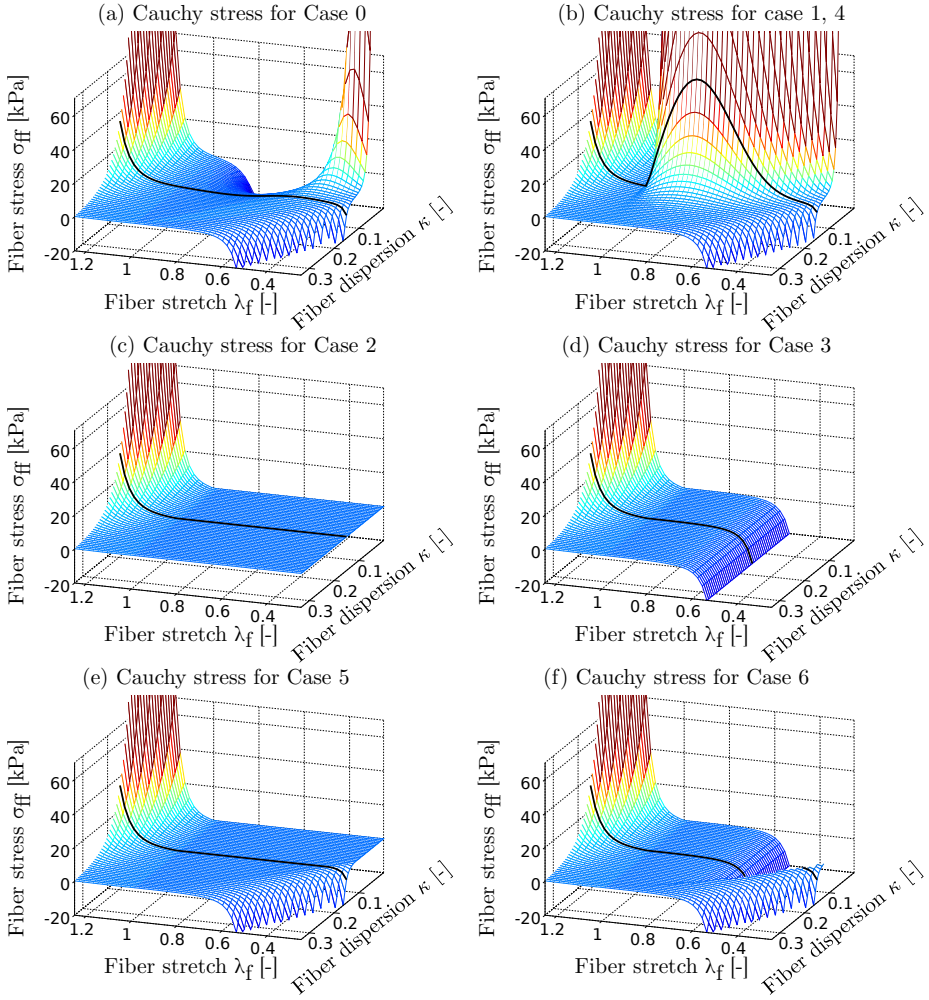

Figure 6.2.: Cauchy stress results in the fiber direction under uniaxial tension-compression for six possible choices of tension-compression switching for the dispersed fiber-reinforced constitutive model presented in [166]. Cases 0–6 shown in (a)–(f), respectively, cf. Table 6.1_5. A solid black line follows the stress results at $\kappa = 0.15$.

to highlight the behavior when $\kappa = 0.15$. Two transparent planes are used as reference planes. The horizontal plane indicates $I_4^* = 1$ and the vertical plane indicates $\lambda_f = 1$. Case 0, seen in Fig. 6.3(a), shows the behavior of the combined invariant when going from tension to compression. Clearly, $I_4^* > 1$ may occur even at a large compression depending on the value of κ. Following the black line, as a representative case, $I_4^* > 1$ occurs at $\lambda_f \sim 0.3$, which corresponds to the compression level when Cases 0, 1, 4 and 5 show negative stresses along the same line (cf. Fig. 6.2(a), (b) and (e)). Following the black line in Fig. 6.3(b) further shows that I_4^* makes a sharp decrease for Case 1 at $\lambda_f = 1$ to $I_4^* \sim 0.45$. Increasing the level of compression yields larger values of I_4^* and again at $\lambda_f \sim 0.3$, $I_4^* > 1$, similar to Case 0. The behavior seen in Fig. 6.3 d) for Case 4, is nearly identical to Case 1,

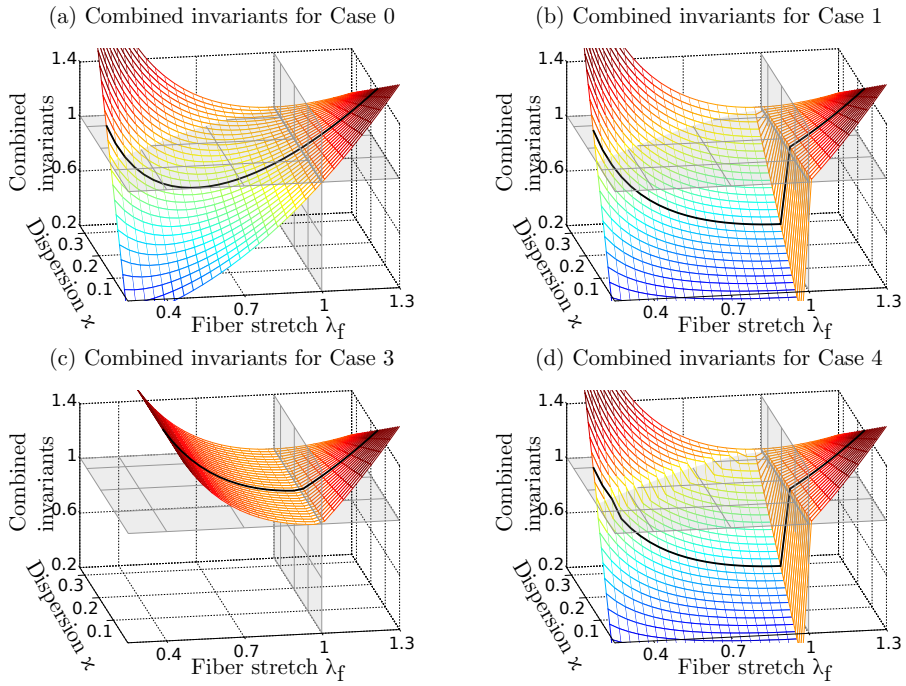

Figure 6.3.: Combined invariant results for 4 possible choices of a combined tension-compression invariant undergoing uniaxial tension-compression for Cases 0, 1, 3 and 4, cf. Table 6.1_3: (a) behavior of the combined invariant without using any switch, i.e. $I_{c0} = I_4^*$; (b) combined invariant $I_{c1} = \kappa I_1$ for Case 1; (c) combined invariant $I_{c3} = 1/3 I_1$ for Case 3; d) combined invariant $I_{c4} = \kappa I_1$ for Case 4, with switching determined by $I_4^* \leq 1$; N.B., all Cases use I_4^* for the combined invariant in tension. A solid black line follows the combined invariant results at $\kappa = 0.15$.

except for a jump in the values of I_4^* around $\lambda_f \sim 0.3$ that is seen when following the black line. For Case 3, however, I_4^* is always ≥ 1, in both tension and compression as seen in Fig. 6.3(c).

(iii) The Cauchy stress – simple shear. As Cases 0, 1, 4 and 6 clearly demonstrate non-physical stress responses in uniaxial compression (cf. Fig. 6.2 (a), (b) and (f)), only Cases 2, 3 and 5 are investigated further in simple shear. Depending on the initial orientation of the fiber direction, simple shear (with applied displacement γ) may result in tension or compression of the Eulerian fiber direction. The stretch is shown in Fig. 6.4(a) as a function of shear γ and the angle α between the fiber and the 11–direction (cf. inset in Fig. 6.4(a)). When the angle is zero, i.e. fibers are aligned in the shear direction, there is no stretch in the fiber direction regardless of the amount of shear. As the angle increases from zero, however, the stretch also increases with shear until $\alpha \sim 52°$, where $\lambda_f \sim 1.28$, after which it decreases again. At $\alpha > 90°$, low values of γ may yield $\lambda_f < 1$ whereas large values of γ yields $\lambda_f > 1$. For $\alpha \sim 142°$ the largest compressive stretch, $\lambda_f \sim 0.78$, is found at $\gamma = 0.5$ and for $142° < \alpha < 180°$ only compressive stretches are seen (while $\gamma \leq 0.5$). In Fig. 6.4(b), (c) and d), the Cauchy stress in the Eulerian fiber direction is

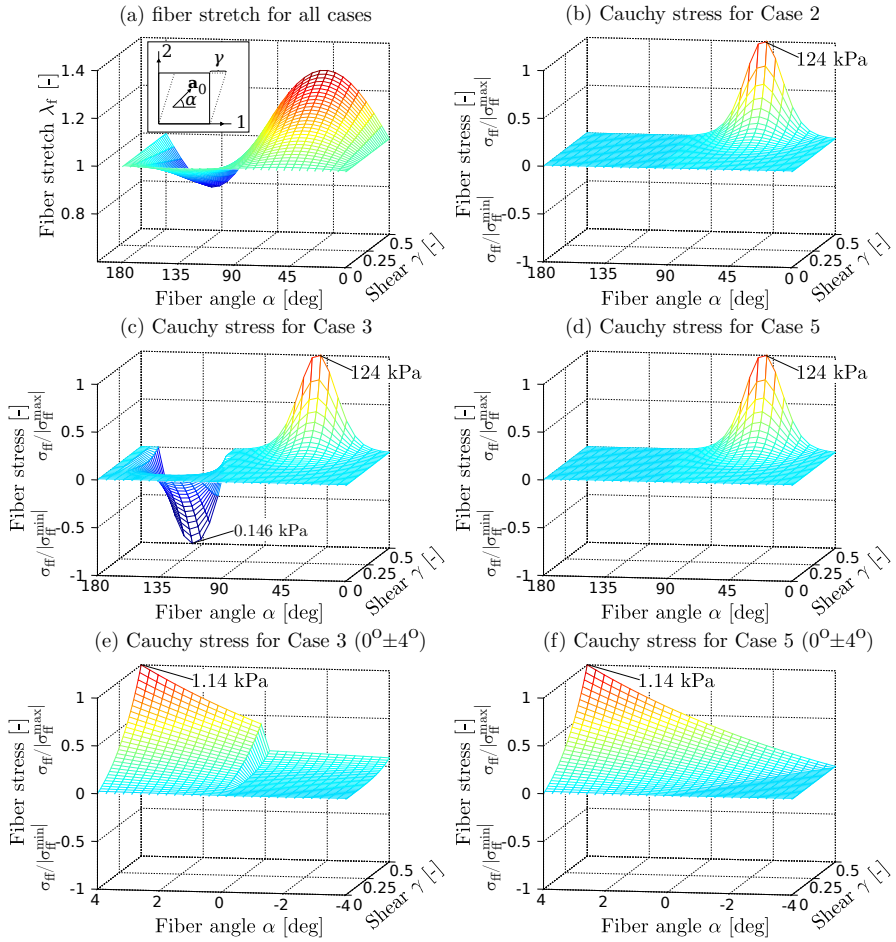

Figure 6.4.: Stretch and Cauchy stress results in the fiber direction with varying Lagrangian fiber angle α and shear γ under simple shear deformation in the 1–2 plane for Cases 2, 3 and 5, cf. Table 6.1$_5$: (a) stretch in the fiber direction for all cases (inset defines simple shear γ on a unit cube and fiber angle α); Cauchy stress in the deformed fiber direction σ_{ff} for: (b) Case 2; (c) Case 3; d) Case 5; Closeup of Cauchy stress in the deformed fiber direction σ_{ff} when $\alpha = 0^\circ \pm 4^\circ$ for: (e) Case 3; (f) Case 5. N.B., positive stresses are normalized by the modulus of the maximum fiber stress $|\sigma_{ff}^{max}|$ while negative stresses are normalized by the modulus of the minimum fiber stress $|\sigma_{ff}^{min}|$ for visual clarity.

shown for Cases 2, 3 and 5, respectively. In Fig. 4, positive stresses are normalized by the modulus of the maximum fiber stress $|\sigma_{ff}^{max}|$ while negative stresses are normalized by the modulus of the minimum fiber stress $|\sigma_{ff}^{min}|$ for visual clarity (as the difference in magnitude between positive and negative stress values is very large). As the Cauchy stress is zero in compression by design for Case 2, only one peak is seen in Fig. 6.4(b). Here the maximum value of the Cauchy stress in tension is 124 kPa and is centered around $\alpha \sim 52^\circ$. Because all cases have the same behavior in tension, the maximum tensile stress for all cases is identical. Case 3 has a minimum compressive stress of -0.146 kPa at

$\alpha \sim 142^\circ$ as seen in Fig. 6.4(c). In Case 5, shown in Fig. 6.4 d), the stress is mostly zero in compression. At closer inspection, however, for very large initial fiber angles, i.e. where $180^\circ > \alpha > 175^\circ$, a small positive stress peak is seen (0.450 kPa) even as the principal fiber direction is in compression. This is illustrated in the closeup of the fiber stress at $\alpha = 0^\circ \pm 4^\circ$ for Case 5 seen in Fig. 6.4(f). However, looking at a similar closeup of the fiber stress for Case 3 in Fig. 6.4(e), we also see small positive stresses.

6.4. Discussion

Large-strain models for dispersed fiber-reinforced materials in, e.g., soft tissue biomechanics, need to solve the problem of switching the form of the fiber potential used in compression from that used in tension, to provide a consistent physical interpretation and to ensure both numerical stability and robustness. Cases 1 and 2, and models with similarities to Case 3, are often used approaches to deal with fiber compression, cf. [166, 182, 184]. In the dispersion models investigated here, Cases 3, 4 and 6 have, to the authors' knowledge, not previously been used or investigated in the mechanics literature (a model similar to Case 5 is employed in [185]).

The 'switch' used in Cases 4, 5 and 6, $I_4^* \leq 1$, correctly switches when $\lambda_\mathrm{f} = 1$ for a uniaxial deformation, and is motivated by the comparison of (6.1) and (6.6). However, in contrast to the relation $I_4 < 1$ which is always true in fiber compression, the relation $I_4^* \not< 1$ for large fiber compressions, as seen in Fig. 6.3(a). The combined invariant I_4^* may become positive in compression because under increasingly large compression (λ_f increasingly < 1), I_1 becomes $\gg 3$ while I_4 is only < 1, as seen in Fig. 6.1(b). At which compression point the combined invariant will shift from negative to positive depends on the value of the dispersion parameter κ. With progressively larger values of κ, i.e. larger dispersion, $I_4^* > 1$ will occur at progressively lower levels of compression in the fibers. Hence, with this switching approach the dispersion parameter κ has a non-physical and ambiguous meaning (cf. Cases 4–6), as it reflects both the fiber dispersion and some arbitrary switch whereby, e.g., negative/positive fiber stresses may occur in compression. For this reason, we believe that the switch parameter $I_4^* \leq 1$ should only be used under loading conditions which do not trigger $I_4^* > 1$ while $\lambda_\mathrm{f} < 1$.

Perhaps the most startling results in this study are the positive stresses generated in compression for Cases 1 and 4 in uniaxial tension-compression and for Case 5 in simple shear (while the principal fiber direction is in compression). Clearly in the uniaxial case, when compressing a fiber reinforced material in the principal fiber direction, a positive stress in the direction of compression is not physiologically relevant, but it is seen nonetheless in Fig. 6.2(b) for Cases 1 and 4. The reason for the positive stress in these two cases is clear when looking at the combined invariants $I_{\mathrm{c}1} = I_{\mathrm{c}4} = \kappa I_1$, in compression. For any value of $\kappa \neq 1/3$, Fig. 6.3(b) and d) show that $I_4^* < 1$ at $\lambda_\mathrm{f} = 1$, which leads to $\tilde{\boldsymbol{\sigma}}_\mathrm{f}^{\mathrm{c}1*} > 1$ and $\tilde{\boldsymbol{\sigma}}_\mathrm{f}^{\mathrm{c}4*} > 1$ according to (6.7). This occurrence violates a fundamental requirement that the

reference configuration should be stress-free, i.e. here we see that $\Psi_{\mathrm{f}}^{*}(\mathbf{F}=\mathbf{I}) \neq 0$ and thus $\tilde{\boldsymbol{\sigma}}_{\mathrm{f}}^{*}(\mathbf{F}=\mathbf{I}) \neq \mathbf{0}$, which should not be, cf. [6]. The condition requiring a stress-free reference state is naturally fulfilled for Cases 2 and 5, where $\Psi_{\mathrm{f}}^{\mathrm{c2}*} = \Psi_{\mathrm{f}}^{\mathrm{c5}*} = 0$ gives $\tilde{\boldsymbol{\sigma}}^{\mathrm{c2}*} = \tilde{\boldsymbol{\sigma}}^{\mathrm{c5}*} = \mathbf{0}$, cf. Fig. 6.2(c), (e) and 6.4(a), (c). Similarly, this condition is fulfilled for Case 3, whereby in compression the dispersion parameter is set to $\kappa = 1/3$, and thus $\Psi_{\mathrm{f}}^{*}(\mathbf{F}=\mathbf{I}) = 0$ as $I_{\mathrm{c3}}(\mathbf{F}=\mathbf{I}) = 1$.

The reason for positive stresses for Case 5 in simple shear (while the principal fiber direction is in compression) is perhaps not clear. For α close to (but less than) 180°, the isotropic response projected in the fiber direction is actually positive as seen, e.g., in Case 3 Fig. 6.4(e), or when using a neo-Hookean strain-energy function for this deformation (not shown here). The positive stress in Case 5 may be physiological as it incorporates a positive stress response for small perturbations of the principal fiber angle around 0 (equivalently 180°), given some level of dispersion. However, κ still has a dual meaning, the same as was seen for Case 5 in uniaxial tension-compression. Thus, in Case 5, κ determines both the degree of dispersion and the amount of shear required to generate positive stresses while the principal fiber direction is in compression. Therefore, it is less clear what the parameter κ represents for Case 5.

Although not shown here, using different material parameters in (6.6), within the required range ($k_1 > 0$ and $k_2 > 0$), only changes the magnitude of the stress response or the compression point where, e.g., $I_4^{*} > 1$ may occur. It does not alter the trends shown or the conclusions drawn from this analysis. We have shown that Cases 2 and 3 generate the most desirable results, both in terms of a physically consistent morphological interpretation, robustness and also consistency in the interpretation of the structural parameter κ. We implemented both of these models in the finite element analysis software FEAP [8], and verified that they yield numerically stable results identical to those shown in Fig. 6.2(c), d) and 6.4(a), (b). Case 2, in the physical interpretation, corresponds to the situation wherein the fibers buckle under compression and are essentially uncoupled to the ground matrix (and furthermore, are not cross-linked). Thus, when the principal direction of fiber reinforcement is in compression the dispersed fibers have no stiffness and do not store strain-energy. Case 3, conversely, corresponds to another situation, wherein a matrix-fiber bonding does exist, and which results in an isotropic positive fiber potential (the dispersed fibers store strain-energy) even in compression.

We have further shown that Case 5 may be used with caution. Although it may yield negative stresses in uniaxial deformation at some arbitrary (but high) level of compression, such levels are rarely reached in the physiological applications where the model is most often used. In effect, Case 5 will thus render an equal stress response as Case 2. However, as seen in Fig. 6.4(f), Case 5 may advantageously be used to capture positive stress responses for small perturbations of the principal fiber direction around some critical angle where the principal fiber direction switches between tension and compression and where, e.g., Case 2 would instantly set the stress values to zero. Case 5, using $I_4^{*} \leq 1$ as the switch, may

thus be advantageous for numerical convergence in, e.g., a FE simulation, but as we have shown that this effect is regulated by the dispersion parameter κ, it is unclear how (or if) this phenomenon has a physical interpretation.

As a final note on numerical stability, we investigated the convexity and ellipticity of the strain-energy functions shown here in Appendix B.2. Therein we show that the strain-energy function, proposed by Gasser, Holzapfel and Ogden [166], and also used here, is locally convex in $\mathbf{C}$ for both tension and compression. However, from two simple examples we also show that ellipticity can not be guaranteed in general for incompressible models that couple the invariants I_1 and I_4. Nevertheless, the strain-energy function (6.6) has been implemented in the FE framework FEAP [8], and for all types of deformations tested it has remained stable. Future investigations are needed to determine the conditions under which ellipticity is lost.

Acknowledgements

This project is supported in part by the SFB Research Center 'Mathematical Optimization and Applications in Biomedical Sciences', project F3210-N18 granted by the Austrian Science Fund. This support is gratefully acknowledged.

A. APPENDIX FOR CHAPTER 5

A.1. Elasticity Tensors for the Active Stress

Using the definition $\mathbf{M}_0 := \mathbf{f}_0 \otimes \mathbf{f}_0$ and the abbreviation (5.15), (5.14) may be written as

$$\mathbf{S}_\mathrm{a} = S_\mathrm{a} \left(\frac{\kappa_\mathrm{f}}{1-2\kappa_\mathrm{f}} \mathbf{C}^{-1} + \frac{1-3\kappa_\mathrm{f}}{1-2\kappa_\mathrm{f}} I_{4\mathrm{f}}^{-1} \mathbf{M}_0 \right). \tag{A.1}$$

The Lagrangian elasticity tensor is given by $\mathbb{C}_\mathrm{a} = 2\partial \mathbf{S}_\mathrm{a} / \partial \mathbf{C}$ which leads to

$$\mathbb{C}_\mathrm{a} = 2 \frac{S_\mathrm{a}}{1-2\kappa_\mathrm{f}} \left[\kappa_\mathrm{f} \frac{\partial \mathbf{C}^{-1}}{\partial \mathbf{C}} + (1-3\kappa_\mathrm{f}) \frac{\partial I_{4\mathrm{f}}^{-1} \mathbf{M}_0}{\partial \mathbf{C}} \right]. \tag{A.2}$$

Using the derivative $\partial (I_{4\mathrm{f}}^{-1} \mathbf{M}_0) / \partial \mathbf{C} = -I_{4\mathrm{f}}^{-2} \mathbf{M}_0 \otimes \mathbf{M}_0$, (A.2) can be written as

$$\mathbb{C}_\mathrm{a} = 2 \frac{S_\mathrm{a}}{1-2\kappa_\mathrm{f}} \left[\kappa_\mathrm{f} \frac{\partial \mathbf{C}^{-1}}{\partial \mathbf{C}} - (1-3\kappa_\mathrm{f}) I_{4\mathrm{f}}^{-2} \mathbf{M}_0 \otimes \mathbf{M}_0 \right], \tag{A.3}$$

and by using the push-forward operation of $\mathbb{C}_\mathrm{a}$ according to

$$[\mathbb{c}_\mathrm{a}]_{abcd} = J^{-1} F_{aA} F_{bB} F_{cC} F_{dD} [\mathbb{C}_\mathrm{a}]_{ABCD}, \tag{A.4}$$

this leads to

$$\mathbb{c}_\mathrm{a} = -2 \frac{S_\mathrm{a}}{J(1-2\kappa_\mathrm{f})} \left[\kappa_\mathrm{f} \mathbb{I} + (1-3\kappa_\mathrm{f}) \hat{\mathbf{M}} \otimes \hat{\mathbf{M}} \right], \tag{A.5}$$

where the fourth-order identity tensor $\mathbb{I}$, defined in index notation as $[\mathbb{I}]_{abcd} = (\delta_{ac}\delta_{bd} + \delta_{ad}\delta_{cd})/2$, is introduced from the push-forward of the relation $\partial(\mathbf{C}^{-1})/\partial\mathbf{C}$ according to $F_{aA}F_{bB}F_{cC}F_{dD} \left[\partial(\mathbf{C}^{-1})/\partial\mathbf{C}\right]_{ABCD} = -[\mathbb{I}]_{abcd}$ and the definition $\hat{\mathbf{M}} := \mathbf{F} I_{4\mathrm{f}}^{-1} \mathbf{M}_0 \mathbf{F}^\mathrm{T} = \hat{\mathbf{f}} \otimes \hat{\mathbf{f}}$ has been used.

B. APPENDIX FOR CHAPTER 6

B.1. The Stress Equations as a Function of Applied Stretch λ_f or Applied Shear γ

As all stress components shown in the following are related to the fiber part of the stress, i.e. $\tilde{\boldsymbol{\sigma}}_f$ or $\tilde{\boldsymbol{\sigma}}_f^*$, the subindex f is not shown on a component level to simplify notation. The subindex ff, however, is used and denotes the component of the stress tensor aligned in the deformed fiber direction.

In uniaxial tension in the 11–direction, the corresponding deformation gradient is $\mathbf{F} = \text{diag}(\lambda_f, \lambda_f^{-1/2}, \lambda_f^{-1/2})$ when the fiber $[\mathbf{a}_0] = [1,0,0]^T$ aligned in the 11-direction (meaning that $\tilde{\sigma}_{ff} = \tilde{\sigma}_{11}$). Using (6.4), the only non-zero component of $\tilde{\boldsymbol{\sigma}}_f = \boldsymbol{\sigma}_f - p_h\mathbf{I}$ in tension is

$$\tilde{\sigma}_{11}^t = 2k_1\left(\lambda_f^2 - 1\right)\exp[k_2\left(\lambda_f^2 - 1\right)^2]\lambda_f^2, \tag{B.1}$$

where p is determined from $\tilde{\sigma}_{33} = 0$, and in compression $\tilde{\sigma}_{11}^c = 0$. Using (6.7), the only non-zero component of $\tilde{\boldsymbol{\sigma}}_f^* = \boldsymbol{\sigma}_f^* - p_h\mathbf{I}$ in tension is

$$\begin{aligned}\tilde{\sigma}_{11}^{t*} = 2k_1[(1-2\kappa)\lambda_f^2 + 2\kappa\lambda_f^{-1} - 1]\exp\{k_2[(1-2\kappa)\lambda_f^2 \\ + 2\kappa\lambda_f^{-1} - 1]^2\}[(1-2\kappa)\lambda_f^2 - \kappa\lambda_f^{-1}],\end{aligned} \tag{B.2}$$

where p is determined from $\tilde{\sigma}_{33}^* = 0$. In compression the Cauchy stresses in the 11-direction are instead

$$\tilde{\sigma}_{11}^{c1*} = 2k_1[\kappa\left(\lambda_f^2 + 2\lambda_f^{-1}\right) - 1]\exp\{k_2[\kappa(\lambda_f^2 + 2\lambda_f^{-1}) - 1]^2\}\kappa(\lambda_f^2 - \lambda_f^{-1}), \tag{B.3}$$

$$\tilde{\sigma}_{11}^{c2*} = \tilde{\sigma}_{11}^{c5*} = 0, \tag{B.4}$$

$$\tilde{\sigma}_{11}^{c3*} = 2k_1[1/3(\lambda_f^2 + 2\lambda_f^{-1}) - 1]\exp\{k_2[1/3(\lambda_f^2 + 2\lambda_f^{-1}) - 1]^2\}1/3(\lambda_f^2 - \lambda_f^{-1}), \tag{B.5}$$

$$\tilde{\sigma}_{11}^{c4*} = \tilde{\sigma}_{11}^{c1*}, \tag{B.6}$$

$$\tilde{\sigma}_{11}^{c6*} = \tilde{\sigma}_{11}^{c3*}, \tag{B.7}$$

where the superscript ci, $i \in \{1,\ldots,6\}$ represent the six cases shown in Table 6.1. Case 0 in compression equals the formulation in tension shown in (B.2), i.e. $\tilde{\sigma}_{11}^{c0*} = \tilde{\sigma}_{11}^{t*}$.

Similarly, during simple shear the deformation gradient is

$$[\mathbf{F}] = \begin{bmatrix} 1 & \gamma & 0 \\ 0 & 1 & 0 \\ 0 & 0 & 1 \end{bmatrix},$$

and with the fiber direction $[\mathbf{a}_0] = [\cos(\alpha), \sin(\alpha), 0]^{\mathrm{T}}$ in the Lagrangian description, the 33-direction is stress free and is used to determine p. The non-zero components of $\tilde{\boldsymbol{\sigma}}_{\mathrm{f}}^{*}$ in tension are

$$\tilde{\sigma}_{11}^{\mathrm{t}*} = 2\psi_4^{\mathrm{t}*}\left[\kappa\gamma^2 + (1-3\kappa)A_1^2\right], \tag{B.8}$$

$$\tilde{\sigma}_{12}^{\mathrm{t}*} = \tilde{\sigma}_{21}^{\mathrm{t}*} = 2\psi_4^{\mathrm{t}*}[\kappa\gamma + (1-3\kappa)A_1\sin(\alpha)], \tag{B.9}$$

$$\tilde{\sigma}_{22}^{\mathrm{t}*} = 2\psi_4^{\mathrm{t}*}(1-3\kappa)\sin^2(\alpha), \tag{B.10}$$

where $A_1(\gamma,\alpha) := \gamma\sin(\alpha) + \cos(\alpha)$ is used to shorten notation, and $\psi_4^{\mathrm{t}*} = \partial\Psi^{\mathrm{t}*}/\partial I_4^{*}$ is given by

$$\psi_4^{\mathrm{t}*} = k_1\left[\kappa(\gamma^2+3) + (1-3\kappa)A_2 - 1\right]\exp\left\{k_2\left[\kappa(\gamma^2+3) + (1-3\kappa)A_2 - 1\right]^2\right\}, \tag{B.11}$$

where $A_2(\gamma,\alpha) := (\gamma\sin(\alpha)+\cos(\alpha))^2 + \sin^2(\alpha)$ is used to shorten notation, N.B., $A_2 = I_4$ for this deformation. Depending on Table 6.1_2, the value used to determine if the fiber direction is in compression is thus either $A_2 \leq 1$ or $I_4^{*} = \kappa(\gamma^2+3) + (1-3\kappa)A_2 \leq 1$. To determine the Cauchy stresses in compression, it is necessary to derive the derivatives of the strain-energy functions with respect to the combined invariants for Cases 1–6 in compression, i.e. $\psi_{ci}^{ci*} = \partial\Psi^{ci*}/\partial I_{ci}$, for $i = 1,2,\ldots,6$:

$$\psi_{\mathrm{c}1}^{\mathrm{c}1*} = \psi_{\mathrm{c}4}^{\mathrm{c}4*} = k_1\left[\kappa(\gamma^2+3) - 1\right]\exp\{k_2\left[\kappa(\gamma^2+3) - 1\right]^2\}, \tag{B.12}$$

$$\psi_{\mathrm{c}2}^{\mathrm{c}2*} = \psi_{\mathrm{c}5}^{\mathrm{c}5*} = 0, \tag{B.13}$$

$$\psi_{\mathrm{c}3}^{\mathrm{c}3*} = \psi_{\mathrm{c}6}^{\mathrm{c}6*} = k_1\left[1/3(\gamma^2+3) - 1\right]\exp\{k_2\left[1/3(\gamma^2+3) - 1\right]^2\}. \tag{B.14}$$

Now, for Cases 1–6, the 11-component of the Cauchy stresses in compression are

$$\tilde{\sigma}_{11}^{\mathrm{c}1*} = \tilde{\sigma}_{11}^{\mathrm{c}4*} = 2\psi_{\mathrm{c}1}^{\mathrm{c}1*}\kappa\gamma^2, \tag{B.15}$$

$$\tilde{\sigma}_{11}^{\mathrm{c}2*} = \tilde{\sigma}_{11}^{\mathrm{c}5*} = 0, \tag{B.16}$$

$$\tilde{\sigma}_{11}^{\mathrm{c}3*} = \tilde{\sigma}_{11}^{\mathrm{c}6*} = 2\psi_{\mathrm{c}3}^{\mathrm{c}3*}1/3\gamma^2, \tag{B.17}$$

and the 12-components (equally the 21-components) are

$$\tilde{\sigma}_{12}^{\mathrm{c}1*} = \tilde{\sigma}_{12}^{\mathrm{c}4*} = 2\psi_{\mathrm{c}1}^{\mathrm{c}1*}\kappa\gamma, \tag{B.18}$$

$$\tilde{\sigma}_{12}^{\mathrm{c}2*} = \tilde{\sigma}_{12}^{\mathrm{c}5*} = 0, \tag{B.19}$$

$$\tilde{\sigma}_{12}^{\mathrm{c}3*} = \tilde{\sigma}_{12}^{\mathrm{c}6*} = 2\psi_{\mathrm{c}3}^{\mathrm{c}3*}1/3\gamma, \tag{B.20}$$

and finally, the 22-direction components of the Cauchy stresses are all zero for all cases in compression, i.e. $\tilde{\sigma}_{22}^{ci*} = 0$. The projection of the stress tensor in the fiber direction, i.e. $\tilde{\boldsymbol{\sigma}}_{\mathrm{f}}^{*} : \mathbf{a}\otimes\mathbf{a}$, yields the following fiber component of the stress in tension

$$\begin{aligned}\sigma_{\mathrm{ff}}^{\mathrm{t}*} = 2\psi_4^{\mathrm{t}*}\{&A_1^2[\gamma^2\kappa + (1-3\kappa)A_1^2] \\ &+ 2\sin(\alpha)A_1[(1-3\kappa)\sin(\alpha)A_1 + \gamma\kappa] + (1-3\kappa)\sin^4(\alpha)\},\end{aligned} \tag{B.21}$$

and in compression

$$\sigma_{\mathrm{ff}}^{\mathrm{c1}*} = \sigma_{\mathrm{ff}}^{\mathrm{c4}*} = 2\psi_4^{\mathrm{c1}*}\kappa\gamma\left[\gamma A_1^2 + 2A_1\sin(\alpha)\right], \tag{B.22}$$

$$\sigma_{\mathrm{ff}}^{\mathrm{c2}*} = \sigma_{\mathrm{ff}}^{\mathrm{c5}*} = 0, \tag{B.23}$$

$$\sigma_{\mathrm{ff}}^{\mathrm{c3}*} = \sigma_{\mathrm{ff}}^{\mathrm{c6}*} = 2\psi_4^{\mathrm{c1}*}1/3\gamma\left[\gamma A_1^2 + 2A_1\sin(\alpha)\right]. \tag{B.24}$$

To summarize, (B.1) and $\tilde{\sigma}_{11}^{c} = 0$ are used to generate Fig. 6.1, (B.2) and (B.3)–(B.7) are used to generate Fig. 6.2, while (B.11) and (B.12)–(B.14) together with (B.21) and (B.22)–(B.24) are used to generate Fig. 6.4.

B.2. Convexity and Ellipticity of Distributed Functions

In this section, convexity of Eq. (6.6) and ellipticity of models that include a coupling between invariants I_1 and I_4 are investigated. First considering tension only, the function $\mathcal{T}(I_4^*) := k_1/(2k_2)\left(\exp[k_2(I_4^*-1)^2]-1\right)$ is defined, which has the relations

$$\frac{\partial\mathcal{T}(I_4^*)}{\partial\mathbf{C}} = \mathcal{T}'(I_4^*)\mathbf{H} \quad \text{and} \quad \frac{\partial^2\mathcal{T}(I_4^*)}{\partial\mathbf{C}\partial\mathbf{C}} = \mathcal{T}''(I_4^*)\mathbf{H}\otimes\mathbf{H}, \tag{B.25}$$

where the primes denotes the differentiation of $\mathcal{T}(I_4^*)$ with respect to I_4^* and $\mathbf{H}$ is the Lagrangian distributed structure tensor given by

$$\mathbf{H} = \frac{\partial I_4^*}{\partial\mathbf{C}} = \kappa\mathbf{I} + (1-3\kappa)\mathbf{A}_0, \tag{B.26}$$

where $\mathbf{I}$ is the second order identity tensor. Local convexity requires that

$$\mathbf{M} : \frac{\partial^2\mathcal{T}(I_4^*)}{\partial\mathbf{C}\partial\mathbf{C}} : \mathbf{M} \equiv \mathcal{T}''(I_4^*)[\mathbf{H}:\mathbf{M}]^2 \geq 0 \tag{B.27}$$

for all second order tensors $\mathbf{M}$ (cf. Holzapfel and Ogden [42]). Thus, $\mathcal{T}(I_4^*)$ is convex in $\mathbf{C}$ provided that $\mathcal{T}''(I_4^*) \geq 0$. The second derivative of $\mathcal{T}(I_4^*)$ with respect to I_4^* is

$$\mathcal{T}''(I_4^*) = k_1\exp[k_2(I_4^*-1)^2]\left[1+2k_2(I_4^*-1)^2\right], \tag{B.28}$$

and for $k_1 > 0$ and $k_2 > 0$, the inequality $\mathcal{T}''(I_4^*) \geq 0$ is fulfilled showing that $\mathcal{T}(I_4^*)$ is a convex function. In fact, $\mathcal{T}(I_4^*)$ is convex both in tension and in compression. However, given that tension-compression switching is necessary to obtain physically reasonable stresses (cf. Fig. 6.2 (a)), it remains to investigate convexity in compression for Case 3, (as all other cases are either zero or do not generate reasonable stresses in compression). We define a function $\mathcal{S}(I_1) := k_1/(2k_2)\left(\exp[k_2(1/3I_1-1)^2]\right)$, which has the relations

$$\frac{\partial\mathcal{S}(I_1)}{\partial\mathbf{C}} = \mathcal{S}'(I_1)\mathbf{I} \quad \text{and} \quad \frac{\partial^2\mathcal{S}(I_1)}{\partial\mathbf{C}\partial\mathbf{C}} = \mathcal{S}''(I_1)\mathbf{I}\otimes\mathbf{I}, \tag{B.29}$$

where the primes denote differentiation of $\mathcal{S}(I_1)$ with respect to I_1. Again, local convexity requires that

$$\mathbf{M} : \frac{\partial^2 \mathcal{S}(I_1)}{\partial \mathbf{C} \partial \mathbf{C}} : \mathbf{M} \equiv \mathcal{S}''(I_1)(\text{tr}\,\mathbf{M})^2 \geq 0, \tag{B.30}$$

for all second order tensors $\mathbf{M}$, which is fulfilled when $\mathcal{S}''(I_1) \geq 0$. The second derivative of $\mathcal{S}(I_1)$ is

$$\mathcal{S}''(I_1) = k_1 \exp[k_2(1/3I_1 - 1)^2] \left[1 + 2k_2(1/3I_1 - 1)^2\right], \tag{B.31}$$

and for $k_1 > 0$ and $k_2 > 0$, the inequality $\mathcal{S}''(I_1) \geq 0$ is fulfilled showing that $\mathcal{S}(I_1)$ is locally convex.

To demonstrate ellipticity in a 3-D general setting is very challenging. Given an incompressible strain-energy function $\hat{\Psi}(I_1, I_4)$, it was shown by Merodio and Ogden [186] (cf. Eq. 2.50 therein), that for 2-D plain strain, ellipticity is fulfilled in terms of the principal stretches λ_1 and λ_2 if

$$\begin{aligned} &2\hat{\psi}_{11}(\lambda_1^2 - \lambda_2^2)^2 n_1^2 n_2^2 + \hat{\psi}_1(\lambda_1^2 n_1^2 + \lambda_2^2 n_2^2) \\ &+ 4\hat{\psi}_{14}(\lambda_1^2 - \lambda_2^2) n_1 n_2 (n_1 a_1 + n_2 a_2)(n_2 a_1 - n_1 a_2) \\ &+ 2\hat{\psi}_{44}(n_1 a_1 + n_2 a_2)^2 (n_2 a_1 - n_1 a_2)^2 + \hat{\psi}_4 (n_1 a_1 + n_2 a_2)^2 > 0, \end{aligned} \tag{B.32}$$

where $\hat{\psi}_{ij},\ i,j \in \{1,4\}$ are the differentiation of $\hat{\Psi}$ with respect to the invariants I_1 and I_4, respectively, n_1 and n_2 are the components of a unit vector $\mathbf{n}$, and a_1 and a_2 are the components of an Eulerian fiber direction vector $\mathbf{a} = \mathbf{F}\mathbf{A}_0$ (see [186] for details). The relation in (B.32) is here separated into three functions that correlate to the differentiation of $\hat{\Psi}$, namely $\mathcal{F}(\hat{\psi}_1, \hat{\psi}_{11}) + \mathcal{G}(\hat{\psi}_{14}) + \mathcal{H}(\hat{\psi}_4, \hat{\psi}_{44}) > 0$.

For an isotropic material, only $\mathcal{F}(\hat{\psi}_1, \hat{\psi}_{11})$ is non-zero and through manipulation of this function, Merodio and Ogden [186] showed that the relations

$$\hat{\psi}_1 > 0, \quad \text{and} \quad 2(I_1 - 3)\hat{\psi}_{11} + \hat{\psi}_1 > 0 \tag{B.33}$$

can be used to show that ellipticity holds for 2-D plain strain. Given that ellipticity holds for isotropy, i.e. $\mathcal{F}(\hat{\psi}_1, \hat{\psi}_{11}) > 0$, and by assuming that I_1 and I_4 are *uncoupled*, they further showed that the fiber reinforcement is elliptic if $\mathcal{H}(\hat{\psi}_4, \hat{\psi}_{44}) > 0$. Again, through manipulation of $\mathcal{H}$, it became evident that the relations

$$\hat{\psi}_4 \geq 0, \quad \text{and} \quad \hat{\psi}_4 + 2I_4\hat{\psi}_{44} \geq 0 \tag{B.34}$$

are sufficient conditions to show ellipticity of the fiber reinforcement. It remains to investigate if a similar relation can be found when $\hat{\psi}_{14} \neq 0$, i.e. a *coupled* function (in terms of I_1 and I_4) is used. The relation

$$\mathcal{G}(\hat{\psi}_{14}) = 4\hat{\psi}_{14}(\lambda_1^2 - \lambda_2^2) n_1 n_2 (n_1 a_1 + n_2 a_2)(n_2 a_1 - n_1 a_2) \geq 0 \tag{B.35}$$

must then be fulfilled for all allowable combinations of **n** and **a**, where the components of **n** must obey $n_1^2 + n_2^2 = 1$ (**n** is a unit vector). We can relate the deformed fiber direction vector **a** to an angle α by $a_1 = \lambda_1 \cos\alpha$ and $a_2 = \lambda_2 \sin\alpha$ and I_4 may now be written as $I_4 = a_1^2 + a_2^2$. Similarly, the components of the surface vector **n** are related to an angle β (representing the 2D direction) through components $n_1 = \cos\beta$ and $n_2 = \sin\beta$. From the incompressibility condition, $\lambda_1\lambda_2 = 1$, the deformations are related by λ if $\lambda_1 = \lambda$ and $\lambda_2 = 1/\lambda$. Simple calculations using two sets of values for α, β and λ show that (B.35) is not easily fulfilled. For example, defining $\overline{\mathcal{G}} := \mathcal{G}(\hat{\psi}_{14})/\hat{\psi}_{14}$ for a shorter notation, with $\alpha = 45^\circ$ and $\beta = 40^\circ$ we have

$$\overline{\mathcal{G}} < 0 \quad \text{if} \quad \lambda = 1.09 \quad (I_4 > 1), \tag{B.36}$$

$$\overline{\mathcal{G}} > 0 \quad \text{if} \quad \lambda = 1.10 \quad (I_4 > 1), \tag{B.37}$$

while for $\alpha = 125^\circ$ and $\beta = 130^\circ$ we have

$$\overline{\mathcal{G}} < 0 \quad \text{if} \quad \lambda = 1.09 \quad (I_4 < 1), \tag{B.38}$$

$$\overline{\mathcal{G}} > 0 \quad \text{if} \quad \lambda = 1.10 \quad (I_4 < 1). \tag{B.39}$$

A coupled strain-energy function has to meet the requirement that $\mathcal{G}(\hat{\psi}_{14}) \geq 0$ for all deformation modes while the sign of $\overline{\mathcal{G}}$ varies, independent of whether $I_4 > 1$ or $I_4 < 1$, i.e. $\hat{\psi}_{14}$ has to change sign (seemingly) arbitrarily, and independent of the stretch in the fiber direction. Considering the difficulty in constructing such a strain-energy function, it is likely impossible in most (if not all) *coupled* models to guarantee ellipticity either for tension or compression in 2-D plain strain. For example, defining $\hat{\Psi}(I_1, I_4) := (6.6)_1$, the combined second derivative is

$$\hat{\psi}_{14} = k_1\kappa(1-3\kappa)\exp[k_2(I_4^* - 1)^2][1 + 2k_2(I_4^* - 1)^2], \tag{B.40}$$

which is ≥ 0 for all deformation modes, thus showing that (B.35) can not be fulfilled.

REFERENCES

[1] Rayner M, Allender S, Scarborough P, Group BHFHPR. Cardiovascular disease in europe. *Eur. J. Cardiovasc. Prev. Rehabil.* 2009; **16 Suppl 2**:S43–S47.

[2] Roger VL, Go AS, Lloyd-Jones DM, Benjamin EJ, Berry JD, Borden WB, Bravata DM, Dai S, Ford ES, Fox CS, *et al.*. Executive summary: heart disease and stroke statistics–2012 update: a report from the american heart association. *Circulation* 2012; **125**:188–197.

[3] Yang ZJ, Liu J, Ge J, Chen L, Zhao Z, Yang WY, and Metabolic Disorders Study Group CND. Prevalence of cardiovascular disease risk factor in the Chinese population: the 2007-2008 China national diabetes and metabolic disorders study. *Eur. Heart. J.* 2012; **33**:213–220.

[4] NASA. "How much does it cost to launch a space shuttle?". `http://www.nasa.gov/centers/kennedy/about/information/shuttle_faq.html\#10` April 2012.

[5] Kassab GS. Y.C. "Bert" Fung: the father of modern biomechanics. *Mech. Chem. Biosyst.* 2004; **1**:5–22.

[6] Holzapfel GA. *Nonlinear Solid Mechanics. A Continuum Approach for Engineering*. John Wiley & Sons: Chichester, 2000.

[7] Zienkiewicz OC, Taylor RL. *The Finite Element Method. Solid Mechanics*, vol. 2. 5th edn., Butterworth Heinemann: Oxford, 2000.

[8] *FEAP – A Finite Element Analysis Program, Version 8.2 User Manual*. University of California at Berkeley, Berkeley, California, 2008.

[9] van Gijn J, Rinkel GJ. Subarachnoid haemorrhage: diagnosis, causes and management. *Brain* 2001; **124**:249–278.

[10] Juvela S, Porras M, Poussa K. Natural history of unruptured intracranial aneurysms: probability and risk factors for aneurysm rupture. *J. Neurosurg.* 2000; **93**:379–387.

[11] Austin G, Fisher S, Dickson D, Anderson D, Richardson S. The significance of the extracellular matrix in intracranial aneurysms. *Ann. Clin. Lab. Sci.* 1993; **23**:97–105.

[12] Holzapfel GA, Gasser TC, Ogden RW. A new constitutive framework for arterial wall mechanics and a comparative study of material models. *J. Elasticity* 2000; **61**:1–48.

[13] Holzapfel GA, Sommer G, Gasser CT, Regitnig P. Determination of the layer-specific mechanical properties of human coronary arteries with non-atherosclerotic intimal thickening, and related constitutive modelling. *Am. J. Physiol. Heart Circ. Physiol.* 2005; **289**:H2048–2058.

[14] Holzapfel GA, Sommer G, Auer M, Regitnig P, Ogden RW. Layer-specific 3D residual deformations of human aortas with non-atherosclerotic intimal thickening. *Ann. Biomed. Eng.* 2007; **35**:530–545.

[15] Liu SQ, Fung YC. Change of residual strains in arteries due to hypertrophy caused by aortic constriction. *Circ. Res.* 1989; **65**:1340–1349.

[16] Humphrey JD, Rajagopal KR. A constrained mixture model for growth and remodeling of soft tissues. *Math. Model. Meth. Appl. Sci.* 2002; **12**:407–430.

[17] Baek S, Rajagopal KR, Humphrey JD. A theoretical model of enlarging intracranial fusiform aneurysms. *J. Biomech. Eng.* 2006; **128**:142–149.

[18] Driessen NJB, Wilson W, Bouten CVC, Baaijens FPT. A computational model for collagen fibre remodelling in the arterial wall. *J. Theor. Biol.* 2004; **226**:53–64.

[19] Watton PN, Hill NA, Heil M. A mathematical model for the growth of the abdominal aortic aneurysm. *Biomech. Model. Mechanobiol.* 2004; **3**:98–113.

[20] Kroon M, Holzapfel GA. A model for saccular cerebral aneurysm growth by collagen fibre remodelling. *J. Theor. Biol.* 2007; **247**:775–787.

[21] Harvey PA, Leinwand LA. The cell biology of disease: cellular mechanisms of cardiomyopathy. *J. Cell. Biol.* 2011; **194**:355–365.

[22] Streeter, Jr DD, Spotnitz HM, Patel DP, Ross, Jr J, Sonnenblick EH. Fibre orientation in the canine left ventricle during diastole and systole. *Circ. Res.* 1969; **24**:339–347.

[23] Usyk TP, Mazhari R, McCulloch AD. Effect of laminar orthotropic myofiber architecture on regional stress and strain in the canine left ventricle. *J. Elasticity* 2000; **61**:143–164.

[24] Rohmer D, Sitek A, Gullberg GT. Reconstruction and visualization of fiber and laminar structure in the normal human heart from ex vivo diffusion tensor magnetic resonance imaging (DTMRI) data. *Investigative Radiology* 2007; **42**:777–789.

[25] Sands GB, Gerneke DA, Hooks DA, Green CR, Smaill BH, LeGrice IJ. Automated imaging of extended tissue volumes using confocal microscopy. *Microsc. Res. Tech.* 2005; **67**:227–239.

[26] Hort W. Untersuchungen über die Muskelfaserdehnung und das Gefüge des Myokards in der rechten Herzkammerwand des Meerschweinchens. *Virchows Arch.* 1957; **329**:694–731.

[27] Young AA, Legrice IJ, Young MA, Smaill BH. Extended confocal microscopy of myocardial laminae and collagen network. *J Microsc.* 1998; **192**:139–150.

[28] LeGrice IJ, Smaill BH, Chai LZ, Edgar SG, Gavin JB, Hunter PJ. Laminar structure of the heart: Ventricular myocyte arrangement and connective tissue architecture in the dog. *Am. J. Physiol. Heart Circ. Physiol.* 1995; **269**:H571–H582.

[29] Karlon WJ, Covell JW, McCulloch AD, Hunter JJ, Omens JH. Automated measurement of myofiber disarray in transgenic mice with ventricular expression of ras. *Anat. Rec.* 1998; **252**:612–625.

[30] Karlon WJ, McCulloch AD, Covell JW, Hunter JJ, Omens JH. Regional dysfunction correlates with myofiber disarray in transgenic mice with ventricular expression of ras. *Am. J. Physiol. Heart Circ. Physiol.* 2000; **278**:H898–906.

[31] Usyk TP, Omens JH, McCulloch AD. Regional septal dysfunction in a three-dimensional computational model of focal myofiber disarray. *Am. J. Physiol. Heart Circ. Physiol.* 2001; **281**:H506–H514.

[32] Zimmerman SD, Karlon WJ, Holmes JW, Omens JH, Covell JW. Structural and mechanical factors influencing infarct scar collagen organization. *Am. J. Physiol. Heart Circ. Physiol.* 2000; **278**:H194–H200.

[33] Whittaker P, Boughner DR, Kloner RA. Analysis of healing after myocardial infarction using polarized light microscopy. *Am. J. Pathol.* 1989; **134**:879–893.

[34] Strijkers GJ, Bouts A, Blankesteijn WM, Peeters THJM, Vilanova A, van Prooijen MC, Sanders HMHF, Heijman E, Nicolay K. Diffusion tensor imaging of left ventricular remodeling in response to myocardial infarction in the mouse. *NMR Biomed.* 2009; **22**:182–190.

[35] Covell JW. Tissue structure and ventricular wall mechanics. *Circulation* 2008; **118**:699–701.

[36] Hooks DA, Trew ML, Caldwell BJ, Sands GB, LeGrice IJ, Smaill BH. Laminar arrangement of ventricular myocytes influences electrical behavior of the heart. *Circ. Res.* 2007; **101**:e103–e112.

[37] Sands GB, Smaill BH, LeGrice IJ. Virtual sectioning of cardiac tissue relative to fiber orientation. *Proc. 30th Annual Int. Conf. of the IEEE Engineering in Medicine and Biology Society EMBS 2008*, 2008; 226–229.

[38] Coppola BA, Omens JH. Role of tissue structure on ventricular wall mechanics. *Mech. Chem. Biosyst.* 2008; **5**:183–196.

[39] Woods RH. A few applications of a physical theorem to membranes in the human body in a state of tension. *J. Anat. Physiol.* 1892; **26**:362–370.

[40] Wong AY, Rautaharju PM. Stress distribution within the left ventricular wall approximated as a thick ellipsoidal shell. *Am. Heart J.* 1968; **75**:649–662.

[41] Mirsky I. Ventricular and arterial wall stresses based on large deformation analyses. *Biophys. J.* 1973; **13**:1141–1159.

[42] Holzapfel GA, Ogden RW. Constitutive modelling of passive myocardium: a structurally based framework for material characterization. *Philos. T. Roy. Soc. A* 2009; **367**:3445–3475.

[43] Niederer SA, Plank G, Chinchapatnam P, Ginks M, Lamata P, Rhode KS, Rinaldi CA, Razavi R, Smith NP. Length-dependent tension in the failing heart and the efficacy of cardiac resynchronization therapy. *Cardiovasc. Res.* 2011; **89**:336–343.

[44] Fung YC. Mathematical representation of the mechanical properties of the heart muscle. *J. Biomech.* 1970; **269**:441–515.

[45] Omens JH, MacKenna DA, McCulloch AD. Measurement of strain and analysis of stress in resting rat left ventricular myocardium. *J. Biomech.* 1993; **26**:665–676.

[46] Costa KD, Hunter PJ, Wayne JS, Waldman LK, Guccione JM, McCulloch AD. A three-dimensional finite element method for large elastic deformations of ventricular mycardium: II–Prolate spheroidal coordinates. *J. Biomech. Eng.* 1996; **118**:464–472.

[47] Costa KD, Holmes JW, McCulloch AD. Modeling cardiac mechanical properties in three dimensions. *Philos. T. Roy. Soc. A* 2001; **359**:1233–1250.

[48] Hunter PJ, Smaill BH, Nielsen PMF, LeGrice IJ. A mathematical model of cardiac anatomy. *Computational Biology of the Heart*, Panfilov AV, Holden AV (eds.), John Wiley & Sons: Chichester, 1997; 171–215.

[49] Schmid H, Nash MP, Young AA, Hunter PJ. Myocardial material parameter estimation-a comparative study for simple shear. *J. Biomech. Eng.* 2006; **128**:742–750.

[50] Schmid H, O'Callaghan P, Nash MP, Lin W, LeGrice IJ, Smaill BH, Young AA, Hunter PJ. Myocardial material parameter estimation: a non-homogeneous finite element study from simple shear tests. *Biomech. Model. Mechanobiol.* 2008; **7**:161–173.

[51] Dokos S, Smaill BH, Young AA, LeGrice IJ. Shear properties of passive ventricular myocardium. *Am. J. Physiol.* 2002; **283**:H2650–H2659.

[52] Ambrosi D, Pezzuto S. Active stress vs. active strain in mechanobiology: constitutive issues. *J. Elasticity* 2012; **107**:199–212.

[53] Rossi S, Ruiz-Baier R, Pavarino LF, Quarteroni A. Orthotropic active strain models for the numerical simulation of cardiac biomechanics 2012; Doi: 10.1002/cnm.2473.

[54] Taber LA, Perucchio R. Modeling heart development. *J. Elasticity* 2000; **61**:165–197.

[55] Nardinocchi P, Teresi L. On the active response of soft living tissues. *J. Elasticity.* 2007; **88**:27–39.

[56] Smith RL, Carter DR, Schurman DJ. Pressure and shear differentially alter human articular chondrocyte metabolism: a review. *Clin. Orthop. Relat. Res.* 2004; **(427 Suppl)**:S89–95.

[57] Pathmanathan P, Chapman SJ, Gavaghan DJ, Whiteley JP. Cardiac electromechanics: The effect of contraction model on the mathematical problem and accuracy of the numerical scheme. *Quart. J. Mech. Appl. Math.* 2010; **63**:375–399.

[58] Niederer SA, Smith NP. An improved numerical method for strong coupling of excitation and contraction models in the heart. *Prog. Biophys. Mol. Biol.* 2008; **96**:90–111.

[59] Nash MP, Hunter PJ. Computational mechanics of the heart. *J. Elasticity* 2000; **61**:113–141.

[60] Nash MP, Panfilov AV. Electromechanical model of excitable tissue to study reentrant cardiac arrhythmias. *Prog. Biophys. Mol. Biol.* 2004; **85**:501–522.

[61] Watanabe H, Sugiura S, Kafuku H, Hisada T. Multiphysics simulation of left ventricular filling dynamics using fluid-structure interaction finite element method. *Biophys. J.* 2004; **87**:2074 – 2085.

[62] Skallerud B, Prot V, Nordrum IS. Modeling active muscle contraction in mitral valve leaflets during systole: a first approach. *Biomech. Model. Mechanobiol.* 2011; **10**:11–26.

[63] Trayanova NA, Rice JJ. Cardiac electromechanical models: from cell to organ. *Front. Physiol.* 2011; **2**:43.

[64] Sundnes J, Nielsen BF, Mardal KA, Cai X, Lines GT, Tveito A. On the computational complexity of the bidomain and the monodomain models of electrophysiology. *Ann. Biomed. Eng.* 2006; **34**:1088–1097.

[65] Sano T, Takayama N, Shimamoto T. Directional difference of conduction velocity in the cardiac ventricular syncytium studied by microelectrodes. *Circ. Res.* 1959; **7**:262–267.

[66] Caldwell BJ, Trew ML, Sands GB, Hooks DA, LeGrice IJ, Smaill BH. Three distinct directions of intramural activation reveal nonuniform side-to-side electrical coupling of ventricular myocytes. *Circ. Arrhythm. Electrophysiol.* 2009; **2**:433–440.

[67] Bishop MJ, Plank G. Representing cardiac bidomain bath-loading effects by an augmented monodomain approach: application to complex ventricular models. *IEEE T. Biomed. Eng.* 2011; **58**:1066–1075.

[68] Hodgkin AL, Huxley AF. A quantitative description of membrane current and its application to conduction and excitation in nerve. *J. Physiol.* 1952; **117**:500–544.

[69] Fitzhugh R. Impulses and physiological states in theoretical models of nerve membrane. *Biophys. J.* 1961; **1**:445–466.

[70] Fenton F, Karma A. Vortex dynamics in three-dimensional continuous myocardium with fiber rotation: Filament instability and fibrillation. *Chaos* 1998; **8**:20–47.

[71] Mahajan A, Shiferaw Y, Sato D, Baher A, Olcese R, Xie LH, Yang MJ, Chen PS, Restrepo JG, Karma A, *et al.*. A rabbit ventricular action potential model replicating cardiac dynamics at rapid heart rates. *Biophys. J.* 2008; **94**:392–410.

[72] Clayton RH, Bernus O, Cherry EM, Dierckx H, Fenton FH, Mirabella L, Panfilov AV, Sachse FB, Seemann G, Zhang H. Models of cardiac tissue electrophysiology: progress, challenges and open questions. *Prog. Biophys. Mol. Biol.* 2011; **104**:22–48.

[73] Kerckhoffs RCP, Bovendeerd PHM, Kotte JCS, Prinzen FW, Smits K, Arts T. Homogeneity of cardiac contraction despite physiological asynchrony of depolarization: A model study. *Ann. Biomed. Eng.* 2003; **31**:536–547.

[74] Provost J, Gurev V, Trayanova N, Konofagou EE. Mapping of cardiac electrical activation with electromechanical wave imaging: An in silico-in vivo reciprocity study. *Heart Rhythm.* 2011; **8**:752–759.

[75] Panfilov AV, Keldermann RH, Nash MP. Drift and breakup of spiral waves in reaction-diffusion-mechanics systems. *Proc. Natl. Acad. Sci. U.S.A.* 2007; **104**:7922–7926.

[76] Pathmanathan P, Whiteley JP. A numerical method for cardiac mechanoelectric simulations. *Ann. Biomed. Eng.* 2009; **437**:860–876.

[77] Nordsletten DA, Niederer SA, Nash MP, Hunter PJ, Smith NP. Coupling multiphysics models to cardiac mechanics. *Prog. Biophys. Mol. Biol.* 2011; **104**:77–88.

[78] Royse CF, Royse AG. The myocardial and vascular effects of bupivacaine, levobupivacaine, and ropivacaine using pressure volume loops. *Anesth. Analg.* 2005; **101**:679–687.

[79] Usyk TP, LeGrice IJ, McCulloch AD. Computational model of three-dimensional cardiac electromechanics. *Comput. Visual. Sci.* 2002; **4**:249–257.

[80] Otto F. Die Grundform des arteriellen Pulses. *Z. Bio.* 1899; **37**:483–586.

[81] Quick CM, Berger DS, Noordergraaf A. Apparent arterial compliance. *Am. J. Physiol.* 1998; **274**:H1393–H1403.

[82] Raamat R, Talts J, Jagomägi K. Application of amplitude-based and slope-based algorithms to determine beat-to-beat finger arterial compliance during handgrip exercise. *Med. Eng. Phys.* 2008; **30**:67–74.

[83] Kerckhoffs R, Neal M, Gu Q, Bassingthwaighte J, Omens J, McCulloch A. Coupling of a 3d finite element model of cardiac ventricular mechanics to lumped systems models of the systemic and pulmonic circulation. *Ann. Biomed. Eng.* 2007; **35**:1–18.

[84] Kim C, Cervos-Navarro J. Spontaneous saccular cerebral aneurysm in a rat. *Acta Neurochir.* 1991; **109**:63–65.

[85] Schievink WI. Intracranial aneurysms. *N. Engl. J. Med.* 1997; **336**:28–40.

[86] Steiger HJ. Pathophysiology of development and rupture of cerebral aneurysms. *Acta Neurochir. Suppl. (Wien)* 1990; **48**:1–57.

[87] Kroon M, Holzapfel GA. Modeling of saccular aneurysm growth in a human middle cerebral artery. *J. Biomech. Eng.* 2008; **130**:051 012.

[88] Whittaker P, Schwab ME, Canham PB. The molecular organization of collagen in saccular aneurysms assessed by polarized light microscopy. *Connect. Tissue Res.* 1988; **17**:43–54.

[89] Canham PB, Talman EA, Finlay HM, Dixon JG. Medial collagen organization in human arteries of the heart and brain by polarized light microscopy. *Connect. Tissue Res.* 1991; **26**:121–134.

[90] Rowe AJ, Finlay HM, Canham PB. Collagen biomechanics in cerebral arteries and bifurcations assessed by polarizing microscopy. *J. Vasc. Res.* 2003; **40**:406–415.

[91] Canham PB, Korol RM, Finlay HM, Hammond RR, Holdsworth DW, Ferguson GG, Lucas AR. Collagen organization and biomechanics of the arteries and aneurysms of the human brain. *Mechanics of Biological Tissue*, Holzapfel GA, Ogden RW (eds.), Springer-Verlag: Heidelberg, 2006; 307–322.

[92] Coulson RJ, Cipolla MJ, Vitullo L, Chesler NC. Mechanical properties of rat middle cerebral arteries with and without myogenic tone. *J. Biomech. Eng.* 2004; **126**:76–81.

[93] Finlay HM, McCullough L, Canham PB. Three-dimensional collagen organization of human brain arteries at different transmural pressures. *J. Vasc. Res.* 1995; **32**:301–312.

[94] Holzapfel GA, Gasser TC, Stadler M. A structural model for the viscoelastic behavior of arterial walls: Continuum formulation and finite element analysis. *Eur. J. Mech. A/Solids* 2002; **21**:441–463.

[95] Holzapfel GA, Sommer G, Regitnig P. Anisotropic mechanical properties of tissue components in human atherosclerotic plaques. *J. Biomech. Eng.* 2004; **126**:657–665.

[96] Monson KL, Goldsmith W, Barbaro NM, Manley GT. Significance of source and size in the mechanical response of human cerebral blood vessels. *J. Biomech.* 2005; **38**:737–744.

[97] Smith JFH, Canham PB, Starkey J. Orientation of collagen in the tunica adventitia of the human cerebral artery measured with polarized light and the universal stage. *J. Ultrastruct. Res.* 1981; **77**:133–145.

[98] Chuong CJ, Fung YC. Three-dimensional stress distribution in arteries. *J. Biomech. Eng.* 1983; **105**:268–274.

[99] Chatziprodromou I, Tricoli A, Poulikakos D, Ventikos Y. Haemodynamics and wall remodelling of a growing cerebral aneurysm: a computational model. *J. Biomech.* 2007; **40**:412–426.

[100] Schulze-Bauer CAJ, Regitnig P, Holzapfel GA. Mechanics of the human femoral adventitia including high-pressure response. *Am. J. Physiol. Heart Circ. Physiol.* 2002; **282**:H2427–H2440.

[101] Schulze-Bauer CAJ, Mörth C, Holzapfel GA. Passive biaxial mechanical response of aged human iliac arteries. *J. Biomech. Eng.* 2003; **125**:395–406.

[102] Monson KL, Goldsmith W, Barbaro NM, Manley GT. Axial mechanical properties of fresh human cerebral blood vessels. *J. Biomech. Eng.* 2003; **125**:288–294.

[103] Humphrey JD. *Cardiovascular Solid Mechanics. Cells, Tissues, and Organs*. Springer-Verlag: New York, 2002.

[104] MacDonald DJ, Finlay HM, Canham PB. Directional wall strength in saccular brain aneurysms from polarized light microscopy. *Ann. Biomed. Eng.* 2000; **28**:533–542.

[105] Hunter PJ. Proceedings: Development of a mathematical model of the left ventricle. *J. Physiol.* 1974; **241**:87P–88P.

[106] Ashihara T, Constantino J, Trayanova NA. Tunnel propagation of postshock activations as a hypothesis for fibrillation induction and isoelectric window. *Circ. Res.* 2008; **102**:737–745.

[107] Ten Tusscher KHWJ, Hren R, Panfilov AV. Organization of ventricular fibrillation in the human heart. *Circ. Res.* 2007; **100**:e87–101.

[108] Deo M, Boyle P, Plank G, Vigmond E. Arrhythmogenic mechanisms of the purkinje system during electric shocks: a modeling study. *Heart Rhythm.* 2009; **6**:1782–1789.

[109] Plank G, Burton RA, Hales P, Bishop M, Mansoori T, Bernabeu MO, Garny A, Prassl AJ, Bollensdorff C, Mason F, *et al.*. Generation of histo-anatomically representative models of the individual heart: tools and application. *Philos. Transact. A Math. Phys. Eng. Sci.* 2009; **367**:2257–2292.

[110] Bishop MJ, Plank G, Burton RA, Schneider JE, Gavaghan DJ, Grau V, Kohl P. Development of an anatomically detailed MRI-derived rabbit ventricular model and assessment of its impact on simulations of electrophysiological function. *Am. J. Physiol. Heart Circ. Physiol.* 2010; **298**:H699–H718.

[111] Plank G, Zhou L, Greenstein JL, Cortassa S, Winslow RL, O'Rourke B, Trayanova NA. From mitochondrial ion channels to arrhythmias in the heart: computational techniques to bridge the spatio-temporal scales. *Philos. Transact. A Math. Phys. Eng. Sci.* 2008; **366**:3381–3409.

[112] Romero D, Sebastian R, Bijnens BH, Zimmerman V, Boyle PM, Vigmond EJ, Frangi AF. Effects of the Purkinje system and cardiac geometry on biventricular pacing: a model study. *Ann. Biomed. Eng.* 2010; **38**:1388–1398.

[113] Nickerson D, Smith N, Hunter P. New development in a strongly coupled cardiac electromechanical model. *Eurospace* 2005; **7**:S118–S127.

[114] Kerckhoffs RCP, Faris OP, Bovendeerd PHM, Prinzen FW, Smits K, McVeigh ER, Arts T. Electromechanics of paced left ventricle simulated by straightforward mathematical model: comparison with experiments. *Am. J. Physiol-Heart. C.* 2005; **289**:H1889–H1897.

[115] Kerckhoffs RCP, Faris OP, Bovendeerd PHM, Prinzen FW, Smits K, McVeigh ER, Arts T. Timing of depolarization and contraction in the paced canine left ventricle: model and experiment. *J. Cardiovasc. Electrophysiol.* 2003; **14**:S188–S195.

[116] Usyk TP, McCulloch AD. Electromechanical model of cardiac resynchronization in the dilated failing heart with left bundle branch block. *J. Electrocardiol.* 2003; **36**:57–61.

[117] Van Der Toorn A, Barenbrug P, Snoep G, Van Der Veen FH, Delhaas T, Prinzen FW, Maessen J, Arts T. Transmural gradients of cardiac myofiber shortening in aortic valve stenosis patients using MRI tagging. *Am. J. Physiol-Heart. C.* 2002; **283**:H1609–H1615.

[118] Dang ABC, Guccione JM, Zhang P, Wallace AW, Gorman RC, Gorman JH 3rd, Ratcliffe MB. Effect of ventricular size and patch stiffness in surgical anterior ventricular restoration: a finite element model study. *Ann. Thorac. Surg.* 2005; **79**:185–193.

[119] Niederer SA, Smith NP. The role of the Frank-Starling law in the transduction of cellular work to whole organ pump function: a computational modeling analysis. *PLoS Comput. Biol.* 2009; **5**:e1000 371.

[120] LeGrice IJ, Takayama Y, Covell JW. Transverse shear along myocardial cleavage planes provides a mechanism for normal systolic wall thickening. *Circ. Res.* 1995; **77**:182–193.

[121] Cheng A, Nguyen TC, Malinowski M, Daughters GT, Miller DC, Ingels Jr NB. Heterogeneity of left ventricular wall thickening mechanisms. *Circulation* 2008; **118**:713–721.

[122] Spotnitz HM, Spotnitz WD, Cottrell TS, Spiro D, Sonnenblick EH. Cellular basis for volume related wall thickness changes in the rat left ventricle. *J. Mol. Cell. Cardiol.* 1974; **6**:317–331.

[123] Costa KD, Takayama Y, McCulloch AD, Covell JW. Laminar fiber architecture and three-dimensional systolic mechanics in canine ventricular myocardium. *Am. J. Physiol.* 1999; **276**:H595–H607.

[124] Wu Y, Bell SP, Trombitas K, Witt CC, Labeit S, LeWinter MM, Granzier H. Changes in titin isoform expression in pacing-induced cardiac failure give rise to increased passive muscle stiffness. *Circulation* 2002; **106**:1384–1389.

[125] Omens JH, Usyk TP, Li Z, McCulloch AD. Muscle LIM protein deficiency leads to alterations in passive ventricular mechanics. *Am. J. Physiol-Heart. C.* 2002; **282**:H680–H687.

[126] Demer LL, Yin FCP. Passive biaxial mechanical properties of isolated canine myocardium. *J. Physiol. London* 1983; **339**:615–630.

[127] Taber LA, Yang M, Podszus WW. Mechanics of ventricular torsion. *J. Biomech.* 1996; **29**:745–752.

[128] Hunter PJ, Nash MP, Sands GB. Computational electromechanics of the heart. *Computational Biology of the Heart*, Panfilov AV, Holden AV (eds.), John Wiley & Sons: Chichester, 1997; 345–407.

[129] Yin FCP, Strumpf RK, Chew PH, Zeger SL. Quantification of the mechanical properties of noncontracting canine myocardium under simultaneous biaxial loading. *J. Biomech.* 1987; **20**:577–589.

[130] Schmid H, Wang YK, Ashton J, Ehret AE, Krittian SBS, Nash MP, Hunter PJ. Myocardial material parameter estimation: a comparison of invariant based orthotropic constitutive equations. *Comput. Methods Biomech. Biomed. Engin.* 2009; **12**:283–295.

[131] Lin DH, Yin FC. A multiaxial constitutive law for mammalian left ventricular myocardium in steady-state barium contracture or tetanus. *J. Biomech. Eng.* 1998; **120**:504–517.

[132] Vetter FJ, McCulloch AD. Three-dimensional analysis of regional cardiac function: A model of the rabbit ventricular anatomy. *Prog. Biophys. Mol. Biol.* 1998; **69**:157–183.

[133] Ghaemi H, Behdinan K, Spence AD. In vitro technique in estimation of passive mechanical properties of bovine heart part I. Experimental techniques and data. *Med. Eng. Phys.* 2009; **31**:76–82.

[134] Costa KD, Hunter PJ, Rogers JM, Guccione JM, Waldman LK, McCulloch AD. A three-dimensional finite element method for large elastic deformations of ventricular myocardium: I–Cylindrical and spherical polar coordinates. *J. Biomech. Eng.* 1996; **118**:542–463.

[135] Nielsen PMF, LeGrice IJ, Smaill BH, Hunter PJ. Mathematical model of geometry and fibrous structure of the heart. *Am. J. Physiol. Cell Physiol.* 1991; **260**:H1365–H1378.

[136] McCulloch AD. Cardiac biomechanics. *Biomechanics: Principles and Applications*, Peterson DR, Bronzino JD (eds.). 2nd edn., CRC Press: Boca Raton, Florida, 2007; 1–20. Chapter 8.

[137] Waldman LK, Covell JW. Effects of ventricular pacing on finite deformation in canine left ventricles. *Am. J. Physiol. Heart Circ. Physiol.* 1987; **252**:H1023–H1030.

[138] Wilson JR, Douglas P, Hickey WF, Lanoce V, Ferraro N, Muhammad A, Reichek N. Experimental congestive heart failure produced by rapid ventricular pacing in the dog: cardiac effects. *Circulation* 1987; **75**:857–867.

[139] Gaasch WH, Zile MR, Hoshino PK, Apstein CS, Blaustein AS. Stress–shortening relations and myocardial blood flow in compensated and failing canine hearts with pressure–overload hypertrophy. *Circulation* 1989; **79**:872–883.

[140] Ashikaga H, Omens JH, Ingels NB, Covell JW. Transmural mechanics at left ventricular epicardial pacing site. *Am. J. Physiol. Heart Circ. Physiol.* 2004; **286**:H2401–H2407.

[141] Costa KD, May-Newman K, Farr D, O'Dell WG, McCulloch AD, Omens JH. Three-dimensional residual strain in midanterior canine left ventricle. *Am. J. Physiol.* 1997; **273**:H1968–H1976.

[142] LeGrice IJ, Hunter PJ, Young A, Smaill BH. The architecture of the heart: A data-based model. *Philos. T. Roy. Soc. A* 2001; **359**:1217–1232.

[143] Remme EW, Hunter PJ, Smiseth O, Stevens C, Rabben SI, Skulstad H, Angelsen BB. Development of an in vivo method for determining material properties of passive myocardium. *J. Biomech.* 2004; **37**:669–678.

[144] Göktepe S, Kuhl E. Electromechanics of the heart: a unified approach to the strongly coupled excitation-contraction problem. *Comput. Mech.* 2010; **45**:227–243.

[145] Göktepe S, Abilez OJ, Kuhl E. A generic approach towards finite growth with examples of athlete's heart, cardiac dilation, and cardiac wall thickening. *J. Mech. Phys. Solids* 2010; **58**:1661–1680.

[146] Bovendeerd PHM, Arts T, Huyghe JM, van Campen DH, Reneman RS. Dependence of local left ventricular wall mechanics on myocardial fiber orientation: A model study. *J. Biomech.* 1992; **25**:1129–1140.

[147] Takeuchi M, Nakai H, Kokumai M, Nishikage T, Otani S, Lang RM. Age-related changes in left ventricular twist assessed by two-dimensional speckle-tracking imaging. *J. Am. Soc. Echocardiogr.* 2006; **19**:1077–1084.

[148] Carreras F, Garcia-Barnes J, Gil D, Pujadas S, Li CH, Suarez-Arias R, Leta R, Alomar X, Ballester M, Pons-Llado G. Left ventricular torsion and longitudinal shortening: two fundamental components of myocardial mechanics assessed by tagged cine-MRI in normal subjects. *Int. J. Cardiovasc. Imaging* 2011; **16**:1–12.

[149] Monasky MM, Varian KD, Davis JP, Janssen PM. Dissociation of force decline from calcium decline by preload in isolated rabbit myocardium. *Pflügers Arch. – Eur. J. Physiol.* 2008; **456**:267–276.

[150] Prassl AJ, Kickinger F, Ahammer H, Grau V, Schneider JE, Hofer E, Vigmond EJ, Trayanova NA, Plank G. Automatically generated, anatomically accurate meshes for cardiac electrophysiology problems. *IEEE T. Biomed. Eng.* 2009; **56**:1318–1330.

[151] Holzapfel GA. Structural and numerical models for the (visco)elastic response of arterial walls with residual stresses. *Biomechanics of Soft Tissue in Cardiovascular Systems*, Holzapfel GA, Ogden RW (eds.), Springer-Verlag: Wien, New York, 2003; 109–184. CISM Courses and Lectures no. 441.

[152] Rocha BM, Kickinger F, Prassl AJ, Haase G, Vigmond EJ, Weber dos Santos R, Plank SZG. A macro finite-element formulation for cardiac electrophysiology simulations using hybrid unstructured grids. *IEEE T. Biomed. Eng.* 2011; **58**:1055–1065.

[153] Balay S, Brown J, Buschelman K, Eijkhout V, Gropp WD, Kaushik D, Knepley MG, Curfman McInnes L, Smith BF, Zhang H. PETSc users manual. *Technical Report*, Argonne National Laboratory 2010.

[154] Rush S, Larsen H. A practical algorithm for solving dynamic membrane equations. *IEEE T. Biomed. Eng.* 1978; **25**:389–392.

[155] Vigmond EJ, Hughes M, Plank G, Leon LJ. Computational tools for modeling electrical activity in cardiac tissue. *J. Electrocardiol.* 2003; **36 Suppl**:69–74.

[156] Vigmond EJ, Weber dos Santos R, Prassl AJ, Deo M, Plank G. Solvers for the cardiac bidomain equations. *Prog. Biophys. Mol. Biol.* 2008; **96**:3–18.

[157] Karypis G, Schloegel K, Kumar V. *ParMETIS: Parallel Graph Partitioning and Sparse Matrix Ordering Library*. University of Minnesota, Minneapolis, MN, Version 3.1 2003. URL `http://glaros.dtc.umn.edu/gkhome/metis/parmetis/overview`.

[158] Shinmura K, Tang XL, Wang Y, Xuan YT, Liu SQ, Takano H, Bhatnagar A, Bolli R. Cyclooxygenase-2 mediates the cardioprotective effects of the late phase of ischemic preconditioning in conscious rabbits. *PNAS* 2000; **97**:10 197–10 202.

[159] Ashikaga H, Coppola BA, Yamazaki KG, Villarreal FJ, Omens JH, Covell JW. Changes in regional myocardial volume during the cardiac cycle: implications for transmural blood flow and cardiac structure. *Am. J. Physiol. Heart Circ. Physiol.* 2008; **295**:H610–H618.

[160] Stypmann J, Engelen MA, Breithardt AK, Milberg P, Rothenburger M, Breithardt OA, Breithardt G, Eckardt L, Cordula PN. Doppler echocardiography and tissue Doppler imaging in the healthy rabbit: differences of cardiac function during awake and anaesthetised examination. *Int. J. Cardiol.* 2007; **115**:164–170.

[161] Parkinson J, Brass A, Canova G, Brechet Y. The mechanical properties of simulated collagen fibrils. *J. Biomech.* 1997; **30**:549–554.

[162] Helm PA, Tseng HJ, Younes L, McVeigh ER, Winslow RL. Ex vivo 3d diffusion tensor imaging and quantification of cardiac laminar structure. *Magn. Reson. Med.* 2005; **54**:850–859.

[163] Sun JP, Stewart WJ, Yang XS, Donnell RO, Leon AR, Felner JM, Thomas JD, Merlino JD. Differentiation of hypertrophic cardiomyopathy and cardiac amyloidosis from other causes of ventricular wall thickening by two-dimensional strain imaging echocardiography. *Am. J. Cardiol.* 2009; **103**:411–415.

[164] Niederer S, Mitchell L, Smith N, Plank G. Simulating a human heart beat with near-real time performance. *Front. Physio.* 2011; **2**:1–7.

[165] Tseng WYI, Dou J, Reese TG, Wedeen VJ. Imaging myocardial fiber disarray and intramural strain hypokinesis in hypertrophic cardiomyopathy with MRI. *J. Musculoskel. Neuron. Interact.* 2006; **23**:1–8.

[166] Gasser TC, Ogden RW, Holzapfel GA. Hyperelastic modelling of arterial layers with distributed collagen fibre orientations. *J. R. Soc. Interface* 2006; **3**:15–35.

[167] Holzapfel GA, Ogden RW. Constitutive modelling of arteries. *Proc. R. Soc. Lond. A* 2010; **466**:1551–1597.

[168] Pierce DM, Trobin W, Raya JG, Trattnig S, Bischof H, Glaser C, Holzapfel GA. DT-MRI based computation of collagen fiber deformation in human articular cartilage: a feasibility study. *Ann. Biomed. Eng.* 2010; **38**:2447–2463.

[169] Colli Franzone P, Pavarino LF, Taccardi B. Simulating patterns of excitation, repolarization and action potential duration with cardiac bidomain and monodomain models. *Math. Biosci.* 2005; **197**:35–66.

[170] Nielsen BF, Ruud TS, Lines GT, Tveito A. Optimal monodomain approximations of the bidomain equations. *Appl. Math. Comput.* 2007; **184**:276–290.

[171] Dong SJ, MacGregor JH, Crawley AP, McVeigh E, Belenkie I, Smith ER, Tyberg JV, Beyar R. Left ventricular wall thickness and regional systolic function in patients with hypertrophic cardiomyopathy. A three-dimensional tagged magnetic resonance imaging study. *Circulation* 1994; **90**:1200–1209.

[172] Carasso S, Yang H, Woo A, Vannan MA, Jamorski M, Wigle ED, Rakowski H. Systolic myocardial mechanics in hypertrophic cardiomyopathy: novel concepts and implications for clinical status. *J. Am. Soc. Echocardiogr.* 2008; **21**:675–683.

[173] Roth BJ. Electrical conductivity values used with the bidomain model of cardiac tissue. *IEEE T. Biomed. Eng.* 1997; **44**:326–328.

[174] Lanir Y. Constitutive equations for fibrous connective tissues. *J. Biomech.* 1983; **16**:1–12.

[175] Weiss JA, Maker BN, Govindjee S. Finite element implementation of incompressible, transversely isotropic hyperelasticity. *Comput. Meth. Appl. Mech. Eng.* 1996; **135**:107–128.

[176] Fung YC, Fronek K, Patitucci P. Pseudoelasticity of arteries and the choice of its mathematical expression. *Am. J. Physiol.* 1979; **237**:H620–H631.

[177] Zulliger MA, Fridez P, Hayashi K, Stergiopulos N. A strain energy function for arteries accounting for wall composition and structure. *J. Biomech.* 2004; **37**:989–1000.

[178] Wilson W, van Donkelaar CC, van Rietbergen B, Ito K, Huiskes R. Stresses in the local collagen network of articular cartilage: a poroviscoelastic fibril-reinforced finite element study. *J. Biomech.* 2004; **37**:357–366.

[179] Pierce DM, Trobin W, Trattnig S, Bischof H, Holzapfel GA. A phenomenological approach toward patient-specific computational modeling of articular cartilage including collagen fiber tracking. *J. Biomech. Eng.* 2009; **131**:091 006.

[180] Holzapfel GA, Stadler M, Gasser TC. Changes in the mechanical environment of stenotic arteries during interaction with stents: Computational assessment of parametric stent design. *J. Biomech. Eng.* 2005; **127**:166–180.

[181] Freed AD, Einstein DR, Vesely I. Invariant formulation for dispersed transverse isotropy in aortic heart valves: An efficient means for modeling fiber splay. *Biomech. Model. Mechanobiol.* 2005; **4**:100–117.

[182] Ateshian GA, Rajan V, Chahine NO, Canal CE, Hung CT. Modeling the matrix of articular cartilage using a continuous fiber angular distribution predicts many observed phenomena. *J. Biomech. Eng.* 2009; **131**:61 003.

[183] Pierce DM, Ricken T, Holzapfel GA. A hyperelastic biphasic fibre-reinforced model of articular cartilage considering distributed collagen fibre orientations: continuum basis, computational aspects and applications. *Comput. Methods Biomech. Biomed. Engin.* 2012; In press.

[184] Federico S, Gasser TC. Nonlinear elasticity of biological tissues with statistical fibre orientation. *J. R. Soc. Interface* 2010; **7**:955–966.

[185] Weisbecker H, Pierce DM, Regitnig P, Holzapfel GA. Layer-specific damage experiments and modeling of human thoracic and abdominal aortas with non-atherosclerotic intimal thickening. *J. Mech. Behav. Biomed. Mater.* 2012; **12**:93–106.

[186] Merodio J, Ogden RW. Material instabilities in fiber-reinforced nonlinearly elastic solids under plane deformation. *Arch. Mech.* 2002; **54**:525–552.

Monographic Series TU Graz

Computation in Engineering and Science

Vol. 1 Steffen Alvermann

Effective Viscoelastic Behaviour of Cellular Auxetic Materials
2008
ISBN 978-3-902465-92-4

Vol. 2 Sendy Fransiscus Tantono

The Mechanical Behaviour of a Soilbag under Vertical Compression
2008
ISBN 978-3-902465-97-9

Vol. 3 Thomas Rüberg

Non-conforming FEM/BEM Coupling in Time Domain
2008
ISBN 978-3-902465-98-6

Vol. 4 Dimitrios E. Kiousis

Biomechanical and Computational Modeling of Atherosclerotic Arteries
2008
ISBN 978-3-85125-023-7

Vol. 5 Lars Kielhorn

A Time-Domain Symmetric Galerkin BEM for Viscoelastodynamics
2009
ISBN 978-3-85125-042-8

Vol. 6 Gerhard Unger

Analysis of Boundary Element Methods for Laplacian Eigenvalue Problems
2009
ISBN 978-3-85125-081-7

Monographic Series TU Graz

Computation in Engineering and Science

Vol. 7 Gerhard Sommer

Mechanical Properties of Healthy and Diseased Human Arteries
2010
ISBN 978-3-85125-111-1

Vol. 8 Mathias Nenning

Infinite Elements for Elasto- and Poroelastodynamics
2010
ISBN 978-3-85125-130-2

Vol. 9 Thanh Xuan Phan

Boundary Element Methods for Boundary Control Problems
2011
ISBN 978-3-85125-149-4

Vol. 10 Loris Nagler

Simulation of Sound Transmission through Poroelastic Plate-like Structures
2011
ISBN 978-3-85125-153-1

Vol. 11 Markus Windisch

Boundary Element Tearing and Interconnecting Methods for Acoustic and Electromagnetic Scattering
2011
ISBN: 978-3-85125-152-4

Monographic Series TU Graz

Computation in Engineering and Science

Vol. 12 Christian Walchshofer

Analysis of the Dynamics at the Base of a Lifted Strongly Buoyant Jet Flame Using Direct Numerical Simulation
2011
ISBN 978-3-85125-185-2

Vol. 13 Matthias Messner

Fast Boundary Element Methods in Acoustics
2012
ISBN 978-3-85125-202-6

Vol. 14 Peter Urthaler

Analysis of Boundary Element Methods for Wave Propagation in Porous Media
2012
ISBN 978-3-85125-216-3

Vol. 15 Peng Li

Boundary Element Method for Wave Propagation in Partially Saturated Poroelastic Continua
2012
ISBN 978-3-85125-236-1

Vol. 16 Jörg Schriefl

Quantification of Collagen Fiber Morphologies in Human Arterial Walls
2012
ISBN 978-3-85125-238-5

Vol. 17 Thomas S. E. Eriksson

Cardiovascular Mechanics
2013
ISBN 978-3-85125-277-4